

CRANFIELD UNIVERSITY

ABDENOUR ACHOUR

In-Situ TUNING OF CATALYTIC ACTIVITY
BY THERMOELECTRIC EFFECT

School of Aerospace, Transport and Manufacturing

PhD

Academic Year: 2014 - 2017

Supervisor: Dr Zhaorong Huang
May 2017

CRANFIELD UNIVERSITY

School of Aerospace, Transport and Manufacturing

PhD

Academic Year 2014 – 2017

ABDENOUR ACHOUR

In-Situ TUNING OF CATALYTIC ACTIVITY BY THERMOELECTRIC
EFFECT

Supervisor: Dr Zhaorong Huang

May 2017

This thesis is submitted in partial fulfilment of the requirements for the
degree of Doctor of Philosophy

© Cranfield University 2017. All rights reserved. No part of this
publication may be reproduced without the written permission of the
copyright owner.

ABSTRACT

For the first time, a new type of reactor which can combine thermoelectric energy harvesting and electrochemical promotion of catalysis was developed. A novel use of thermoelectric material as a catalyst support and promoter was investigated. A facile, cost-effective and scalable synthesis of thermoelectric material BiCuSeO has been developed.

It was discovered that the catalytic activity of Pt supported on the thermoelectric material BiCuSeO, through the ethylene oxidation, can be increased by several tens to several hundreds of times by a thermoelectric voltage. We call this Thermoelectric Promotion of Catalysis (TEPOC). The catalytic activity under fuel-lean and fuel-rich conditions was also investigated for ethylene oxidation. It is believed that oxygen was more strongly and C₂H₄ was weakly adsorbed on the catalyst Pt surface under lean-fuel conditions ($O_2/C_2H_4 > 1$). However, under rich-fuel conditions ($C_2H_4/O_2 > 1.4$), C₂H₄ became strongly adsorbed (probably chemisorbed) to the surface especially at a high Seebeck voltage, this blocked the catalyst surface, reduced the catalytic active site, hence the rate became smaller.

To further investigate the TEPOC effect, the CO₂ hydrogenation over the same catalysts supported on the thermoelectric BiCuSeO was also studied and the results confirmed similar significant promotional effect. It also was found that a negative thermoelectric voltage shifted chemical equilibrium towards the reverse water gas shift (RWGS) reaction and CO selectivity. As a results, the CO₂ hydrogenation conversion reached 48.4% (CO₂:H₂ = 1:4) with 100% CO selectivity for Pt(80)/BCSO at 656 K, which was above the thermodynamic equilibrium conversion (TEC) under no Seebeck voltage without methanation.

It was established a linear relationship between $\ln(r)$ and $-eV/k_bT$, where $-eV/k_bT$ is the ratio between the extra electrochemical energy induced by thermoelectric effect and the thermal energy of an electron. From this it was derived that the promotional effect was attributed to the change of work function of the catalyst surface, accompanied by charge transfer from the bulk to the surface due to the thermoelectric effect.

The discovery of TEPOC prompts that many catalytic chemical reactions can be tuned *in-situ* and independently from the change of conditions within the reaction chamber, to achieve much higher reaction rate, or at lower temperature, or have better desired selectivity through changing the backside temperature of the thermoelectric catalyst support.

Keywords

Heterogeneous catalysis; catalyst promoters; BiCuSeO; thermoelectric effect; thermoelectric promotion of catalysis

ACKNOWLEDGEMENTS

First, I wish to express my sincerest gratitude to Dr. Zhaorong Huang for giving me the opportunity to conduct this research, who also believing in me as a researcher. Thank you very much for your continuous supervision that had shaped me during this PhD study.

Sincerest thanks for all the collaborators that teamed up with me during this thesis: Professor Michael J. Reece and Dr. Kan Chen from School of Engineering and Materials Science, Queen Mary University of London for consolidate my thermoelectric materials samples and their transport properties measurements and Professor Ping Peng and Jian Liu from School of Materials Science and Engineering, Hunan University, Changsha for the modelling and simulation.

For their endless time, and patience for their help on all technical supports I would like to thank Mr Tim Pryor and Mr Andrew Stallard. Many thanks are also expressed to Drs. Christopher Shaw and Glenn Leighton for their advice and contribution on catalysts sputtering, as well for Drs. Xianwei Liu and Tracey Roberts for their help on materials characterisations.

I would like to express my appreciation to my colleagues at Surface Engineering and Nanotechnology Institute (SENTi) group at Cranfield University. I am also grateful to the funding received through the Leverhulme Trust to undertake my research.

Lastly, but most importantly, I am greatly indebted to my parents who have always been incredibly supporting and motivating me. My thanks also go out to my brothers, sister and wife for their continued encouragement and support during this PhD. My gratitude to them is beyond words.

TABLE OF CONTENTS

ABSTRACT	i
ACKNOWLEDGEMENTS.....	iii
LIST OF FIGURES.....	viii
LIST OF TABLES	xiii
LIST OF EQUATIONS.....	xiv
LIST OF ABBREVIATIONS	xvi
1 Introduction.....	1
1.1 Brief Background	1
1.2 Aim and Objectives	3
1.3 Thesis Structure.....	4
2 Literature Review	5
2.1 Literature Review on Thermoelectricity.....	5
2.1.1 Thermoelectric Effects.....	5
2.1.2 Thermoelectric Properties	8
2.1.3 Applications of Thermoelectric Effects	12
2.1.4 State of the Art of Thermoelectric materials	14
2.2 Literature Review on Heterogeneous Catalysis	22
2.2.1 Catalysis and Catalysts Promotions	22
2.2.2 Metal – Support Interaction	27
2.2.3 Catalyst Supports	29
2.2.4 In Situ and Controlled Promotion – NEMCA.....	30
2.2.5 Self-Sustain Electrochemical Promotion – SSEP	37
3 Materials Processing and Characterizations	39
3.1 Introduction	39
3.2 Electrochemical and Thermo-electrochemical Cells.....	39
3.2.1 Catalyst Supports	39
3.2.2 Catalysts Electrode Preparation.....	41
3.3 Characterization Methods	43
3.3.1 Microstructure Characterizations.....	43
3.3.2 Thermoelectric Properties Characterization	44
3.3.3 Simulation and modelling using ab initio method	45
3.3.4 Experimental Set-up for Catalytic Chemical Reactions	47
4 Fabrication and Characterization of Thermoelectric Ceramics	53
4.1 Introduction	53
4.2 Results and Discussion.....	54
4.2.1 Fabrication Process and Structure Analysis.....	54
4.2.2 Morphology and Microstructure Analysis of the SPS'ed samples	59
4.2.3 Thermal and Chemical Stability.....	60
4.2.4 Thermoelectric Properties Characterisation	63

4.3 Conclusions	71
5 Validation of the Experimental Setup	72
5.1 Introduction	72
5.2 Results and Discussion.....	72
5.2.1 XRD and TEM of Pt Nanoparticles Catalysts	72
5.2.2 XRD and SEM of Pt Film Deposited on YSZ.....	75
5.2.3 GC Development and Validation	76
5.2.4 Ethylene Oxidation on Blank Reactor.....	77
5.2.5 Ethylene Oxidation on Supported Pt Nanoparticles.....	79
5.2.6 Ethylene Oxidation on Pt/YSZ with NEMCA Effect.....	80
5.3 Conclusions	82
6 In-situ Tuning of Catalytic Activity by Thermoelectric Effect for Ethylene Oxidation Reaction	83
6.1 Introduction	83
6.2 Results and Discussion.....	83
6.2.1 Characterisation of Pt Catalysts	83
6.2.2 Substantial Higher Catalytic Activity on TE Materials.....	85
6.2.3 Tuning of Catalytic Activity by Seebeck Effect	89
6.2.4 Relationships Between Thermoelectric Effect and Catalytic Activity under Fuel-Lean Conditions.....	91
6.2.5 Test the Prediction of the Thermoelectric Inhibition of Catalysis	98
6.2.6 Simulation of Pt/BCSO Interaction and the Mechanism for Thermoelectric Promotion of Catalysis.....	100
6.2.7 Dependence of Catalytic Activity on Oxygen Pressure under Fuel-Lean Conditions	104
6.2.8 Relationships between Thermoelectric Voltage and Catalytic Activity under Fuel-Rich Conditions	106
6.2.9 Dependence of Catalytic Activity on Ethylene Pressure under Fuel-Rich Conditions	110
6.3 Conclusions	113
7 In-situ Tuning of Catalytic Activity by the Thermoelectric Effect for Carbon Dioxide Hydrogenation	115
7.1 Introduction	115
7.2 Results and Discussion.....	116
7.2.1 Brief Experimental Introduction	116
7.2.2 Substantial Higher Catalytic Activity under Large TE Effect	119
7.2.3 Selectivity of CO ₂ Hydrogenation into CO under Thermoelectric ...	120
7.2.4 Relationships between Thermoelectric Effect and Catalytic Activity	122
7.2.5 In-situ Modification of Catalytic Activity via Seebeck Effect.....	129
7.3 Conclusions	131
8 Conclusions and Recommendations for Future Work	132

8.1 Conclusions	132
8.2 Recommendations for Future Work	135
REFERENCES	137
APPENDICES.....	158
Appendix A – Analytical Method Development and Validation.....	158
Appendix B – Supplementary Information for Chapter 6.....	164
Appendix C – Scholarly Contributions.....	168

LIST OF FIGURES

Figure 2-1. The Seebeck effect of two dissimilar metals in an open circuit.	5
Figure 2-2. The Seebeck effect of a single compound in an open circuit.	6
Figure 2-3. The scheme of the Peltier effect.	7
Figure 2-4. A positive Thomson efficient at a given temperature gradient and electric current to absorb heat.	8
Figure 2-5. The ZT maximum involves compromised thermal conductivity and Seebeck coefficient, with electrical conductivity (Dughaish, 2002).	12
Figure 2-6. Thermoelectric modules for power generation (a); cooling (b).	13
Figure 2-7. ZT of the current bulk thermoelectric materials as a function of year (Zhang and Zhao, 2015).	14
Figure 2-8. Schematics of (a) Eley-Rideal; (b) Langmuir-Hinshelwood mechanisms.	22
Figure 2-9. Schematic diagram of the energy bands in the case of metal having a larger work function than the n-type semiconductor.	28
Figure 2-10. Basic electrochemical cell of electrochemical promotion NEMCA.	32
Figure 2-11. Galvanostatic transient of electrochemical promotion NEMCA.	33
Figure 2-12. Oxygen spillover mechanism in catalytic system.	33
Figure 2-13. (a) NEMCA; (b) Metal – Support interaction, the location of the classical double layers formed at the metal-support interface and the effective double layers formed at the metal-gas interface adapted from (Nicole et al., 2001).	36
Figure 2-14. Schematic of electrochemically promoted partial oxidative reforming of fuel C_mH_n	38
Figure 3-1. Schematic and actual pictures of three electrodes in a single pellet configuration for TEPOC investigation.	41
Figure 3-2. (a) Schematic; (b) actual picture of the single chamber reactor; (c) a disc sample onto a custom-built glass ceramic holder.	48
Figure 3-3. Schematic of the arrangement of the sample and the measured parameters for all the catalytic reaction experiments: (a) TEPOC conditions; (b) TE inhibition conditions.	49
Figure 3-4. Schematic of the experimental set-up for C_2H_4 oxidation reaction characterisation.	50

Figure 3-5. Schematic of the experimental set-up for CO ₂ hydrogenation reaction characterisation.	52
Figure 4-1. Fabrication process of BCSO samples: (a) alumina crucible filled with raw chemicals; (b) broken alumina crucible after flux synthesis; (c) as – synthesized products after the removal of B ₂ O ₃ ; (d) a SPS'ed pellet.	54
Figure 4-2. (a) Photograph; (b) XRD patterns for different positions Z1, Z2, Z3, and a cross section of as-synthesised undoped BCSO.	55
Figure 4-3. (a) XRD patterns of pure BCSO powder and SPS'ed pellet (b) enlargement patterns for a section of (a).	56
Figure 4-4. (a) XRD patterns; (b) enlargement patterns sections of (a); (c) lattice parameters of Bi _{1-x} Cs _x CuSeO.	58
Figure 4-5. SEM cross section micrographs of Bi _{1-x} Cs _x CuSeO (x = 0 – 0.025) synthesized by flux – SPS'ed: (a) x = 0; (b) x = 0.005; (c) x = 0.01; (d) x = 0.015; (e) x = 0.025.	59
Figure 4-6. (a) Differential scanning calorimetry; and (b) thermogravimetric analysis of Bi _{1-x} Cs _x CuSeO (x = 0 – 0.025) samples under flowing argon and air.	61
Figure 4-7. Bar-sample of Cs Doped BCSO after TE measurements: (a) 0.5%; (b) 1%.	62
Figure 4-8. SEM image, EDS spectrums and elemental quantification results showing the typical composition found at Bi _{0.99} Cs _{0.01} CuSeO sample.	63
Figure 4-9. Temperature dependence of thermoelectric properties for the BCSO synthesized by SSR, SHS and the flux methods: (a) electrical conductivity; (b) Seebeck coefficient; (c) power factor.	65
Figure 4-10. Temperature dependence of SPS'ed BCSO synthesized by SSR, SHS and flux methods: (a) thermal conductivity; (b) thermoelectric figure of merit.	66
Figure 4-11. Temperature dependence of SPS'ed Bi _{1-x} Cs _x CuSeO (x = 0 – 0.01) synthesized by the flux method: (a) electrical conductivity; (b) Seebeck coefficient; (c) power factor.	68
Figure 4-12. Temperature dependence of Bi _{1-x} Cs _x CuSeO (x = 0 – 0.01) synthesized by the flux method: (a) thermal conductivity; (b) thermoelectric figure of merit.	69
Figure 5-1. (a) X-ray diffraction patterns of Pt/YSZ and Pt/ γ-Al ₂ O ₃ . (b) enlargement patterns of Pt (111) peaks.	73
Figure 5-2. TEM images: (a) Pt/γ-Al ₂ O ₃ ; (b) Pt/YSZ and the corresponding histograms; (c) EDS spectra of clustered Pt particles on YSZ as shown in (b) Pt/YSZ selected area.	74

Figure 5-3. XRD patterns of platinum film on YSZ after the thermal treatment. Inset: $\theta/2\theta$ scan in the range of 38.50° and 42.5° of the freshly deposited platinum film on YSZ before and after the pre-treated in 5% H_2 /Ar at 603 K for 2h.	75
Figure 5-4. SEM micrographs of the Pt film on YSZ: (a) before; (b) after catalytic chemical condition; (c) a boundary area includes Pt/YSZ and pure YSZ; (d) back-scattered electron image from the same area shown in (c).	76
Figure 5-5. A typical chromatogram via GC/TCD of a mixture containing O_2 , CO_2 , and C_2H_4 in helium carrier gas, from a gas standard.	77
Figure 5-6. Blank tests for empty reactor. Reaction conditions: C_2H_4/O_2 : 907 ppm/3.3%, feed gas flow rate 100 mL min^{-1} for cycle 1, 2 and 3; $PC_2H_4/PO_2=0.189/3.01\text{ kPa}$; feed gas flow rate 200 mL min^{-1} for the cycle 4 was after 2 weeks.	78
Figure 5-7. Catalytic activity as represented by C_2H_4 Conversion for the blank supports and nanoparticles Pt catalysis for ethylene oxidation. Reaction conditions: C_2H_4/O_2 : 907 ppm/3.3% O_2 , feed gas flow rate 100 mL min^{-1}	80
Figure 5-8. Ethylene oxidation conversion and rate as a temperature function of YSZ-Au and Pt/YSZ/Au. Reaction conditions: $PC_2H_4/PO_2=0.189/3.01\text{ kPa}$; feed gas flow rate 200 mL min^{-1} under Open Circuit (OC).	81
Figure 5-9. Electrochemical promotion of ethylene oxidation on Pt/YSZ/Au catalyst. Gas composition: Reaction conditions: $T = 643\text{ K}$; $V_{wr} = -1\text{ V}$; $PC_2H_4/PO_2=0.189/3.01\text{ kPa}$; feed gas flow rate 200 mL min^{-1}	82
Figure 6-1. X-ray diffraction patterns of catalyst systems after catalytic chemical reaction characterisation for the samples: BCSO; Pt(NP)/BCSO; Pt(15)/BCSO; Pt(80)/BCSO and Pt(80)/(BCSO) $_{0.9}$ (YSZ) $_{0.1}$	84
Figure 6-2. SEM micrographs of the five samples: (a) BCSO; (b) low and (c) high magnification for Pt(15)BCSO; (d) Pt(80)/ BiCuSeO $_{0.9}$ YSZ $_{0.1}$; (e) Pt(80)/BCSO; (f) Pt(NP)/BCSO.	85
Figure 6-3. Ethylene oxidation rates as a function of temperature at the catalyst surfaces, for Pt(80)/YSZ which has no thermoelectric effect, and for Pt(80)/BCSO under large TE effect (Pt(80)/BCSO TE) and reduced TE effect (RTE) conditions.	86
Figure 6-4. X-ray diffraction patterns of the Pt(NP)/BCSO after catalytic reaction measurement for the cold side (top) and the hot side (bottom).	89
Figure 6-5. Ethylene oxidation rate as a function of the Seebeck voltage $-V$ for ethylene oxidation at constant temperatures $T_h=705\text{ K}$ and $T_c=339\text{ K}$ for Pt(NP)/BCSO.	90
Figure 6-6. Typical time profile of recorded Seebeck voltage. Time profile of the recorded Seebeck voltage during catalytic reaction characterisation experiments of BCSO.	91

Figure 6-7. Reaction rate r as a temperature function of the five samples: BCSO, Pt(NP)/BCSO, Pt(15)BCSO, Pt(80)/BCSO and Pt(80)/BiCuSeO _{0.9} YSZ _{0.1} .	92
Figure 6-8. Measured Seebeck voltage as functions of temperature difference across the sample thickness.	93
Figure 6-9. Arrhenius law for ethylene oxidation on Pt. $\ln(r)$ as a function of $1/T$ for ethylene oxidation rate on Pt(80)/YSZ. YSZ is not a thermoelectric material.	94
Figure 6-10. A linear relationship between $\ln(r)$ and $-eV/k_bT_h$ of the five samples: BCSO, Pt(NP)/BCSO, Pt(15)BCSO, Pt(80)/BCSO and Pt(80)/BiCuSeO _{0.9} YSZ _{0.1} .	96
Figure 6-11. The rate r is proportional to the Seebeck voltage V of the five samples: BCSO, Pt(NP)/BCSO, Pt(15)BCSO, Pt(80)/BCSO and Pt(80)/BiCuSeO _{0.9} YSZ _{0.1} .	97
Figure 6-12. The ethylene oxidation rate as a function of temperature T_c of bare BCSO TE materials when it was placed directly onto the hot stainless steel floor of the reaction chamber. The calculated reaction rate was obtained using the equation $r = k_0 \cdot \exp(-E_a/k_bT_c) \cdot \exp(-\gamma eV/k_bT_c)$ with the fitting parameters $k_0 = 7.127 \times 10^8$, $E_a = 56.1$ kJ/mol, and $\gamma = 27.8$.	99
Figure 6-13 (a) The distribution of electrostatic potential; (b) the charge density difference.	100
Figure 6-14. (a) The Fermi level dependence on temperature at different charge carrier concentrations for n-type and p-type BCSO; (b) The calculated temperature dependence of charge transfer from a BCSO to Pt assuming a donor concentration 10^{19} /cm ³ .	101
Figure 6-15. Schematic of energy bands and Fermi levels for p-type and n-type TE materials and a metal particle supporting on the TE materials at the hot side. T_c and T_h are the temperatures at the cold and hot ends respectively. The arrow heads point the electric field direction within the TE material.	103
Figure 6-16. Ethylene oxidation reaction rate as a function of oxygen partial pressure of Pt(15)BCSO, Pt(80)/BCSO, Pt(80)/ BiCuSeO _{0.9} YSZ _{0.1} and bare BCSO with thermoelectric promotion of catalysis effect.	104
Figure 6-17. Reaction rate as a function of temperature T_h of the four samples: BCSO, Pt(15)BCSO, Pt(80)/BCSO and Pt(80)/BiCuSeO _{0.9} YSZ _{0.1} .	107
Figure 6-18. Measured Seebeck voltage as functions of temperature difference across the sample thickness of the four samples: BCSO, Pt(15)BCSO, Pt(80)/BCSO and Pt(80)/BiCuSeO _{0.9} YSZ _{0.1} .	108
Figure 6-19. (a) The reaction rate r as a function of Seebeck voltage V ; (b) relationship between $\ln(r)$ and $-eV/k_bT_h$ of the four samples: BCSO, Pt(15)BCSO, Pt(80)/BCSO and Pt(80)/BiCuSeO _{0.9} YSZ _{0.1} .	109

Figure 6-20. Ethylene oxidation reaction rate (a); conversion (b) as a function of ethylene partial pressure of Pt(15)BCSO, Pt(80)/BCSO, Pt(80)/BiCuSeO_{0.9}YSZ_{0.1} and bare BCSO with thermoelectric promotion of catalysis. 111

Figure 7-1. Measured Seebeck voltage as a function of elapsed time during the catalytic reaction characterisation experiment of Pt(80)/BCSO at CO₂/H₂=1: 4. 117

Figure 7-2. CO₂ conversion rate as a function of temperature of Pt(80)/BCSO and BCSO under TE and RTE effect conditions at CO₂/H₂=1. 119

Figure 7-3. A linear relationship between Ln(X) and $-eV/k_bT_h$ of Pt(80)/BCSO and BCSO under TE and RTE effect conditions at CO₂/H₂=1. 120

Figure 7-4. CO selectivity as a temperature function of BCSO, Pt(15)BCSO, Pt(80)/BCSO and Pt(NP)/BiCuSeO: (a) CO₂/H₂ = 1; (b) CO₂/H₂ = 1/4. ... 121

Figure 7-5. Measured thermoelectric voltage as a function of temperature difference across the sample thickness under TE effect of different samples BCSO at gas feed (a) CO₂:H₂ = 1; (b) CO₂:H₂ = 1/4. 122

Figure 7-6. Effect of temperature on CO₂ conversion of the four samples under TE effect at gas feed (a) CO₂/H₂ = 1; (b) CO₂/H₂ = 1/4. 124

Figure 7-7. The CO₂ conversion proportional to the Seebeck voltage V of the four samples at gas feed (a) CO₂:H₂ = 1; (b) CO₂:H₂ = 4. 125

Figure 7-8. CO and CH₄ yields as a function of temperature for BCSO, Pt(15)BCSO, Pt(80)/BCSO and Pt(80)/BCSO: (a) CO₂:H₂ = 1 and (b) CO₂:H₂ = 1/4. 126

Figure 7-9. A linear relationship between Ln(r) and $-eV/k_bT_h$ under TE condition for BCSO, Pt(15)BCSO, Pt(80)/BCSO and Pt(80)/BCSO with CO₂:H₂ = 1 and CO₂:H₂ = 1/4. 127

LIST OF TABLES

Table 2-1 Comparison at room temperature of typical thermoelectric properties of metal, semiconductor and insulator.	11
Table 2-2. Seebeck Coefficient of different metals and alloys (Blatt <i>et al.</i> , 1976).	15
Table 2-3. Thermoelectric properties between different classes of thermoelectric materials.	21
Table 2-4. Examples of promoters in the chemical industry.	25
Table 5-1. Characteristic of Pt nanoparticles catalysts prepared by polyol reduction method.	73
Table 5-2. Material balance calculation of blank reactor from 296 K to 688 K..	79
Table 6-1. Summary of experimental conditions and catalytic reaction measurement results of Pt(80)/BCSO in Figure 6-4. T_c and T_h are the temperatures at the top cold surface and bottom hot surfaces respectively, V the Seebeck voltage. Every catalyst chemical reaction testing experiment generated a table like this.	88
Table 6-2. Summary of Seebeck voltage and reaction rate and ethylene conversion at constant temperature $T_h = 705$ K and $T_c = 339$ K of the sample Pt(NP)/BCSO. The change in the Seebeck coefficient leads to the change of the Seebeck voltage, which resulted in the increase of catalytic reaction rate.	90
Table 6-3. Summary of the measured Seebeck voltage, reaction rate (nmolO/s) and ethylene conversion at different “cold” side temperatures T_c of the bare BCSO sample.	98
Table 6-4. Summary of ethylene oxidation rate and conversion under different oxygen partial pressures of Pt(15)BCSO, Pt(80)/BCSO, Pt(80)/BiCuSeO _{0.9} YSZ _{0.1} and bare BCSO with a specific Seebeck voltage and fixed temperature for each sample.	105
Table 6-5. Summary of ethylene oxidation rate and conversion under different ethylene partial pressures for Pt(15)BCSO, Pt(80)/BCSO, Pt(80)/BiCuSeO _{0.9} YSZ _{0.1} and bare BCSO with a specific Seebeck voltage and fixed temperature for each sample.	112
Table 7-1. Summary of experimental conditions and CO ₂ hydrogenation reaction measurement results of Pt(80)/BCSO. T_c , T_h were the temperatures at the top cold surface and bottom hot surface respectively, V the Seebeck voltage. Gas amounts were obtained from their measured respective peak areas in GC.	118

LIST OF EQUATIONS

Equation 2-1	6
Equation 2-2	6
Equation 2-3	7
Equation 2-4	7
Equation 2-5	8
Equation 2-6	9
Equation 2-7	9
Equation 2-8	10
Equation 2-9	10
Equation 2-10	11
Equation 2-11	31
Equation 2-12	32
Equation 2-13	32
Equation 2-14	34
Equation 2-15	34
Equation 2-16	34
Equation 2-17	34
Equation 2-18	34
Equation 2-19	35
Equation 3-1	43
Equation 3-2	44
Equation 3-3	46
Equation 3-4	46
Equation 3-5	46
Equation 3-6	46
Equation 3-7	46
Equation 3-8	50
Equation 3-9	51

Equation 3-10.....	51
Equation 3-11.....	51
Equation 3-12.....	51
Equation 3-13.....	51
Equation 3-14.....	52
Equation 3-15.....	52
Equation 3-16.....	52
Equation 3-17.....	52
Equation 6-1.....	93
Equation 6-2.....	95
Equation 6-3.....	95
Equation 6-4.....	95
Equation 6-5.....	99
Equation 6-6.....	102
Equation 6-7.....	102
Equation 7-1.....	127
Equation 7-2.....	130

LIST OF ABBREVIATIONS

BCSO	BiCuSeO
DSC	Differential Scanning Calorimetry
EDS	Energy Dispersive Spectroscopy
EMSI	Electronic Metal – Support Interaction
EPOC	Electrochemical Promotion of Catalysis
FWHM	Full-Width at Half-Maximum
GC	Gas Chromatography
MEPR	Monolithic Electrochemically Promoted Reactor
MIEC	Mixed Ionic-Electronic Conductor
MSI	Metal-Support Interaction
NEMCA	Non-Faradaic Electrochemical Modification of Catalytic Activity
RTE	Reduced Thermoelectric Effect
RSD	Relative Standard Deviation
RWGS	Reverse Water Gas Shift
TE	Thermoelectric Effect
TEG	Thermoelectric Generator
TEM	Transmission Electron Microscopy
TEPOC	Thermoelectric Promotion of Catalysis
TCD	Thermal Conductivity Detector
TGA	Thermal Gravimetric Analysis
TPB	Triple Phase Boundary
SEM	Scanning Electron Microscopy
SHS	Self-propagating High Temperature Synthesis
SMSI	Strong Metal – Support Interaction
SPS	Spark Plasma Sintering
SSEP	Self-Sustained Electrochemical Promotion
SSR	Solid-State Reaction
YSZ	Yttria Stabilized Zirconia
ZT	Figure of Merit
XRD	X-Ray Diffraction

1 Introduction

1.1 Brief Background

More than 90% of the chemical industrial processes in use throughout the world utilize catalysts in one form or another. A catalyst is a substance that increases the rate of attainment of chemical equilibrium without itself enduring chemical change. Heterogeneous catalysis refers to the form of catalysis where the phase of the catalyst differs from that of the reactants. It consists of one bulk catalyst or two major components (active metal and the support). In theory, the reactants diffuse to the catalyst surface and are adsorbed onto it physically or by the formation of a chemisorption bond. After reaction, the products desorb and diffuse away from the surface (Thomas and Thomas, 1996; Niemantsverdriet, 2007).

A good catalyst must possess both long-term stability and high activity accompanied with an important attribute – selectivity, which reflects its ability to direct conversion of the reactants along one specific pathway. The technology and science of catalysis are therefore of central practical importance. Until recently, new tools and techniques rather than new concepts are responsible for progress in the identification of elementary steps and have deepened the understanding of electron transfer and atomic transformations at solid surfaces (catalytic mechanisms).

This project is related to the more effective use of catalysts. Catalyst promoters improve the activity, selectivity or lifetime of a catalyst, and can generally be divided into structural and electronic promoters. Structural promoters enhance and stabilize the dispersion of the catalyst on the support. Electronic promoters induce changes of electronic state of the catalyst near the Fermi level (Vayenas *et al.*, 2001; Vayenas, Brosda and Pliangos, 2003). A well-known example of the later is the use of alkalis (K) on Fe for Fischer-Tropsch synthesis. It is believed that the low ionization potential of alkali K lead to a charge transfer to the Fe catalyst surface, modifying the Fermi level and the associated density of states of the catalyst (Kotarba *et al.*, 2004).

Catalyst supports, usually insulating or semiconducting oxides, can also play a direct or indirect role which influences significantly the catalytic properties (Wieckowski, Savinova and Vayenas, 2003; Matsubu *et al.*, 2016). For example, ethylene oxidation rate on Rh supported on doped TiO₂ was 120 times higher than Rh supported on

undoped TiO₂ (Nicole *et al.*, 2001). This metal-support-induced promotional phenomena is explained based on the framework of metal-semiconductor contact theory (Ioannides and Verykios, 1996; Zhang and Yates, 2012). The electron transfer has been proposed to account for the changes in the adsorptive and catalytic properties of the metal on semiconductor system: when a metal is supported on a semiconductor oxide, the difference in work functions or Fermi levels between the metal and the support lead to a charge transfer from the support to the metal, the transferred charge is believed to lie at the metal-semiconductor interface, on the side of the metal (Zhang and Yates, 2012).

The above promoters are added and fixed during catalyst preparation, therefore cannot be altered and are subject to degradation during catalytic process. On the other hand, electrochemical promotion of catalysis, also called Non-Faradaic Electrochemical Modification of Catalytic Activity (NEMCA), which can alter reversibly the catalytic selectivity and activity of catalytic active ingredient deposited on solid electrolyte by applying constant voltage or constant current to the catalyst/electrolyte interface (Harkness *et al.*, 1996; Konsolakis *et al.*, 2000; Vayenas *et al.*, 2001; Poulidi, Anderson and Metcalfe, 2008; De Lucas-Consuegra, González-Cobos, Gacia-Rodríguez, *et al.*, 2012; De Lucas-Consuegra, González-Cobos, García-Rodríguez, *et al.*, 2012; Kambolis *et al.*, 2012). NEMCA has proved to be an excellent research techniques but its use in large scale industry is limited mainly due to its low efficiency of catalyst materials (which are often expensive noble metals) because it requires a continuous electrode to maintain electrical conductivity (Tsiplakides and Balomenou, 2008). Recently, metal nanoparticles catalysts deposited on a high surface area support have been observed to show much improved catalytic activity, and this is called strong-metal-support-interaction (SMSI) (Tauster, 1987; Campbell, 2012)

In fact, most catalytic chemical reactions are carried out at high temperatures. So, there is a natural temperature difference between a reaction chamber and an outside ambient environment. A benefit of this temperature gradient is that it could be used by utilising thermoelectric materials to convert it directly into electricity via Seebeck coefficient (S). In this thesis, the realization of in-situ, and significant modification of catalytic activity is conducted under operation conditions for thin film and non-continuous nanoparticles Pt, by creating a temperature difference across the thickness of the thermoelectric catalyst support. Ethylene oxidation (S. Bebelis and Vayenas,

1989; C. Pliangos *et al.*, 1996) and CO₂ hydrogenation (Solymosi *et al.*, 1982; Wang *et al.*, 2011) reactions are used as model reactions for this investigation.

The original aim of this research was to use the nanocomposites, which consisted of thermoelectric nanowires embedded in ion-conducting solid-state electrolyte, as catalyst support, to achieve the ultimate goal of electrochemical promotion of catalysis for highly dispersed, non-continuous catalysts. However, after some initial studies using the thermoelectric-electrolyte composites as a catalyst support, it was soon realized that significant promotional effect of catalysis can be achieved without solid state electrolytes, and the thermoelectric material alone as a catalyst support can change the catalytic activity profoundly due to the generated Seebeck voltage due to the change of catalyst work function.

1.2 Aim and Objectives

The aim of the project is to achieve significant promotion of catalysis for non-continuous nanoparticles in real catalyst through the use of thermoelectric materials as a catalyst support and promoter. To achieve this aim, the following objectives will be fulfilled:

1. Design and manufacture a reactor which can combine thermoelectric energy harvesting with the electrochemical promotion of catalysis.
2. Develop a cost-effective and scalable method to synthesise thermoelectric materials, which are stable at mid-to-high temperatures and of high Seebeck coefficient and low thermal conductivity.
3. Prepare continuous thin film and non-continuous nanoparticles catalyst systems, so that a direct comparison to the NEMCA can be investigated, and the promotion to the non-continuous nanoparticles catalysts can be demonstrated.
4. Demonstrate the new concept of thermoelectric promotion of catalysis in an oxidation catalytic reaction.
5. Demonstrate the new concept of thermoelectric promotion of catalysis in a reducing catalytic reaction.
6. Investigate the underlining mechanism of the thermoelectric promotion of catalysis.
7. Compare the newly discovered thermoelectric promotion of catalysis with NEMCA.

1.3 Thesis Structure

This thesis is divided into eight chapters of which this is the first Chapter. Each chapter is briefly described below. After providing a literature review on thermoelectric materials and heterogeneous catalysis (Chapter 2), the preparation and characterisation of a thermoelectric material most suitable for this project, and catalysts are presented in Chapters 3 and 4. The description and validation of the new reactor which can combine thermoelectric energy harvesting and electrochemical promotion of catalysis are presented in Chapters 3 and 5. The investigation and demonstration of a new phenomenon, called thermoelectric promotion of catalysis (TEPOC), on ethylene oxidation and CO₂ hydrogenation reactions, can be found in Chapters 6 and 7. This dissertation finishes with Chapter 8 which summarises the main conclusions of this work as well as recommendations for further studies.

2 Literature Review

2.1 Literature Review on Thermoelectricity

The thermoelectric (TE) materials are able to convert a temperature gradient into electrical power, and inversely, electricity into a temperature gradient. These materials can generate electricity from waste heat or be used as solid-state Peltier coolers, which could play an important role in a global sustainable energy solution. These energy converters require no moving parts or working fluids. Moreover, they can operate without maintenance. There are three well-known major effects involved in the thermoelectric phenomenon: the Seebeck, Peltier and Thomson effects. In this section, the fundamentals of thermoelectric effects, their properties and applications will be introduced and discussed.

2.1.1 Thermoelectric Effects

2.1.1.1 Seebeck Effect

In 1821, A German physicist Thomas Johann Seebeck found that a circuit made from two dissimilar metals with junctions at different temperatures would deflect a compass magnet (Martin, Tritt and Uher, 2010). Initially, Seebeck believed this was the thermomagnetic effect due to magnetism induced by the temperature difference. Afterwards, Danish physicist Hans Christan Ørsted realized the thermomagnetic force was induced by an electric current produced by the temperature difference and gave the term thermoelectricity.

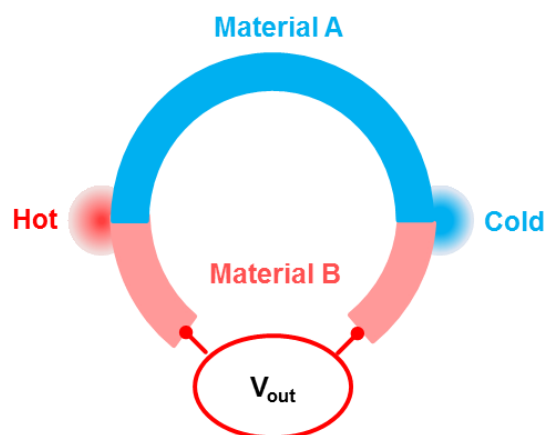


Figure 2-1. The Seebeck effect of two dissimilar metals in an open circuit.

At the junctions of two dissimilar materials (A and B), the two temperatures are different ($T_1 > T_2$). As a result, a voltage (and hence the current) is developed across two points (end of the B material). In other words, at an open circuit condition, with the temperature difference at the two junctions an electrical potential difference (voltage, V_{out}) would build up, as illustrated in Figure 2-1. A linear relationship exists between the temperature gradient (ΔT) and the voltage (V):

$$V_{out} = S_{AB} \cdot \Delta T \quad \text{Equation 2-1}$$

where S_{AB} is called Seebeck coefficient between the two materials A and B (Martin, Tritt and Uher, 2010).

The Seebeck effect can also occur in a single compound, as illustrated in Figure 2-2. When its ends are subjected to a temperature gradient (ΔT), a non-uniform carrier energy distribution occurs, and higher energy carriers at the hot end tend to diffuse to the cold end, establishing an electric field, a space charge region and potential difference inside the materials (V). The Seebeck coefficient of this material is given as

$$S = - \frac{V}{\Delta T} \quad \text{Equation 2-2}$$

where V is the thermoelectric voltage between the two ends and S is the Seebeck coefficient of the material.

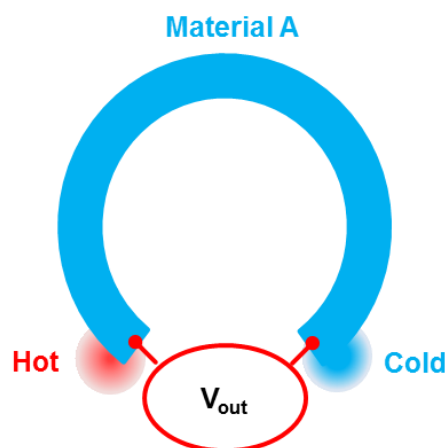


Figure 2-2. The Seebeck effect of a single compound in an open circuit.

2.1.1.2 Peltier Effect

This effect was discovered by Jean Charles Peltier in 1834. He showed that if an electric current (or voltage) is applied across the B material (Figure 2-3), there will be flow of current through the same material. The junctions of the dissimilar materials (A and B) attain different temperatures. Then heating-absorption or cooling-emission (Q) may be generated at one junction but removed at another junction depending on the direction of the current as illustrated on Figure 2-3, and expressed as

$$Q = \Pi \cdot I \quad \text{Equation 2-3}$$

where Π is the Peltier coefficient, I current flow.

As the Peltier effect is the reverse process to the Seebeck effect, hence these two effects are related to each other according to the Onsager reciprocal relation (Onsager, 1931), which states that S and Π satisfy the relation as

$$\Pi = S \cdot T \quad \text{Equation 2-4}$$

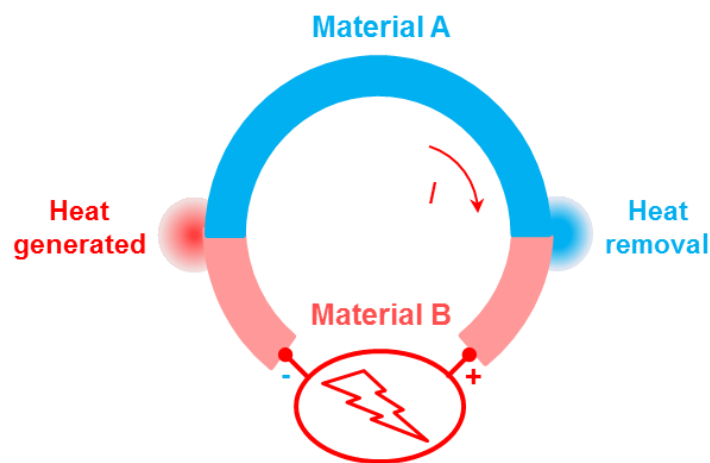


Figure 2-3. The scheme of the Peltier effect.

2.1.1.3 Thomson Effect

In 1851 (Goddard, 2011), William Thomson published a comprehensive explanation of the Seebeck and Peltier effects and described their interrelationship – Kelvin Relation which are related through thermodynamics. In the Thomson effect, heat is absorbed or produced when current flows in a material with a temperature gradient. The heat is proportional to both the temperature gradient (ΔT) and the electric current

(l). The proportionality, Thomson coefficient, is related by thermodynamics to Seebeck coefficient, which can be calculated as

$$q = \tau \cdot I \cdot \Delta T \quad \text{Equation 2-5}$$

In which q is the heat absorption or release rate and τ is the Thomson coefficient. With the electric current flowing towards the hot side and a positive temperature gradient, a positive Thomson coefficient means the material absorbs heat (Figure 2-4).

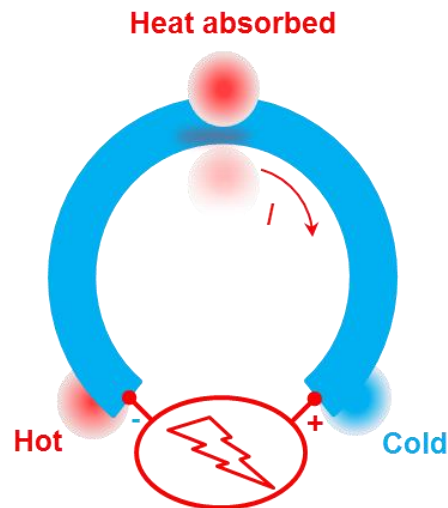


Figure 2-4. A positive Thomson efficient at a given temperature gradient and electric current to absorb heat.

2.1.2 Thermoelectric Properties

2.1.2.1 Seebeck Coefficient

The Seebeck effect is defined as “the amount of thermoelectric voltage (V) induced between the two thermocouples per unit temperature difference”. It is mainly depending on their electronic band structure which depends on the density of State (DOS) in the range of Fermi level. A high DOS and medium carrier concentration produces a large Seebeck coefficient. However, these are not parameters readily accessible and they require more detailed measurements of the electrical transport properties. The sign of Seebeck coefficient depends on the type of carriers conducting electricity. If electricity is produced by electrons, then the coefficient sign is negative or by holes then the sign is positive.

2.1.2.2 Electric Conductivity

It is a property of material which measures its ability to conduct electricity by either electron, holes or both. It can be expressed in the form of equation as

$$\sigma = n e \mu \quad \text{Equation 2-6}$$

Where σ is the electrical conductivity, n is the carrier charge per unit volume, e is the charge of the electron and μ is the mobility of carriers. The electrical conductivity values are finite numbers since there are no pure materials on earth and each material is associated with some impurities which can act as barrier for flow of the electron and scatter the electron inside the materials. Ioffe observed that the carrier concentration of good thermoelectrics $n \sim 10^{18} - 10^{20} \text{ cm}^{-3}$, which corresponds to doped semiconductors (Dughaish, 2002; Hsu *et al.*, 2004). As temperature is increased, the electrical conductivity of thermoelectric materials also increases. The increase of carrier concentration with temperature overcomes the drop in the carrier mean free time and results in the electrical conductivity enhancement (Sze and Ng, 2006). Moreover, the electrical conductivity in thermoelectric materials can also be altered by doping or having a small band gap. Doping of a thermoelectric material is an effective way to increase carrier concentration. However, as can be seen in Figure 2-5, higher carrier concentration leads to the decrease of Seebeck coefficient (Shakouri, 2011).

2.1.2.3 Thermal Conductivity

Thermal conductivity is a property of material which measures the material's ability to conduct heat either by the phonons, the charge carriers, electromagnetic waves, spin waves or other excitations (Chasmar and Stratton, 1959). The thermal conductivity κ of TE materials consists of two parts, i.e. the lattice thermal conductivity κ_L , and electrical thermal conductivity κ_E as:

$$\kappa = \kappa_L + \kappa_E \quad \text{Equation 2-7}$$

The ratio of thermal conductivity (κ) to electrical conductivity (σ) is proportional to temperature by a factor known as the Lorenz number (L_0) through the Wiedemann-Franz relationship:

$$\kappa_E = L_0 \cdot \sigma \cdot T$$

Equation 2-8

where the Lorentz number $L_0 = 2.45 \times 10^{-8} \text{ W}\Omega\text{K}^{-2}$. Hence, reducing the lattice part of thermal conductivity, κ_L is essential to enhance the efficiency of thermoelectric materials. There are essentially two ways to minimize the lattice thermal conductivity: (i) decreasing thermal diffusivity; (ii) lower constant volume specific heat, which is essentially temperature-independent in typical materials. Therefore, the magnitude and temperature-dependence of κ_L are basically determined by thermal diffusivity (D), or the mean free path of the phonons.

$$\kappa = C_p \cdot \rho \cdot D$$

Equation 2-9

where D is the thermal diffusivity, C_p the specific heat and ρ the mass density. Introducing phonon scattering can reduce the lattice thermal conductivity. This can be realised using a variety of methods, such as mass fluctuation scattering, rattling scattering, grain-boundary scattering, and interface scattering in thin films (Tritt and Subramanian, 2006).

Materials can be classified into metals, semiconductor, and insulators. These three different classes of materials are usually characterized by zero, small and large energy band gaps, respectively, or by different free charge carrier concentrations. Table 2-1 illustrates typical values for the Seebeck coefficient S, the electrical conductivity and the total thermal conductivity. In metals, the Seebeck coefficient is much too low while in insulators the electrical conductivity is very small. Only semiconductors possess high Seebeck coefficient, and high electrical conductivity, which is all between metals and insulators, as well as low thermal conductivity (See Figure 2-5). Therefore, the semiconductors were considered ideal for thermoelectric applications (Birkholz, Fetting and Rosenzweig, 1987; Bulusu and Walker, 2008).

2.1.2.4 Figure of Merit

To describe the efficiency of a specific material, figure of merit (ZT) is usually used. Thermoelectric efficiency enhances with the increases of the dimensionless figure of merit (ZT) which only depends on intrinsic properties of the materials, defined as

$$ZT = \frac{S^2 \sigma T}{\kappa}$$

Equation 2-10

where σ is the electrical conductivity, S is the Seebeck coefficient, κ is the thermal conductivity and T is the absolute temperature (Harman *et al.*, 2002; Hsu *et al.*, 2004). It is clear in order to obtain a high figure of merit ZT , a large Seebeck coefficient and high electrical conductivity are required, as well as low thermal conductivity (Figure 2-5). There are a number of parameters to consider in the search to maximize ZT , including density of states, effective mass, and nanosize grains for maximum phonon scattering. Usually doping to increase the charge carrier density can increase the power factor $S^2\sigma$, thereby enhancing ZT . Also, high mobility carriers are most needed in order to have higher electrical conductivity (Tritt and Subramanian, 2006).

Table 2-1 Comparison at room temperature of typical thermoelectric properties of metal, semiconductor and insulator.

Properties	Metal	Semiconductor	Insulator
S (μVK^{-1})	~ 5	~ 200	~ 1000
σ (Scm^{-1})	~ 10^6	~ 10^3	~ 10^{-12}
K ($\text{Wm}^{-1}\text{K}^{-1}$)	~ 10 – 1000	~ 1 – 100	~ 0.1 – 1
ZT	~ 10^{-3}	~ 0.1 – 1.0	~ 10^{-14}

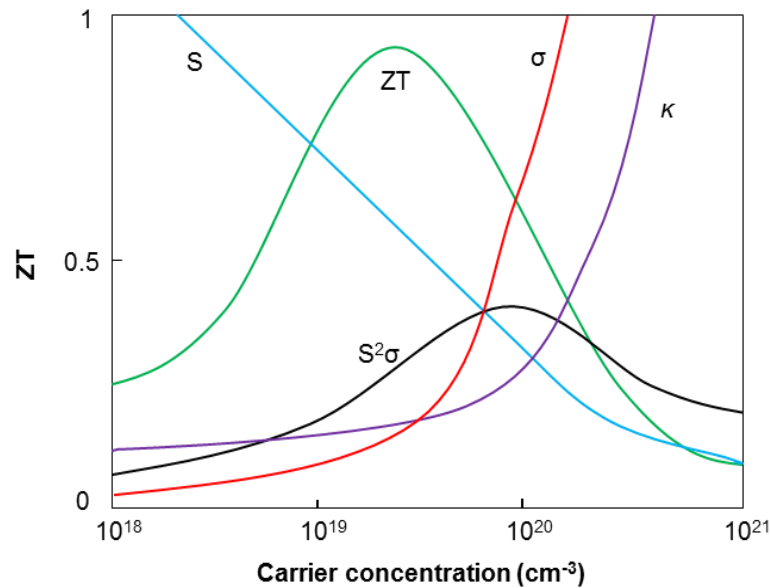


Figure 2-5. The ZT maximum involves compromised thermal conductivity and Seebeck coefficient, with electrical conductivity (Dughaish, 2002).

2.1.3 Applications of Thermoelectric Effects

Based on the thermoelectric properties described above, one can build a thermoelectric module for power generation or cooling system (Figure 2-6). The history of thermoelectric materials is strongly associated with their efficiency. Therefore, there is a significant interest in improving ZT in thermoelectric materials for many industrial and energy applications. From the late 1950s, research on semiconducting thermocouples appeared, and semiconducting thermoelectric devices have been applied in terrestrial cooling and power generation and later in space power generation (Wood, 1988). By the 1990s, many thermoelectric-based refrigerators can be found in the market. Moreover, in earlier 2000 the thermoelectric technology has been used to enhance the functions of automobiles such as thermoelectric heated and cooled seats (Zheng, 2008). However, the low ZT efficiency has limited their application. Recently, many new materials have been discovered and thereby opened up to new potential application of thermoelectric technology.

Due to the versatility of TE devices, it is easier to categorize the TE applications by their functionality. Conventionally, thermoelectric power generation (TEG) is based on the Seebeck effect. The simplest TEG is made of a thermocouple consisting of n-type

and p-type elements connected thermally in parallel and electrically in series (Figure 2-6a). A TEG consists of heat source at one end (kept at high temperature) and heat sink at the other end (temperature maintained lower than the heat source). The temperature difference causes the electrons to flow away from the heat junction which generates an electrical potential difference. This basic concept can be used for waste heat recovery, power for remote sensors, or emergency power sources. One of the basic methods for waste heat recovery is to produce electricity from the hot exhaust gases of a car engine. This application is being investigated by the automotive industry (BMW, Ford, Renault, and Honda) for possible use in the next generation vehicles (Orr *et al.*, 2016).

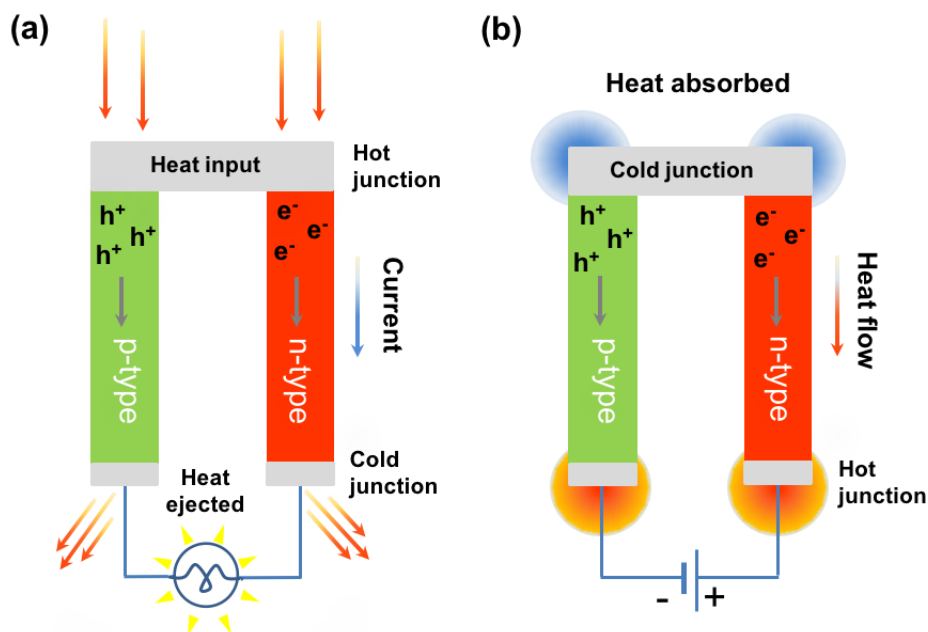


Figure 2-6. Thermoelectric modules for power generation (a); cooling (b).

Conversely, thermoelectric heating and cooling devices are based on Peltier effect (Figure 2-6b). When an electric input is applied through the module, the electrons flow from p-type material to n-type material absorbing thermal energy at the cold junction. The electrons dump their extra energy at the hot junction as they move from n-type back to the p-type material through the electric connector. Typical application for these specialised Peltier Coolers including IR detectors, Close-Cycle Refrigerators (CCR) arrays, electro-optics, and electronics, as well as many other applications which are suitable for low temperature applications where a moderate cooling capacity is required. That makes TE modules critical components in these systems. TE devices

are generally more compact, lighter, and easy to handle than other cooling methods. For instance, the multi-stage Peltier coolers in Ferrotec's Deep-Cooling Thermoelectric Module series offer deep cooling due to improved material efficiency and provide significantly higher temperature differentials than are obtainable with standard single-stage modules (Snyder *et al.*, 2002). Therefore, the performance of the optical telecom-component is improved.

2.1.4 State of the Art of Thermoelectric materials

Since Seebeck's discovery, many materials have been considered useful for power generation or cooling system. From a history point of view, the discovery of thermoelectric materials started from simple metal, conventional semiconductor such as group III-V (e.g., InSb), IV-IV (e.g., SiGe), group IV chalcogenides (e.g., PbTe), group V chalcogenides (Bi₂Te₃, Sb₂Te₃) (Slack and Tsoukala, 1994; Hsu *et al.*, 2004; D. Das *et al.*, 2016) to recent complex materials e.g., skutterudites (Nordström and Singh, 1996; Rull and Fernández, 2015; Rogl and Rogl, 2017), Clathrates (Wang *et al.*, 2017; Yan *et al.*, 2017), half-Heusler alloys (Vikram *et al.*, 2017), complex chalcogenides (Han *et al.*, 2016), cobaltites (Baran *et al.*, 2015), and so on. The trend of finding new thermoelectrics from complex materials or nanostructured materials seems clearer. A brief review of these typical thermoelectric materials will be given. Figure 2-7 represents the historic development of TE materials (Zhang and Zhao, 2015).

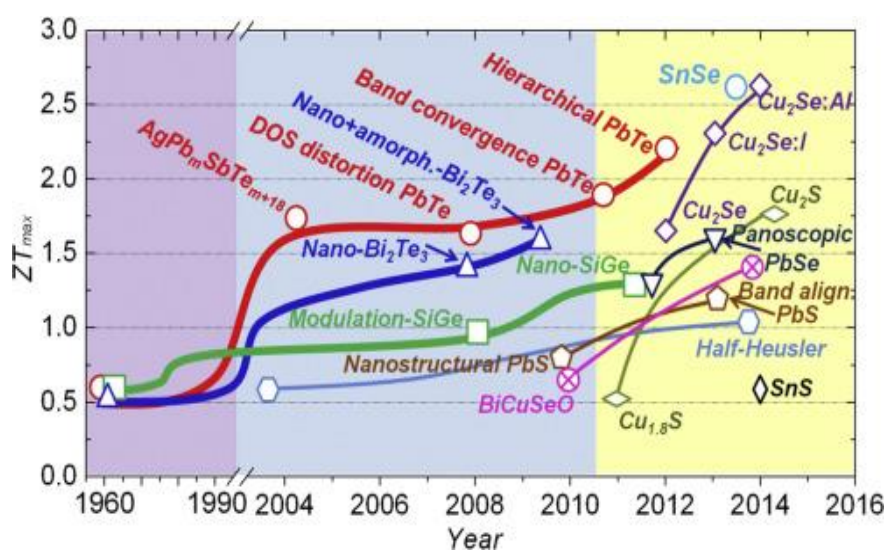


Figure 2-7. ZT of the current bulk thermoelectric materials as a function of year (Zhang and Zhao, 2015).

2.1.4.1 Simple elemental TE Materials

Many research has successfully been done to find the Seebeck coefficient of common metals and alloys. Even though metals have large amount of carriers, they have been known to have smaller Seebeck coefficient values due to their large electronic contribution to the thermal conductivity. Typically, metal have low Seebeck coefficient ($\sim \pm 0-3 \mu\text{V/K}$) (Blatt *et al.*, 1976; Kasap, 2001). The following table (Table 2-2) provides approximate Seebeck coefficients for a variety of different metals and alloys.

Table 2-2. Seebeck Coefficient of different metals and alloys (Blatt *et al.*, 1976).

Metal or Alloy	Seebeck Coefficient relative to platinum ($\mu\text{V/K}$)
Bismuth	-72
Constantan	-35
Cobalt	-13.3
Alumel	-12.9
Mercury	-6.0
Palladium	-5.7
Calcium	-5.1
Gold-chromium	-1.7
Thorium	-1.3
Platinum	0
Alloy 11	+1.3
Tantalum	+3.3
Aluminium	+3.5

2.1.4.2 Half Heusler Materials

The potential of the class of intermetallic compounds known as half-Heusler phases for high-temperature thermoelectric power generation has recently been identified. The structure of half Heusler, generally denoted as ABX, is a simple rock salt structure formed by A and X and filled with element B. The crystal structure MgAgAs is face centred cubic and consists of three interpenetrating filled sublattices, and a fourth open sublattice of vacancies. The challenges of having high ZT (Alam and Ramakrishna, 2013) due to the small band gap ($E_G \approx 0.1-0.5 \text{ eV}$) were solved with series of researches by increasing the phonon scattering via chemical substitutions and

nanocomposites inclusions. Introducing the phonon scattering by alloying Hf on Zr site (ZrNiSn) led to an overall reduction of the total thermal conductivity. Some recent investigations explored the effect of less than 1% Sb doping on the Sn site, which results in several orders of magnitude lowering of the resistivity without significantly reducing the Seebeck effect and leading to large power factor (Shen *et al.*, 2001). Another interesting half Heusler material ZrNiSn variation were suggested with various chemical substitutions to enhance the ZT. For example, the substitutions and additional of the excess of nickel to ZrNiSn were applied from room temperature to 1000K, it was found that the excess of nickel caused a dramatic reduction of the lattice thermal conductivity up to 700K, which was explained by the hole transport properties (Muta *et al.*, 2006). Moreover, thermoelectric properties of ZrNiSn were improved by changing the degree of antisites defects of Zr and Sn atoms (Qiu *et al.*, 2010) by shrinking the band gap to improve electrical transport properties. Many other researches were conducted on half Heusler materials and other are less studied such as NbCoSn, NbRhSn, ZrCoBi for p-type and ZrCoBi, YNiSb, NdCoSn for n-type materials (Liu *et al.*, 2012).

2.1.4.3 Structures with "Rattlers" – Clathrates and Skutterudites

These complex structures have received a lot of attention in TE research since 1990s. However, their problem due to their strong bonding led to high thermal conductivity (LeBlanc *et al.*, 2014). Avoiding this limitation, Slack's concept of a phonon glass and electron crystal (PGEC), was implemented. In addition to that, alloying with transition metals, rare-earth or heavy atoms can fill empty cages or voids (partially or completely) to lower the thermal conductivity. The general formula of type 1 clathrates is $A_xB_yC_{46-y}$. The most interesting clathrates with low thermal conductivity is n-type semiconducting $Sr_8Ga_{16}Ge_{30}$ that has four cornered diamond lattice structure of Ge with Sr inside the cage. The atom inside the cage donate the electrons to the frame which causes the rattling ions scattering conduction electrons that lowering the thermal conductivity, thus the experiment shows the high Seebeck coefficient $S = - 320$ mV/K with low thermal conductivity $k = 0.9$ W/mK at the room temperature (Nolas *et al.*, 1998). $Sr_8Ga_{16}Ge_{30}$ was investigated with a variety ratio of Ga/Ge. It was found the decreasing of the Seebeck coefficient is correlated with decreasing Ga/Ge ratio (Alam and Ramakrishna, 2013). Other different clathrates type 1 were well studied such as

$\text{Ba}_8\text{Ga}_{16}\text{Ge}_{30}$, $\text{Ba}_8\text{Zn}_8\text{Ge}_{38}$ and many others. Nevertheless, the type 2 clathrates were ignored due to their difficulties of synthesise (Bobev and Sevov, 2002).

The skutterudite possesses voids in its structure. Within their high degree of covalent bonding between binary compounds, they exhibit high carrier mobilities and good electron crystal properties. These properties in skutterudite cause to increase thermal conductivity, and hence the challenge to reduce it. The solution of maintaining the stability of the structure is by doping and filling with electropositive ions in the void that replace the electron deficient neighbour (Shi *et al.*, 2005). Many studies found the increased Seebeck coefficient, decreased thermal conductivity such as $\text{CeFe}_3\text{CoSb}_{12}$, n-type Ba_xY by $\text{Co}_4\text{Sb}_{12}$, $\text{In}_{0.25}\text{Co}_{3.9}\text{Ni}_{0.1}\text{Sb}_{12}$ and many others (Sze and Ng, 2006; Tritt and Subramanian, 2006; Pei, Wang and Snyder, 2012; Koumoto *et al.*, 2013; Caballero-Calero and Martín-González, 2016).

2.1.4.4 Thin Films Materials

The study of the size effect of thermoelectric power of thin films in semiconducting materials gives information about the nature of carrier scattering, mean free path, Fermi energy and other parameters. The first approach to enhance density of the states near Fermi energy have been achieved in quantum dot structures such as $\text{PbSe}_{0.98}\text{Te}_{0.02}/\text{PbTe}$, where ZT of 0.9 at 300 K and 2.0 at 550 K were achieved. The acoustic mismatch was utilized between superlattices components to reduce the thermal conductivity and increase power factor that also known as controlling the transport of phonon and electron transmitting (Alam and Ramakrishna, 2013).

2.1.4.5 Nanocomposites based bulk TE

The nanostructure bulk materials were proposed as an alternative to thin film material in order to use them in large scale applications. The main purpose of designing these materials is to introduce many interfaces for reducing the thermal conductivity more than the electrical conductivity by interface scattering. Thus, it is essential to reduce thermal conductivity without compromising electrical conductivity (Zhao *et al.*, 2005). Holey nanocomposite structures influence the power factor, Bi_2Te_3 nanowires inclusion cause the reduction of thermal conductivity without affecting electrical conductivity and that 25% increase of ZT was demonstrated in (Zhang *et al.*, 2012). Many new nanocrystalline bulk materials were synthesized. Initially, ball milling followed by DC hot pressing showed very interesting results with a challenge of grain

growth which occurred during the DC hot pressing. Qian Zhang (Zhang *et al.*, 2012) solved this issue by adding Organic Agents (OA) such as oleic acid-AO. Different methods were used such as micro-wave plasma induced thermal decomposition of gaseous precursors, hydrothermal method, high energy ball milling, chemical-vapour doped deposition method, polyol method and so forth. For some materials such as Si₈₀Ge₂₀ doped with boron, the ZT improved 50%, the main reason was due to the increased phonon scattering from the high density nano-grain interfaces in the nanocomposites (Joshi *et al.*, 2008).

2.1.4.6 Metal Oxide Thermoelectric Materials

As mentioned above that the most currently used thermoelectric materials are heavy-metal-based, such as Bi₂Te₃ and PbTe due to their high ZT. However, these materials have several disadvantages such as thermal instability due to vaporisation or melting, harmful to environment, and scarcity of constituent elements (Tritt and Subramanian, 2006; LeBlanc *et al.*, 2014). The interest in oxide thermoelectric materials as candidates for mid-high temperature applications has attracted extensive effort during the last decade due to their earth abundant elements, being of relatively low toxicity and synthesized through an easy process, as well as their thermal and chemical stabilities at high temperatures in air. The research on oxide thermoelectric materials has advanced dramatically since the discovery of a large power factor ($S^2\sigma$) in cobaltites (Terasaki *et al.*, 1997; Foo *et al.*, 2004). Thereby, various oxide thermoelectric materials are reviewed below.

2.1.4.6.1 Layered Cobaltites

The thermoelectric p-type cobalt-based oxides include two promising materials Na_xCoO₂ and Ca₃Co₄O₉. Their power factor at room temperature was found to be even higher than the state of the art Bi₂Te₃. Currently a ZT value around 1 has been achieved due to the good electronic transport properties and a low thermal conductivity of 2 W m⁻¹ K⁻¹ (Ruleova *et al.*, 2010), which represented the state-of the art p-type oxide materials (Lan *et al.*, 2013; Sui *et al.*, 2013; Pei *et al.*, 2014). These two cobalt-based materials have layered structures. They exhibit a host of interesting properties. The charge conduction occurs within the CoO₂ layers (Liu *et al.*, 2013). The high Seebeck coefficient is originated from the presence of the low spin state of Co³⁺ or the spin orbital entropy. Also, it has been suggested that there is a significant

concentration of oxygen vacancies for $\text{Ca}_3\text{Co}_4\text{O}_9$ at elevated temperature (Madre *et al.*, 2013). Furthermore, the misfit cobaltites layers resist the phonon transport, causing a low thermal conductivity which enhances ZT.

2.1.4.6.2 Perovskites

Perovskites have a general formula ABO_3 . The most studied perovskite thermoelectrics are SrTiO_3 and CaMnO_3 due to their large Seebeck coefficient and low thermal conductivity at high temperatures. Contrary to Co-ion that can be explained by the spin-orbital configuration, the Mn-ion exhibits a strong spin-blockade effect which is not expected to occur when Mn^{3+} electrons move on a background of Mn^{4+} ions. It has been reported that in oxides like SrTiO_3 oxygen vacancies scatter the phonons effectively (Yu *et al.*, 2008). Moreover, doped SrTiO_3 was found to have enhanced electrical conductivity due to the increased carrier concentration (Sameera Devi, *et al.*, 2015).

2.1.4.6.3 Zinc Oxide

These binary oxides are also called transparent conductive oxides, which consist of a material with optical transparency for visible light and high electrical conductivity. Mainly ZnO , In_2O_3 , SnO_2 and related oxides have a promising electrical conductivity and carrier mobility (Minami *et al.*, 1998; Mihaiu *et al.*, 2015). ZnO is considered as a cheap, abundant and promising high ZT thermoelectric for power harvesting from waste heat due to its high melting point, high electrical conductivity and Seebeck coefficient. However, its practical use is limited by a high lattice thermal conductivity ($k \approx 40 \text{ Wm}^{-1}\text{K}^{-1}$). Nanostructuring of the undoped and doped ZnO can reduce the thermal conductivity (Fujishiro *et al.*, 2005; Jood *et al.*, 2011). This results in a significant increase in ZT, showing values of doped and co-doped ZnO , up to 0.65 (Jood *et al.*, 2011).

2.1.4.6.4 Oxyselenides BiCuSeO

BiCuSeO systems are the most recently discovered oxide based thermoelectrics. BiCuSeO is a p-type thermoelectric material composed of stacked “conductive” layers $[\text{Cu}_2\text{Se}_2]^{2-}$ and “insulating” layers $[\text{Bi}_2\text{O}_2]^{2+}$. These layers are composed of edge sharing (CuSe_4) and (OBi_4) tetrahedra respectively, and are stacked along the c axis of the tetragonal cell. The approaches that have successfully enhanced the thermoelectric performances in the BiCuSeO system are outlined by Zhao *et al.* (Li-

Dong Zhao *et al.*, 2014a; Zhang *et al.*, 2017), these include increasing carrier concentration via multifunctional doping, optimizing Cu vacancies, tuning of band gap, increasing carrier mobility through texturing, and so forth (Lan *et al.*, 2013; Sui *et al.*, 2013; Li-Dong Zhao *et al.*, 2014a; Pei *et al.*, 2014). Recently, Das *et al.* reported that the oxygen vacancies, and all-length scale phonon scattering, lowers the thermal conductivity of the undoped BiCuSeO thermoelectric and achieved a maximum ZT of 1.09 at 773 K (S. Das *et al.*, 2016). Furthermore, the ZT has been boosted to the maximum value of 1.5 at 873 K via a dual-doping approach (Liu *et al.*, 2016). Table 2-3 summarizes the reported thermoelectric properties between different thermoelectric materials. These results inspired us to investigate the BiCuSeO materials in this project.

Table 2-3. Thermoelectric properties between different classes of thermoelectric materials.

Material	Composition	Temp.(K)	S ($\mu\text{V/K}$)	σ (S/cm)	K (W/mK)	ZT	Ref.
PbTe Based	Pb _{0.99} Bi _{0.01} Te	675	-240	4	1	1.35	Yang <i>et al.</i>
TAGS based	GeSb _{0.96} Zn _{0.04} Te ₂	585	290	210	0.52	1.9	Sabhajit <i>et al.</i>
Skutterudites	Ce _{0.92} Fe ₄ Sb ₁	763	170	19	2.3	0.91	Liu <i>et al.</i>
Half-Heusler	Hf _{0.5} Zr _{0.5} Co _{0.9} Ni _{0.1} Sb	1073	-225	6.2	3.5	1.05	He <i>et al.</i>
Si-Based	Si _{0.8} Ge _{0.2}	800	270	275	3.0	0.72	Usenko <i>et al.</i>
Oxide Based	NaCo ₂ O ₄	500	80	0.003	20	0.62	Pei <i>et al.</i>
	Sr _{0.98} La _{0.02} TiO ₃	800	-260	0.001	11	0.18	Yu <i>et al.</i>
	Zn _{0.98} Al _{0.02} O	873	-140	10	6	0.02	Drebler <i>et al.</i>
	BiCuSeO	923	425	14	0.4	0.5	Li-Dong Zhao <i>et al.</i>

2.2 Literature Review on Heterogeneous Catalysis

Today, catalysis plays a prominent role in our society, and more than 90% of the chemical industrial processes in use throughout the world utilize catalyst in one form or another. It has become indispensable in environmental pollution control. One clear example is the way in which a three-way catalyst leads to an effective reduction in the pollution from car engines. In short, it will become increasingly important in the future. This thesis focuses on heterogeneous catalyst systems only. It usually involves the adsorption of reactants from a fluid phase onto a solid surface, chemical reactions on the surface of the solid catalyst, and then desorption of products into the fluid phase. This process can usually be represented by the Eley-Rideal (E-R) (Eley and Rideal, 1941; Rideal, 2008) and Langmuir-Hinshelwood (L-H) (Langmuir, 1918, 1922; Hinshelwood, 1926) mechanisms. In the former mechanism, some of the reactants were adsorbed and underwent reactions with the gaseous, while in the latter mechanism all the reactants were adsorbed onto the catalyst surface and underwent surface reactions (Figure 2-8).

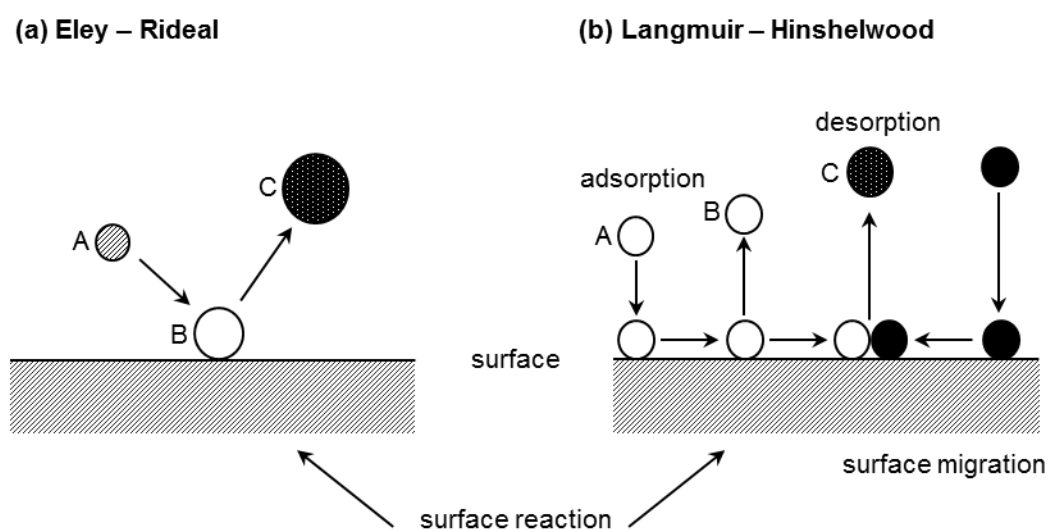


Figure 2-8. Schematics of (a) Eley-Rideal; (b) Langmuir-Hinshelwood mechanisms.

2.2.1 Catalysis and Catalysts Promotions

In heterogeneous catalysis, only the surface atoms are considered active for catalytic reactions and most of the bulk material is not being used (low volume to surface area ratio). It implies that each significant portion of the active phase atoms are on the gas-

exposed surface of the crystallites and are thus catalytically active. This portion is termed catalyst dispersion, which is defined as the ratio of the number of gas-exposed surface atoms to the total number of catalyst atoms. As the active phase is often expensive (noble metals), the introduction of nanostructured catalysts altered the catalytic ability to consider the optimization of the volume to surface area ratio. Successful and reproducible preparation of highly dispersed catalysts crucially depends on the state of the support and on the different parameters such as solution concentration, pH, surface area, temperature and so on. There are several methods that have been developed to prepare highly dispersed nanostructured catalysts such as impregnation, co-precipitation, deposition-precipitation, polyol, physical and chemical vapour deposition (Ertl, Knözinger and Weitkamp, 1997; Wieckowski, Savinova and Vayenas, 2003; Alcalá and Real, 2006; Li, Comotti and Schüth, 2006; Regalbuto, 2006; E. A. Baranova *et al.*, 2010; Katsaounis, 2010; Wang *et al.*, 2011; Sasajima and Uchida, 2011; Unde, 2012; Vernoux *et al.*, 2013; Dole *et al.*, 2014).

It is well known that the dispersion increases with decreasing particle size i.e. more efficiently dispersed metal over the support brings about higher efficiency in heterogeneous metal-catalyst (Dispersion ~ 100% for particles with diameter in the range of 1 nm). This trend has been shown for the same support materials synthesized with different surface areas (Mitsui *et al.*, 2008a). Moreover, the catalytic activity of supported metal can be further enhanced or stabilized by using catalyst promoters or through the metal-support interaction (MSI) phenomenon. A commercial catalyst usually consists of several phases containing a number of species. These are due to impurities, small amounts of promoters or modifiers, that are intentionally added during the catalyst synthesis. Adding these promoters (chemical species) improves the catalyst activity, selectivity and lifetime of a catalyst. The additional of such species can result in a change in the electrical and/or crystal structure of the catalyst.

Promoters can generally be divided into structural (e.g. Al₂O₃) and electronic promoters (e.g., alkali metal atoms). The structural promoters do not contribute in the catalytic reaction itself (elementary steps) but stabilize and enhance the active – phase on the catalyst support (Ertl, Knözinger and Weitkamp, 1997). On the contrary, the electronic promoters enhance the catalytic properties of the active phase by changing its adsorption properties. The drawback for classical promotion is that the promoter cannot be modified or controlled in the course of the catalytic operation, as it is fixed

during the 'ex situ' catalyst preparation. For example, adding of alkalis K on Fe for the ammonia synthesis are completed during catalyst preparation, therefore can be subjected to degradation during catalytic process (Schlögl, 2008).

Promoters are the subject of interest in catalyst research due to their remarkable influence on the activity, selectivity, and stability. This sector of catalysts research is often the scene of surprising discoveries. Table 2-4 gives an overview of promoters and their correspond applications. Promoters can also influence catalytically active phases by stabilizing surface atoms in certain valence states. A recent review on the epoxidation of ethylene to ethylene oxide (EO) over a silver catalyst demonstrated the industrial application of using caesium and chlorine as promoters for the selectivity of EO (Mitsui *et al.*, 2008a). Silver oxide chloride phases were detected on the surface. The selective epoxidation between the electrophilic oxygen and the electron-rich double bond of ethylene is optimized. It is proposed that the Cl blocks the nonselective sites and promotes the active oxygen while Cs acts as a structural promoter. It is said that the Cl promoters weaken the Ag–O bond creating more reactive oxygen to enhance the EO isomerization. On the other hand, Cs interacts with the Ag₂O surface and subsurface oxygen resulting in CsO_x-type complexes.

The hydrogenation of CO and ammonia synthesis are two well-known examples. The most commonly used electronic promoters include potassium (Ertl, Lee and Weiss, 1982; Bécue, Davis and Garces, 1998) and sodium (Yentekakis *et al.*, 1998). The strongly electropositive potassium (or, more often, the oxide K₂O) provides electrons that flow to the metal and then into the chemisorbed molecule. A fundamental study was done on a single crystal less active (100) and (110) iron surfaces showing a pronounced electron transfer from K to the Fe surfaces; this is attributed to the lowering of the "local" work function near where the potassium atoms are adsorbed (Ertl, Lee and Weiss, 1982). In investigation of the chemisorption of N₂, it was shown that low concentration of K increases the heat of chemisorption of molecular nitrogen and increase the rate of N₂ dissociation. This is direct evidence that the rate-determining step in ammonia synthesis is the chemisorption of nitrogen.

Table 2-4. Examples of promoters in the chemical industry.

Promoters	Catalyst	Application	Ref.
K	Fe (111), Fe(100)	Adsorption of N ₂	Ertl, and Weiss, 1982
	Ru/Zeolite-X, Fe ₃ O ₄	NH ₃ synthesis	Huazhang <i>et al.</i> , 2000; Saadatjou, <i>et al.</i> , 2015 Shekhah <i>et al.</i> , 2004
	Fe ₃ O ₄ , A-Fe ₂ O ₃ , K-Fe	Dehydrogenation ethylbenzene	Carlsson, 2015
	Ni/Ceramic support	Steam reforming	
Na	Pd/YSZ, Pt/YAl ₂ O ₃	NO _x reduction by C ₃ H ₆	Yentekakis <i>et al.</i> , 1998
	Pt/YAl ₂ O ₃	NO _x reduction by C ₃ H ₆ and CO	Yentekakis <i>et al.</i> , 1999
	Rh/YSZ	NO _x reduction by CO	Yentekakis <i>et al.</i> , 1994
	Pt/YSZ	C ₂ H ₄ oxidation	Ibrahim <i>et al.</i> , 2013
Cs	Ru/Cs _x	NH ₃ synthesis	Bécue <i>et al.</i> , 1998
	Ag ₂ O	Epoxidation of C ₂ H ₄	Özbek <i>et al.</i> , 2013
Cl	Ag ₂ O	Epoxidation of C ₂ H ₄	Özbek <i>et al.</i> , 2013
Mg, Ba, Ca, Sr	Au/Al ₂ O ₃	Partial oxidation of methanol to H ₂	Hereijgers <i>et al.</i> , 2009
Ba	Pt/γ-Al ₂ O ₃	NO _x reduction by C ₃ H ₆	Konsolakis <i>et al.</i> , 2001
Mg, Ba	Ru/BaX, Ru/MgX	NH ₃ synthesis	Bécue <i>et al.</i> , 1998
Co, Cr, Mo	VPO/TiO ₂	Amoxidation of 2-chloro benzaldehyde to 2-chloro benzonitrile	Nagaraju <i>et al.</i> , 2008
	VPO/γ-Al ₂ O ₃		
Al₂O₃	Fe ₃ O ₄	NH ₃ synthesis	Fagherazzi <i>et al.</i> , 1972
Re	Pt/Al ₂ O ₃	Reforming	Jothimurugesan <i>et al.</i> , 1985
Ni, Co	MoO ₃ /Al ₂ O ₃	hydrotreating, HDS, HDN	Morales and de Agudelo, 1986

Similar effects were found in the hydrogenation of CO with the transition metals Pt, Ni, and Ru. Potassium increases the reaction rate and the selectivity for C₂₊ hydrocarbons, as would be expected if dissociation of CO is more facile. Evidence for this is that in the presence of potassium, the CO desorption temperature is 100–200 K higher and the heat of chemisorption increases by 20–50 kJ/mol. Thus, the influence of potassium lowers the CO bond order from 2 to 1.5, so that CO dissociation can more readily occur. It was also shown for rhodium catalysts that at low pressures CO is molecularly adsorbed but dissociates in the presence of potassium promoters (Hagen, 2006).

Besides the alkali metals, the use of alkaline earth metals (i.e., Mg, Ca, Sr, Ba) as promoters was shown in one study to enhance both the activity and selectivity of supported gold catalysts (Au/Al₂O₃) in the partial oxidation of methanol to H₂ (Hereijgers and Weckhuysen, 2009). It was found that H₂ selectivity increased with increasing basicity of the promoting oxide species (i.e., unpromoted < MgO < CaO < SrO < BaO); however, the opposite trend was observed for the selectivity toward CO and CH₄. Similarly, the effect of transition metal additives on the catalytic properties of a vanadium phosphate (VPO) catalyst was studied for the selective ammoxidation of 2-chloro benzaldehyde to 2-chloro benzonitrile (Nagaraju *et al.*, 2008).

More recently, cobalt and molybdenum salts are calcined on the support and form oxides such as MoO₃, CoO, Co₃O₄, and CoAl₂O₄ in a solid-state reaction. The key precursor of the active component is MoO₃, which is activated by sulfiding to give microcrystalline MoS₂ in which small amounts of Co²⁺ ions are incorporated. Active “CoMoS” centres increase the activation of hydrogen and thus facilitate the cleavage of sulfur. It is assumed that Co acts as a structure promoter and leads to increased dispersion of the sulfided species. To observe the effect of such promoters, Co, Mo, and Cr were added to the VPO structure and supported on two different oxide supports – TiO₂ and γ-Al₂O₃. It was observed that a significant improvement in both selectivity and activity existed compared to the bulk VPO catalyst. More specifically, in the case of TiO₂-supported VPO, the addition of Cr exhibited the best performance followed by Mo. From these results, it was also found that the ability of the promoter appears to depend on the nature of the support and its interaction with the catalyst (Nagaraju *et al.*, 2008).

An alternative phenomenon which explains the changed catalytic activity for supported catalyst is referred to as metal – support interaction (MSI), where the support plays a key role in changing the properties of the catalyst due the interaction between the two materials, usually resulting in higher catalytic activity (Schwab, 1969, 1970, 1983). It should be noted that despite the vast amount of MSI studies reported up-to-date, the exact mechanisms are still subjects of debate.

2.2.2 Metal – Support Interaction

2.2.2.1 Metal – Semiconductor Contact Theory

There are two possible types of contact resulting from a metal and a semiconductor contact, rectifying and ohmic contacts. This is depending on the combination of semiconductor and metal. The rectifying contact allows the current to pass in one direction only, namely Schottky barrier contact (Φ_{SB}). The ohmic contact is named when the current can pass in either direction. The concept based on metal – Semiconductor contact was first proposed by Schwab (Schwab, 1969, 1970, 1983) and Solymosi (Solymosi, *et al* 1982). It was suggested that the electronic interactions associate with the two phases in contact ‘Metal – Support’. The condition of thermodynamic equilibrium requires that the Fermi levels in the two solids should be uniform.

Prior to contact, these solids possess different work functions Φ_M and Φ_s . After the contact is established (at equilibrium), charges were transported from one material to another until their electrochemical potentials are equalized. Take an example of metal on n-type TiO_2 , if the metal's work function is larger than the semiconductor's work function ($\Phi_M > \Phi_s$), then the electron flux will be from the semiconductor towards the metal, as is shown in Figure 2-9 (Nicole *et al.*, 2001). This charge transfer causes significant alterations in catalytic properties of the dispersed metal particles (Solymosi, Tombácz and Kocsis, 1982; Sharma, 1984).

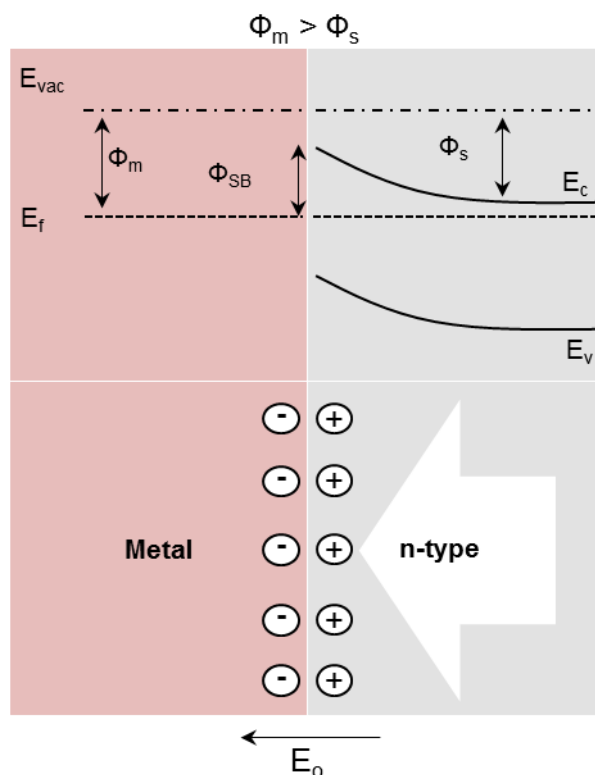


Figure 2-9. Schematic diagram of the energy bands in the case of metal having a larger work function than the n-type semiconductor.

2.2.2.2 Strong Metal – Support Interactions

In 1978, the strong metal – support interactions (SMSI) concept was first introduced by Tauster (Tauster *et al.*, 1978) and attracted intensive interest of the catalyst community (Haller *et al.*, 1989). The SMSI was pronounced the significant change on the catalytic activity of group VIII noble metals when deposited on partially reducible (i.e., CeO_2 , TiO_2) supports. Typically, under non-reducible supports (e.g., Al_2O_3), the metal has the ability to chemisorb H_2 atom or CO_2 per metal atom when they are subjected at high temperatures ($> 773 \text{ K}$). However, the chemisorption capacity of the metal supported on a reducible or partially reducible support decreased or vanished completely (Tauster *et al.*, 1978).

A number of theoretical and experimental investigations have been carried out to better understand its nature. The loss of hydrogenation activity could be due to a geometric blocking effect resulting from the migration of TiO_x across the metal surface (Tauster *et al.*, 1978). According to Tauster, the charge transfer results in polar-covalent bond formation which can suppress dissociative chemisorption of H_2 on the

metal (Tauster *et al.*, 1978). Among other theories, the possibility of the formation of intermetallic bonds with charge transfer from the reduced TiO₂ support to the metal which decreased the work function of the metal, hence modifying the catalyst activity (Mériaudeau *et al.*, 1982). Another suggestion was by diffusion of a sub-oxide species to the surface of the metals which rendered them partially inaccessible to chemisorption and catalytic action (Haller and Resasco, 1989). Overall, support effects are mainly attributed to electronic type of interactions such as M/TiO₂ and M/CeO₂ (Mériaudeau *et al.*, 1982).

More recently, Rodriguez and co-workers showed an unexpected electronic influence of a CeO₂ support exerting on the reactivity of tiny platinum particles for reactions involving water split (Bruix *et al.*, 2012). The remarkable tuned electronic and chemical properties of the active sites have not been observed previously on any Pt-group metal (Goodman, 1995; Valden, 1998; Haruta, 2002; Rodriguez *et al.*, 2007; McClure, Lundwall and Goodman, 2011). As described by Campbell, the terminology 'Electronic Metal – Support Interaction' (EMSI) is more appropriate than what we commonly call SMSI (Campbell, 2012). EMSI has been used to describe the effect of the d-orbital electrons on the interaction between the support and metal. This new interaction produces large electronic perturbations for metal in contact with ceria that is induced by a subtle change in the structure of the support with a strong influence on the intrinsic reactivity. The re-distributed electrons were suggested to come from the ionization of the oxygen vacancies (Campbell, 2012). For ceria, the conversion of Ce³⁺ to Ce⁴⁺ is facile which is known for its oxygen storage capability and a crucial property of the Three-Way Catalysts (TWCs) (Pakulska *et al.*, 2007; Cai *et al.*, 2012; Lin *et al.*, 2014).

2.2.3 Catalyst Supports

Supported catalysts play a significant role in many industrial processes. The oxide support materials are the most commonly used, they provide high surface area, high melting point and are, therefore, very stable under most operating conditions. However, these metal oxides must be examined in detail to make sure that they do not sinter or suffer from phase transition under operating conditions. Supported metal oxide catalysts consist of at least one active metal oxide component dispersed on the surface of an oxide support (Derouane, 1990; Regalbuto, 2006; Pakulska, Grgicak and Giorgi, 2007; Lin *et al.*, 2014). The active oxides are often transition metal oxides,

while the support oxides typically include transitional alumina, SiO₂, TiO₂, ZrO₂, CeO₂ and carbon. For instance, alumina is one of the most versatile materials used in the preparation of heterogeneous catalysts. As catalyst support, alumina provide high surface area coupled with readily accessible pore structures compared to ionic and mixed ionic conductors (Derouane, 1990; Thomas and Thomas, 1996; Vayenas *et al.*, 2001).

These supported catalysts are therefore often named 'monolayer catalysts', although the support surface is typically not entirely covered, even at loadings equal to or exceeding the theoretical monolayer coverage. The surface properties of oxides can be significantly changed by deposition of modifiers (e.g., acidic or basic). For instance, the acid strength of alumina is strongly enhanced by incorporation of Cl⁻ into or on the surface. This may occur during impregnation with solutions containing chloride precursors of an active component. This chlorine plays a significant role in catalytic reforming with Pt/alumina catalysts. Strongly basic materials are obtained by supporting alkali metal compounds on the surface of alumina (Baba *et al.*, 1982; Baba and Ono, 1986; Ertl, Knözinger and Weitkamp, 1997).

2.2.4 *In Situ* and Controlled Promotion – NEMCA

2.2.4.1 NEMCA Background and Definitions

The Electrochemical Promotion of Catalysis (EPOC), also referred to as non-faradaic electrochemical modification of catalytic activity (NEMCA), was discovered in the 1980' by Vayenas and his group (Stoukides and Vayenas, 1981). The NEMCA is considered as a new class of promotion in heterogeneous catalysis and interfered with electrochemistry. Since then many other groups have made significant contributions in this area (Bockris and Minevski, 1994; Pacchioni, Lomas and Illas, 1997) and discussed the effect of NEMCA in electrochemistry (Vayenas and Brosda, S. Pliangos, 2002), surface science and heterogeneous catalysis fields. It has been studied for more than 100 catalytic systems and does not appear to be limited to any specific type of catalytic reaction, solid electrolyte or metal catalyst (Katsaounis, 2008). Upon polarization between the catalyst (working electrode) and solid electrolyte (counter electrode) interface, it was found that the catalytic activity and selectivity can be significantly altered. This effect is generally explained by the migration of charged ions

(spillover/backspillover) originating from the electrolyte onto the surface of the catalyst, hence modifying the electronic properties of the catalyst.

The basic experimental setup and operating principles used to investigate NEMCA are presented in Figure 2-10 (e.g., O₂ react with C₂H₄). Under open-circuit condition (I=0, no electrochemical promotion existed) a catalytic rate r₀ for ethylene oxidation is produced. By applying an electrical current, I ≠ 0, or a potential difference between the working and counter electrode, U_{WR}, causes modification to the catalytic rate, r. The provoked steady-state change in catalytic rate can be up to 300 times higher than the open circuit catalytic rate, and up to 3x10⁵ higher than the Faradaic rate (r >> r_F = I/2F), of ionic supply to (or removal from) the catalyst electrode. Moreover, the use of ¹⁸O₂ led to the direct confirmation of the promotion mechanism during CO and propane oxidation on Pt/YSZ (M. N. Tsampas, 2015). Xia et al. have attempted to quantify this difference in promotion parameters compared to the conventional equations (Xia et al., 2011). The use of isotopically labelled oxygen (¹⁸O₂) allowed the discrimination of the Faradaic process (¹⁶O from YSZ) from the non-Faradaic process (¹⁸O from ¹⁸O₂). Thereby, the formation of C¹⁶O₂ (Faradaic reaction; ¹⁶O from YSZ) and C¹⁶O¹⁸O (non-Faradaic reaction; ¹⁸O from ¹⁸O₂) is observed (Xia et al., 2010, 2011). It was observed that the increase in the rate of C¹⁶O₂ formation practically coincides with the rate (I/2F) of O²⁻ supply to the catalyst (Λ ≈ 1).

After current interruption (I=0), the rate usually goes back to the initial rate r₀ (Harkness et al., 1996; Konsolakis et al., 2000; Vayenas et al., 2001; Poulidi, Anderson and Metcalfe, 2008) (Figure 2-11). Thus, spillover and backspillover of promoters from one phase to another is an important phenomenon. The formation of these backspillover O^{δ-} species at the Triple Phase Boundary (TPB) corresponding to its image charge δ⁺ and can be written as:



where (O^{δ-} - δ⁺) denotes the overall neutral species formed at the catalyst-gas interface by the spillover oxygen species (Vayenas et al., 2001).

The NEMCA is usually quantified by two parameters ρ and Λ. The rate enhancement ration, ρ, defined as:

$$\rho = \frac{r}{r_0} \quad \text{Equation 2-12}$$

where r_0 is the catalytic rate at open circuit, and r is the catalytic rate for an applied current or potential. The apparent faradaic efficiency, Λ , is defined as the following:

$$\Lambda = \frac{(r-r_0)}{I/2F} = \frac{\Delta r}{r_F} \quad \text{Equation 2-13}$$

where I is the current measured across the cell, F is Faraday's constant, r_F is the rate of ionic species supply to (or removal from) the catalyst. The enhancement of the electrochemical promotion is efficient only when the $|\Lambda| > 1$, that indicates a non-Faradaic enhancement (Vayenas *et al.*, 2001).

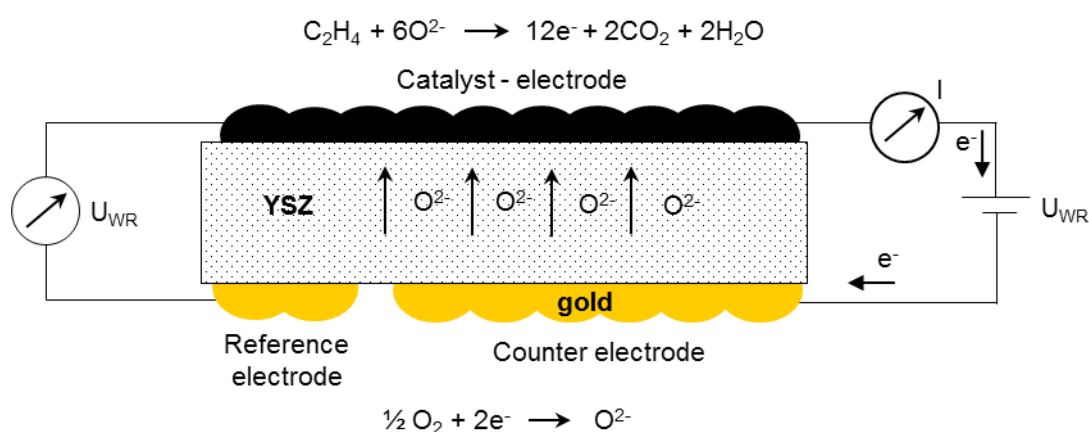


Figure 2-10. Basic electrochemical cell of electrochemical promotion NEMCA.

The NEMCA phenomenon has been shown to be effective for various reactions. However, the most common model reaction used to study this effect is the total ethylene oxidation. In addition to O^{2-} conducting solid electrolytes, the NEMCA effect has also been demonstrated using $Na^{\delta+}$ conducting solid electrolytes such as $\beta''-Al_2O_3$, H^+ -conducting solid electrolytes such as $CsHSO_4$ and, very recently, F^- -conducting solid electrolytes, such as CaF_2 . Moreover, the NEMCA effect has been demonstrated for dehydrogenation, hydrogenation, decomposition reactions and so forth (Katsaounis, 2008).

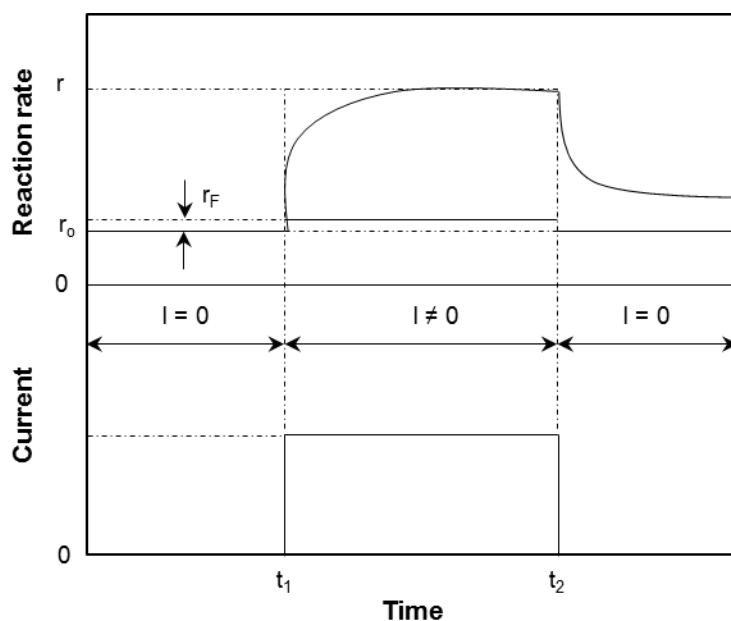


Figure 2-11. Galvanostatic transient of electrochemical promotion NEMCA.

2.2.4.2 NEMCA Mechanism

In general, the NEMCA phenomenon can be described as the mobility of sorbed species from one phase (donor) to another phase where they do not directly adsorb (acceptor). In this way, apparently inert material can acquire catalytic activity. In certain cases, the acceptor can remain active even after separation from the donor. As shown by Delmon and co-worker (Figure 2-12), simple mechanical mixing of the donor and acceptor phases is sufficient for spillover to occur and influence catalytic kinetics leading to a remote control mechanism. Spillover may lead, not only to an improvement of catalytic activity and selectivity but also to an increase in lifetime and regeneration of catalyst (Delmon *et al.*, 1996).

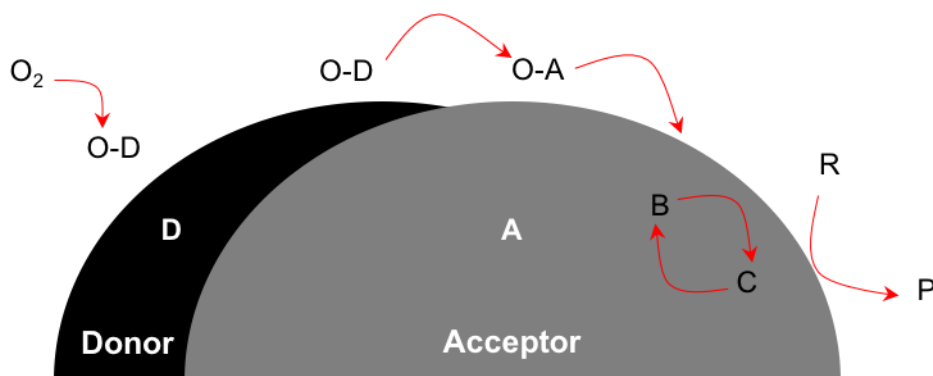


Figure 2-12. Oxygen spillover mechanism in catalytic system.



A general reaction scheme of oxygen spillover in a catalytic system may be formulated as follows: Equations 2-14 and 2-15 describe the dissociative adsorption of molecular oxygen from the gas phase onto the donor and the corresponding reverse action. The transfer of spillover oxygen between donor and acceptor is represented in equation 2-16. Spillover over O-A is a mobile species present on the acceptor surface that is not associated with particular surface site. Equation 2-17 reflects the reaction of spillover oxygen with a particular surface site B represents the deactivation of the active site C by interaction with a reactant R to final the formation of product P (equation 2-18).

The NEMCA phenomenon has been investigated using catalytic rate measurements, solid-state cyclic voltammetry, and many more sophisticated techniques to identify and monitor the promoting species such as Kelvin probe, Ultraviolet Photoemission spectroscopy (UPS), Temperature Program Desorption (TPD), and Photoemission Electron Spectroscopy (PEEM). For instance, X-ray Photoelectron Spectroscopy (XPS) is playing a great role in confirming the ion backspillover mechanism of electrochemical promotion and in providing useful information about the nature of the backspillover species. For the case of Pt/YSZ, when a positive potential is applied to the catalyst electrode, the area of the oxygen peak increased reversibly by 40%, conforming the backspillover of oxygen from the electrolyte. The additional characterization by Scanning Tunnelling Microscope (STM) has been used to confirm the Na⁺ backspillover mechanism of NEMCA (Harkness *et al.*, 1996; Ioannides *et al.*, 1996; Metcalfe, 2001; Nicole *et al.*, 2001; Vayenas, *et al.*, 2003; Tsiplakides *et al.*, 2008).

2.2.4.3 NEMCA and MSI Interconnection

Nicole *et al.* have provided evidence that NEMCA and MSI are concepts with identical functionality but dissimilar operationally (Varkaraki *et al.*, 1995; Nicole and

Comninellis, 1998; Nicole *et al.*, 2001). For the former, the charge transfer is induced by applying an electric polarization (in-situ control of species). However, the charge migration is induced thermally for MSI (difference in work function of two materials). A series of catalysts IrO₂–TiO₂ with varied composition were investigated. It was observed that adding TiO₂ to IrO₂ affects catalyst activity by a factor of 12, and the same maximum rate enhancement is obtained via electrochemical promotion on IrO₂/YSZ. Therefore, the mechanism of MSI for IrO₂ supported on TiO₂ is proved identical to that of the electrochemically promoted IrO₂ supported on YSZ system (Nicole *et al.*, 2001; Matsubu *et al.*, 2016). Therefore, the promotional rate enhancement (ρ_{MSI}) was defined as following:

$$\rho_{\text{MSI}} = \frac{r}{r_u} \quad \text{Equation 2-19}$$

where r_u is the catalytic rate of the unpromoted catalyst, and r is the catalytic rate for the promoted catalyst (mol/s). Similar results were observed and supported by independent kinetic and X-ray photoelectron spectroscopy (XPS) studies for Pt/TiO₂ (not YSZ) catalyst for the total ethylene oxidation (C. Pliangos *et al.*, 1996; Nicole *et al.*, 2001). It was observed that electrochemical promotion is an electrically-controlled metal support interaction and that at least certain types of metal – support interactions are induced by O²⁻ reverse spillover from the support onto the surface of the metal (Figure 2-13). Recently, the use of mixed ionic-electronic (MIEC) materials has attracted interest in the study of metal nanocatalysts. Vernoux *et al.* have proposed the term self-induced NEMCA for the MSI mechanism when the support is an ionic/mixed ionic conductor (Vernoux, *et al.*, 2009). No electrical contact is required to overcome the limitation of the electrical connectivity of nanocatalysts. Therefore, the driving force of reverse spillover is a difference in the work functions of Pt nanoparticles and YSZ.

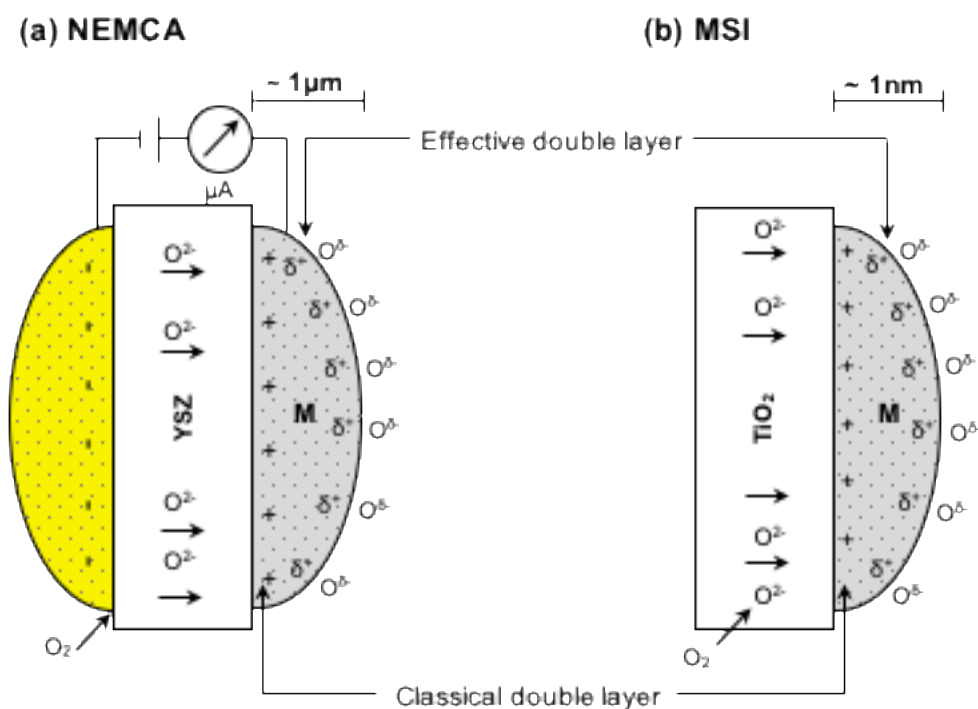


Figure 2-13. (a) NEMCA; (b) Metal – Support interaction, the location of the classical double layers formed at the metal-support interface and the effective double layers formed at the metal-gas interface adapted from Nicole et al., 2001.

2.2.4.4 Recent Developments on NEMCA

It is helpful to mention briefly some of the recent developments on NEMCA. For instance, the high dispersion of the catalyst using MIEC materials is critically important and it can be realized using a nanoparticles metal catalyst (Kambolis *et al.*, 2012; Dole *et al.*, 2014). It was found that decrease in the average particle size of Pt/YSZ led to the increase in CO oxidation at low temperature. This was explained by the thermally induced of reverse spillover from YSZ to Pt nanoparticles in agreement with the NEMCA mechanism. From the commercialisation perspective, the best reactor using NEMCA principle is called Monolithic Electrochemically Promoted Reactor (MEPR), which is considered as a hybrid between a classical monolithic honeycomb reactor and a planar solid oxide fuel cell (Marwood and Vayenas, 1998; Balomenou *et al.*, 2006; Dorado *et al.*, 2007; Souentie, Hammad and Vayenas, 2009; Hammad *et al.*, 2011; Dole *et al.*, 2014). The requirement of external electric power and the associated electric connections are quite restrictive for the NEMCA technology, as many chemical reactions are carried out at high temperatures and in a corrosive environment, which is harsh for electrics. To overcome the complexity associated with external electric

connections, a group in Taiwan led by Prof Huang have investigated using a standalone power generation system, such as Solid Oxide Fuel Cell (SOFC) modules, to drive the electrochemical promoted catalyst converter for exhaust emission control (Huang, Hsu and Wu, 2012).

2.2.5 Self-Sustain Electrochemical Promotion – SSEP

A new approach has been reported recently by a group in University of Miami through self-sustained electrochemical promotion (SSEP) catalysts for partial oxidation reforming of heavy hydrocarbons at temperatures between 723 and 923 K (Huang *et al.*, 2012; Wang *et al.*, 2012; Zhou *et al.*, 2013). The SSEP catalyst consists of four components (cathode, anode, ion conductor and electronic conductor) in the form of micro or nanoparticles. Due to the difference of the electrochemical potentials between the selective cathode and anode, no external power was needed. They have observed that the SSEP catalyst performed better than a commercial Pt/CeO₂ catalyst, especially at low temperatures (Wang *et al.*, 2012; Zhou *et al.*, 2013).

2.2.5.1 SSEP Mechanism in Partial Oxidation Reforming

As illustrated in Figure 2-14, the new concept SSEP catalyst requires no external current and is easily prepared to take advantage of NEMCA effect. It was suggested that the difference in the electrochemical potentials between the selective cathodic phase and the selective anodic phase caused the oxygen ionic species produced at the cathodic phase to be driven to the anodic phase through the oxygen ionic conductive support and participate in the oxidation of hydrocarbons. The electrons resulting from the oxidation reactions are then driven to the cathodic phase through the electrically conductive phase and participate in reduction reactions. Thus, the SSEP catalyst utilises the non-Faradaic electrochemical promotion, i.e. a NEMCA effect, without an external power supply. Distances from about 20 nm to about 20 μm between the anodic phases and cathodic phases allow efficient transfer of electrons and oxygen ions and enables effective coupling between the half-cell electrochemical reactions (Zhou, 2012).

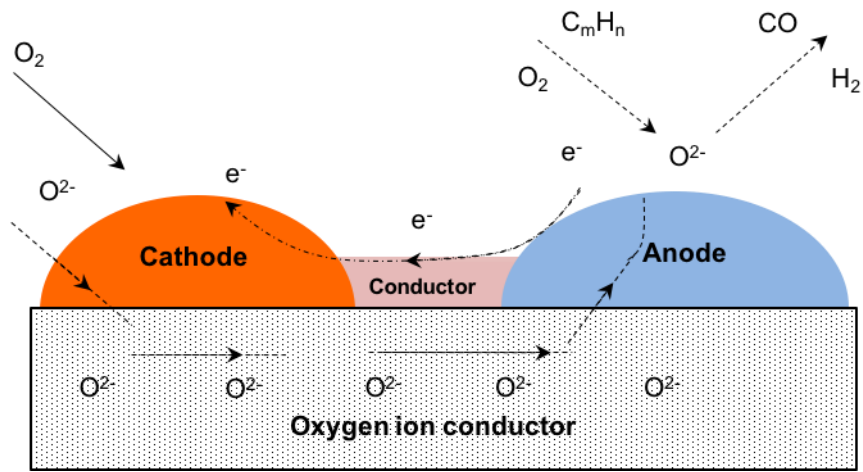


Figure 2-14. Schematic of electrochemically promoted partial oxidative reforming of fuel C_mH_n .

3 Materials Processing and Characterizations

3.1 Introduction

In this chapter, a description of materials and methods used in this project is given. The first part of this chapter focuses on the preparation of thermoelectric materials, solid electrolyte, solid electrolyte-thermoelectric composite and catalyst electrodes, followed by the techniques used to characterise these materials. The simulation and modelling method for the Pt/BCSO is presented as well. The last part is dedicated to the experimental set-up that describes a new reaction chamber, which can combine thermoelectric energy harvesting and catalytic chemical reactions together, and catalytic activity measurements for oxidation and reduction reactions.

3.2 Electrochemical and Thermochemical Cells

3.2.1 Catalyst Supports

3.2.1.1 Thermoelectric Material

A series of polycrystalline $\text{Bi}_{1-x}\text{Cs}_x\text{CuSeO}$ ($x = 0 - 0.025$) were synthesized by a facile one-step boron oxide flux method in air. Stoichiometric amounts of Bi_2O_3 (99.9%, Alfa-Aesar), Bi (99.999%, Alfa-Aesar), Cu (99.99%, Alfa-Aesar), Se (99.999%, Alfa-Aesar), and Cs_2CO_3 (99.99%, Alfa-Aesar) powders were weighed, homogeneously ground in an agate mortar, and then transferred into an alumina crucible. The latter was covered by B_2O_3 (99%, Alfa-Aesar) powder and compacted. The crucible was placed into a chamber furnace, heated at 873 K for 10 hours and finally cooled down to room temperature. After smashing the alumina crucible, the obtained product and the B_2O_3 flux were easily separated from each other. During the flux synthesis, the boron oxide melts and serves as a liquid-seal on the top of the crucible. The obtained product of each sample was then ground to a fine powder.

For thermoelectric properties measurements, sintered powders of $\text{Bi}_{1-x}\text{Cs}_x\text{CuSeO}$ ($x = 0 - 0.025$) were consolidated using a Spark Plasma Sintering (SPS) technique (HP-D-25/1, manufactured by FCT Systeme GmbH, Frankenblick, Germany). It is also important to mention that it was a challenging task to optimize SPS condition to obtain dense un-cracked pellet, while restricting the sintering reactions. After numerous trials, the optimal SPS processing conditions were identified as: at 923 K and 50 MPa pressure with holding time of 10 minutes under argon. The densities of the samples

were measured using the Archimedes method. On the other hand, BCSO undoped powders for catalytic activity measurements were densified at 150 MPa using a hydraulic press system to form a dense pellet of 20 mm in diameter and 2-3 mm in thickness. Then, the green pellet was sintered at 923 K for 10 hours under an argon atmosphere.

The SPS processing and density measurement were carried out in collaboration with the group of Prof. Mike J Reece from Queen Mary University of London, UK.

3.2.1.2 Thermoelectric – Electrolyte Composites

The composite pellets of $(\text{BiCuSeO})_{0.9}(\text{YSZ})_{0.1}$ were synthesized by mixing commercial YSZ powders (CoorsTeK, 99.99%; average grain size, 0.5-0.7 μm) and lab prepared BCSO powders (prepared by the flux method – 3.2.1.1) in ethanol. The composite suspension was homogenized and gently stirred for ~ 30 minutes, followed by ball milling for 24 hours with zirconia milling media to powders weight ratio 5:1. The ethanol solvent was evaporated in an oven with enforced air circulation (Mettler model UNE 300). The resulting powders were densified at 150 MPa using a hydraulic press system to form a dense pellet of 20 mm in diameter and 2-3 mm in thickness. The green pellet was then sintered at 923 K for 10 hours under an argon atmosphere.

3.2.1.3 Solid Electrolyte

In recent studies on NEMCA, Yttria Stabilized Zirconia (YSZ) has been extensively used (Tsiplakides *et al.*, 1998; Katsaounis, 2008, 2010; Vernoux *et al.*, 2013). From the point of view of NEMCA, the YSZ electrolyte is involved in back-spillover the oxygen-ions toward the catalytic film upon an applied potential. This solid electrolyte is an oxygen-ion conducting membrane made of 8 mol% Y_2O_3 doped ZrO_2 . In this research, the dense YSZ pellets were prepared from 8 mol% YSZ powders (CoorsTeK, 99.99%; average grain size, 0.5-0.7 μm), and sintered at 1773 K for 2 hours in air. After sintering, YSZ discs were about 16 mm in diameter and 1.5-2.0 mm in thickness.

3.2.2 Catalysts Electrode Preparation

3.2.2.1 Preparation of Pt Catalysts by Sputtering

The catalyst electrode films were prepared by the sputtering of noble metal on the catalyst support. The sputtered platinum and gold electrodes were deposited onto the substrates using a Nordiko Magnetron System. The sputtering device is consisted of a 40 L chamber filled with pure Ar at a pressure of 5 mTorr. Inert gold counter (CE) and reference (RE) electrodes were deposited on the one side of the pellet using a radio frequency (RF) magnetron mode. On the opposite side, the Pt working electrode (WE) was deposited by direct current (DC) magnetron mode (Figure 3-1).

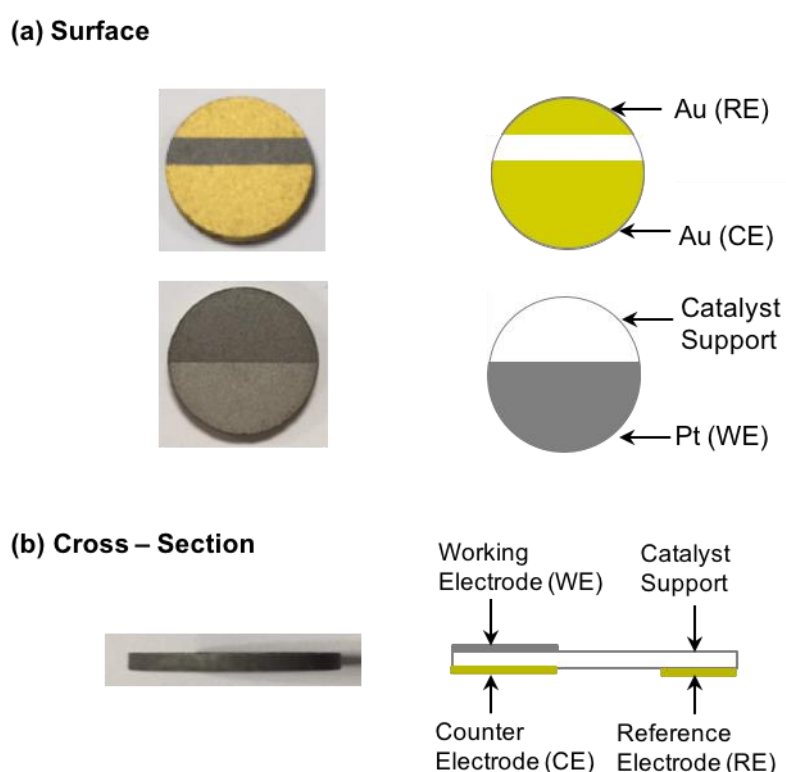


Figure 3-1. Schematic and actual pictures of three electrodes in a single pellet configuration for TEPOC investigation.

The Pt films (WE) were prepared using pure Pt (99.99%) as the sputtering target. The discharge was controlled using a variable DC power supply (1 KV and 2 A). In all experiments, the discharge current was maintained at a constant value of 0.2 A. Prior to achieve the desired thickness, the substrates were placed into a rotating multi-holder. Under these conditions, the deposition rate of Pt was 0.45 nm s^{-1} . The thicknesses of the Pt films were $\sim 80 \text{ nm}$ for three minutes and $\sim 15 \text{ nm}$ for 33 seconds

of the sputtering time. The film thickness was measured using a profilometer (Dektak XT, Bruker) with a smooth silicon wafer treated simultaneously. The Pt/YSZ/Au, Pt/BCSO/Au, and Pt/(BCSO)_{0.9}(YSZ)_{0.1}/Au cells, consisted of YSZ, BCSO and (BCSO)_{0.9}(YSZ)_{0.1} supports covered on both sides by three electrodes, were prepared as labelled above in Figure 3-1. The BCSO, Pt(80)/BCSO and Pt(15)/BCSO discs were weighed 5.8g.

3.2.2.2 Preparation of Nanoparticles Pt/BiCuSeO Catalyst by Impregnation

Another platinum nanoparticle sample (Pt(NP)/BCSO) was prepared using an impregnation method (Alcalá and Real, 2006; Li, Comotti and Schüth, 2006; Mitsui *et al.*, 2008b; Fortunato *et al.*, 2011). First, the Pt nanoparticles were prepared by mixing BCSO powders (prepared by the flux method – 3.2.1.1) with hexachloroplatinic acid solution (H₂PtCl₆, Sigma-Aldrich, 8wt% water) at 313 K for 3 hours. Then, the excess water was evaporated overnight at 383 K. The obtained product was then ground to a fine powder and densified at 150 MPa using a hydraulic press system to form a dense pellet of 20 mm in diameter and 2-3 mm in thickness. The green pellet was calcinated at 823 K for 1 hour under argon atmosphere. Pt(NP)/BCSO discs were weighed 5.02g.

3.2.2.3 Preparation of Pt Nanoparticles by Modified Polyol Method

1 wt. % Pt/ γ -Al₂O₃ and Pt/YSZ catalysts were prepared using a modified polyol reduction technique (Bock *et al.*, 2004; E. A. Baranova *et al.*, 2010; E. Baranova *et al.*, 2010). These catalysts were used to validate the experimental set-up. A metal salt of PtCl₂ (98%, Sigma-Aldrich) was dissolved into diluted ethylene glycol anhydrous (99.8%, Sigma-Aldrich). For the Pt/YSZ, the solution was adjusted at pH = 4 by adding acid chloride solution (HCl, Fluka analytical) dropwise. This was to facilitate the dispersion of the catalyst. Both solutions were stirred for 30 minutes at room temperature till a dark brown solution were formed. The resulting dark brown Pt solutions were deposited on different support γ -Al₂O₃ and YSZ. Subsequently, the mixture of the supported nanoparticles was heated and refluxed overnight at 353 K to achieve high dispersion of the metal nanoparticles on supports. The nanoparticles catalysts were washed with deionized water and then dried overnight at 353 K. Prior to submitting to the ethylene oxidation, all supported Pt catalysts were calcined and reduced at 773 K for 4 hours in 5% H₂/Ar flow.

3.3 Characterization Methods

3.3.1 Microstructure Characterizations

3.3.1.1 X-Ray Diffraction

The X-ray Diffraction (XRD) is an analytical technique for providing detailed information about the structure of crystalline substances. A primary use of this tool is the characterization and identification of compounds based on their diffraction pattern. In this research, XRD (Siemens 5005) scans were carried out at 40 kV with a Cu K α X-ray source at a 2 θ range of 20 $^{\circ}$ - 70 $^{\circ}$ with a step size of 0.06 $^{\circ}$. Crystalline structures were identified and evaluated using a XRD Evaluation software and compared to Joint Committee on Powder Diffraction Standards (JCPDS) patterns. In addition, the Debye-Scherrer formula is applied to estimate the crystallite size from Pt (111) reflection.

$$D = \frac{K \lambda}{\beta \cos \theta} \quad \text{Equation 3-1}$$

where D is the crystallite size, K is a dimensionless Debye-Scherrer constant (0.9), λ is the X-ray wavelength, β is the line broadening at half the maximum intensity (FWHM), and θ is the Bragg angle.

3.3.1.2 Scanning Electron Microscopy

The microstructural investigations were carried out using a scanning electron microscope (SEM) (Philips, FEI XL30 SFEG). The SEM is equipped with Energy Dispersive X-Ray Spectroscopy (EDS) to detect and quantify elements from Beryllium upwards. Also, it is important to note that the EDS measures elements present to a depth of several micrometers into the samples.

3.3.1.3 Transmission Electron Microscopy

Transmission electron microscopy (TEM) is a powerful tool for material science which transmits a focused high-energy electron beam through a sample. The morphology and particle size were directly observed using Philips CM20. The thermoelectric and catalyst samples were dispersed in ethanol at a ratio of 1:5. Then, the mixture was sonicated for 20 minutes. Following the sonication, a drop of a mixture was deposited onto an amorphous carbon coated copper grid and dried under a fume hood prior to the characterisation. The ImageJ software was used to determine the particles size

distribution of Pt catalysts. The dispersion of Pt/ γ -Al₂O₃ and Pt/YSZ catalysts were estimated from average particle diameter using the following formula, considering spherical particles:

$$\text{Dispersion (\%)} = \frac{600 M_{\text{Pt}}}{\rho d_{\text{nm}} a_{\text{Pt}} N_{\text{a}}} \quad \text{Equation 3-2}$$

where M_{Pt} is the molecular weight (195.08 g/mol), a_{Pt} is the atomic surface area (8.06×10^{-20} m²/atom), ρ is the metal density (21.09 g/cm³), N_{a} is Avogadro's number, and d_{nm} is the average particle diameter estimated from ImageJ software in nanometres (Boudart, 1969).

3.3.1.4 Thermogravimetric and Differential Scanning Calorimetry

Setaram Setsys Evolution 16/18 is a method of combined differential scanning calorimetry (DSC) and thermogravimetry (TG) used to determine the oxidation and the decomposition properties of the bulk pieces of materials in an argon or air atmosphere. This method is based on the simultaneous measurement of the heat flux and mass change during oxidation or reduction. The DSC signal reflects the heat flux from the sample to the instrument chamber and was compared to the heat flow of a alumina crucible as a reference. The TG signal analyses the mass change as a function of temperature to determine characteristics of the materials e.g., decomposition points. The temperature range from 300 K to 1010 K should be good enough for investigating the stability of the thermoelectric materials intended for mid-temperature thermoelectric applications. Typically, a sample about 80-120 mg was heated from room temperature to 1010 K at 10 K min⁻¹ with a purge rate of 20 mL min⁻¹.

3.3.2 Thermoelectric Properties Characterization

3.3.2.1 Seebeck Coefficient and Electric Resistivity

Seebeck coefficient and electrical resistivity were measured simultaneously by using a LSR-3 Linseis for the undoped BCSO sample at range of a 300 K - 764 K and using a ZEM-3 ULVAC-RIKO for the doped BCSO samples at range of a 300 K - 680 K. These systems have a primary heating chamber. The sample is vertically clamped in between two platinum electrodes, which serve as the current electrodes for the four-point resistivity measurements. The set temperature gradient is generated by activating the secondary heater in the lower electrode block. The two contacting

thermocouples measure the temperature gradient by determining the temperature of the sample at points T_1 and T_2 . Using the same thermocouples, the generated Seebeck voltage is determined between the same electrodes. The electrical resistivity is measured by means of the standard four-probe techniques. A constant current is applied to the electrodes while the voltage generated across the sample is measured by two contacting electrodes.

3.3.2.2 Thermal Conductivity

The thermal diffusivity (D) is determined by using a LFA-457 Netzsch laser flash method under a continuous argon flow. This non-destructive measurement technique can be employed for a large temperature range ($300\text{ K} < T < 1273\text{ K}$). The front side of a plane parallel is heated by a short laser pulse. The heat propagates through the sample and causes a temperature increase on the rear surface. By using an infrared detector, the temperature increase is measured versus time. In order to calculate the thermal conductivity from equation (2-9), the density and specific heat of the pellet must be known. The sample density (ρ) was determined using the Archimedes method, while the specific heat (C_p) was determined using a differential scanning calorimeter (DSC) instrument.

These thermoelectric property measurements were carried out in collaboration with the group of Prof. Mike Reece of School of Engineering and Materials Science, Queen Mary University of London, UK.

3.3.3 Simulation and modelling using *ab initio* method

The modelling was built with eight layers of Pt on top of two unit cells of BCSO along Z directions. Above Pt there was at least 1.5 nm of vacuum to ensure an accurate energy level for the vacuum was obtained. First principle calculations was carried out using VASP (Vienna ab initio simulation package). The exchange- correlation term was described within the generalized gradient approximation (GGA) parameterized by Perdew-Burke-Ernzerh (PBE) functional (Kresse and Furthmüller, 1996; Shao *et al.*, 2016).

For intrinsic semiconductor, the Fermi level is

$$E_i = \frac{E_c + E_v}{2} + \frac{3k_0T}{4} \ln \frac{m_p^*}{m_n^*} \quad \text{Equation 3-3}$$

The intrinsic carrier concentration is

$$n_i = \left[\frac{2(2\pi k_0T)^{3/2} (m_p^* m_n^*)^{3/4}}{\hbar^3} \right] \exp\left(-\frac{E_g}{2k_0T}\right) \quad \text{Equation 3-4}$$

Here \hbar is Planck's constant, E_c and E_v are the energy at the bottom of the conduction band, and maximum of the valance band, respectively. m_p^* and m_n^* are the effective mass for holes and electrons respectively, E_g the band gap. After the band structure has been obtained, the effective mass was obtained using

$$m^* = \hbar^2 \left(\frac{\partial^2 E}{\partial k^2} \right)^{-1} \quad \text{Equation 3-5}$$

The obtained values, $m_p^* = 0.54m_0$ and $m_n^* = 0.23m_0$, agree with those in references (Pei *et al.*, 2013; Yang *et al.*, 2014). So, the term $\frac{3k_0T}{4} \ln \frac{m_p^*}{m_n^*}$ in eq. (3-3) is less than 0.02 eV, which is negligible compared with E_g (0.80 eV) (Pei *et al.*, 2013). This indicates that the intrinsic Fermi level is in the middle of the band gap, and independent with temperature. The work function can be obtained as the difference between the energy of the vacuum and this Fermi level.

The Fermi level of a doped BCSO can be obtained using eq. (3-6),

$$E_f = E_i + k_0T \cdot \text{sh}^{-1} \left(\frac{N_d}{2N_i} \right) \quad \text{Equation 3-6}$$

Charge transfer as a function of temperature is also calculated for Pt supported on a BCSO with donor concentration 10^{19} cm^{-3} . The amount of charge transferred upon the contact between Pt and BCSO can be calculated (Ioannides and Verykios, 1996) using eq. (3-7):

$$Q = e(N_d + n_i)W = [2\varepsilon_s e(N_d + n_i)|V_0|]^{1/2} \quad \text{Equation 3-7}$$

Here N_d is the donor concentration, n_i the intrinsic carrier concentration, ε_s the dielectric constant, V_0 the difference in work function between the metal Pt and the semiconductor BCSO.

The modelling and simulation were carried out in collaboration with the group of Prof. Ping Peng of School of Materials Science and Engineering, Hunan University, Changsha 410082, China.

3.3.4 Experimental Set-up for Catalytic Chemical Reactions

3.3.4.1 Thermoelectrochemical Reaction Chamber

Chemical reactions were performed in a single chamber reactor. The reactor was designed to facilitate the creation of a temperature gradient and allow the reactive mixture to reach the catalyst and the thermoelectric material surface. The schematic and actual pictures of the chamber reactor are shown in Figures 3-2a and 3-2b. The reactor consisted of a stainless-steel cylinder of 40 cm³, capped with a cover plate and tightened with O-ring and screws (M5 x 25mm, RS). The cover plate was cooled with continuous running water. Gold wires (Agar Scientific, Ø 0.2 mm) were used as electrical contacts for the three electrodes (WE, CE and RE), and temperatures (cold T_c and hot T_h sides) were measured with K-type thermocouples (Ø 0.25mm, TC Direct) placed onto the sample surfaces with a high temperature tape.

Gold and thermocouples wires were led out of the reactor chamber through two four-hole alumina tubes (Omegatite 350). A high temperature hot plate 1500F model (HP99YX, Wenesco, Inc.) with a temperature controller was used to provide the heating for the reaction chamber. The reactor was placed directly onto the hotplate, together with the cooling system in the top cover plate; a temperature gradient was created in the reaction chamber, with a very hot bottom and the top never exceeding 373 K. The stainless-steel reaction line tubes were wrapped with ceramic fiber cottons to retain the heat.

A disc sample pellet was placed into a custom-built glass ceramic (MACOR) holder (Figure 3-2c) and attached to the cooling surface of the cover plate for normal thermoelectric effect experiments, so that its top side (T_c) was always below 373 K (Figure 3-3a). Its bottom side faces toward the hot bottom of the reaction chamber, and can reach temperatures as high as 750 K. The Seebeck voltage, or catalyst potential difference according to the procedures generally used in conventional NEMCA three-electrode electrochemical cells, were measured between the bottom hot and upper cold surfaces, or between the working electrode (Pt) and the reference

electrode (Au) using a potentiostat-galvanostat (VersaStat 3F, Princeton Applied Research).

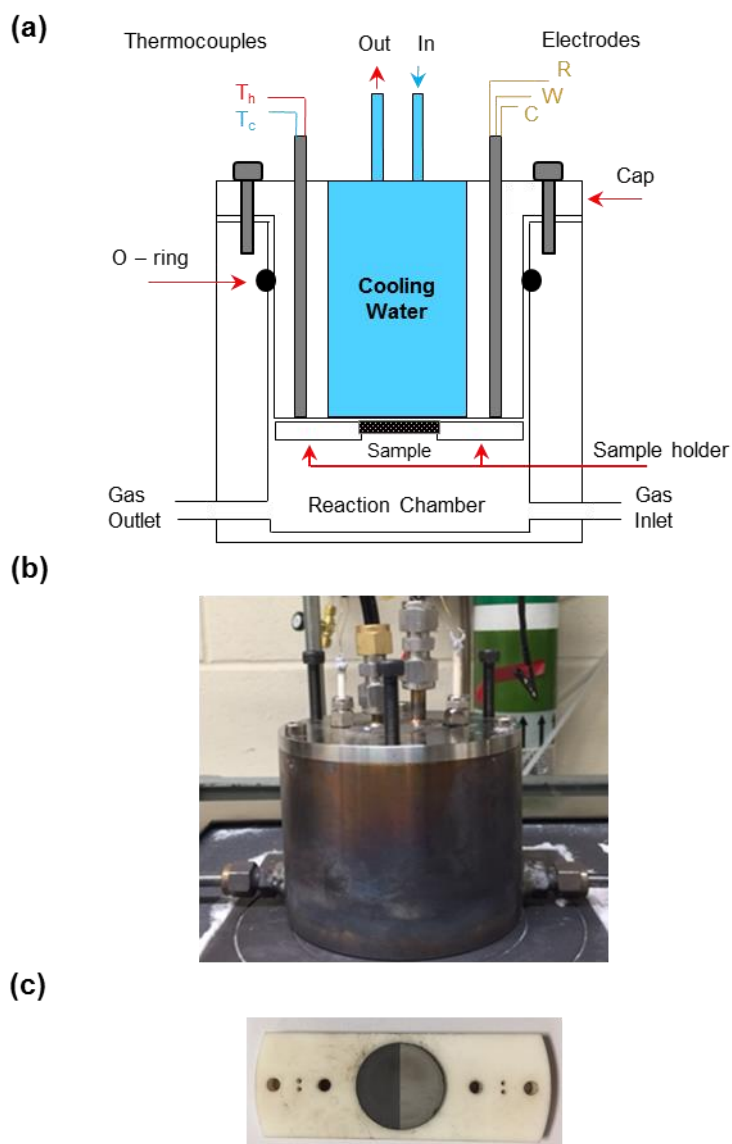


Figure 3-2. (a) Schematic; (b) actual picture of the single chamber reactor; (c) a disc sample onto a custom-built glass ceramic holder.

Gold was selected as CE and RE electrodes because of its negligible catalytic activity in ethylene oxidation and carbon dioxide hydrogenation, which were verified through blank experiments under experimental conditions (See Chapter 5). In order to eliminate artefacts that could compromise the integrity of results, gas leaks were carefully monitored throughout the experiments.

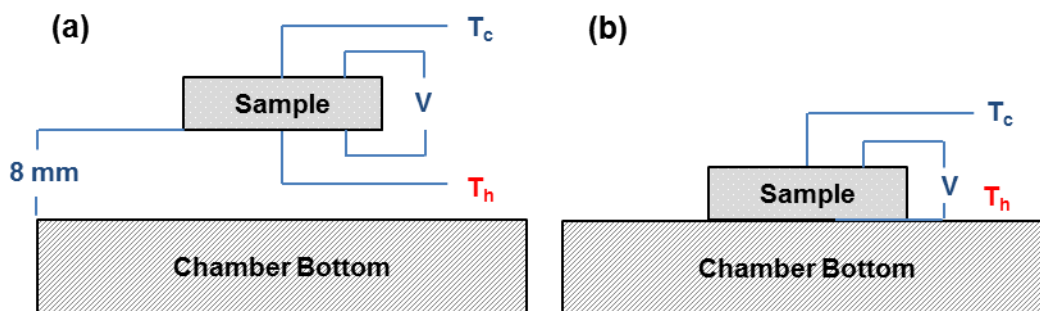


Figure 3-3. Schematic of the arrangement of the sample and the measured parameters for all the catalytic reaction experiments: (a) TEPOC conditions; (b) TE inhibition conditions.

3.3.4.2 Catalytic Activity Experimental

The catalytic activity measurements for different catalysts were carried out at atmospheric pressure in a continuous flow apparatus equipped with a stainless-steel reactor as cited above. A set of three gas mass flow controllers (MKS, 1679B Series, Unit UFC-1100) were used to control the gas composition and flowrate. The reaction reactants and products were continuously monitored using an online Gas Chromatograph (GC8340, CE instruments) and on-line IR analyser (G-150 O₂ and CO₂, Gem Scientific) to quantify the concentration of H₂, CO, CH₄, C₂H₄, O₂ and CO₂. The gas chromatograph (GC) is equipped with a Thermal Conductivity Detector (TCD) and two columns, Molecular Sieve 5A and a Porapak Q. Data acquisition and manipulation were performed using the TotalChrom Workstation (Version 6.2.1 for Windows) data system.

To monitor the temperature, a K-type thermocouple was attached (and fixed using a high temperature Kapton® polyimide tape) onto the catalyst surface for T_h measurement. Another K-type thermocouple was placed in proximity of the top surface for T_c measurement (with a thin mica sheet in between for electrical insulation). Each experiment was repeated for three cycles to test the stability and reproducibility. At each temperature, the catalyst was allowed to reach a steady state for 20-30 minutes and then three injections were performed for GC measurements. The average of three GC measurements at each temperature is recorded. The empty reactor and all samples were tested in the temperature range of 300 – 723 K.

3.3.4.3 Ethylene Oxidation Experimental

For ethylene oxidation reaction (Figure 3-4), the reactants were BOC certified standards of O₂ supplied as a 20% mixture in He, 4% C₂H₄ mixture in He, and the gases were balanced using a pure helium gas (BOC, 99.996%) to obtain desired concentrations. The feed reactant partial pressures were varied between 0.20 and 3.96 KPa for C₂H₄ and 0.50 – 7.23 KPa for O₂. All samples were tested at an overall flow rate of 200 mL min⁻¹. The reactants and products were analysed by online gas chromatography. As in all previous atmospheric pressure of NEMCA studies (Tsiplakides *et al.*, 1998; Vayenas *et al.*, 2001), the ethylene oxidation reaction (equation 3-8) was evaluated using rate of carbon dioxide production r_{CO_2} and ethylene conversion %C₂H₄ from the outlet carbon percentage values obtained by the gas analysis.

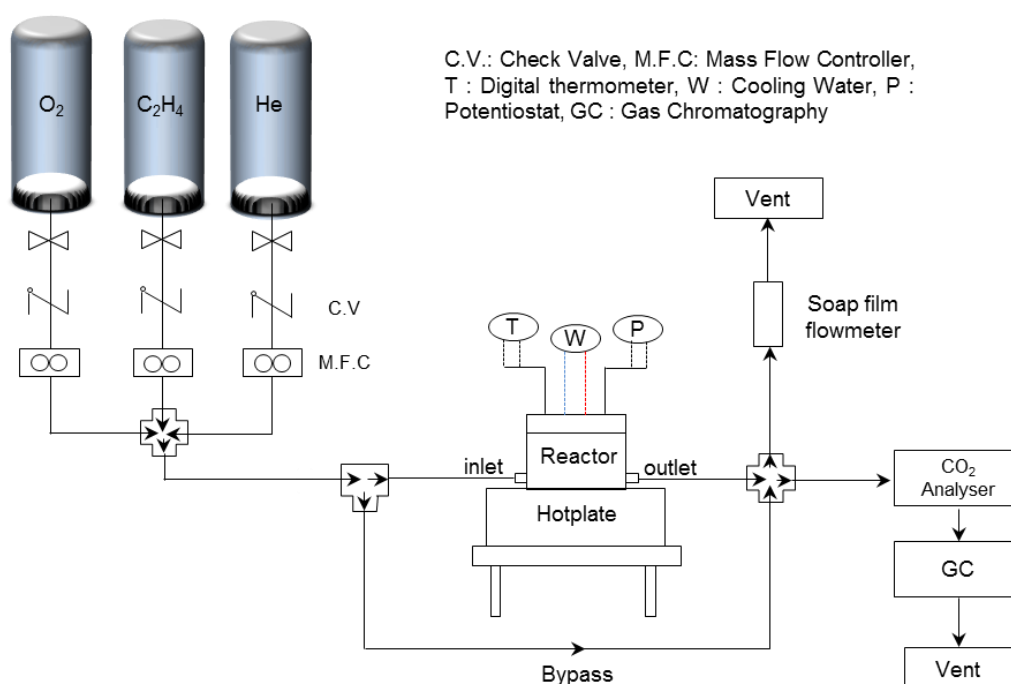


Figure 3-4. Schematic of the experimental set-up for C₂H₄ oxidation reaction characterisation.

The detected CO₂ as a product of ethylene oxidation reaction was converted to area specific molar flow rate in mol s⁻¹ by using the following equation:

$$r_{\text{CO}_2} = \frac{X_{\text{CO}_2} \cdot f_v}{22400 \cdot 60} \quad \text{Equation 3-9}$$

where f_v is the volumetric flow rate at the outlet of the reactor in ml min^{-1} and X_{CO_2} is the mol fraction of CO_2 in the outlet of the reactor.

The rate of consumption of oxygen r (molO/s) was calculated as:

$$r = 3 \cdot r_{\text{CO}_2} \quad \text{Equation 3-10}$$

The ethylene conversion into CO_2 was defined as:

$$\text{C}_2\text{H}_4 \text{ Conversion (\%)} = \frac{X_{\text{CO}_2}}{X_{\text{CO}_2} + 2 X_{\text{C}_2\text{H}_4}} \cdot 100 \quad \text{Equation 3-11}$$

Where X_{CO_2} and $X_{\text{C}_2\text{H}_4}$ were the mole fractions of CO_2 and C_2H_4 in the outlet, respectively.

3.3.4.4 Carbon Dioxide Hydrogenation Experimental

The same reactor was used for the hydrogenation of carbon dioxide (Figure 3-5), the reactants were BOC standards of H_2 supplied as a 30% mixture in He, 3% CO_2 mixture in He, and the gases were diluted using helium gas (BOC, 99.996%) to obtain the desired concentrations. The catalyst activities were investigated with a composition of carbon dioxide and hydrogen at a ratio $\text{CO}_2:\text{H}_2 = 1:1$, intended for high CO selectivity; and at a ratio $\text{CO}_2:\text{H}_2 = 1:4$ intended for high CH_4 selectivity. All samples were tested at an overall flow rate of 100 mL min^{-1} . The CO_2 hydrogenation may undergo two reactions. The first reaction is the reverse water-gas shift (RWGS) reaction (eq. 3-12) and the second leads to the formation of hydrocarbons (eq. 3-13).



where $x = 1$, $y = 4$ and $z = 0$ (i.e. the inlet gas ratio $\text{CO}_2/\text{H}_2 = 1:4$) one has the methanation reaction. The conversion of CO_2 and the selectivity of CO and CH_4 were evaluated from the outlet carbon percentage values obtained by the gas analysis. As carbon monoxide and methane are the only detectable products of CO_2 hydrogenation reaction. CO_2 conversion, and the product selectivity, S_i , can be calculated as:

$$\text{CO}_2 \text{ Conversion (\%)} = \frac{X_{\text{CO}} + X_{\text{CH}_4}}{X_{\text{CO}} + X_{\text{CH}_4} + X_{\text{CO}_2}} \cdot 100 \quad \text{Equation 3-14}$$

where X_{CO_2} , X_{CO} and X_{CH_4} were the mole fractions of CO_2 , CO and CH_4 in the outlet, respectively.

$$S_i (\%) = \frac{X_i}{X_{\text{prod tot}}} \cdot 100 \quad \text{Equation 3-15}$$

where X_i is the mole fractions of product i and $X_{\text{prod tot}}$ is the total mole fractions of total products.

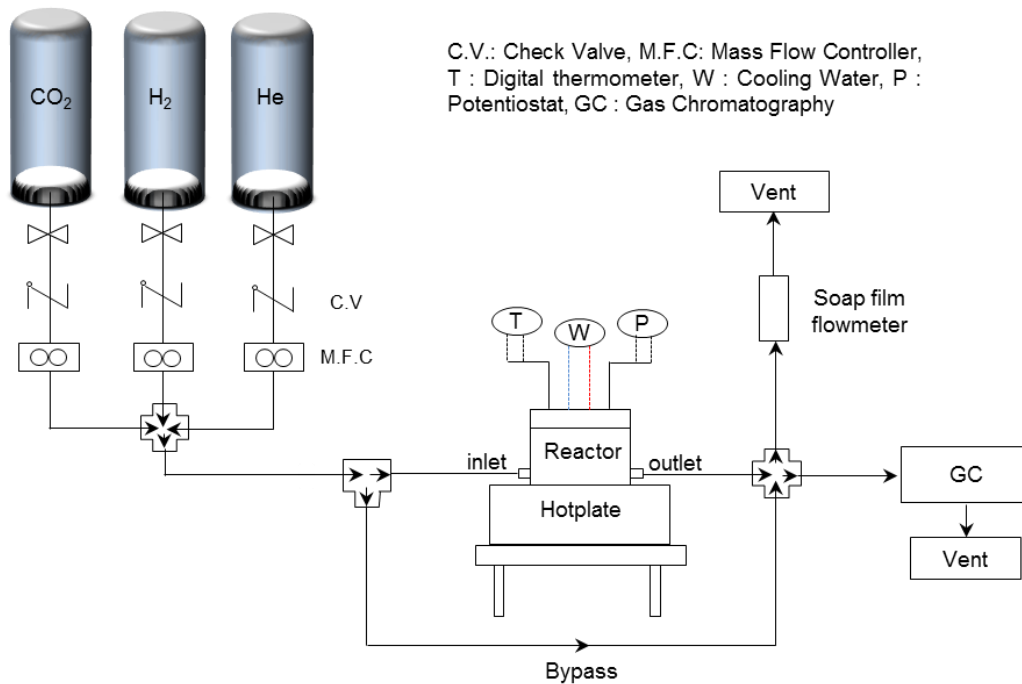


Figure 3-5. Schematic of the experimental set-up for CO_2 hydrogenation reaction characterisation.

The CO and CH_4 yields were calculated using the following formula:

$$Y \text{ yield (\%)} = \frac{X_i (\text{out})}{X_{\text{CO}_2} (\text{feed})} \cdot 100 \quad \text{Equation 3-16}$$

where $X_i (\text{out})$ is the mole fractions of product and $X_{\text{CO}_2} (\text{feed})$ is the total mole fractions of CO_2 feed.

$$r_{\text{CO}_2} = \frac{X_{\text{CO}_2} \cdot f_v}{22400 \cdot 60} \quad \text{Equation 3-17}$$

where f_v is the volumetric flow rate at the outlet of the reactor in ml min^{-1} and X_{CO_2} is the mol fraction of CO_2 consumed.

4 Fabrication and Characterization of Thermoelectric Ceramics

4.1 Introduction

Recently, a promising middle temperature range TE system based on the oxyselenides BiCuSeO (BCSO) has been reported. BCSO materials have high ZT values due to their intrinsically low thermal conductivity and relatively large Seebeck coefficient (S). As a p-type TE, the Seebeck coefficient for BCSO was found to be over 300 $\mu\text{V}/\text{K}$ at about 600 K (Li *et al.*, 2013; Li-Dong Zhao *et al.*, 2014b; Liu *et al.*, 2014; Ren *et al.*, 2014, 2015), as compared to less than 200 $\mu\text{V}/\text{K}$ for other p-type TE materials such as $\text{Na}_{0.85}\text{CoO}_2$ and $\text{Ca}_3\text{Co}_4\text{O}_9$ at 673K (Wu *et al.*, 2014; Altin *et al.*, 2015). Moreover, their ZT value has been improved by optimizing electrical conductivity through the partial substitution of Bi^{3+} with bivalent elements (ZT values for Mg, Sr, Ca and Ba were 0.67, 0.76, 0.9 and 1.1 respectively at 923 K) and a monovalent element (ZT values for Na was 0.97 at 873 K) (Barreteau *et al.*, 2012; J. Li, Sui, Barreteau, *et al.*, 2012; J. Li, Sui, Pei, *et al.*, 2012; Li *et al.*, 2013; Sun Lee *et al.*, 2013; J. Li *et al.*, 2014). More recently, a high ZT value of 1.4 was reported for Ba-doped BCSO via grain-texturing and modulated doping has been obtained (Sui *et al.*, 2013; Pei *et al.*, 2014). Furthermore, the ZT has been boosted to the maximum value of 1.5 at 873 K via a Dual-Doping approach (Liu *et al.*, 2016). However, little attention has been paid to new methods of synthesis.

In this chapter, using a novel B_2O_3 flux method to synthesise BCSO thermoelectric compounds in air is reported. Boron oxide serves as a liquid-seal on the top of the raw materials during the reaction process. This can significantly inhibit the oxidation of Bi, Se and Cu. Furthermore, there is no need to maintain a vacuum or use a sealed evacuated quartz tube, conditions which makes it easier for scaling up for batch production. Herein, the microstructure, thermal and chemical stability and electro-thermal properties of BCSO have been investigated systematically and compared to previously reported methods. It has also been demonstrated that Cs doping improves the ZT by enhancing the electrical conductivity and reducing the thermal conductivity.

4.2 Results and Discussion

4.2.1 Fabrication Process and Structure Analysis

The fabrication procedures used to prepare the $\text{Bi}_{1-x}\text{Cs}_x\text{CuSeO}$ ($x = 0 - 0.025$) samples are presented in Figure 4-1. As shown in Figure 4-1a, the starting materials were loaded into a crucible, compacted and covered with boron oxide powder. Despite the low melting points of Se ($T_m \sim 490 \text{ K}$, $\rho \sim 4.81 \text{ g/cm}^3$) and Bi ($T_m \sim 544 \text{ K}$, $\rho \sim 9.78 \text{ g/cm}^3$) compared to the B_2O_3 ($T_m \sim 723 \text{ K}$, $\rho \sim 2.46 \text{ g/cm}^3$), Figure 4-2b indicated that boron oxide did not infiltrate into the BCSO, at least at the end of the synthesis. This suggested that the protective B_2O_3 liquid-seal was formed on the top of the BCSO, due to its lower density than the other raw materials. The separation of the produced BCSO and the B_2O_3 was very simple. Hence, the obtained material was uniform and rigid as shown in Figure 4-1c. The obtained product was ground to a powder and SPS'ed to produce dense pellets for further structural and TE properties characterizations (Figure 4-1d).

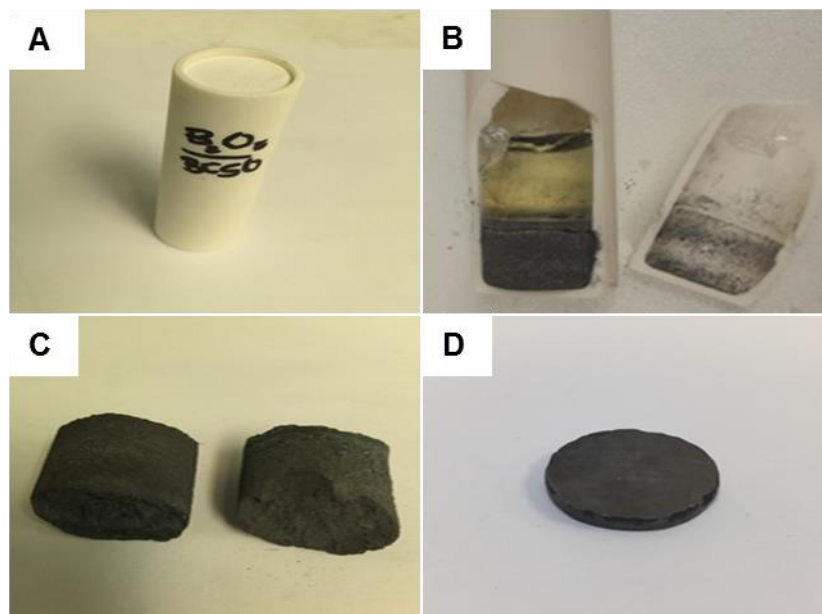


Figure 4-1. Fabrication process of BCSO samples: (a) alumina crucible filled with raw chemicals; (b) broken alumina crucible after flux synthesis; (c) as – synthesized products after the removal of B_2O_3 ; (d) a SPS'ed pellet.

Figure 4-2a shows the different positions and a cross-section of a BCSO sample where the X-ray diffraction were performed. Top (Z1) and middle (Z2) positions were about 1 mm, and 5 mm from the glassy B_2O_3 respectively. The bottom position (Z3)

was on the bottom side of the produced BCSO. The cross section was cut through the middle of the same sample. Figure 4-2b shows XRD patterns for these three different positions and the cross section. The pure BCSO delineated a single-phase ZrSiCuAs-type tetragonal crystal structure (space group, $P4/nmm$), except that a minor amount of Bi_2O_3 impurity was detected at all three positions. The cross-section sample showed a very small, almost non-visible peak of Bi_2O_3 . This suggested that reaction to form the BCSO crystal phase was complete at the centre of the crucible at least, incomplete reaction occurred at the outmost part of the sample only. The lack of boron oxide peaks indicated that either the diffusion between boron oxide and raw materials did not occur, or only happened at the top of the sample which had already been removed.

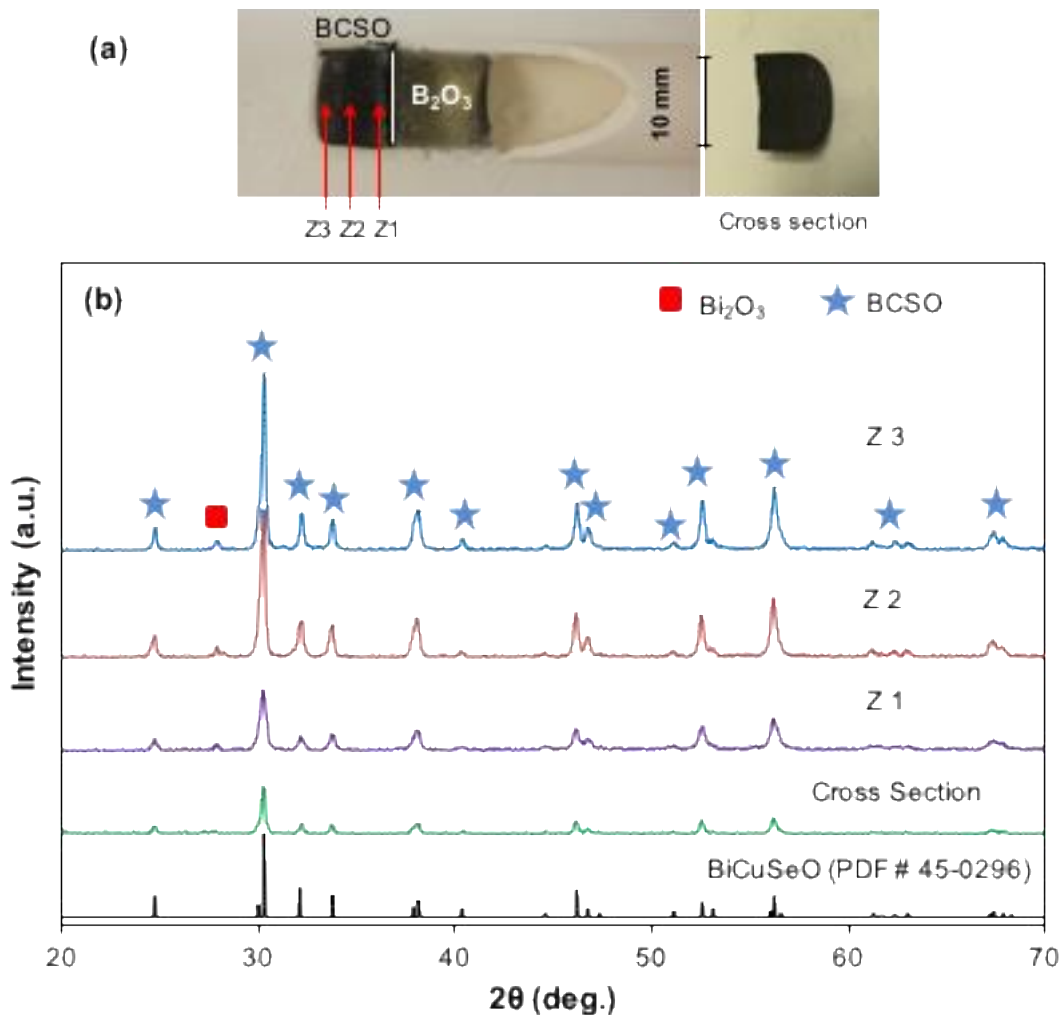


Figure 4-2. (a) Photograph; (b) XRD patterns for different positions Z1, Z2, Z3, and a cross section of as-synthesised undoped BCSO.

The product as synthesized is rigid and can be easily ground. Shown in Figure 4-3 are XRD patterns of the product after grinding and the following SPS'ed pellets. The SPS was used in order to further densify the TE material and improve their thermoelectric properties. One sees that no Bi_2O_3 peak was observed and all the XRD peaks were indexed to the BCSO (PDF#45-0296). This indicated that the Bi_2O_3 peak observed in Figure 4-2. existed at only the outmost part of the sample, the vast majority of the powders were single phased ZrSiCuAs -type crystal structure. After grinding of the as-prepared sample, the tiny amount of Bi_2O_3 as compared to the total amount of BCSO made the Bi_2O_3 concentration beyond the detection limit of the XRD in the mixed and grinded sample. However, it is observed from the XRD result (Figure 4-3) that there was a slight change in relative intensity of peak (104) after SPS process which differs distinctly from the powder BCSO. This suggests that textural or preferential growth for some directions may have happened for SPS'ed samples. In fact, the intensity of peak (104) change has also been observed for the self-propagating high-temperature synthesis (SHS) after SPS'ed (Ren *et al.*, 2015).

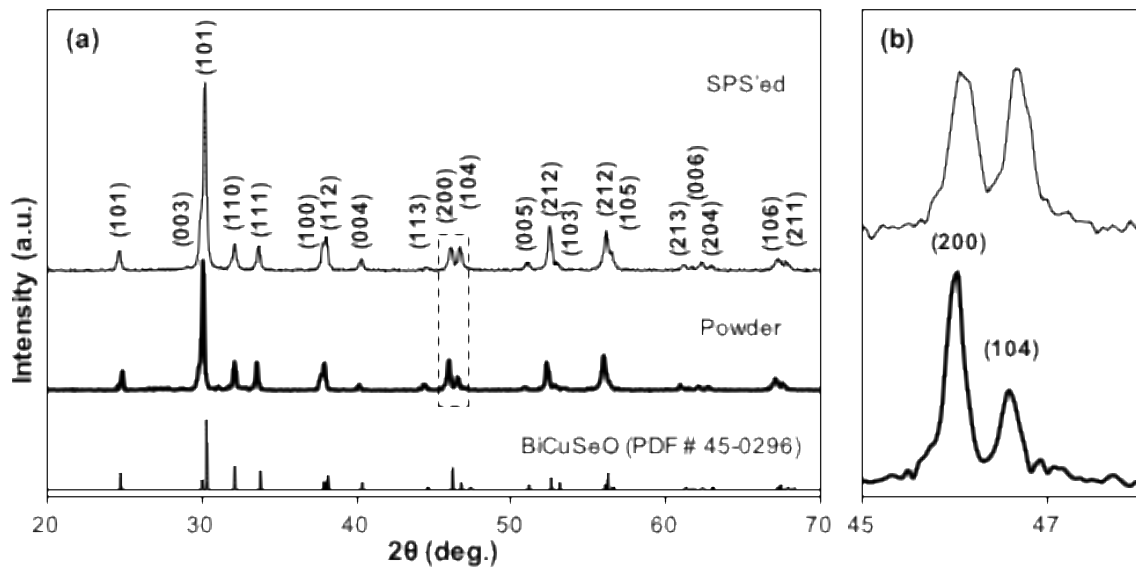


Figure 4-3. (a) XRD patterns of pure BCSO powder and SPS'ed pellet (b) enlargement patterns for a section of (a).

Figure 4-4a shows the XRD patterns of the $\text{Bi}_{1-x}\text{Cs}_x\text{CuSeO}$ after SPS treatment. All samples with different doping concentrations ($x = 0 - 0.025$) demonstrated a pure phase of tetragonal crystal structure as indexed by PDF#45-0296. For the 2.5 mol% highly Cs-doped sample, a minor Bi_2O_3 impurity phase was observed. Of course, a

tiny amount of Bi_2O_3 phase may have existed in the lower doped samples, but it could not be detected using XRD analysis due to the limited sensitivity of the technique. Recently, it was reported that elemental doping at Bi sites generally leads to a Bi_2O_3 impurity phase, which can affect the phase purity and thermoelectric performance of the materials by adversely affecting the mobility carriers and thereby lowering the electrical conductivity (Zhao *et al.*, 2010; F. Li *et al.*, 2012). Figure 4-4b shows the magnified XRD pattern which shows clearly the shift of peaks between 29.5° and 30.5° , and also in the range from 52° to 57° with the increasing doping concentration.

The lattice parameters for these doped samples were obtained using the XRD data. As can be observed in Figure 4-4c, the lattice constants increased linearly with doping concentration and this can be explained by the Cs introduced into BCSO. However, for 2.5% Cs doped the lattice parameters appeared to have decreased, which was consistent with the presence of an amount of secondary phase. This observation confirms that the solubility limit was reached for Cs content between 1.5% and 2.5%, as lattice parameters reduced. The expansion of the unit cell along the c axis might be related to the much larger ionic radius of Cs^+ (1.67 Å) as compared to that of Bi^{3+} (1.03 Å) and Cu^+ (0.77 Å). The pronounced effect to the lattice parameters can also be attributed to weakening of the Coulombic forces between the layers due to the aliovalent doping, which modifies the electronic charge of each layers.

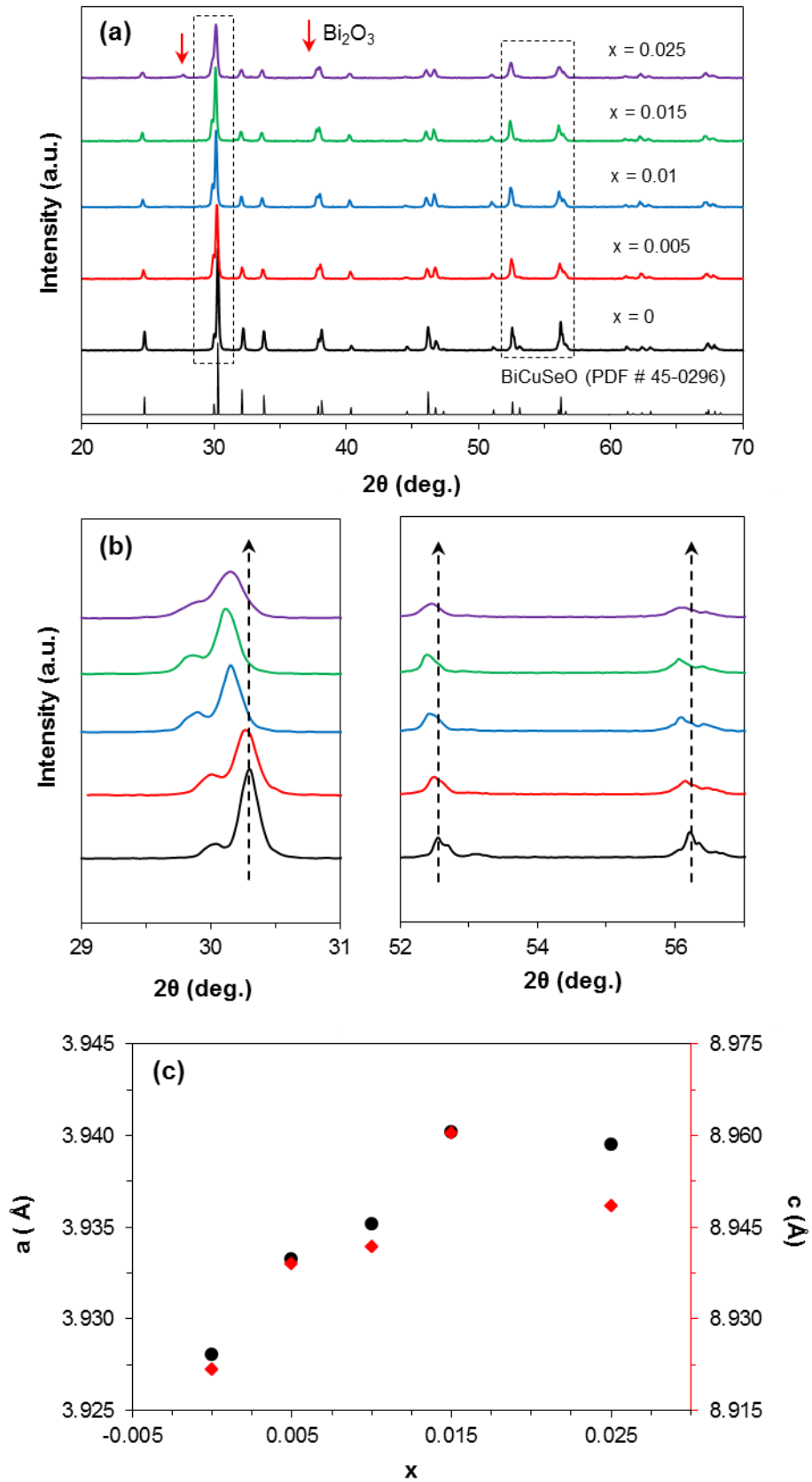


Figure 4-4. (a) XRD patterns; (b) enlargement patterns sections of (a); (c) lattice parameters of $\text{Bi}_{1-x}\text{Cs}_x\text{CuSeO}$.

4.2.2 Morphology and Microstructure Analysis of the SPS'ed samples

The morphology and microstructure of the freshly broken cross section of SPS'ed samples of the pristine BiCuSeO and Cs-doped samples are shown in Figure 4-5.

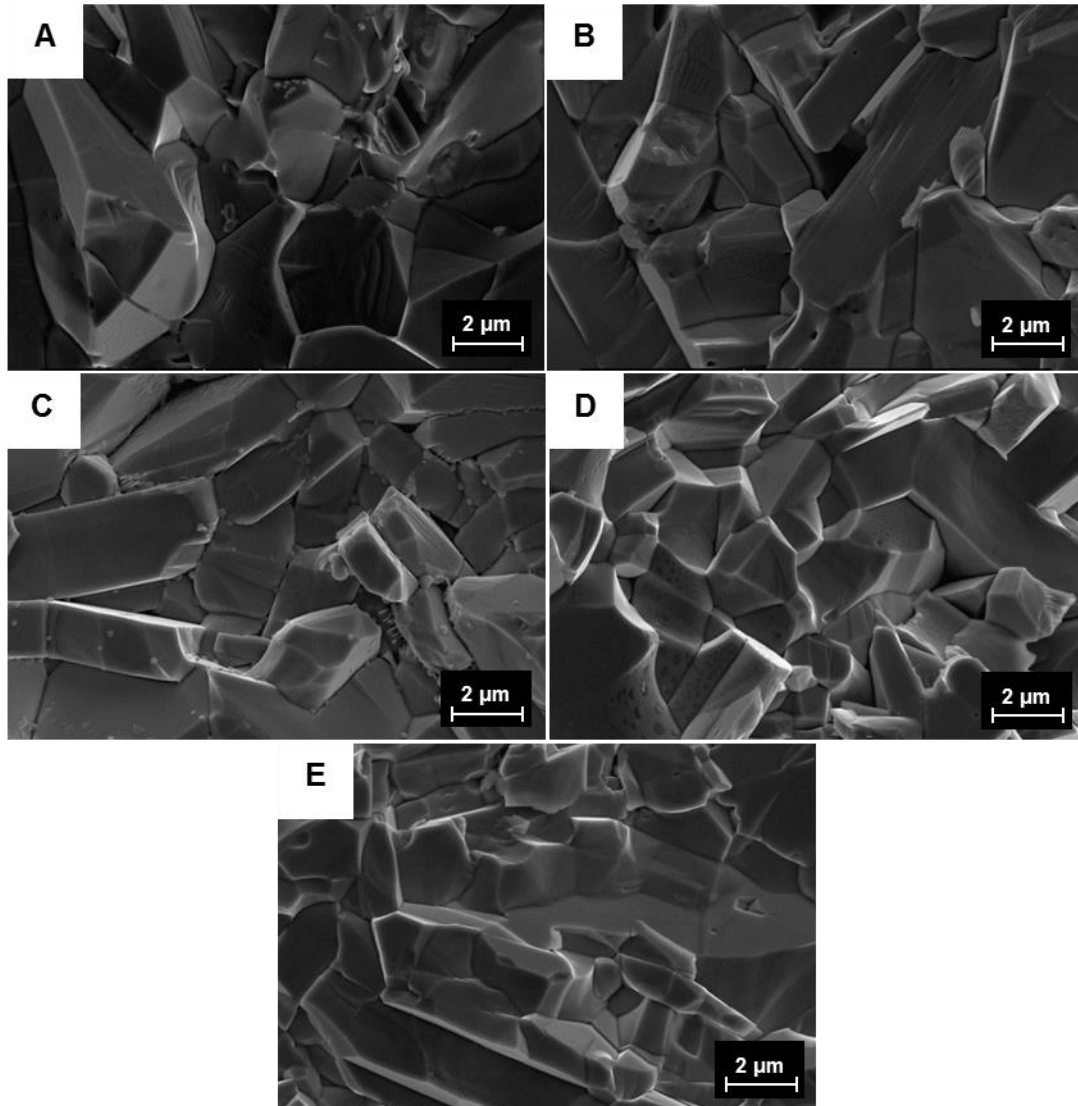


Figure 4-5. SEM cross section micrographs of $\text{Bi}_{1-x}\text{Cs}_x\text{CuSeO}$ ($x = 0 - 0.025$) synthesized by flux – SPS'ed: (a) $x = 0$; (b) $x = 0.005$; (c) $x = 0.01$; (d) $x = 0.015$; (e) $x = 0.025$.

From the SEM, a high dense morphology can be observed. The bulk density of the sintered materials was measured by Archimedes' method. The relative density of all bulk samples reached above 98%. As shown in Figure 4-5a, a larger grain size of 2-6 μm was observed for the SPS'ed-flux BCSO, which was larger than 1-2 μm synthesized by using the SHS method (Ren *et al.*, 2015) and much larger than 400-800 nm obtained using the solid-state reaction route (SSR) (J. Li *et al.*, 2014).

SEM images showed that the grain size was progressively reduced with the increased Cs doping. Reduced grain size generated a larger number of grain boundaries, which may reduce the thermal conductivity via phonon scattering. Furthermore, the grain size of the doped sample was much smaller than that of the pure BCSO (Figure 4-5a). This indicates that the grain size reduction might be due to the repressed growth with Cs doping.

4.2.3 Thermal and Chemical Stability

Thermoelectric generator devices are usually subjected to large thermal stresses and strains for a long period of time. Therefore, it is necessary to study their thermal and chemical stability. Figure 4-6 shows the differential scanning calorimetry (DSC) and thermogravimetric analysis (TGA) curves of SPS'ed $\text{Bi}_{1-x}\text{Cs}_x\text{CuSeO}$ under either flowing argon or air. Below a Cs content of $x = 0.005$, no obvious endothermic or exothermic peaks appeared in the range of the whole measured temperature up to 923 K, which indicated the stability of these materials (Figure 4-6a). However, a clear endothermic peak was observed around 1000K, accompanied by $\sim 1.5\%$ weight loss in the TGA curves (Figure 4-6b). The undoped BCSO result is similar to the one reported by Barreteau and Li who did observe DSC peaks at 1023 K (F. Li *et al.*, 2014; Barreteau, Berardan and Dragoe, 2015).

At and above a Cs content of $x = 0.01$, a clear change of the slope of the curve was observed from 680 K where decomposition starts under argon and air conditions (Figure 4-6a). Upon further heating, two endothermic peaks were observed, a small peak around 750 – 850 K and a broader peak between 900 – 1010 K, and the accompanied total weights loss were about 2.3 % (Figure 4-6b). It is noteworthy that the stability of the phase was reduced starting from 680 K and the onset temperature of the broader peak decreased with increasing Cs content. Although the selenium (Se) element can be partially volatilized at atmospheric oxidizing condition at temperatures as low as 473 K (Desborough *et al.*, 2000; F. Li *et al.*, 2014; C. Barreteau, Berardan and Dragoe, 2015), that could degrade the stability of the compound, the BCSO samples also exhibit good resistivity versus volatility.

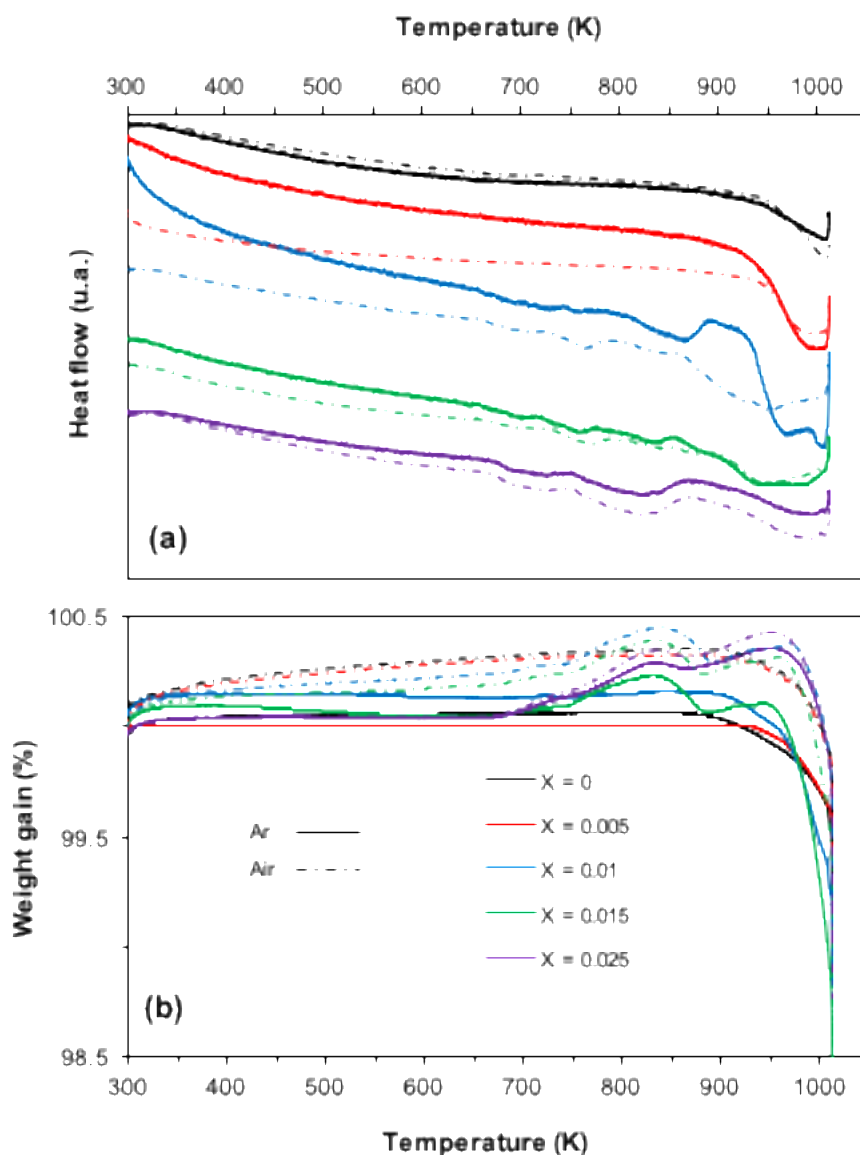


Figure 4-6. (a) Differential scanning calorimetry; and (b) thermogravimetric analysis of $\text{Bi}_{1-x}\text{Cs}_x\text{CuSeO}$ ($x = 0 - 0.025$) samples under flowing argon and air.

Gaining mass was observed in all samples under air flow from 300 to ~ 960 K and then a significant decrease of mass above 960 K. This indicates oxidation of the BCSO happened when it was heated in air. TGA curves show a maximum of 0.4 % gain in weight at 850 K for $\text{Bi}_{0.99}\text{Cs}_{0.01}\text{CuSeO}$. However, no obvious exothermic peak (reflecting the formation of a second phase) on DSC was observed. Surprisingly, mass gaining was observed from 700 K to 950 K for 1.5% and 2.5% Cs doped samples under pure argon flow, suggesting a gas leakage of the system at temperatures above 700 K at least.

Further investigations were carried out for the stability of the doped samples. Figure 4-7 displays bar samples of Cs doped BCSO (0.5 and 1%) after thermoelectric property measurements. The image discloses an obvious change at the surface of the sample of 1% doping (Figure 4-7b). The deposit formed on the surface was observed for 1% Cs and above, not for the 0.5% Cs doped BCSO. This confirms the changes of the slope of the DSC curves that was observed in Figure 4-6a. Moreover, compositional morphology was obtained by EDS (Figure 4-8). The elemental quantitative data of the $\text{Bi}_{0.99}\text{Cs}_{0.01}\text{CuSeO}$ sample confirmed there were two coexisting areas, each had different elemental composition (Figure 4-8d): (1) the dark area, which had a high Cs concentration of more than 80 Wt. %; (Figure 4-8b), and (2) the bright or white area, where the Cs content was close to the stoichiometric concentration (Figure 4-8c). These results suggest that the highly-doped $\text{Bi}_{1-x}\text{Cs}_x\text{CuSeO}$ ($x \geq 0.01$) materials were not stable when heated (during the TE property measurement) in air, and suggest the dark aggregates were Cs oxide.

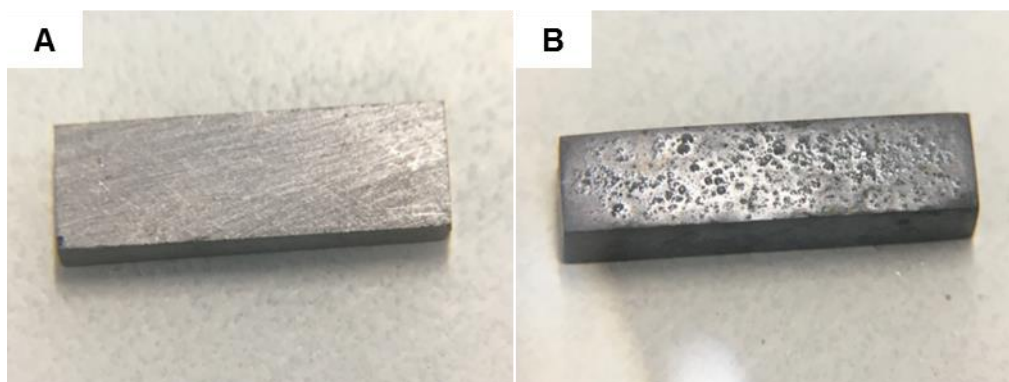


Figure 4-7. Bar-sample of Cs Doped BCSO after TE measurements: (a) 0.5%; (b) 1%.

These results suggest that the undoped BCSO and up to 0.5% Cs-doped BCSO materials were stable under argon atmosphere below 923 K. Moreover, it appears that Se volatilization was not an issue for the use of BCSO based materials as thermoelectric modules under inert atmosphere. Furthermore, it was recently reported that no significant weight loss is observed for SPS'ed pure BCSO for several days at 923 K (Sui *et al.*, 2013). However, using a powder with high specific area of $0.255 \text{ m}^2 \text{ g}^{-1}$, the total weight loss less than 1 % was observed for powders after 3 weeks (C Barreteau, Berardan and Dragoe, 2015). It was further suggested that if the whole

surface of a BCSO bar is exposed to a high temperature of 923 K, it would take more than one year to observe a 1% weight loss (Barreteau, Berardan and Dragoë, 2015).

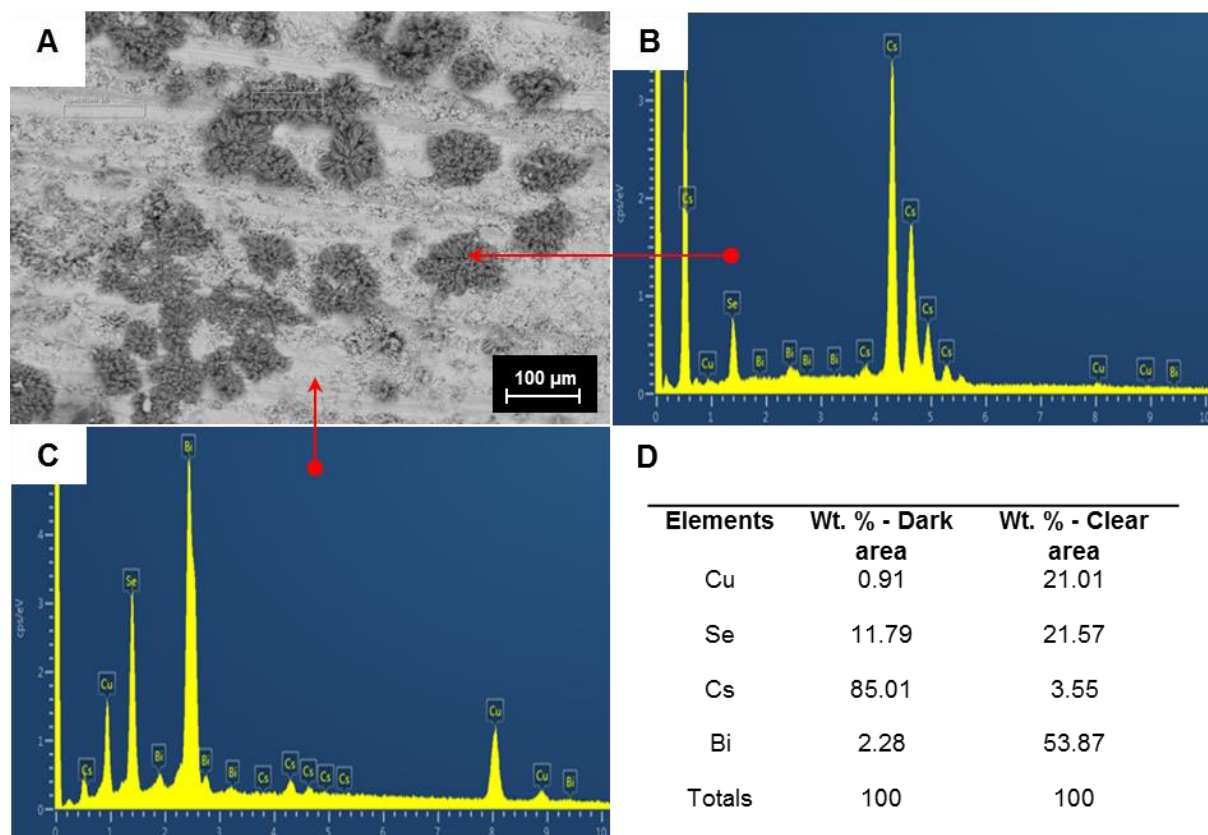


Figure 4-8. SEM image, EDS spectrums and elemental quantification results showing the typical composition found at $\text{Bi}_{0.99}\text{Cs}_{0.01}\text{CuSeO}$ sample.

4.2.4 Thermoelectric Properties Characterisation

This section has two subsections. In the first subsection, the thermoelectric properties of the pristine BCSO, and comparison to those prepared using other synthesis methods, SSR (J. Li *et al.*, 2014; Zhao *et al.*, 2014) and ultrafast SHS, were discussed (Ren *et al.*, 2015). In the second subsection, the enhancement of thermoelectric properties in Cs-doped BCSO was investigated. The electrical transport properties were examined using bar samples obtained by cutting along the longitudinal direction to SPS axial pressure to the disc pellet samples.

4.2.4.1 Pristine BiCuSeO

In order to compare the thermoelectric properties of the novel processing route with other previously reported methods, the temperature dependence of thermoelectric properties of the undoped BCSO were compared over the temperature range 315 –

764 K. These values were compared with undoped BCSOs prepared by SHS and SSR methods (J. Li *et al.*, 2014; Zhao *et al.*, 2014; Ren *et al.*, 2015) and displayed in Figures 4-9 and 4-10. As seen in Figure 4-9a, the electrical conductivity of the sample synthesized using the flux method (18.8 S/cm at 764 K) was higher than that on the SSR route (~ 8 S/cm at 775 K) but lower than that of the SHS synthesis (~ 44.5 S/cm at 775 K).

The comparison of the Seebeck coefficient among these methods was shown in Figure 4-9b. A similar trend of the Seebeck coefficient was observed for the flux and SHS methods, but different to that of the materials prepared using SSR method. At room temperature, the highest Seebeck coefficient was observed for our flux method at 516 $\mu\text{V/K}$, and then decreased with the increase of temperature (328 $\mu\text{V/K}$ at 764 K). In Figure 4-9c, a higher power factor value of ~ 230 $\mu\text{W m}^{-1} \text{k}^{-2}$ at 665 K was obtained for the materials prepared using the flux method, which was higher than that of SSR method (~ 128 $\mu\text{W m}^{-1} \text{k}^{-2}$ at 775 K) but lower than that of SHS (~ 368 $\mu\text{W m}^{-1} \text{k}^{-2}$ at 775 K). The large power factor can be attributed to the high electrical conductivity and the high Seebeck coefficient.

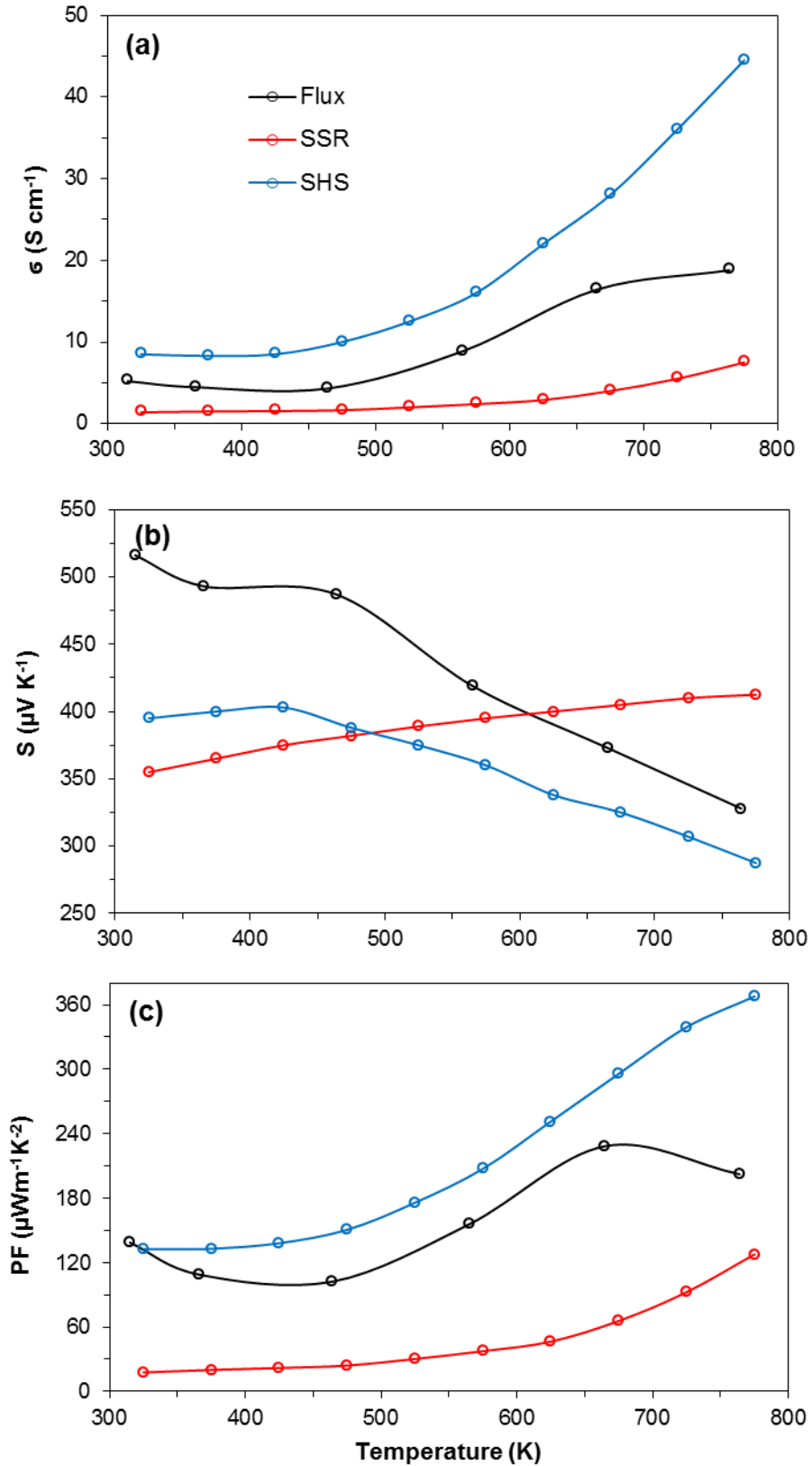


Figure 4-9. Temperature dependence of thermoelectric properties for the BCSO synthesized by SSR, SHS and the flux methods: (a) electrical conductivity; (b) Seebeck coefficient; (c) power factor.

Figure 4-10a shows the thermal conductivity (κ) as a function of temperature for SPS'ed BCSO synthesized by flux methods, which decreased continuously with temperature. Compared to the SHS and SSR methods, the flux method showed the lowest thermal conductivity in the whole temperature range, $\sim 0.84 \text{ Wm}^{-1}\text{K}^{-1}$ at 315 K and $\sim 0.42 \text{ Wm}^{-1}\text{K}^{-1}$ at 765 K. These values are lower than most thermoelectric materials. These relatively low thermal conductivity values were explained by the low lattice contribution and may originate from the weak bonding between the layers and the low Young's modulus (Pei *et al.*, 2013; Shao *et al.*, 2016).

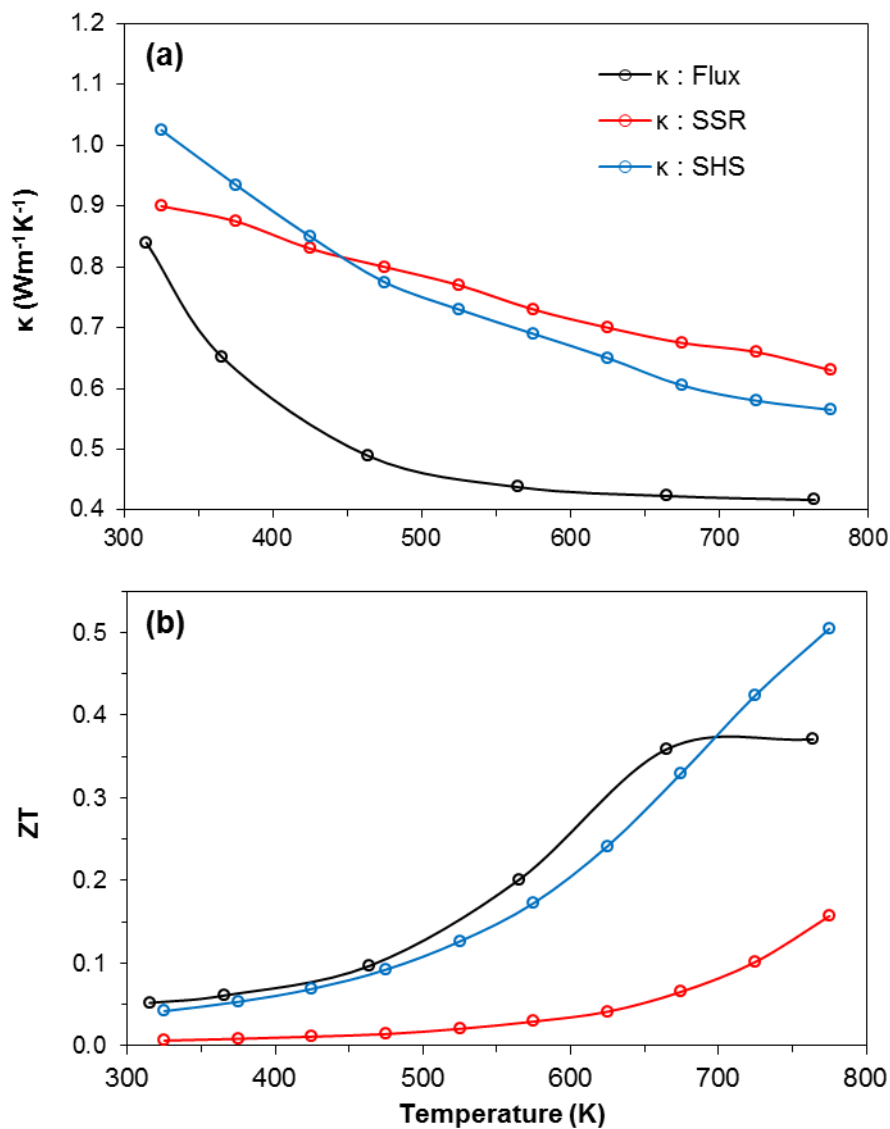


Figure 4-10. Temperature dependence of SPS'ed BCSO synthesized by SSR, SHS and flux methods: (a) thermal conductivity; (b) thermoelectric figure of merit.

Figure 4-10b shows the temperature dependence of ZT values for the pristine BCSO synthesized using SHS-SPS, flux-SPS and SSR-SPS methods. Across a large temperature range, ZT of the materials prepared using the flux method was about the same as that of those prepared using the SHS method, but higher than ZT values prepared using the SSR route. As a result, BCSO showed similar ZT values (0.36 at 665 K and 0.37 at 764 K) as SHS (0.33 at 675 K and 0.50 at 775 K), but higher than that of SSR (0.07 at 675 K and 0.16 at 775K) samples (J. Li *et al.*, 2014; Zhao *et al.*, 2014; Ren *et al.*, 2015)

4.2.4.2 Caesium Doped BCSO

The electronic and thermal transport properties can be tuned by doping and controlling the non-stoichiometry tuning of materials (Enescu and Virjoghe, 2014; Hamid Elsheikh *et al.*, 2014; Nag and Shubha, 2014; Zheng *et al.*, 2014). Figures 4-11 and 4-12 show the temperature dependence of thermoelectric transport properties for $\text{Bi}_{1-x}\text{Cs}_x\text{CuSeO}$ ($x = 0 - 0.01$) samples after SPS treatment from 300 K to 680 K. As shown in Figure 4.11a, the electrical conductivity of the doped samples increased with temperature. This also indicated that the monovalent Cs^+ ion was an effective dopant for BCSO. This enhancement can be further explained by the presence of increased carriers in the conductive layers, leading to increase in the electrical conductivity. The highest electrical conductivity of $\sim 25 \text{ Scm}^{-1}$ was obtained for $\text{Bi}_{0.995}\text{Cs}_{0.005}\text{CuSeO}$ at 680 K.

The temperature dependence of the Seebeck coefficient of $\text{Bi}_{1-x}\text{Cs}_x\text{CuSeO}$ is shown in Figure 4-11b. At room temperature, the 1 mol% Cs doped sample exhibited a high Seebeck coefficient value of $\sim 550 \mu\text{V/K}$. However, the Seebeck coefficient value decreased over the whole temperature range and a similar Seebeck value of $\sim 370 \mu\text{V/K}$ at 680 K was observed for all samples. It is noteworthy that the trend of decreasing Seebeck coefficient with increasing temperature was observed for monovalent Cs, and an opposite effect was observed with monovalent K and Na doping (Sun Lee *et al.*, 2013; J. Li *et al.*, 2014). This moderately decreased Seebeck coefficient and enhanced electrical conductivity of the doped samples produced a high-power factor value of $340 \mu\text{W m}^{-1} \text{K}^{-2}$ for $\text{Bi}_{0.995}\text{Cs}_{0.005}\text{CuSeO}$ at 680 K, as shown in Figure 4-11c.

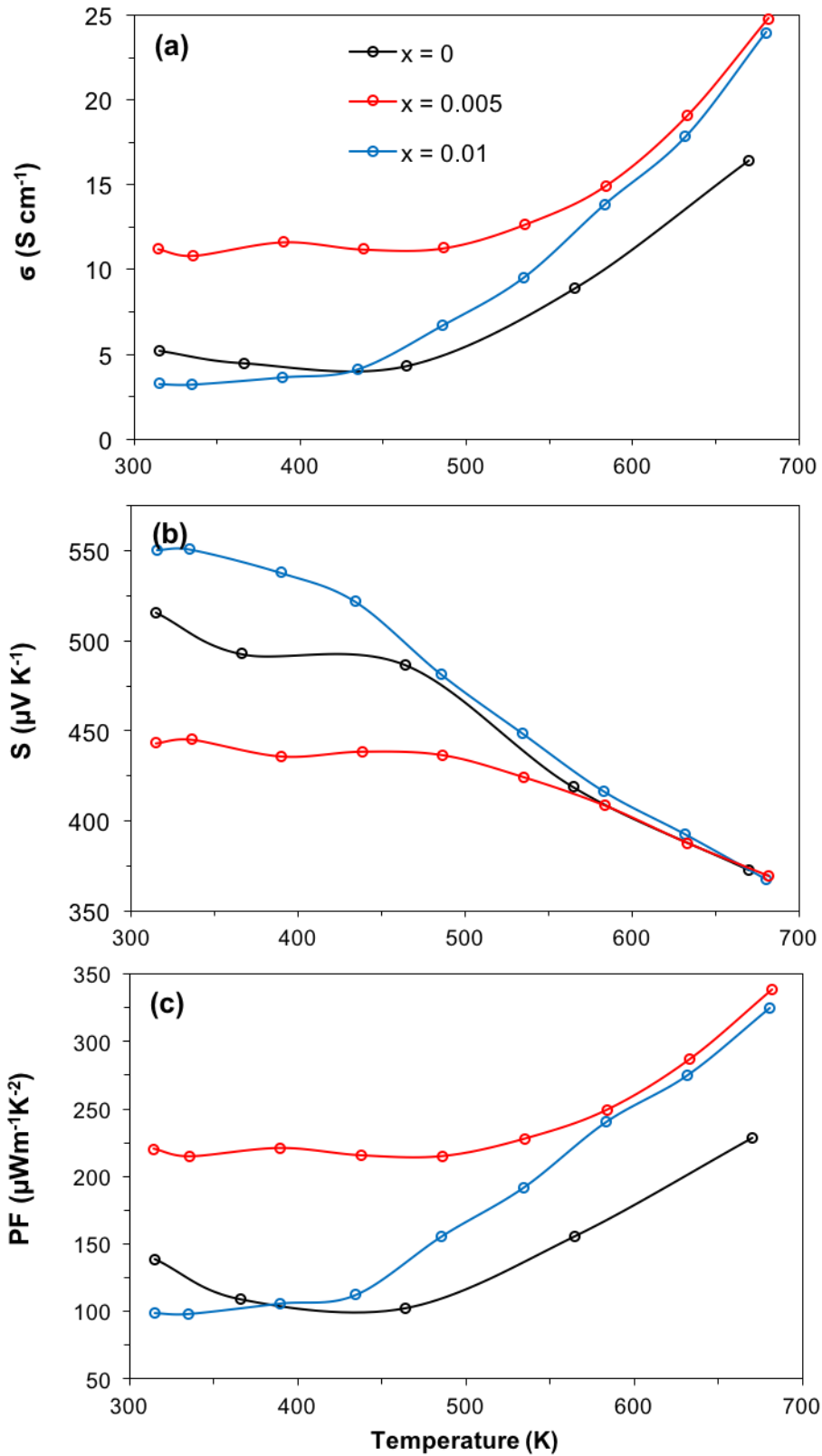


Figure 4-11. Temperature dependence of SPS'ed $\text{Bi}_{1-x}\text{Cs}_x\text{CuSeO}$ ($x = 0 - 0.01$) synthesized by the flux method: (a) electrical conductivity; (b) Seebeck coefficient; (c) power factor.

Figure 4-12a shows total thermal conductivity as a function of temperature for the $\text{Bi}_{1-x}\text{Cs}_x\text{CuSeO}$ ($x = 0 - 0.01$) samples. For all of the samples, the thermal conductivity decreased with rising temperature. For the undoped BCSO, a value of $0.84 \text{ Wm}^{-1}\text{K}^{-1}$ at room temperature was observed, and dropped to $0.42 \text{ Wm}^{-1}\text{K}^{-1}$ at 680 K. These values were lower than most thermoelectric materials (Amani, Tougas and Gregory, 2012; Nag and Shubha, 2014). Upon doping with Cs, the thermal conductivity decreased further to a minimum of $0.35 \text{ Wm}^{-1}\text{K}^{-1}$ for $\text{Bi}_{0.995}\text{Cs}_{0.005}\text{CuSeO}$ at 680K.

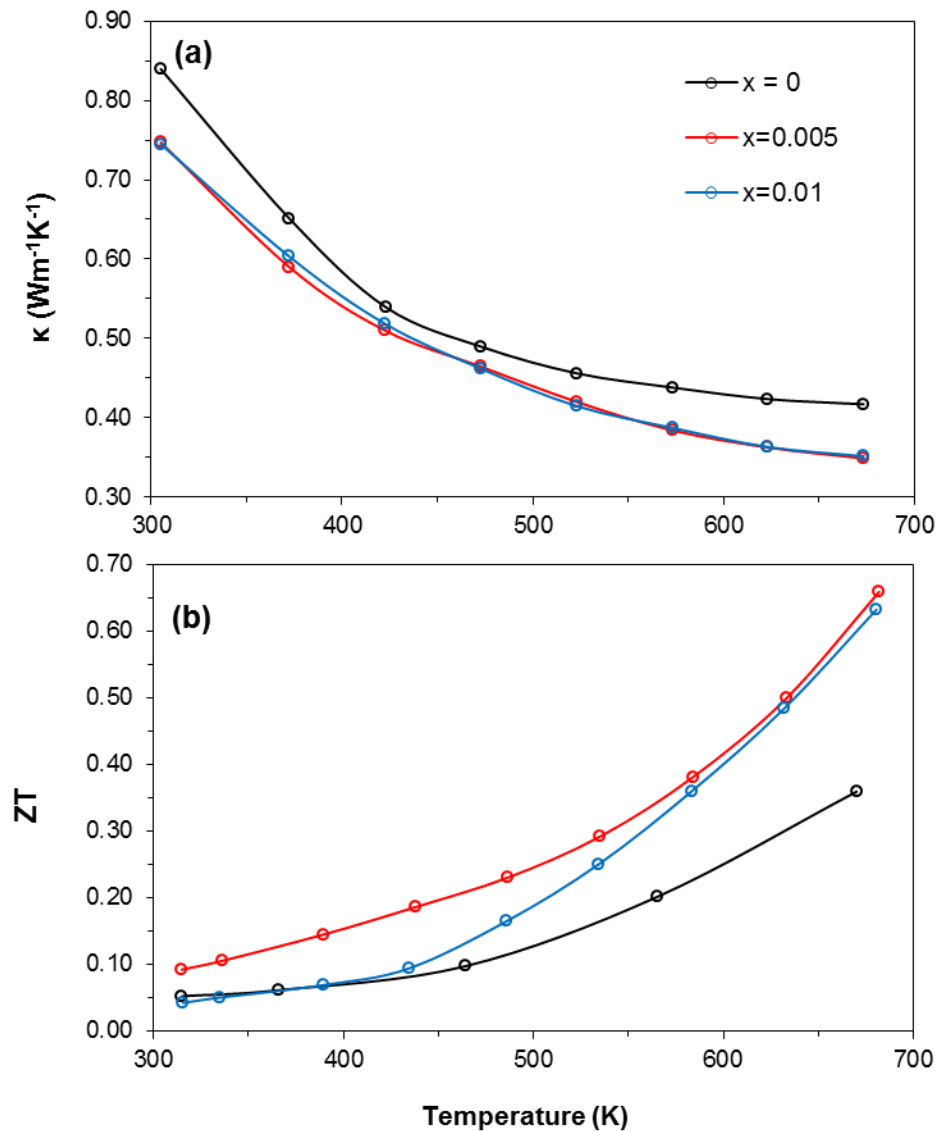


Figure 4-12. Temperature dependence of $\text{Bi}_{1-x}\text{Cs}_x\text{CuSeO}$ ($x = 0 - 0.01$) synthesized by the flux method: (a) thermal conductivity; (b) thermoelectric figure of merit.

The relationships between the microstructure and the electro-thermal properties of the TE materials are often complex. Generally, charge carrier density and defect density (including grain boundary density) are the most important factors. Our flux prepared pristine BCSO displayed largest grain size, highest Seebeck coefficient and lowest thermal conductivity, as compared to the SHS and SSR prepared samples. One possible explanation is that our flux prepared BCSO had a lower charge carrier density than the SHS samples at least. A lower electrical conductivity for the flux sample than for the SHS sample supports this hypothesis. This lower charge carrier density could be due to lower impurity or defect introduced in the flux method than for the SHS method.

The incorporation of Cs on BSCO resulted in the decrease of the grain size, Seebeck coefficient, and thermal conductivity, also an increase of the electrical conductivity. One plausible explanation is that the Cs doping increased the charge carrier density. Another consequence of the incorporation of Cs into the BCSO could be the increase of point defects. This could be the reason why the 0.5% and 1% Cs doped BCSO had their thermal conductivity reduced further from that of the non-doped BCSO. Considering the hypothesis that doped BCSO had higher charge carrier density, the electrical contribution to the thermal conductivity must be much smaller than the lattice contribution for the BCSO samples. The reduction of the grain size with doping may also contributed to the reduction of the thermal conductivity, as this increased the density of grain boundary. Furthermore, the presence of high Cs concentration areas observed for doping higher than 0,5% may be also another reason. Indeed, nanoinclusions of high Cs content can also exist and so play a role by phonon scattering in the thermal transport properties of prepared samples. Besides, the point defect scattering could also originate from mass fluctuations and interatomic force differences between the impurity Cs (atomic mass 133) and Bi (atomic mass 209), which contributes to the lattice thermal conduction reduction, as described by the Callaway model (Callaway and Von Baeyer, 1960; Callaway, 1961; Wan *et al.*, 2006). The dimensionless figure of merit ZT is shown in Figure 4-12b. ZT values increased with temperature, a maximum ZT value of 0.66 was obtained for the $\text{Bi}_{0.995}\text{Cs}_{0.005}\text{CuSeO}$ at 680 K, which was about 78 % higher than that of the pure BCSO.

4.3 Conclusions

The BCSO thermoelectric materials have been successfully synthesized using an eco-friendly B_2O_3 flux method. Compared with other synthesis methods, the flux method can be performed in air below 923 K with little risk of oxidation. Moreover, the BCSO prepared by the flux method had improved the electrical conductivity and Seebeck coefficient, and significantly suppressed thermal conductivity. The ZT at 680 K was increased from 0.37 for pristine BiCuSeO to 0.66 for $Bi_{0.995}Cs_{0.005}CuSeO$. These results showed promising features, such as simplicity and cost effectiveness of BCSO powder synthesis using the flux method, which may be advantageous for large-scale application.

5 Validation of the Experimental Setup

5.1 Introduction

In this chapter, the validation of the catalytic reactor experimental setup is presented. The catalytic chemical reactor was designed to apply the thermoelectric effect for tuning catalyst performance. Prior to the thermoelectric application, preliminary studies were carried out to validate the blank reactor to assess the reactor's catalytic contribution. Moreover, the effect of blank supports such as YSZ, γ -Al₂O₃ and Au-YSZ electrode were investigated, no Pt group metals were used at this stage. Under similar conditions, Pt nanoparticles catalysts supported on YSZ and γ -Al₂O₃ were investigated from 293 K to 673 K. Furthermore, the NEMCA phenomenon for a Pt film on YSZ pellet was studied for ethylene oxidation reaction.

5.2 Results and Discussion

5.2.1 XRD and TEM of Pt Nanoparticles Catalysts

The X-ray diffraction patterns of Pt/ γ -Al₂O₃ and Pt/YSZ are shown in Figure 5-1. These showed the presence of Pt(111) at 2θ value of 39.72°. The Pt (111) peak was used to calculate the average Pt particle size according to the Debye-Scherrer equation (3-1). Figure 5-2 shows TEM micrographs for (a) Pt/ γ -Al₂O₃ and (b) Pt/YSZ catalysts and the corresponding histograms for Pt particles, respectively. Figure 5.2a shows spherical Pt nanoparticles highly dispersed on γ -Al₂O₃. However, aggregation of Pt nanoparticles was observed for Pt/YSZ (Figure 5-2b). Energy dispersive spectroscopy (EDS) analysis with the TEM confirmed that these particles were Pt (Figure 5-2c). Around 2 keV, the peaks associated with Zr, Y and Pt overlapped. However, Pt L _{α} and L _{β} peaks at 9.5 and 10 keV appeared clearly on spectrum. The Cu peaks (0.9 and 8 keV) were from the Cu TEM sample grid and Cr peaks (5.4 and 5.95 keV) were from TEM pole piece or EDS detector. Apparently, Figure 5-2b is not representative for Pt/YSZ, which has a Pt loading of 1% only.

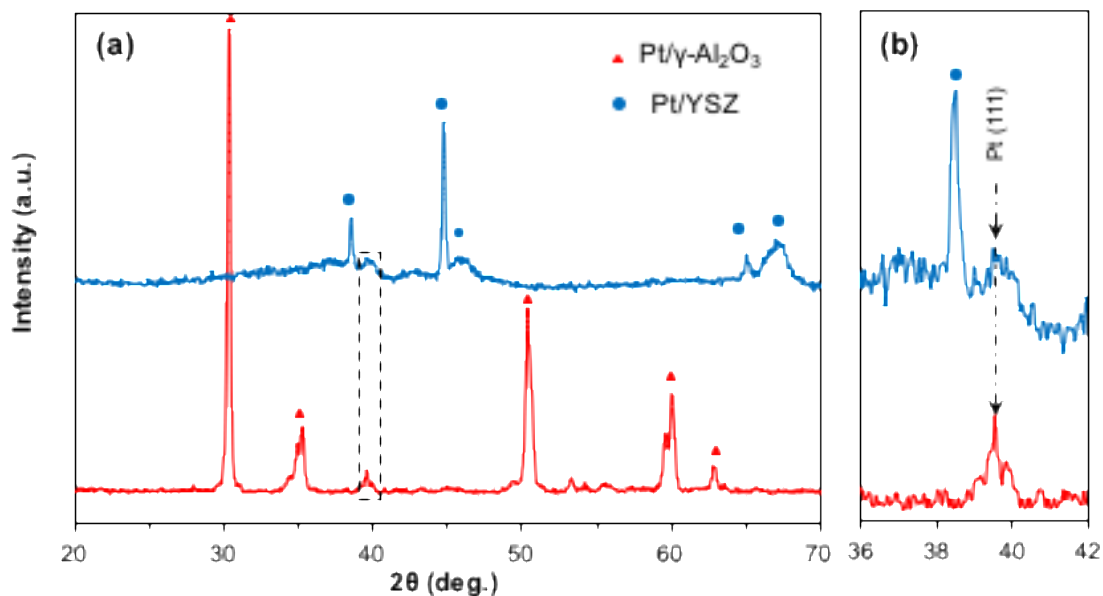


Figure 5-1. (a) X-ray diffraction patterns of Pt/YSZ and Pt/ γ -Al₂O₃. (b) enlargement patterns of Pt (111) peaks.

The estimated size of Pt nanoparticles based on the Debye-Scherrer equation (3-1) was found in a good agreement with the particle size estimated from TEM and ImageJ software. The results are summarized in Table 5-1. It shows that the average size for Pt particles on Pt/ γ -Al₂O₃ is 11.7 nm from TEM analysis, and 16 nm from XRD via the Debye-Scherrer calculation. The corresponding values for Pt/YSZ were 24.2 nm from TEM analysis, and 28.3 nm for XRD analysis.

Table 5-1. Characteristic of Pt nanoparticles catalysts prepared by polyol reduction method.

Catalysts	Metal loading (Wt. %)	Average size from XRD (nm) [#]	Average size from TEM (nm) [*]	Dispersion (%) ^{**}
Pt/ γ -Al ₂ O ₃	1.0	16	11.7	9.8
Pt/YSZ	1.0	28.3	24.2	2.7

[#] determined from Debye-Scherrer equation (3-1).

^{*} determined from TEM images using Image J software.

^{**} estimated from equation (3-2).

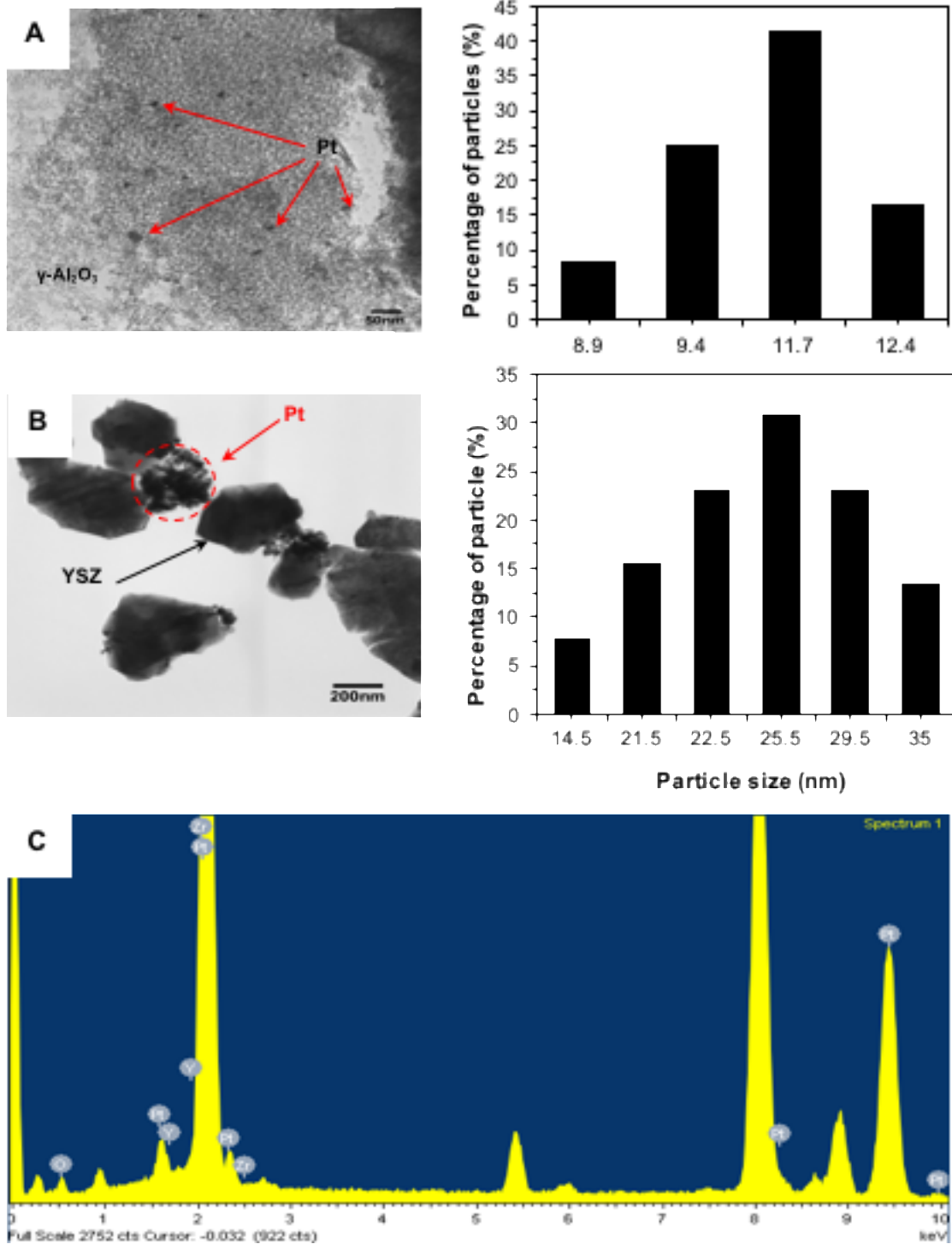


Figure 5-2. TEM images: (a) Pt/γ-Al₂O₃; (b) Pt/YSZ and the corresponding histograms; (c) EDS spectra of clustered Pt particles on YSZ as shown in (b) Pt/YSZ selected area.

5.2.2 XRD and SEM of Pt Film Deposited on YSZ

Figure 5-3 displays the XRD patterns of Pt film on a dense YSZ pellet after the pre-treatment. The strong Pt peak clearly indicates the Pt was (111) orientated. Small platinum peaks (200) and (220) were also observed. As shown in the inset, the (111) peak became much stronger after pre-treatment in 5% H₂/Ar at 603 K for 2 hrs. This means that the platinum film on YSZ(111) is clearly (111)-orientated after annealing. Furthermore, it appeared that the peak width was reduced and shifted to larger 2 θ values. When the Pt film was freshly deposited on YSZ, the crystal size was very small ~ 15 nm. After the pre-treatment, the crystal size increased to approximately 40.7 nm, as determined from the Debye-Scherrer equation (3-1), which corresponds to 2.81% dispersion.

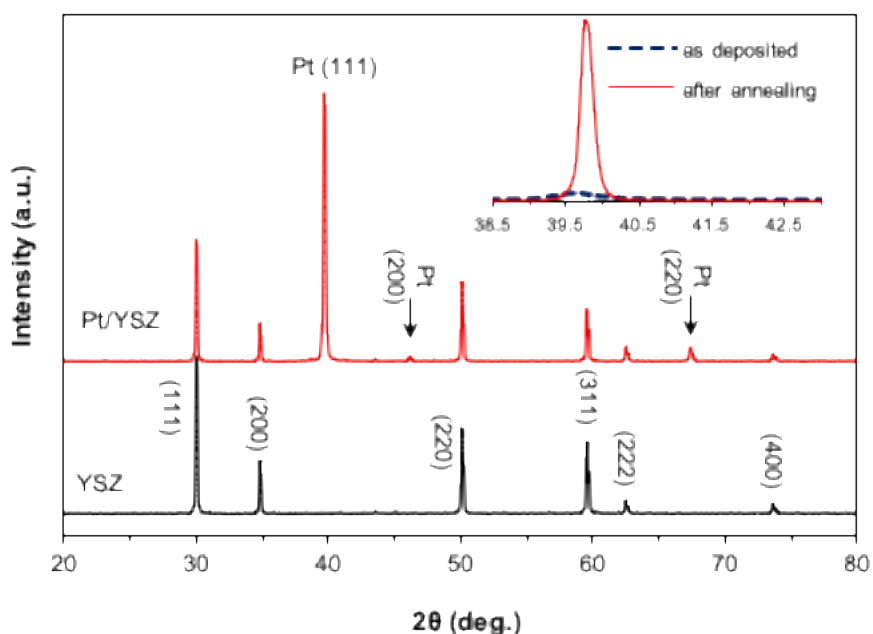


Figure 5-3. XRD patterns of platinum film on YSZ after the thermal treatment. Inset: $\theta/2\theta$ scan in the range of 38.50° and 42.5° of the freshly deposited platinum film on YSZ before and after the pre-treated in 5%H₂/Ar at 603 K for 2h.

Figure 5-4 shows the SEM images of the sputtered Pt on a dense YSZ pellet before and after catalytic chemical reaction. The Pt was in the form of a film. It followed the topography of the YSZ substrate, with no apparent porosity (Figure 5-4c). Even after several hours at high temperature in the reaction chamber, the film did not show apparent porosity or agglomerates (See Figure 5-4a).

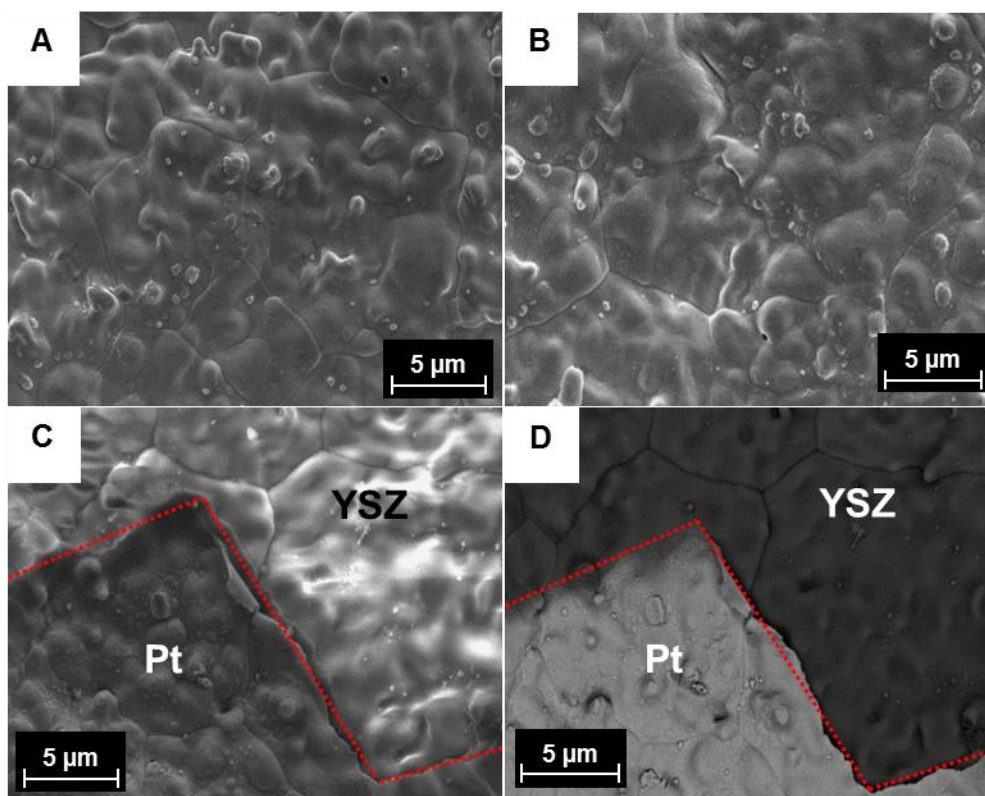


Figure 5-4. SEM micrographs of the Pt film on YSZ: (a) before; (b) after catalytic chemical condition; (c) a boundary area includes Pt/YSZ and pure YSZ; (d) back-scattered electron image from the same area shown in (c).

5.2.3 GC Development and Validation

More detailed information of method development and validation parameters and procedures used for gas chromatography equipped with a thermal conductivity detector (GC-TCD) can be found in Appendix A. Figure 5-5 presents a typical chromatogram of a gas standard via GC-TCD. The chromatogram demonstrated excellent specificity, where no interference from extraneous compounds existed. All peaks were reported as baseline to baseline (BB) signals using the TotalChrom Workstation data system. The resultant calibration curve exhibited excellent linearity results with $R^2 \geq 0.9999$ over 5 levels spanning of the gas concentration from 100 to 1000 ppm. The accuracy of the GC-TCD method was validated against an IR analyser (G150 O₂ and CO₂, Gem Scientific), which was considered to give the true gas concentration. 10 samples of O₂ and CO₂ were analysed by GC-TCD and IR, to determine the accuracy of the GC-TCD method. An excellent agreement was found between the two techniques, with an average relative error of 2.5%.

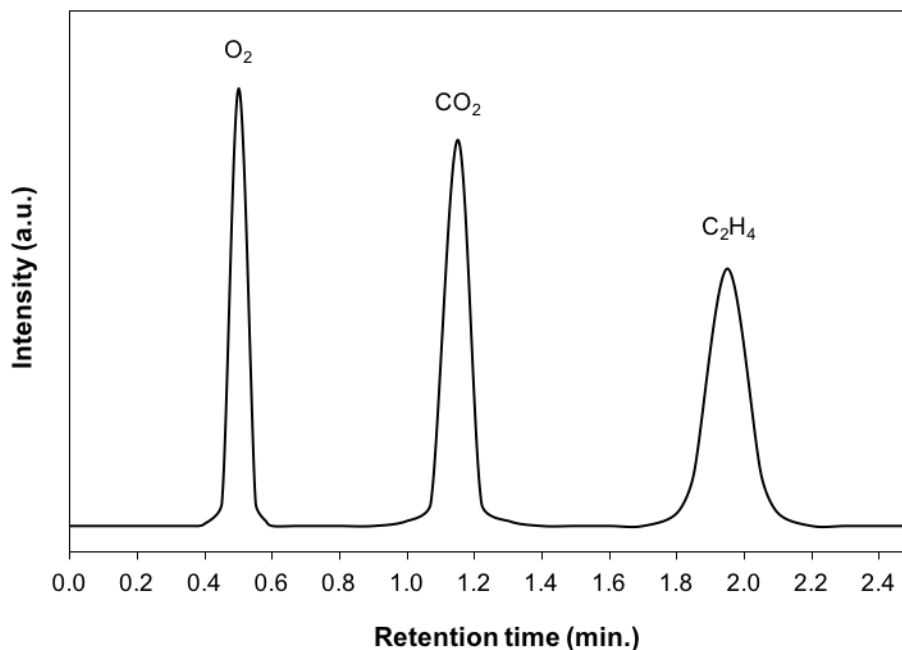


Figure 5-5. A typical chromatogram via GC/TCD of a mixture containing O₂, CO₂, and C₂H₄ in helium carrier gas, from a gas standard.

To examine the repeatability of the method, the average and standard deviation of a set of ten measurements made on the same day and under the same conditions, was determined. The relative standard deviations (RSD) for O₂, CO₂ and C₂H₄ components were lower than 1.2%, 0.7% and 0.9% by using TCD channel respectively. For reproducibility estimation, it was observed that the lowest RSD values at 50 ml/min showed an exceptional repeatability precision, which suggested that the flow rate of 50 ml/min was the most reproducible measurement. The robustness of this GC was demonstrated by the repeated analysis of 10 samples after a period of over 10 and 100 days.

5.2.4 Ethylene Oxidation on Blank Reactor

The blank reactor was tested by admitting the reactants into the system without any catalytic support or metal catalyst. Figure 5-6 shows individually examined thermal reaction test results for the blank reactor. For the first heating up, CO₂ was observed in the temperature range of 523 K to 673 K. The maximum conversion obtained was around 10%. The same reaction conditions were applied for a second blank test. This time it was decreased to about 6.7 % at 673 K. Afterwards, the gas flow was kept on for further 90 minutes at the same temperature (673 K) and the C₂H₄ conversion was

gradually decreased to ~ 2.7%. In the third blank test, the initial C₂H₄ conversion was less than 2.5 % at 653 K. And after a further 90 minutes at the same temperature, the C₂H₄ conversion decreased to less than 0.2%.

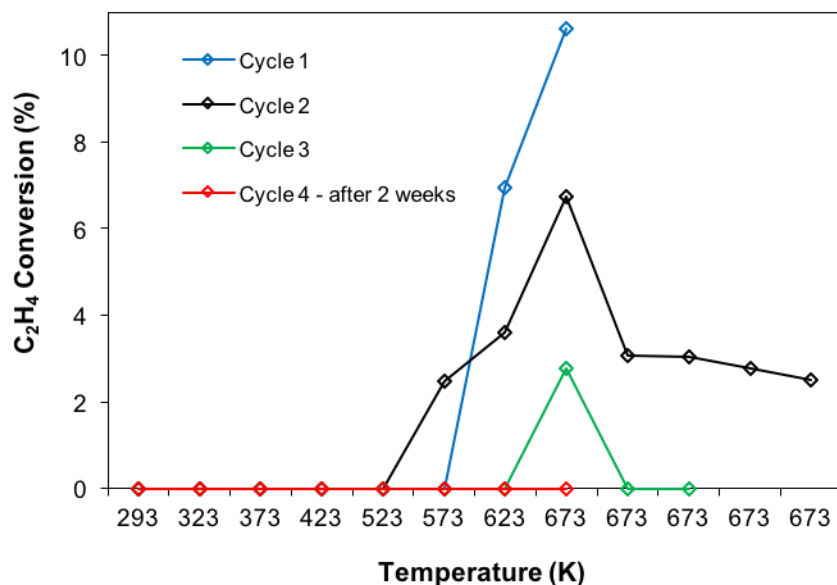


Figure 5-6. Blank tests for empty reactor. Reaction conditions: C₂H₄/O₂: 907 ppm/3.3%, feed gas flow rate 100 mL min⁻¹ for cycle 1, 2 and 3; P_{C₂H₄}/P_{O₂}= 0.189/3.01 kPa; feed gas flow rate 200 mL min⁻¹ for the cycle 4 was after 2 weeks.

The observed conversions in the first three thermal cycles might be due to the stainless steel in the chamber, which contains generally about 10 to 14% of nickel, together with small percentages of carbon, manganese, silicon. Stainless steels containing these materials used for the interior of the reactor can catalyse the transformation of hydrocarbons under oxidative reaction conditions. It has been reported that the catalytic effect of the reactor interior surface in such oxidation reactors can cause the formation of undesirable oxygen containing products such as aldehydes, alcohols, carbon monoxide and carbon dioxide, depending on the O₂/C₂H₄ ratio (Chinta, S. Thorman, 2013). After prolonged heating to high temperatures, the surface of the stainless-steel chamber was oxidised and therefore lost all its catalytic activity.

The experimental setup and reactor were pressure tested using an Alcatel ASM142 leak detector by pressurizing the line and checking for bubbling while spraying a few drops of a soapy solution such as “Snoop”. The leak tightness was checked at different conditions with respect to a blank reactor experiment (after two-week from the initial

checks). As shown in Figure 5-6, CO₂ was not detected across the whole temperature range. Thereby, these results confirmed that the blank reactor test was catalytically inactive under reaction conditions. The carbon balance results for the whole temperature range are presented in Table 5-2.

Table 5-2. Material balance calculation of blank reactor from 296 K to 688 K.

Temperature (K)	C ₂ H ₄ In (KPa)	CO ₂ Out (KPa)	C ₂ H ₄ Out (KPa)	Balance In	Balance Out	Difference (%)
296	0.1985	-	0.1979	0.3969	0.3958	0.29
375	0.1985	-	0.1999	0.3969	0.3999	-0.74
423	0.1985	-	0.1997	0.3969	0.3994	-0.62
473	0.1985	-	0.1988	0.3969	0.3976	-0.17
523	0.1985	-	0.1991	0.3969	0.3983	-0.34
579	0.1985	-	0.1987	0.3969	0.3973	-0.10
629	0.1985	-	0.1999	0.3969	0.3999	-0.74
688	0.1985	-	0.1997	0.3969	0.3993	-0.61

5.2.5 Ethylene Oxidation on Supported Pt Nanoparticles

Figure 5-7 presents the catalytic activity on blank supports and Pt nanoparticles catalysts for ethylene oxidation. To test the catalytic activity for the support, the rig was tested by admitting the reactants in the reactor containing yttrium stabilized zirconia (YSZ) or alumina (γ -Al₂O₃) supports individually. Under the same reaction conditions, the presence of these supports did not induce any oxidation products up to 673 K. Therefore, the γ -Al₂O₃ and YSZ supports were catalytically inactive under tested reaction conditions.

To verify ethylene oxidation on Pt nanoparticles, 60 mg of Pt/ γ -Al₂O₃ and Pt/YSZ were tested for ethylene oxidation (Figure 5-7). The oxidation of 907 ppm ethylene was carried out in the temperature range of 293 – 673 K. It was found that all catalysts showed very stable and reproducible performance. Moreover, it is noted that the similarity in the shapes of the light off curves for both catalysts. As can be observed, Pt/YSZ showed higher catalytic activity at temperatures below 570 K, as compared with Pt/ γ -Al₂O₃. However, a full conversion was reached at a lower temperature for Pt/ γ -Al₂O₃. There was a rapid increase of conversion that reached ~ 70% at 388K for

Pt/YSZ and ~ 60 % at 433 K for Pt/ γ -Al₂O₃, which might be due to direct ethylene oxidation on Pt (Isaifan, 2014). Then, a quite slow increase in conversion rate was observed from 388 K to 663 K (70 % to 93 %) for Pt/YSZ and from 433 K to 563 K (60 % to 83 %) for Pt/ γ -Al₂O₃. A full conversion of ethylene was achieved for both catalysts, at 580 K for Pt/ γ -Al₂O₃ and 673 K for Pt/YSZ. This can be explained from two steps thermal decomposition of PtOx species (Ono *et al.*, 2010). The first rapid conversion (60 – 70%) was obtained through a direct reaction with Pt metal supported catalysts which enhance the chemical reaction. Then at the second stage the increase was slowed, and the conversion of C₂H₄ may be related to the formation of PtOx from 300K to 500K. Further annealing or increase the temperature above 550K leads to the decomposition of PtOx to Pt⁰. Thereby, complete decomposition of PtOx species leads to enhanced and total conversion of the ethylene.

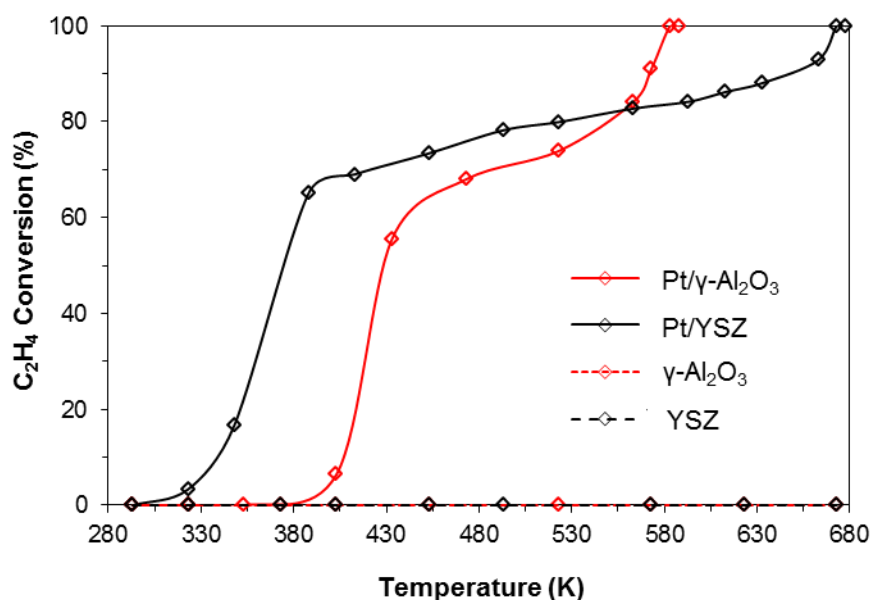


Figure 5-7. Catalytic activity as represented by C₂H₄ Conversion for the blank supports and nanoparticles Pt catalysis for ethylene oxidation. Reaction conditions: C₂H₄/O₂: 907 ppm/3.3% O₂, feed gas flow rate 100 mL min⁻¹.

5.2.6 Ethylene Oxidation on Pt/YSZ with NEMCA Effect

The catalytic activities of YSZ-Au and Pt/YSZ/Au cells under a typical NEMCA configuration were investigated for the oxidation of ethylene, the results are depicted in Figure 5-8. At first, the catalysts were maintained for 20 minutes at stable temperature under open circuit condition, and then the GC measurements were performed between 290 K and 723 K.

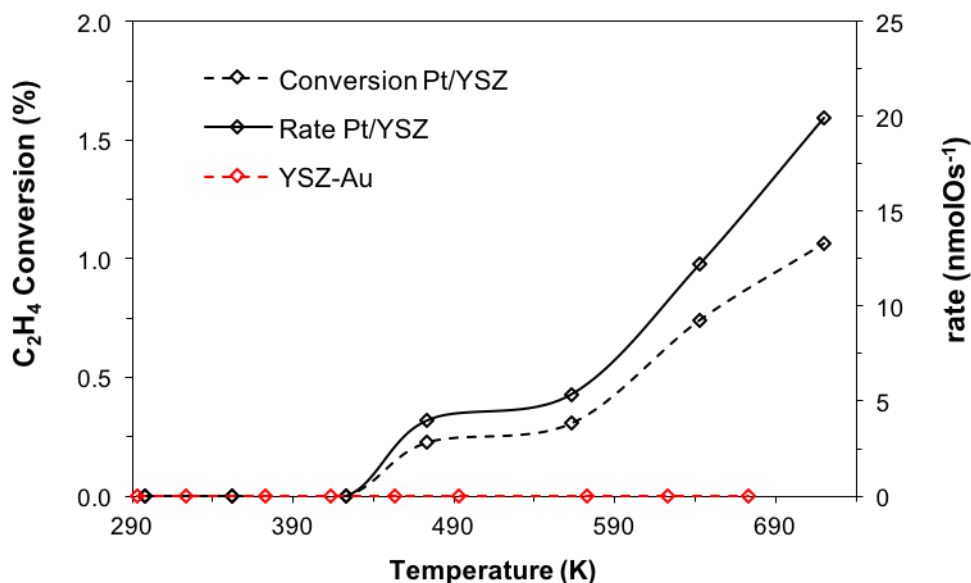


Figure 5-8. Ethylene oxidation conversion and rate as a temperature function of YSZ-Au and Pt/YSZ/Au. Reaction conditions: $P_{C_2H_4}/P_{O_2} = 0.189/3.01$ kPa; feed gas flow rate 200 mL min^{-1} under Open Circuit (OC).

As expected, catalytic behaviours were different according to the nature of the cells. The YSZ-Au electrode showed a negligible activity for temperatures up to 720 K. However, under open circuit (OC) condition, the Pt film on YSZ showed a conversion of $\sim 1.06 \%$ and a reaction rate of 19.95 nmolO/s at 723 K. NEMCA phenomenon was investigated and validated using the oxidation of ethylene on Pt/YSZ/Au under close circuit condition. Figure 5-9 shows the transient effect of an applied potential on the reaction rate, and the C_2H_4 conversion. The ethylene conversion was 0.74% at 643 K for 80 nm Pt film deposited on YSZ, which corresponds to a rate of 12.26 nmolO/s . It is important to note that the catalytic activity was related to both the Pt dispersion and the total surface area. As shown in the Figure, a negative polarization (-1 V) caused a decrease in the catalytic rate to $r = 2.54 \text{ nmolO/s}$, corresponding to 0.29% of C_2H_4 conversion. This means the rate enhancement ratio ρ was 0.21, and the Faradaic efficiency Λ was 4.75. At intermediate oxygen-fuel ratio, higher temperatures ($T > 623\text{K}$), it was found that the reaction rate dependence is purely electrophobic behaviour (Peng-Ont *et al.*, 2013). It is noteworthy to mention that the carbon mass balances for all these ethylene oxidation experiments were very good, less than 5% in all cases.

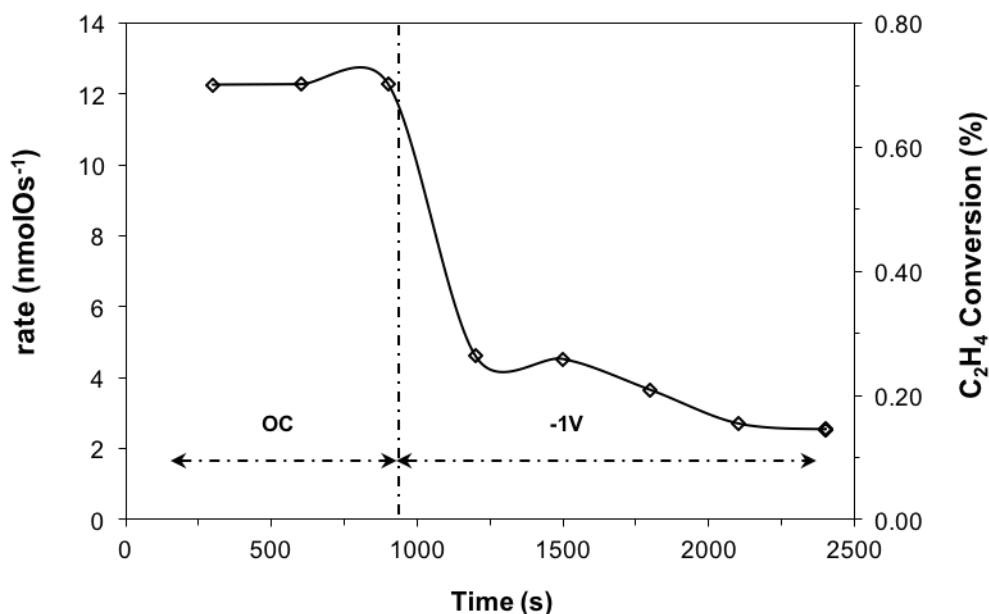


Figure 5-9. Electrochemical promotion of ethylene oxidation on Pt/YSZ/Au catalyst. Gas composition: Reaction conditions: T = 643 K; $V_{wr} = -1$ V; $P_{C_2H_4}/P_{O_2} = 0.189/3.01$ kPa; feed gas flow rate 200 mL min^{-1} .

5.3 Conclusions

Catalytic activity measurements were carried out on the designed experimental setup under different conditions. The blank (empty reactor or blank supports) measurements confirmed that the reactor chamber had negligible catalytic activity for ethylene oxidation. However, full conversions of ethylene were achieved for Pt containing catalysts. Furthermore, NEMCA phenomenon was observed on similar reactor systems using a thin Pt film on YSZ, under excess of oxygen at 643 K. Negative polarization causes a decrease of the reaction rate, and the rate enhancement ratio ρ was 0.21, and the apparent Faradaic efficiency Λ was 4.75.

6 *In-situ* Tuning of Catalytic Activity by Thermoelectric Effect for Ethylene Oxidation Reaction

6.1 Introduction

Heterogeneous catalytic oxidation is regarded as one of the most promising technologies to control Volatile Organic Compounds (VOCs) emissions with low energy consumption and selective conversion into harmless molecules. In this context, many different catalysts and support have been studied, including recent developments in material chemistry to achieve more efficient processes (He, Yu, Shen, *et al.*, 2014; He, Yu, Yue, *et al.*, 2014). In this chapter, the complete oxidation of ethylene as a model VOC pollutant to CO₂ was investigated for thin film and non-continuous nanoparticles Pt catalysts, by creating a temperature difference across the thickness of the thermoelectric (TE) catalyst support. An in-situ and significant modification of catalytic activity was discovered. This profound promotional effect enables the oxide thermoelectric material itself to possess high catalytic activity. Furthermore, the relationship between thermoelectric effect and catalytic activity was used to explain the underlining mechanism.

6.2 Results and Discussion

6.2.1 Characterisation of Pt Catalysts

Figure 6-1 displays the relevant X-ray diffraction patterns of BCSO, Pt(NP)/BCSO, Pt(15)/BCSO, Pt(80)/BCSO and Pt(80)/(BCSO)_{0.9}(YSZ)_{0.1} samples after catalytic chemical reaction. The XRD patterns were all single-phased BCSO (PDF#45-0296) with the ZrSiCuAs type structure, no impurity peak was found. The Pt peak was very strong for all of the samples with a 80 nm Pt thick films, but no Pt peak could be seen for Pt(15)/BCSO, indicating the Pt grain size in the Pt(15)/BCSO was below the XRD detection limit, probably less than 20 nm, therefore the Pt in Pt(15)/BCSO existed as separate nano-particles.

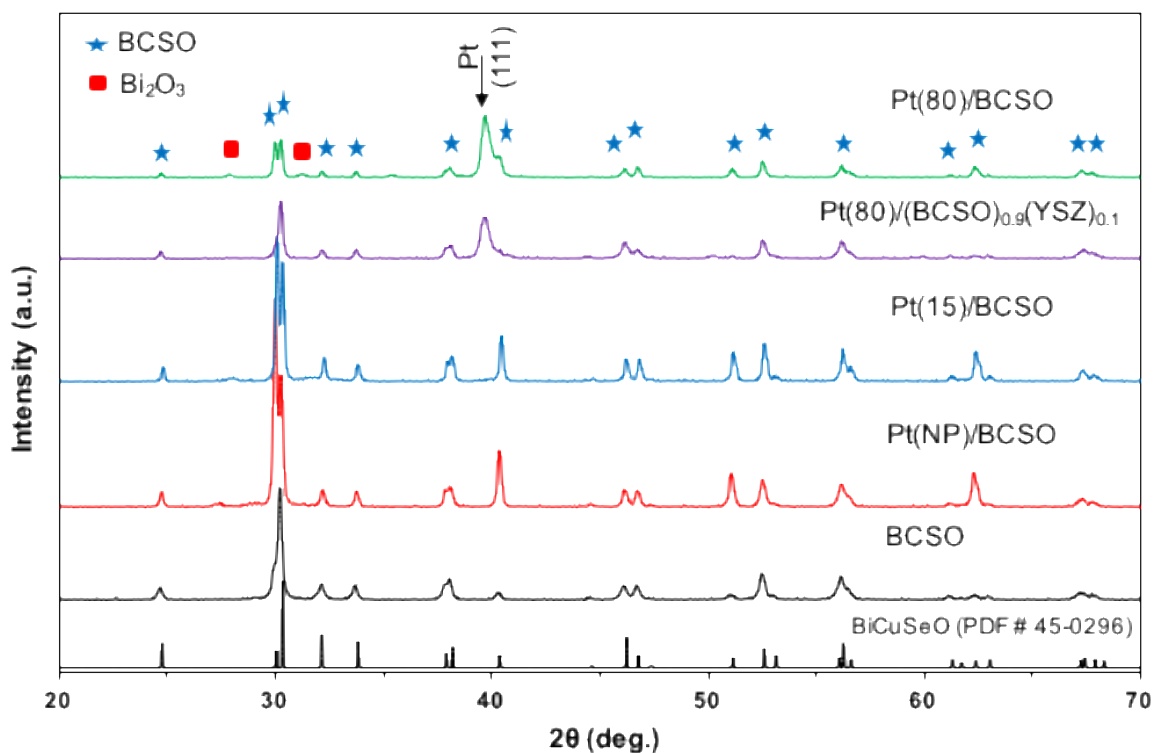


Figure 6-1. X-ray diffraction patterns of catalyst systems after catalytic chemical reaction characterisation for the samples: BCSO; Pt(NP)/BCSO; Pt(15)/BCSO; Pt(80)/BCSO and Pt(80)/(BCSO)_{0.9}(YSZ)_{0.1}.

Scanning electron microscopy (SEM) surface morphology micrographs for the samples BCSO, Pt(15)/BCSO, Pt(80)/BCSO, Pt(80)/BiCuSeO_{0.9}YSZ_{0.1}, Pt(80)/BCSO, and Pt(NP)/BCSO after they have been subjected to catalytic reaction experiments are shown in Figure 6-2. It can be observed that the BCSO had grain size between 2 and 8 μm , with very clean surface (Figure 6-2a). Small Pt grains can be observed on the surface of Pt(15)/BCSO (Figure 6-2c), at low magnification the difference between the area with Pt (upper half) and the area without (lower half) can be observed clearly (Figure 6-2b). Pt(80)/BiCuSeO_{0.9}YSZ_{0.1} were consisted of large BCSO grains with much smaller ($\sim 0.1 \mu\text{m}$) YSZ grains (Figure 6-2d). For Pt(80)/BCSO, small Pt particles on the surface of BCSO grains were apparent (Figure 6-2e). Small BCSO grain (up to 2 μm) was observed for Pt(NP)/BCSO (Figure 6-2f). It is noteworthy that Pt(80)/YSZ displayed very different morphology from those of BCSO, with grain size ranged from a few hundred nanometers to 2 μm (Figure 5-4b).

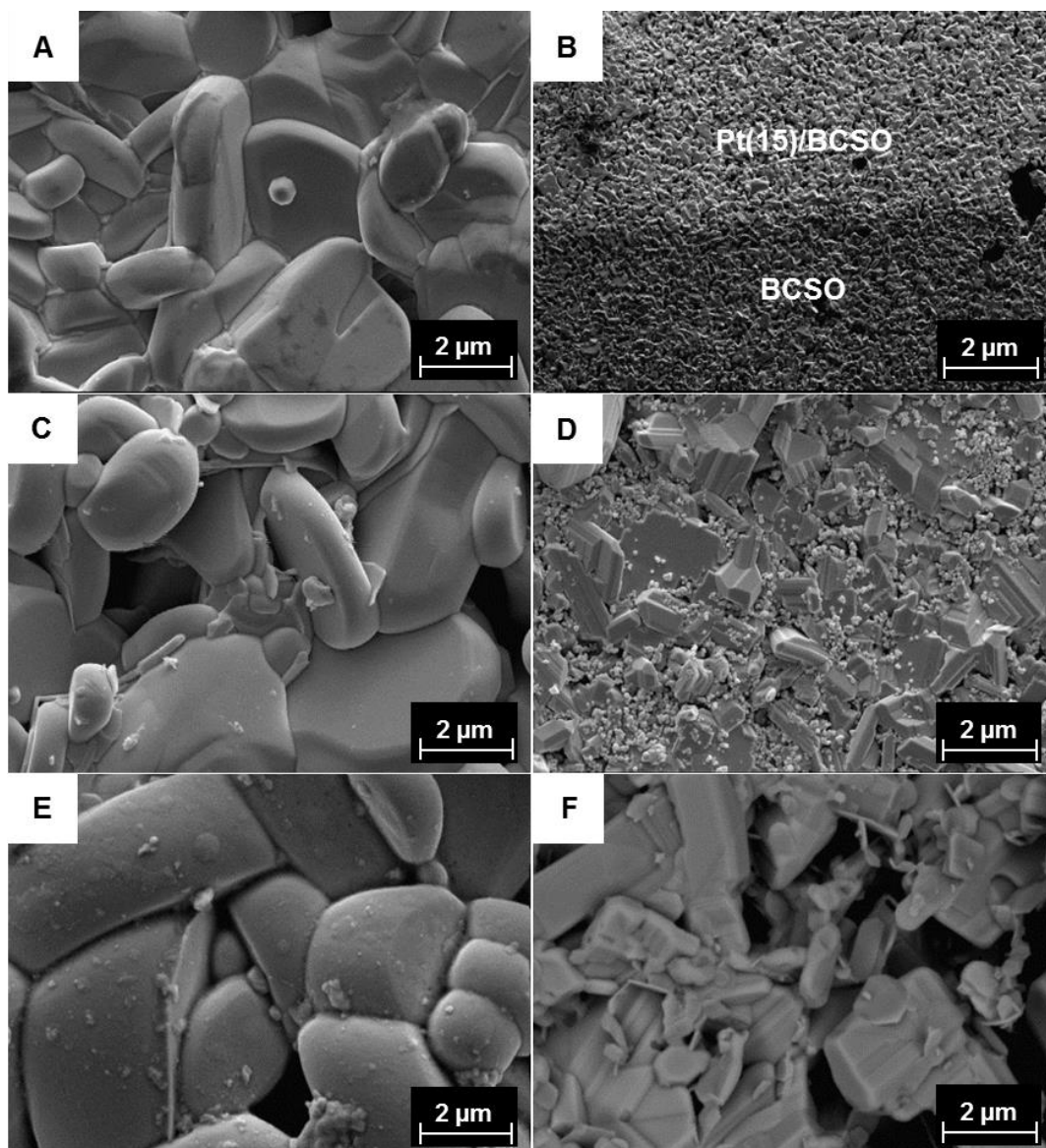


Figure 6-2. SEM micrographs of the five samples: (a) BCSO; (b) low and (c) high magnification for Pt(15)BCSO; (d) Pt(80)/ BiCuSeO_{0.9}YSZ_{0.1}; (e) Pt(80)/BCSO; (f) Pt(NP)/BCSO.

6.2.2 Substantial Higher Catalytic Activity on TE Materials

The schematic of the single chamber reactor, which can combine the thermoelectric effect with a catalytic chemical reaction, was presented in Figure 3-2a. The chamber was placed directly on a hot-plate, and its top cap was water cooled. A disc sample of 20 mm in diameter and about 2 mm in thickness was then placed into a specific glass ceramic holder (Figure 3-2c) and attached to the cold surface of the cap for catalytic reaction investigation under usual TE conditions. As the back side of the disc was in contact with the water cooled stainless steel cap its temperature was never higher

than 373 K, a large temperature gradient therefore a large Seebeck voltage across the disc thickness was created when the front surface of the disc reached a high temperature (Figure 3-3a). Under the reduced thermoelectric (RTE) effect condition, the back surface of the disc was not in contact with the cover plate, therefore the temperature gradient across the disc thickness and the Seebeck voltage were much smaller.

Figure 6-3 shows the ethylene oxidation reaction rates at different front surface temperature T_h for Pt(80)/BCSO with a large TE effect (solid red line, Pt(80)/BCSO TE), and under a reduced TE effect (dashed red line, Pt(80)/BCSO RTE) conditions respectively. For comparison purpose, the ethylene reaction rate on a typical catalyst for this reaction Pt thin films on Y_2O_3 -stabilized ZrO_2 (YSZ, solid black line, Pt(80)/YSZ, YSZ is not a thermoelectric material) is also depicted in Figure 6-3. For Pt(80)/YSZ, as the temperature was increased from 473 to 720 K, the rate was increased from 4 to 19.9 nmolO/s.

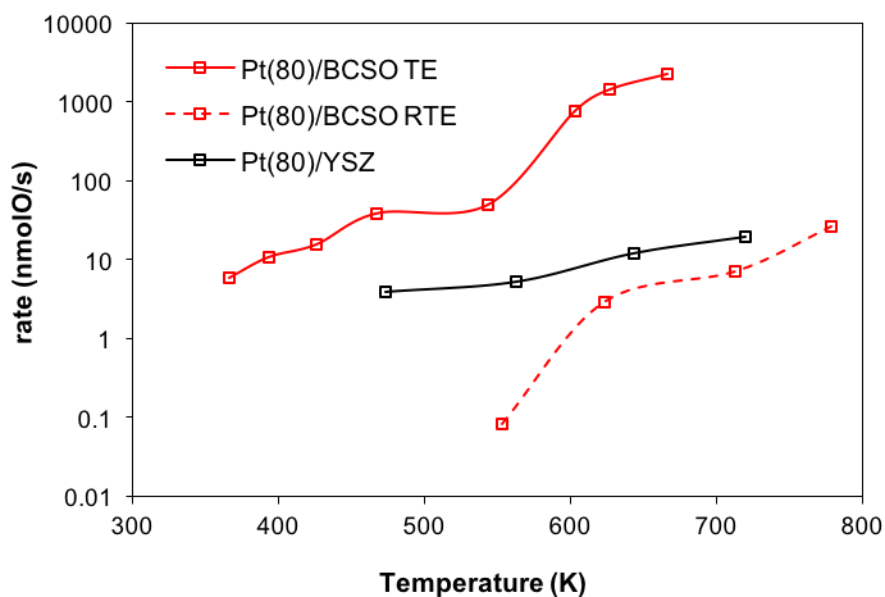


Figure 6-3. Ethylene oxidation rates as a function of temperature at the catalyst surfaces, for Pt(80)/YSZ which has no thermoelectric effect, and for Pt(80)/BCSO under large TE effect (Pt(80)/BCSO TE) and reduced TE effect (RTE) conditions.

For Pt(80)/BCSO TE, when the front hot surface T_h was at 666 K, the backside temperature T_c was 349 K, so a temperature difference of 317 K existed across the BCSO thickness, which generated a Seebeck voltage -71 mV, further details can be found in Table 6-1. The corresponding reaction rate was 2257.6 nmolO/s and the

conversion of C_2H_4 was 99.9%. This rate was 113 times higher than Pt(80)/YSZ at 720 K, and 154 times at 666 K (interpolated data). For the same sample under the reduced TE effect (Pt(80)/BCSO RTE), at 553 K, the measured Seebeck voltage was -3.1 mV, the reaction rate was 0.08 nmolO/s, much lower than the rate (5.4 nmolO/s) for Pt(80)/YSZ at a similar temperature 563 K. This is probably because the YSZ surface was very rough but BCSO was much smoother, therefore the surface area of Pt(80)/BCSO was much smaller than for Pt(80)/YSZ.

With increasing temperature, the reaction rates for Pt(80)/BCSO under TE and RTE conditions increased much faster than for non-thermoelectric YSZ supported catalyst. For Pt(80)/BCSO RTE when the hot surface T_h was at 713K, the measured Seebeck voltage was -8.6 mV, the corresponding reaction rate and C_2H_4 conversion were 7.1 nmolO/s and 1.2%, respectively. This means, for the same surface area (the same sample), the reaction rate under TE condition at 666 K was 318 times of the rate for under RTE conditions at 713 K. The ratio against the rate under RTE (from interpolated data) at the same temperature 666 K was estimated to be 660 times. It is plausible to assume that against the condition without any temperature gradient this ratio will be even higher. The above experiments have been repeated at least once and the results were reproducible (Appendix B), this ruled out the possibility that the rate difference between the TE and RTE was due to particles aggregation at the catalyst surface.

Table 6-1. Summary of experimental conditions and catalytic reaction measurement results of Pt(80)/BCSO in Figure 6-3. T_c and T_h are the temperatures at the top cold surface and bottom hot surfaces respectively, V the Seebeck voltage. Every catalyst chemical reaction testing experiment generated a table like this.

T_c (K)	302.4	302.4	306.5	306.7	308.7	311.6	315.2	319.5	325.6	332.0	339.0	340.0	349.0
T_h (K)	302.5	302.5	315.4	328.4	345	366	393	425.5	467	543	603	627	666
ΔT ($T_h - T_c$)	0.1	0.1	8.9	21.7	36.3	54.4	77.8	106.0	141.4	211.0	264.0	287.0	317.0
Seebeck V (-mv)	-	-	-	-	7.9	12.5	20	29.8	39.5	55	59	68	71
CO₂ (kPa)	0.000	0.000	0.000	0.000	0.000	0.001	0.002	0.004	0.009	0.011	0.175	0.325	0.508
C₂H₄ (kPa)	0.194	0.195	0.197	0.196	0.195	0.194	0.194	0.192	0.187	0.165	0.015	0.001	0.000
O₂ (kPa)	2.987	2.943	2.911	2.851	2.847	2.846	2.847	2.845	2.833	2.839	2.665	2.418	2.226
r (nmolO/s)	0.000	0.000	0.000	0.000	0.000	5.95	10.86	15.70	38.86	49.85	775.1	1444.6	2257.6
C₂H₄ Conv (%)	0.000	0.000	0.000	0.000	0.000	0.34	0.63	0.91	2.29	3.29	84.95	99.11	99.90
ln (r)	-	-	-	-	-	1.78	2.39	2.75	3.66	3.91	6.65	7.28	7.72
-eV/K_bT_h	-	-	-	-	-	0.396	0.590	0.812	0.981	1.174	1.134	1.257	1.236

6.2.3 Tuning of Catalytic Activity by Seebeck Effect

Further experiments were carried out to demonstrate that the Seebeck voltage alone can increase the reaction rate substantially. BCSO powders were mixed with Pt containing solvent H_2PtCl_6 to form a green ceramic and it was sintered at 823 K for 1h before being used as a catalyst for ethylene oxidation (Pt(NP)/BCSO). This ceramic was not fully sintered so BCSO will continue its crystallization processes, therefore changing its thermoelectric properties such as the Seebeck coefficient, in the reaction chamber with time.

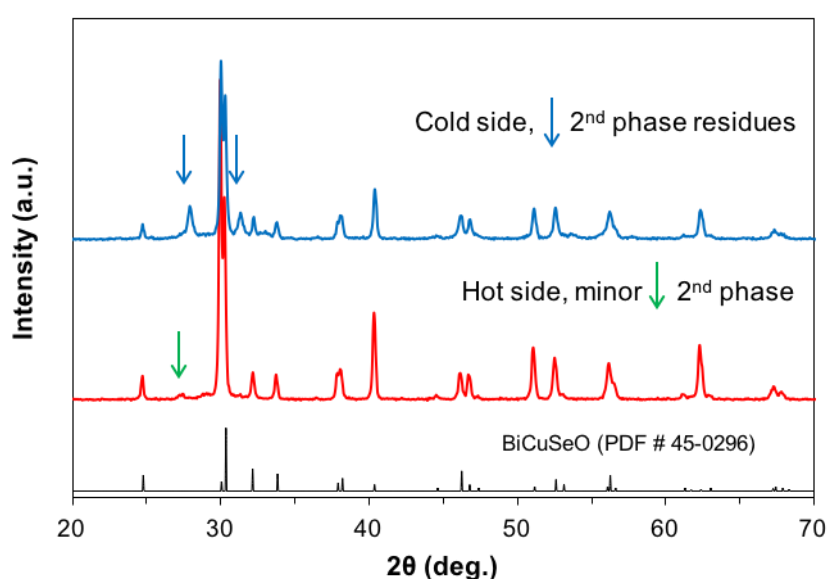


Figure 6-4. X-ray diffraction patterns of the Pt(NP)/BCSO after catalytic reaction measurement for the cold side (top) and the hot side (bottom).

Figure 6-4 shows XRD patterns for the cold (back) side and the hot (front) side of the Pt(NP)/BCSO after catalytic reaction measurement. The cold side's temperature never exceeded 350 K, so no further sintering took place and it maintained the spectra of the as-prepared green ceramics, which contained some Bi_2O_3 secondary phase. The hot side had experienced temperature of up to 773 K for a few hours, therefore it underwent further crystallisation and sintering in the reaction chamber, reduced the amount of secondary phase material Bi_2O_3 and increased the crystallinity, which lead to the increase of its Seebeck coefficient.

Table 6-2. Summary of Seebeck voltage and reaction rate and ethylene conversion at constant temperature $T_h = 705$ K and $T_c = 339$ K of the sample Pt(NP)/BCSO. The change in the Seebeck coefficient leads to the change of the Seebeck voltage, which resulted in the increase of catalytic reaction rate.

Time (hrs)	1.0	1.75	2.5	3.25	3.75
V (-mV)	104	105	106	107	107.5
r (nmolO/s)	123.7	157.0	204.3	249.8	281.2
C₂H₄ Conv (%)	9.58	13.80	19.96	26.77	31.67

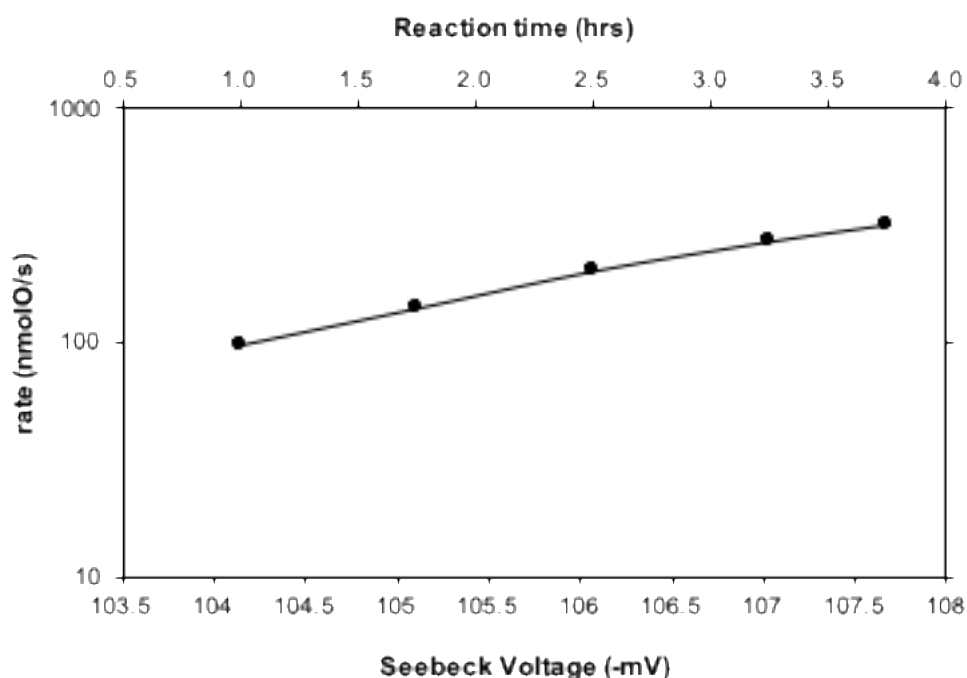


Figure 6-5. Ethylene oxidation rate as a function of the Seebeck voltage $-V$ for ethylene oxidation at constant temperatures $T_h = 705$ K and $T_c = 339$ K of Pt(NP)/BCSO.

The effect of increasing the Seebeck voltage on the reaction rate was monitored as functions of time while the chamber temperature was kept the same ($T_h = 705$ K). Table 6-2 summarises the reactions rates at different Seebeck voltages at the constant T_c and T_h , therefore the increase was due to the change of the Seebeck coefficient. An excellent exponential increase of the reaction rate with the Seebeck voltage $-V$ was

observed (Figure 6-5), demonstrating that the change of Seebeck voltage alone can increase the catalytic reaction rate significantly. Note the logarithm scale for rate.

6.2.4 Relationships Between Thermoelectric Effect and Catalytic Activity under Fuel-Lean Conditions

To investigate further relationships among the temperature, Seebeck voltage, and catalytic activity, ethylene oxidation reactions were carried out on five samples: namely, Pt(80)/BCSO_{0.9}YSZ_{0.1}, Pt(NP)/BCSO, Pt(15)/BCSO, BCSO only, and Pt(80)/BCSO. A typical time profile of the Seebeck voltage, for BCSO, is shown in Figure 6-6. The Seebeck voltage across the sample thickness was recorded continuously during the experiment.

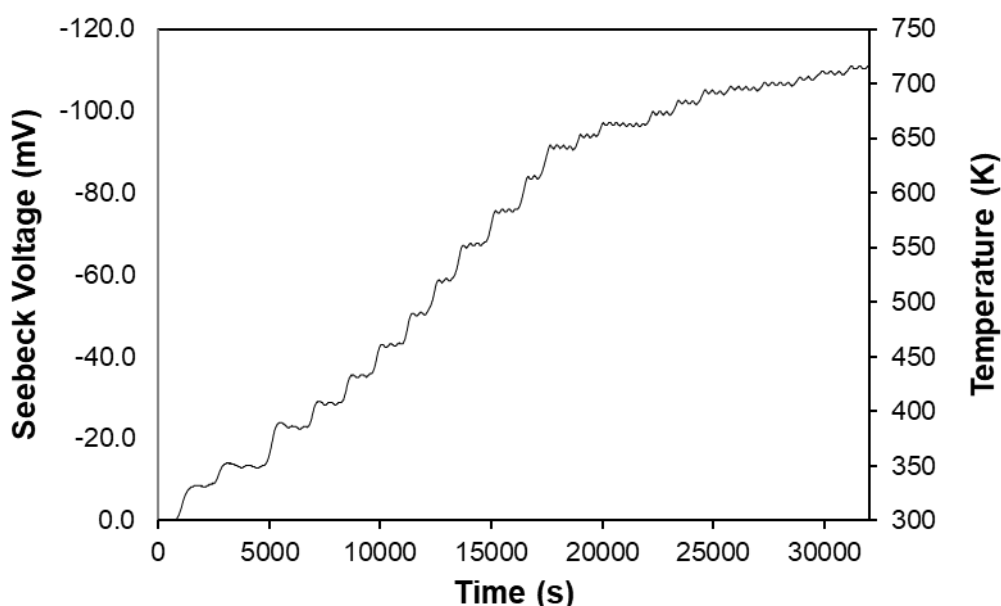


Figure 6-6. Typical time profile of recorded Seebeck voltage. Time profile of the recorded Seebeck voltage during catalytic reaction characterisation experiments of BCSO.

The reaction rate of the five samples as a function of temperature were depicted in Figure 6-7. All four samples, including the BCSO without any Pt, showed a similar behaviour as Pt(80)/BCSO TE (Figure 6-3), i.e. an increase of 3 to 4 orders of reaction rate when the temperature was increased from 300 K to around 700 K. This showed BCSO, like other conductive oxides, such as IrO₂ and RuO₂, have high catalytic activity for ethylene oxidation (Nicole *et al.*, 1997).

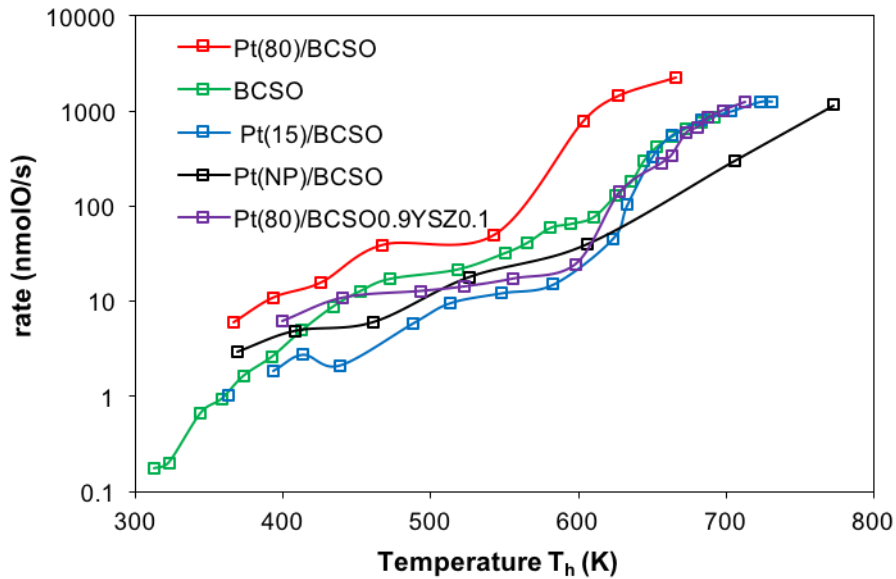


Figure 6-7. Reaction rate r as a temperature function of the five samples: BCSO, Pt(NP)/BCSO, Pt(15)BCSO, Pt(80)/BCSO and Pt(80)/BiCuSeO_{0.9}YSZ_{0.1}.

The Seebeck voltages vs temperature gradient for all five samples are shown in Figure 6-8. The negative voltage means the potential was lower at the hot surface T_h than at the cold surface T_c . All the Seebeck voltages were zero at zero temperature difference (at room temperature), and increased linearly with the temperature difference ΔT . The gradients of these linear relationships, i.e. the Seebeck coefficients, were different between different samples, ranged from 206 $\mu\text{V/K}$ for Pt(80)/BCSO_{0.9}YSZ_{0.1} to 485 $\mu\text{V/K}$ for BCSO. These Seebeck coefficients for BCSO were within the values for BCSO reported in the literature (C. Barreateau *et al.*, 2014; L-D. Zhao *et al.*, 2014; C. Barreateau *et al.*, 2015). At the same temperature, the measured Seebeck voltage was the highest for BCSO, followed by Pt(NP)/BCSO, Pt(80)/BCSO, and Pt(15)/BCSO while the composite Pt(80)/BCSO_{0.9}YSZ_{0.1} had the lowest voltage. The composite sample was expected to have a lower Seebeck coefficient because YSZ is not a TE material. For all these five samples, the Seebeck coefficients decreased at high temperatures. In general, this is not unusual as the Seebeck coefficient of a thermoelectric material is temperature dependent.

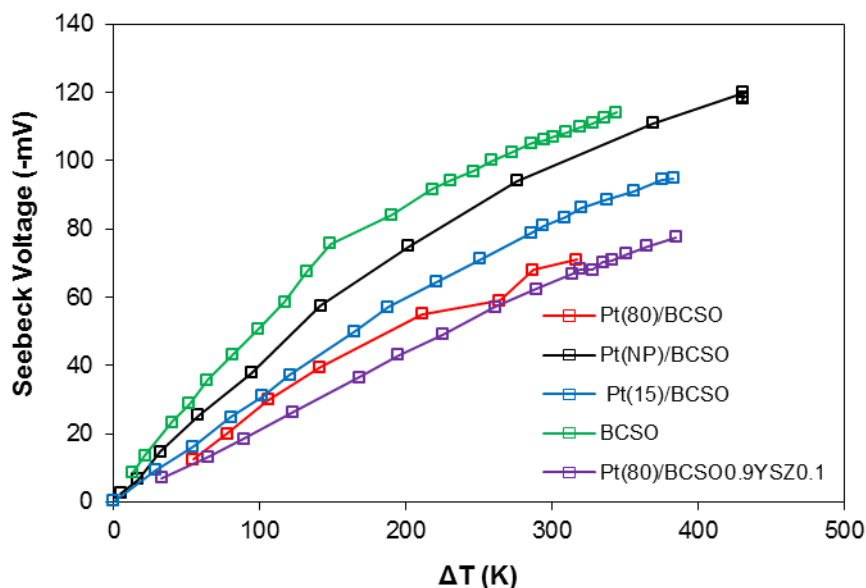


Figure 6-8. Measured Seebeck voltage as functions of temperature difference across the sample thickness.

In the following analysis, it was assumed that the intrinsic ethylene oxidation is the rate limiting step, and there were no mass transportation limitations. There are several reasons to justify this assumption. As shown in Figure 6-2, the samples were not porous, so there was no pore-diffusion limitation. Also, there was a large temperature difference ($\sim 200\text{-}300\text{ K}$ when $T_h > 500\text{ K}$) between the bottom of the chamber and the hot-surface T_h of the sample (see Figure 3-3a), a turbulent gas convection may have existed within the chamber especially in the vertical direction, which can increase the reactants supply to the T_h surface and take away the formed products quickly from there. Furthermore, all the experiments (except for Figure 6-12 and Figure 3-3b) reached 100% ethylene conversion at high temperatures, suggesting the backward reaction of the eq. (3-8) was negligible.

Generally, the rate r of a chemical reaction follows an Arrhenius law as:

$$r = R_0 e^{(-E_a/K_b T)} \quad \text{Equation 6-1}$$

where E_a is the activation energy for the reaction, k_b the Boltzmann constant, R_0 a constant at constant concentrations. $\ln(r)$ versus $1/T$ for Pt(80)/YSZ was depicted in Figure 6-9, indeed demonstrating a linear relationship, which implies that the reaction rate increases exponentially when the activation energy decreases. In addition, the

Arrhenius equation implied that the rate of an uncatalyzed reaction (high activation energy) is more affected by temperature than the rate of a catalysed reaction (low activation energy).

In general, the ethylene oxidation could take place on the front surface T_h (nominal surface area $100\pi \text{ mm}^2$), back surface T_c , and side wall of the disc sample. All measurements data, for example Table 6-1, showed no observable reaction rate below 360 K, and T_c was always below this temperature, so the rate contribution from the T_c surface (nominal surface area $100\pi \text{ mm}^2$) was negligible for all samples with thermoelectric materials under the TE conditions. Assuming this is also true for RTE conditions (this will be discussed later). Furthermore, it was supposed that all five samples with TE materials the rate contribution from the side wall (area size $40\pi \text{ mm}^2$) of the disc (with variable temperatures between T_c and T_h) sample was also negligible, therefore the measured ethylene oxidation rate is attributed to the hot surface T_h only.

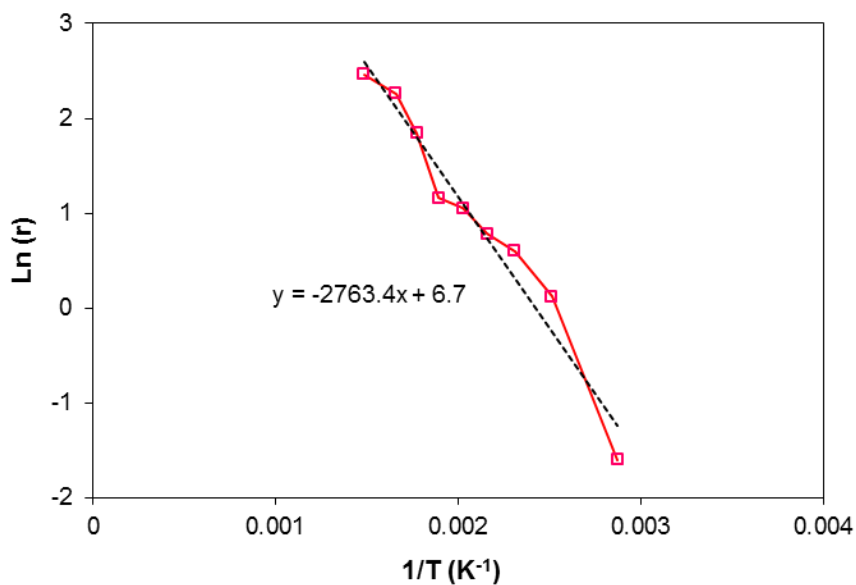


Figure 6-9. Arrhenius law for ethylene oxidation on Pt. Ln(r) as a function of 1/T for ethylene oxidation rate on Pt(80)/YSZ. YSZ is not a thermoelectric material.

Figure 6-10 displays the plot of Ln(r) vs. $-eV/k_bT_h$ for all five samples. It can be seen for each sample, under a certain temperature or Seebeck voltage, a linear relationship existed between Ln(r) and $-eV/k_bT_h$ as presented in equation 6-2.

$$\ln(r/r_0) = -\gamma eV/K_b T_h \quad \text{Equation 6-2}$$

Here γ is a dimensionless positive constant, r_0 is the reaction rate when V equals zero, i.e. when $T_c = T_h$, so $r_0 = k_0 e^{(-E_a/K_b T)}$, here k_0 is a constant. $-e$ is the charge of an electron, the introduction of $-e/k_b T_h$ makes $-eV/k_b T_h$ dimensionless. The best-fit trend line gradients γ were 2.8, 2.4, 2.4, 2.4, 3.2 and 50.8 of Pt(80)/BCSO TE, Pt(80)/BCSO_{0.9}YSZ_{0.1}, Pt(15)/BCSO, Pt(NP)/BCSO, BCSO, and Pt(80)/BCSO RTE, respectively. Eq. (6-2) and Arrhenius law apparently suggest that the activation energy is reduced by $-\gamma eV$ from E_a when there was a Seebeck voltage V .

Combining eq. (6-2) and the definition of Seebeck coefficient S gives:

At hot side T_h

$$\ln(r/r_0) = \gamma e S \Delta T/K_b T = \gamma e S (T_h - T_c) / K_b T_h \quad \text{Equation 6-3}$$

If applying the above discussion for the case where the entire reaction rate is contributed from the cold surface T_c , and the contribution from the hot surface and the side wall of a disc sample is negligible, then eq. (6-3) becomes:

At cold side T_c

$$\ln(r/r_0) = \gamma e S \Delta T/K_b T = \gamma e S (T_c - T_h) / K_b T_c \quad \text{Equation 6-4}$$

When S is not a constant, $S (T_h - T_c)$ should be replaced by $\int_{T_c}^{T_h} S(T) dT$.

From eq. (6-3) it can be observed that for p-type TE materials, S is positive, the reaction rate at the hot side T_h could be much higher with a thermoelectric voltage than without, so we call this thermoelectric promotion of catalysis (TEPOC), or thermoelectrocatalysis as the thermoelectric material itself can have high catalytic activity. Take the data for Pt(80)/BCSO (Table 6-1) when $T_h = 543$ K, $V = -55$ mV, $\ln(r/r_0) = 3.287$, so $r/r_0 = 26.8$. This means at the temperature 543K, the reaction rate was promoted by 26.8 times with a Seebeck voltage -55 mV. It can also be seen from eq. (6-3) that the rate (r) can be tuned by changing the temperature T_c at the back side during the reaction.

Referring to Figure 6-10, the linear relationship between $\ln(r)$ and $-eV/k_b T_h$ was no longer valid with further increase of the temperature and the Seebeck voltage. For all

samples except Pt(80)/BCSO RTE (which has a low Seebeck voltage), at high temperatures, $\ln(r)$ increased very rapidly whilst $-eV/k_bT_h$ changed little, or even reduced for BCSO and Pt(NP)/BCSO. In fact, a good linear relationship between the rate (r) and the Seebeck voltage V could be observed. It is noticed that in Figure 6-11 that $(r) \text{ — } (-V)$ feature resembles the $I \text{ — } V$ curve for a p-n diode under forward bias, where a linear relationship is often observed (Brophy, 1990).

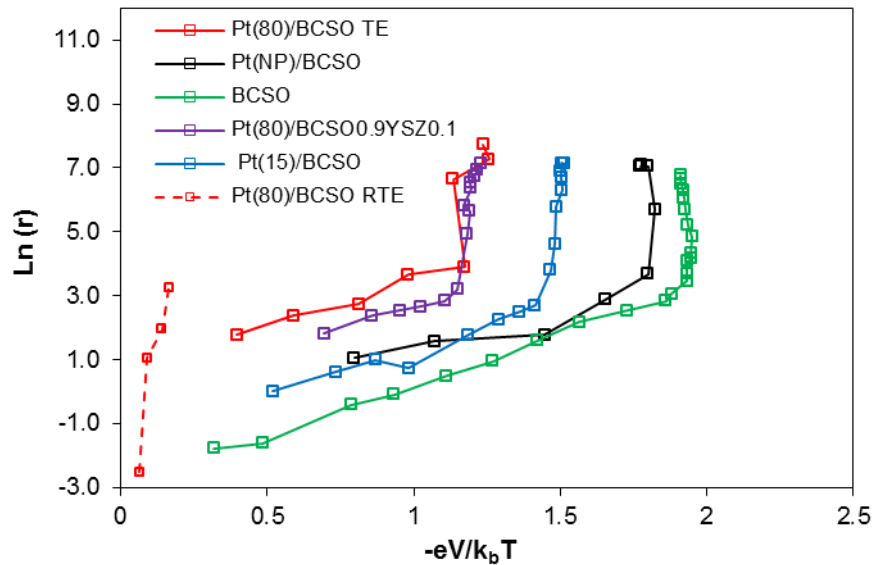


Figure 6-10. A linear relationship between $\ln(r)$ and $-eV/k_bT_h$ of the five samples: BCSO, Pt(NP)/BCSO, Pt(15)BCSO, Pt(80)/BCSO and Pt(80)/BiCuSeO_{0.9}YSZ_{0.1}.

The conditions at which the rate started to increase rapidly (similar to the “knee” point of the I-V curve of a p-n diode at forward bias) were (temperature, Seebeck voltage, $-eV/k_bT_h$, and $\ln(r)$): (543K, -55mV, 1.18, 4.94), (656K, -69mV, 1.18, 4.94), (633K, -81mV, 1.48, 4.6), (606K, -94mV, 1.8, 3.68), (625K, -105.2mV, 1.95, 4.84) for Pt(80)/BCSO, Pt(80)/BCSO_{0.9}YSZ_{0.1}, Pt(15)/BCSO, Pt(NP)/BCSO, and BCSO respectively. The data points for Pt(NP)/BCSO were not dense enough to determine its precise “knee point”. For the other four samples, their knee points had very similar $\ln(r)$ values at about 4.9, suggesting the reaction rate was the main factor to determine the “knee point”. The best-fit trend line gradients of $r \text{ — } (-V)$ for all samples were similar, being 122.4, 101.9, 84.2, 94.2 and 85.5 nmolO/mV for the above five respective samples.

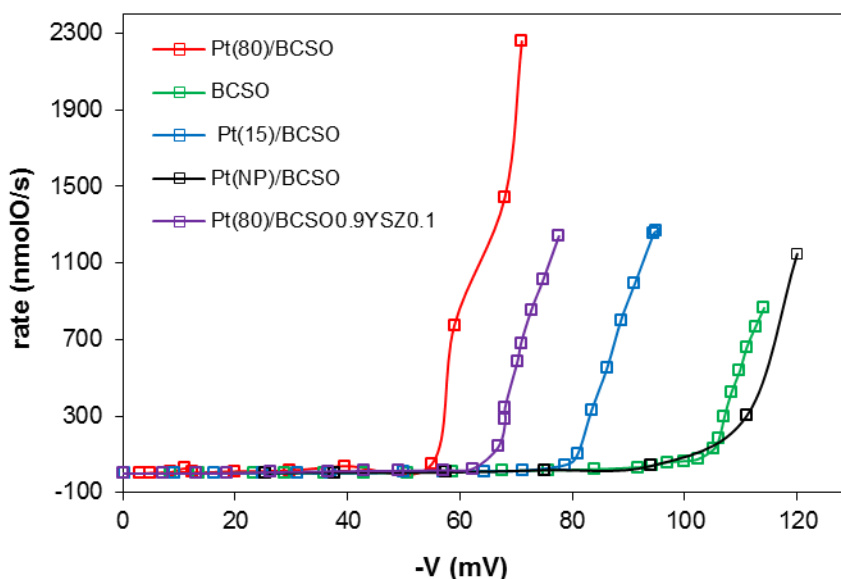


Figure 6-11. The rate r is proportional to the Seebeck voltage V of the five samples: BCSO, Pt(NP)/BCSO, Pt(15)BCSO, Pt(80)/BCSO and Pt(80)/BiCuSeO_{0.9}YSZ_{0.1}.

Figures 6-10 and 6-11 show that once the reaction rate reached about 120-140 nmolO_s⁻¹, the linear relationship between $\ln(r)$ and $-eV/k_bT_h$ no longer existed, instead, a linear relationship between the rate r and the Seebeck voltage V was observed. We believe this was due to the change of the rate limiting mechanism. At low reaction rate ($<120\text{-}140$ nmolO_s⁻¹), the ethylene oxidation was energy barrier (or activation energy) limited. However, at higher rate >140 nmolO_s⁻¹, the ethylene oxidation became either mass transfer limited or charge transfer limited. If it was charge transfer limited, one would expect different materials (BCSO, Pt(80)/BCSO or Pt(15)/BCSO) have different “knee point” because their electrical conductivity should be different. The fact that all the different samples had the same “knee point” suggested that the mass transfer, either oxygen or ethylene transfer, was the rate limiting step. The first order with oxygen partial pressure, and zero order with ethylene partial pressure, indicate that oxygen transport is the rate limiting steps. The gradients for different samples as shown in Figure 6-11 had similar values, further supporting the assumption that the rate limiting factor was the mass transport, independent of the catalyst samples. Both the Seebeck voltage and the oxygen/ethylene diffusion (onto the reaction surface) was proportional to the temperature gradient, which resulted in an apparent linear relationship between the reaction rate and the Seebeck voltage.

6.2.5 Test the Prediction of the Thermoelectric Inhibition of Catalysis

The eq. (6-4) predicts that if the chemical reaction is taking place at the cold surface T_c on a p-type TE material, the rate will be smaller than when V is zero, so TE effect can also inhibit catalytic activity. To test this prediction, a bare BCSO sample was placed directly onto the stainless-steel bottom floor of the reaction chamber (see Figure 3-3b) and the reaction rate was measured at different temperatures T_c when the temperature of the hot-plate was increased (Table 6-3).

Table 6-3. Summary of the measured Seebeck voltage, reaction rate (nmolO/s) and ethylene conversion at different “cold” side temperatures T_c of the bare BCSO sample.

T_c (K)	458	503	538	583	623	658	703	743
V (mV)	7.361	9.508	11.348	13.19	15.34	17.49	20.24	23.92
rate measured	1.146	1.363	2.153	4.917	6.559	5.208	3.01	2.22
C₂H₄ Conv (%)	0.068	0.081	0.127	0.289	0.384	0.308	0.177	0.131
rate calculated	1.566	2.355	2.786	4.489	4.969	4.707	4.438	2.487

As the hot side T_h of the BCSO was in direct contact with the stainless steel, it was effectively connected to earth, any surface charges produced by TE effect will be neutralised by earth, therefore there is no promotion of catalytic activity at the hot-side T_h . Stainless steel has no catalytic activity and there may be mass transportation limitation for gases access to the T_h surface as well, so it was assumed that all the ethylene reaction were due to the reaction carried out on the (top) “cold” surface T_c of the BCSO, therefore the reaction rate can be described by eq. (6-4). Figure 6-12 shows ethylene oxidation rate (green marks) dependence on temperature of the “cold” surface of the bare BCSO sample. It can be seen that the reaction rate increased with temperature at first, reached a maximum, and then decreased with further increase of the temperature.

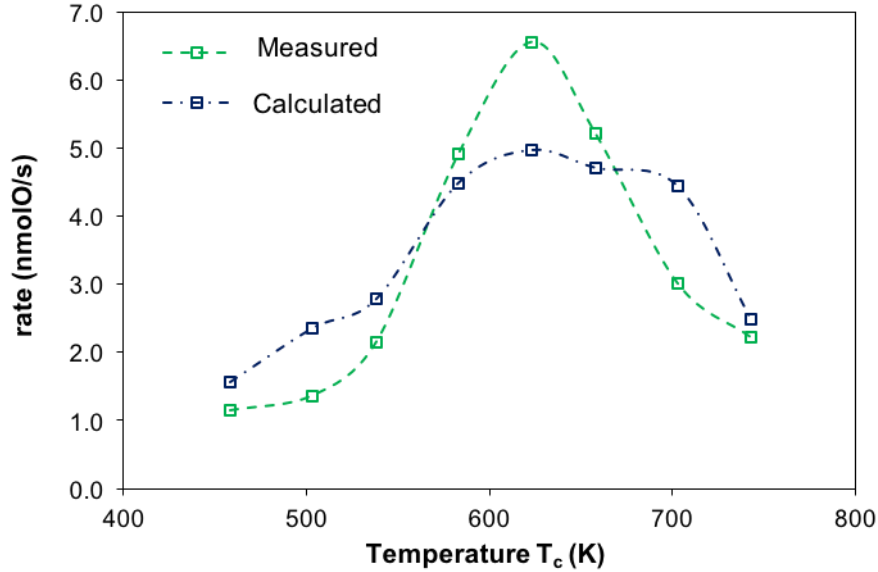


Figure 6-12. The ethylene oxidation rate as a function of temperature T_c of bare BCSO TE materials when it was placed directly onto the hot stainless steel floor of the reaction chamber. The calculated reaction rate was obtained using the equation $r = k_0 \cdot \exp(-E_a/k_b T_c) \cdot \exp(-\gamma e V/k_b T_c)$ with the fitting parameters $k_0 = 7.127 \times 10^8$, $E_a = 56.1$ kJ/mol, and $\gamma = 27.8$.

Per eq. (6-4), the ethylene oxidation reaction rate on the top surface (T_c) can be expressed as:

$$r = k_0 e^{(-E_a/K_b T_c)} \cdot e^{(-\gamma e V/K_b T_h)} \quad \text{Equation 6-5}$$

where V is the voltage between the top T_c and bottom T_h , a positive number in this case. The above equation (6-5) and the MATLAB software were used to model the reaction with k_0 , E_a and γ as the fitting parameters. The best fitting parameters are $k_0 = 7.127 \times 10^8$, $E_a = 56.1$ KJ/Mol, and $\gamma = 27.8$, with coefficient of determination $R^2 = 0.76$, indicating a good fit. The calculated reaction rates using the above equation with the above best fitting parameters are also shown in Figure 6-12 in blue marks. It can be seen this equation describes well the rate dependence of the temperature. The agreement between the calculated and the measured results are good, except for the highest reaction point.

Although the actual temperature of the surface T_c was high > 700 K, the reaction rate was very small. The obtained activation energy $E_a = 56.1$ KJ Mol⁻¹ was very close to the activation energy (56 KJ Mol⁻¹) of ethylene oxidation over Pt (Harkness *et al.*,

1996). This successful prediction of equation (6-4) proves that earlier assumption that the reaction rate contributions from the “other” side and the side wall were negligible was correct. The rate contribution from the side wall was negligible for Figures 6-3, and 6-7 when the rate was high, but could have contributed for the discrepancy between the measured and the calculated rates in Figure 6-12 where the reaction rate was much smaller.

6.2.6 Simulation of Pt/BCSO Interaction and the Mechanism for Thermoelectric Promotion of Catalysis

The above phenomenon can be understood from metal-semiconductor contact theory and the ability of thermoelectric materials to change their Fermi level with temperature. The metal-semiconductor contact theory states that after contact, the Fermi level (also called electrochemical potential) of the metal should be the same as the semiconductor at the surface. Before contact, the metal and the semiconductor have different Fermi levels, then upon contact, charge will flow to the material with the lower Fermi level, until their Fermi levels are equalized. The work function and Fermi level of BCSO and their temperature dependence were calculated using *ab initio* method based on density functional theory (Kresse and Furthmüller, 1996; Perdew, Burke and Ernzerhof, 1996).

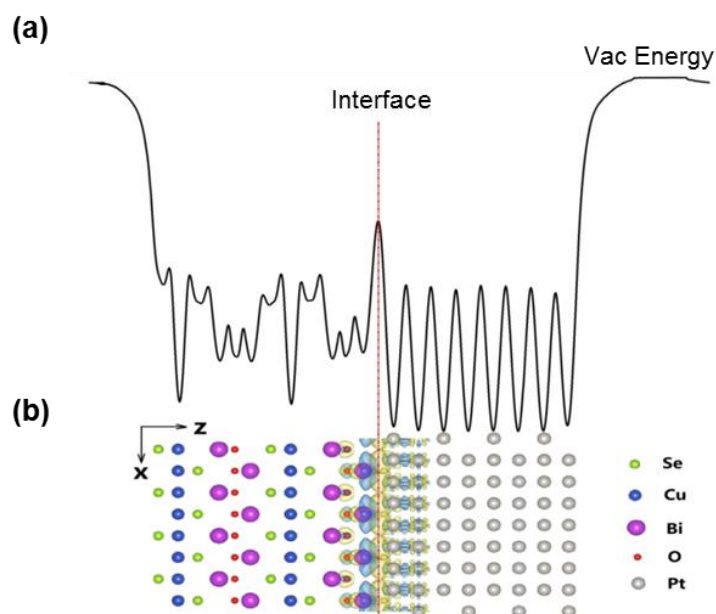


Figure 6-13 (a) The distribution of electrostatic potential; (b) the charge density difference.

Figure 6-13 shows (a) the electrostatic potential distribution, and (b) charge density difference at the interface for the optimised structure of eight layers of Pt on two unit cells of BCSO along the [001] direction. From the first principle calculation, the obtained work function is 3.94 eV for intrinsic BCSO, and 5.67 eV for Pt which is close to its experimental value 5.64 eV (Hölzl and Schulte, 1979). As BCSO has a much smaller work function than Pt, electrons will be transferred from BCSO to Pt. In Figure 6-13b, yellow and blue represent the gaining and losing of electrons respectively, it can be seen the charge transfer happens mainly from Bi to Pt.

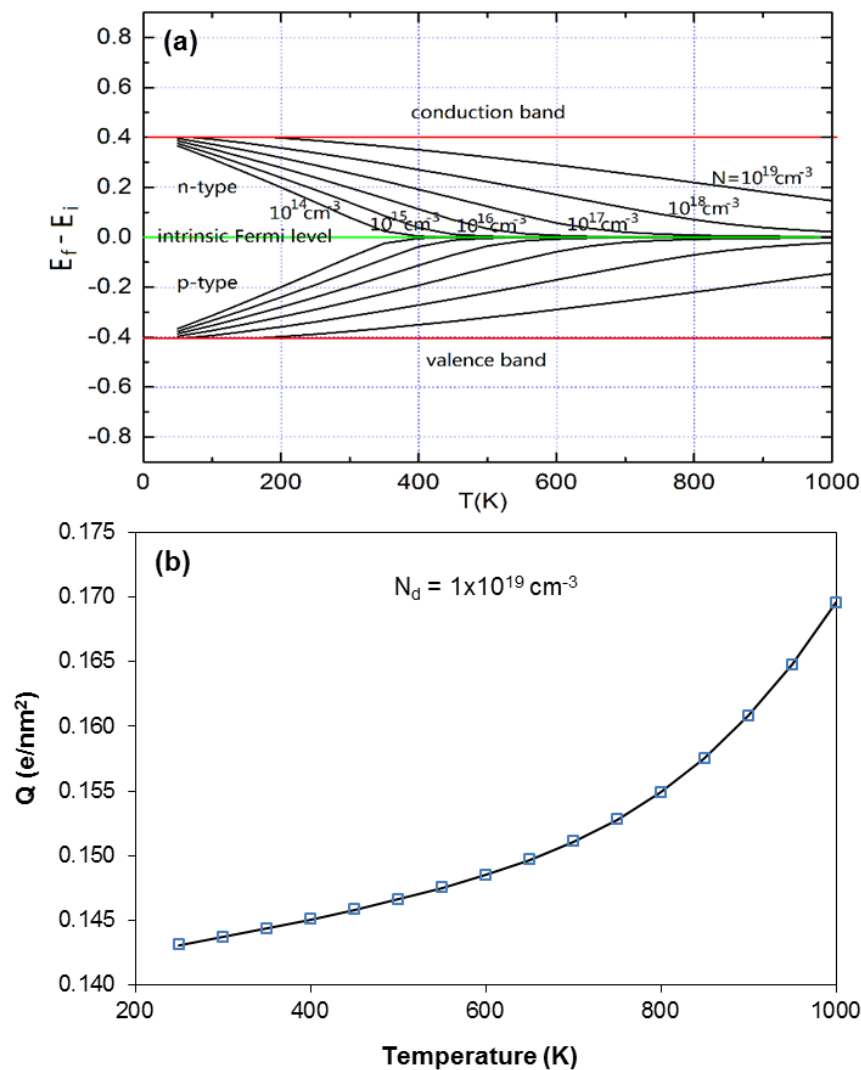


Figure 6-14. (a) The Fermi level dependence on temperature at different charge carrier concentrations for n-type and p-type BCSO; (b) The calculated temperature dependence of charge transfer from a BCSO to Pt assuming a donor concentration $10^{19} /\text{cm}^3$.

Figure 6-14a shows the calculated Fermi level of BCSO at different temperatures and different charge carrier concentrations. At a certain temperature, higher carrier density leads to smaller change in Fermi level. At a particular charge carrier density, higher temperature makes the Fermi level move closer to the intrinsic value (middle of the band gap). For p-type BCSO, the Fermi level increases with increasing temperature, which reduces its work function and leads to even larger differences in work functions between Pt (Pt has a very small Seebeck coefficient $\sim 5 \mu\text{V}/\text{K}$ therefore its Fermi level hardly change with temperature) and BCSO, therefore more charges are transferred from BCSO to Pt with increasing temperature, see calculated transfer charge in Figure 6-14b.

From the above experimental and simulation results the mechanism for the thermoelectric promotion of catalysis can be summarised as follows: BCSO is a p-type thermoelectric material, holes at the hot side diffuse into the cold side upon heating. The Fermi level at the hot side ($\epsilon_{F,h}$) is higher than at the beginning or cold side ($\epsilon_{F,c}$), and this difference in Fermi level is equal to the Seebeck potential difference, i.e.

$$\Delta\epsilon_F = \epsilon_{F,h} - \epsilon_{F,c} = -eV \quad \text{Equation 6-6}$$

where V is the Seebeck voltage. As no net external charges exist, the change of the Fermi level is the inverse of the change of work function $\Delta\phi$, i.e.,

$$\Delta\phi = -\Delta\epsilon_F, \text{ so } \Delta\phi = eV \quad \text{Equation 6-7}$$

If a metal particle is in contact with the thermoelectric material at the hot surface, its Fermi level $\epsilon_{F,m}$ must be the same as the Fermi level of the thermoelectric supporting material, i.e., $\epsilon_{F,m} = \epsilon_{F,h}$. When the temperature is changed, the above relationship must still valid, i.e. $\Delta\phi_m = -\Delta\epsilon_{F,m} = eV$, here $\Delta\phi_m$ is the change of work function for the metal particle. These relationships and the electron energy band of the p-type thermoelectric material are shown schematically in Figure 6-15. For n-type thermoelectric materials, the Fermi level at the cold side is higher than at the hot side, but the relationship $\Delta\phi = -\Delta\epsilon_F = eV$ is still valid, as V is positive for n-type materials and negative for p-type materials between the hot and cold sides. It is well established that a change in work function at catalyst surface will change the catalytic activity exponentially through the eq. (6-2) (Vayenas *et al.*, 1990; Vayenas *et al.*, 2001).

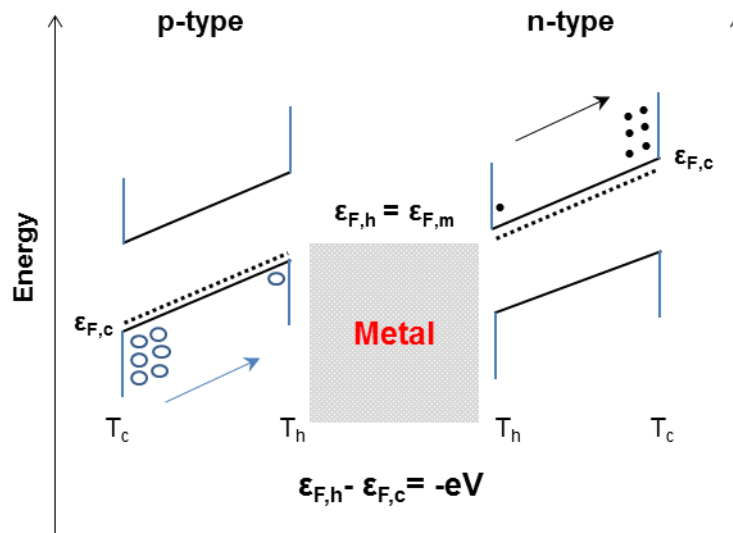


Figure 6-15. Schematic of energy bands and Fermi levels for p-type and n-type TE materials and a metal particle supporting on the TE materials at the hot side. T_c and T_h are the temperatures at the cold and hot ends respectively. The arrow heads point the electric field direction within the TE material.

Moreover, the total amount of the metal particles, indeed any second phase materials, will affect the thermoelectric properties such as Seebeck coefficient and electrical conductivity, as the whole system can be regarded as a thermoelectric composite. This explains the features observed in that all the samples follow a similar trend as functions of Seebeck voltage. This is because all the samples, with or without metal Pt, are just thermoelectric materials with a different Seebeck coefficient. Of course, metallic particle surfaces and TE surfaces may have different adsorption properties, which may lead to different catalytic properties.

Furthermore, notice that this Fermi level change is accompanied by charge transfer through the bulk to the surface of the TE material, or from the bulk TE to the metal particles on the surface. So, the fundamental reason for TEPOC is the same as for electronic promoters, i.e., the charge transfer to the catalytic sites. From the catalytic promotion point of view, there is not much difference between metal particles supported on TE or surface TE particles themselves. As the TE effect can be realised together with chemical reactions, its modification to the catalytic activity can be realised in-situ under operational conditions, and controllable through the control of the back-side temperature of the supporting bed, for example, changing the water cooling to liquid nitrogen cooling.

6.2.7 Dependence of Catalytic Activity on Oxygen Pressure under Fuel-Lean Conditions

To investigate further features of TEPOC, the catalytic activity dependence on oxygen partial pressure under rich oxygen conditions was investigated. The inlet C_2H_4 partial pressure was fixed at 0.195 kPa, and the O_2 partial pressure was varied from 0.2 to 7.23 kPa. Table 6-4 summarises the experimental conditions and the corresponding ethylene oxidation rates and conversions for four samples, namely Pt(80)/BCSO, Pt(80)/(BiCuSeO)_{0.9}(YSZ)_{0.1} Pt(15)/BCSO, and bare BCSO under different O_2 partial pressure, at a fixed thermoelectric voltage (through fixing the temperatures T_c and T_h).

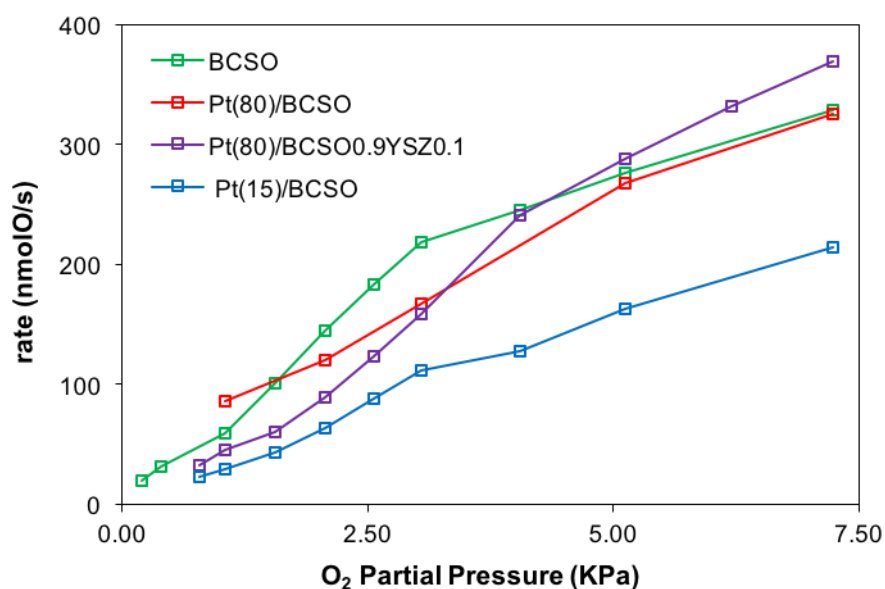


Figure 6-16. Ethylene oxidation reaction rate as a function of oxygen partial pressure of Pt(15)BCSO, Pt(80)/BCSO, Pt(80)/ BiCuSeO_{0.9}YSZ_{0.1} and bare BCSO with thermoelectric promotion of catalysis effect.

Figure 6-16 displays the ethylene oxidation reaction rate as a function of the O_2 partial pressure. The results indicated that the rate increased with the increasing O_2 pressure, but the gradient i.e. the rate of increase, decreased at higher O_2 pressure for all of the four samples. The mechanism for these will be discussed latter after the effect of C_2H_4 pressure had been presented. This is in agreement with previous observation for ethylene oxidation with NEMCA effect, that ethylene oxidation on Pt was a first order effect with O_2 pressure (Vayenas *et al.*, 2001).

Table 6-4. Summary of ethylene oxidation rate and conversion under different oxygen partial pressures of Pt(15)BCSO, Pt(80)/BCSO, Pt(80)/ BiCuSeO_{0.9}YSZ_{0.1} and bare BCSO with a specific Seebeck voltage and fixed temperature for each sample.

T _c = 333 K	BCSO	O ₂ (kPa)	0.20	0.40	1.05	1.56	2.07	2.56	3.04	4.05	5.12	7.23
T _h = 628 K		C ₂ H ₄ Conv (%)	0.73	1.32	5.32	10.58	17.16	23.61	30.70	35.80	40.58	50.08
V = -105 mV		r (nmolO/s)	19.35	31.64	59.49	100.65	144.37	182.73	218.14	245.79	276.21	328.23
T _c = 355 K	Pt(80)/BCSO	O ₂ (kPa)	1.05	2.07	3.04	5.12	7.23	-	-	-	-	-
T _h = 593 K		C ₂ H ₄ Conv (%)	5.74	9.47	15.89	32.12	42.31	-	-	-	-	-
V = -84.7 mV		r (nmolO/s)	85.89	119.80	167.4 0	268.13	325.20	-	-	-	-	-
T _c = 340 K	Pt(80)/BCSO_{0.9}YSZ_{0.1}	O ₂ (kPa)	0.79	1.05	1.56	2.07	2.56	3.04	4.05	5.12	6.20	7.23
T _h = 648 K		C ₂ H ₄ Conv (%)	2.45	3.52	5.30	8.88	14.00	19.47	35.68	44.62	52.21	58.19
V = -64.4 mV		r (nmolO/s)	32.13	44.76	60.28	89.31	123.85	158.64	240.85	287.75	331.53	369.27
T _c = 341 K	Pt(15)/BCSO	O ₂ (kPa)	0.79	1.05	1.56	2.07	2.56	3.04	4.05	5.12	7.23	-
T _h = 633 K		C ₂ H ₄ Conv (%)	1.56	2.10	3.56	5.84	8.71	12.07	14.84	21.67	29.92	-
V = -82.2 mV		r (nmolO/s)	22.87	29.19	43.57	63.88	88.42	112.09	127.89	163.19	214.09	-

6.2.8 Relationships between Thermoelectric Voltage and Catalytic Activity under Fuel-Rich Conditions

Figure 6-17 depicts the ethylene oxidation rate as a function of the hot surface temperature T_h at the gas pressures $P_{C_2H_4} = 1.9$ kPa and $P_{O_2} = 0.5$ kPa for the four samples Pt(15)BCSO, Pt(80)/BCSO, Pt(80)/BiCuSeO_{0.9}YSZ_{0.1} and bare BCSO. It can be seen the rates behaved very differently from Figure 6-7 under fuel-lean conditions. For the two samples Pt(80)/BCSO and Pt(80)/BiCuSeO_{0.9}YSZ_{0.1}, the reaction surface T_h were practically Pt, the rate increased with the increasing temperature until about 500 K where it reached a maximum (1233.16 nmolO/s at 543 K for Pt(80)/BCSO, and 1232.86 nmolO/s at 508 K for Pt(80)/BiCuSeO_{0.9}YSZ_{0.1}), then it decreased with further increasing of the temperature. The bare BCSO did not show notable oxidation rate until 473 K, the first measured rate was 3 nmolO/s at 503 K, and then increased with the increasing temperature till 628 K. Further increase of temperature lead to a decrease of the oxidation rate, similar to the other two samples discussed above. It was noted also even during this decreasing rate staging, the rate was also changed with time at any particular temperature, just the rate of change was much slower than at 628K. The sample Pt(15)BCSO behaved like a mixture of these two cases aforementioned. The rate increased with the increasing temperature until 653 K, where it reached a maximum 1236.81 nmolO/s, and then decreased with further increasing of the temperature, similar to the other three samples. These behaviours were similar to that observed for the effect of C_2H_4 partial pressure on the rate of ethylene oxidation under a positive (+3000 mV) catalyst potential (S Bebelis and Vayenas, 1989; C Pliangos *et al.*, 1996)

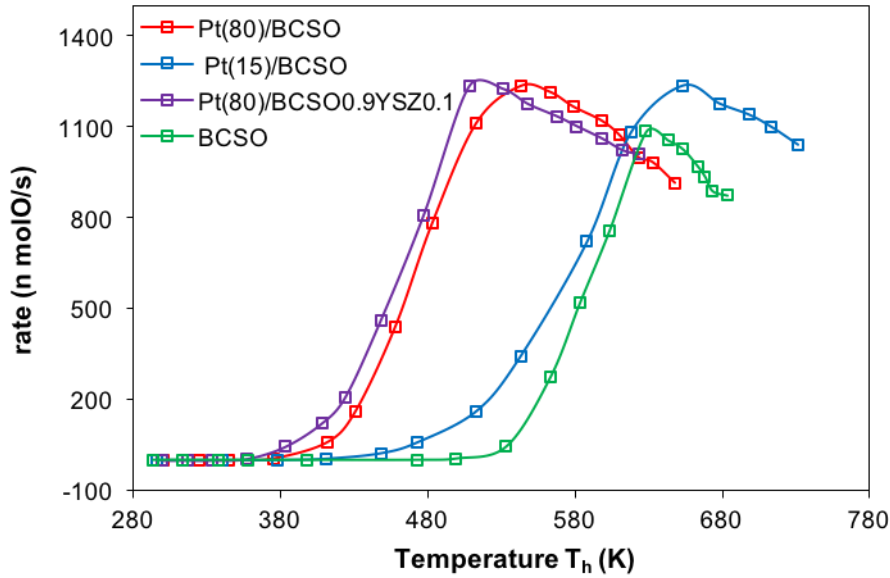


Figure 6-17. Reaction rate as a function of temperature T_h of the four samples: BCSO, Pt(15)BCSO, Pt(80)/BCSO and Pt(80)/BiCuSeO_{0.9}YSZ_{0.1}.

Figure 6-18 displays the measured Seebeck voltage as a function of the temperature differences for the above four samples. Again, the voltage increased almost linearly with the temperature difference, the best-fit trend line gradients were 230, 294, 322, and 275 $\mu\text{V}/\text{K}$ for Pt(15)BCSO, Pt(80)/BCSO, Pt(80)/BiCuSeO_{0.9}YSZ_{0.1} and bare BCSO, respectively. The values of 230 and 250 $\mu\text{V}/\text{K}$ were very close but not exactly the same (250 and 265 $\mu\text{V}/\text{K}$) for Pt(15)BCSO and BCSO respectively as observed in Figures 6-8 and B-3 in appendix B, probably because of slight differences between samples of the same composition or between different experiments.

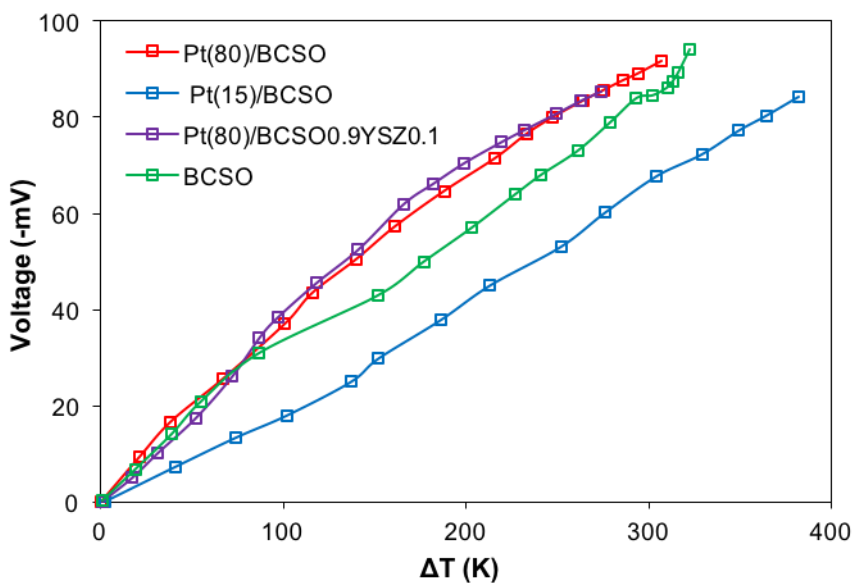


Figure 6-18. Measured Seebeck voltage as functions of temperature difference across the sample thickness of the four samples: BCSO, Pt(15)BCSO, Pt(80)/BCSO and Pt(80)/BiCuSeO_{0.9}YSZ_{0.1}.

The plots of the rate dependence on the Seebeck voltage and $\ln(r)$ vs. $-eV/K_bT_h$ are shown in Figures 6-19 for the above four samples. As shown in Figure 6-19a, the four samples BCSO, Pt(15)BCSO, Pt(80)/BCSO, and Pt(80)/BiCuSeO_{0.9}YSZ_{0.1} behaved similarly, i.e. the rate increased with the Seebeck voltage, reached a maximum, 1084.65 nmolO/s at -79 mV for BCSO, 1236.81 nmolO/s at -67.7 mV for Pt(15)BCSO, 1233.16 nmolO/s at -71.5 mV for Pt(80)/BCSO and 1232.86 nmolO/s at -62 mV for Pt(80)/BiCuSeO_{0.9}YSZ_{0.1}. As mentioned before, no measurable ethylene oxidation rate was obtained until a Seebeck voltage of -50 mV was achieved for BCSO, it then increased with further increasing of the voltage, until it reached -79 mV, where the rate was increased over a few hours despite the Seebeck voltage was kept the same. However, upon further increase of the Seebeck voltage, the rate decreased after reaching a maximum of 1145 nmolO/s for all samples.

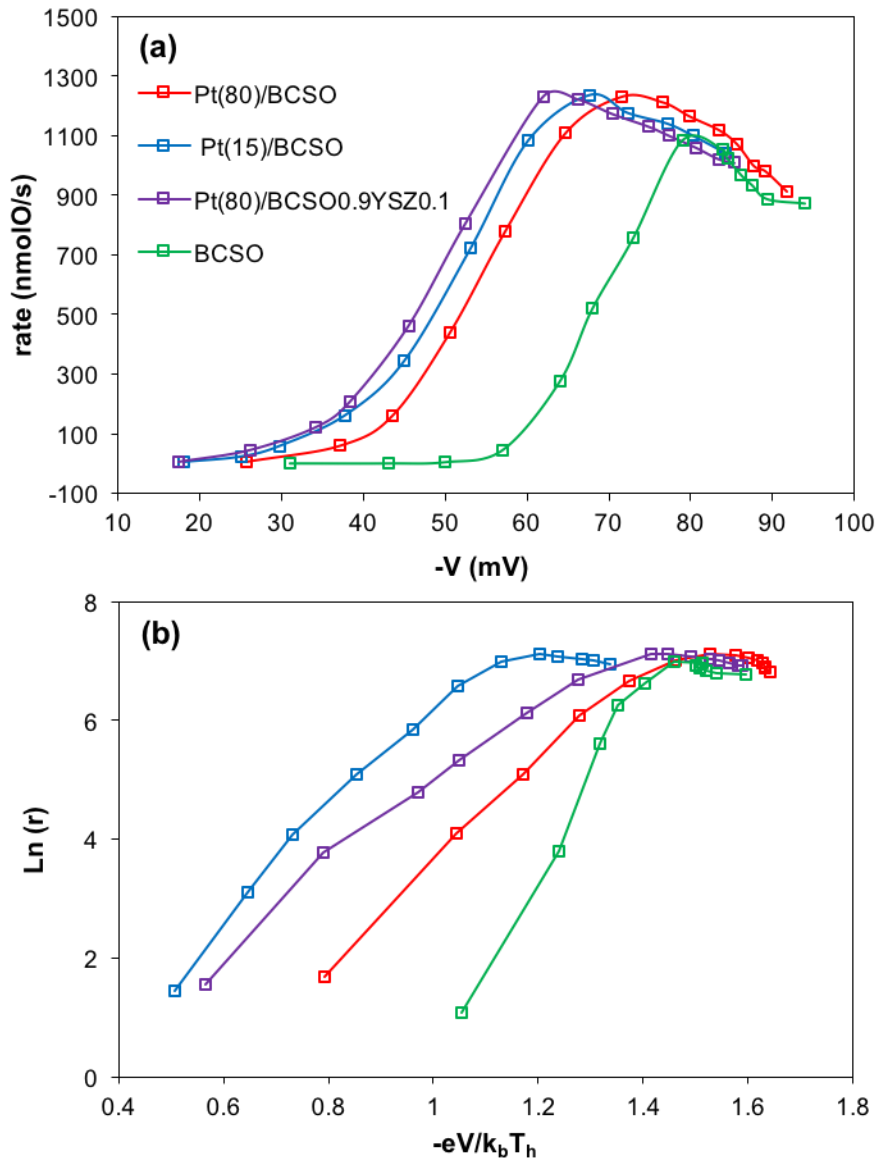


Figure 6-19. (a) The reaction rate r as a function of Seebeck voltage V ; (b) relationship between $\ln(r)$ and $-eV/k_b T_h$ of the four samples: BCSO, Pt(15)BCSO, Pt(80)/BCSO and Pt(80)/BiCuSeO_{0.9}YSZ_{0.1}.

For all of the four samples, at high Seebeck voltages, the decrease of the reaction rate with the Seebeck voltage appeared to follow a linear relationship, the best fit trend line gradients were $-10.28 \text{ nmolO/s} \cdot \text{mV}$ for Pt(80)/BiCuSeO_{0.9}YSZ_{0.1}, $-11.28 \text{ nmolO/s} \cdot \text{mV}$ for Pt(15)BCSO, $-16.36 \text{ nmolO/s} \cdot \text{mV}$ for Pt(80)/BCSO, and $-16.48 \text{ nmolO/s} \cdot \text{mV}$ for BCSO. In Figure 6-19b, the linear relationships between $\ln(r)$ and $-eV/k_b T_h$ can still be observed before reaching a maximum for the Pt catalysts where the reaction surface T_h were practically Pt. However, the gradients appeared to be decreased with higher $-eV/k_b T_h$.

6.2.9 Dependence of Catalytic Activity on Ethylene Pressure under Fuel-Rich Conditions

The catalytic activity dependence on ethylene partial pressure under fuel-rich conditions was then investigated. The inlet O_2 partial pressure was fixed at 0.5 kPa, and the C_2H_4 partial pressure was varied from 0.71 to 3.96 kPa. Table 6-5 summarises the experimental conditions and the corresponding ethylene oxidation rates and conversions for the same four samples, under different C_2H_4 partial pressure, at a specific Seebeck voltage and fixed temperature for each sample.

Figure 6-20 shows the reaction rate and C_2H_4 conversion as a function of the C_2H_4 partial pressure. These results indicated that the ethylene oxidation rate hardly change with the change of C_2H_4 pressure. The results in Figure 6-20a indicate that the reaction rate on the surface of both Pt and BCSO did not change with the changing of C_2H_4 pressure under $C_2H_4/O_2 > 1.4$, the fuel rich condition; however, the results in Figure 6-16 indicate that the rate increased almost linearly with the O_2 pressure under $O_2/C_2H_4 > 1$, fuel lean condition. Ethylene oxidation on Pt supported on ionic or mixed conductive oxides has been extensively studied before. It is believed that O_2 was strongly and C_2H_4 was weakly adsorbed on the catalyst Pt surface (Vayenas *et al.*, 2001). When the temperature was increased, the Seebeck effect made the Pt or BCSO surface negatively charged, this will weaken the oxygen (acceptor) adsorption and strengthen the ethylene (donor) adsorption. The weakening of the strong adsorption and the strengthening of the weak adsorption enabled the reaction rate to increase generally. However, at high Seebeck voltages, particularly for bare BCSO at $V = -79$ mV, C_2H_4 became strongly adsorbed (probably chemisorbed) on to the BCSO surface, this blocked the catalyst surface, reducing the catalytic active area, hence the rate became smaller. These results indicated that the ethylene oxidation rate hardly change with the change of C_2H_4 partial pressure. This agrees with the observation for NEMCA of ethylene oxidation that between the open-circuit and up to +2000 mV applied catalyst potentials the rate of ethylene oxidation was nearly zero-order with C_2H_4 pressure under ethylene-rich conditions (S Bebelis and Vayenas, 1989).

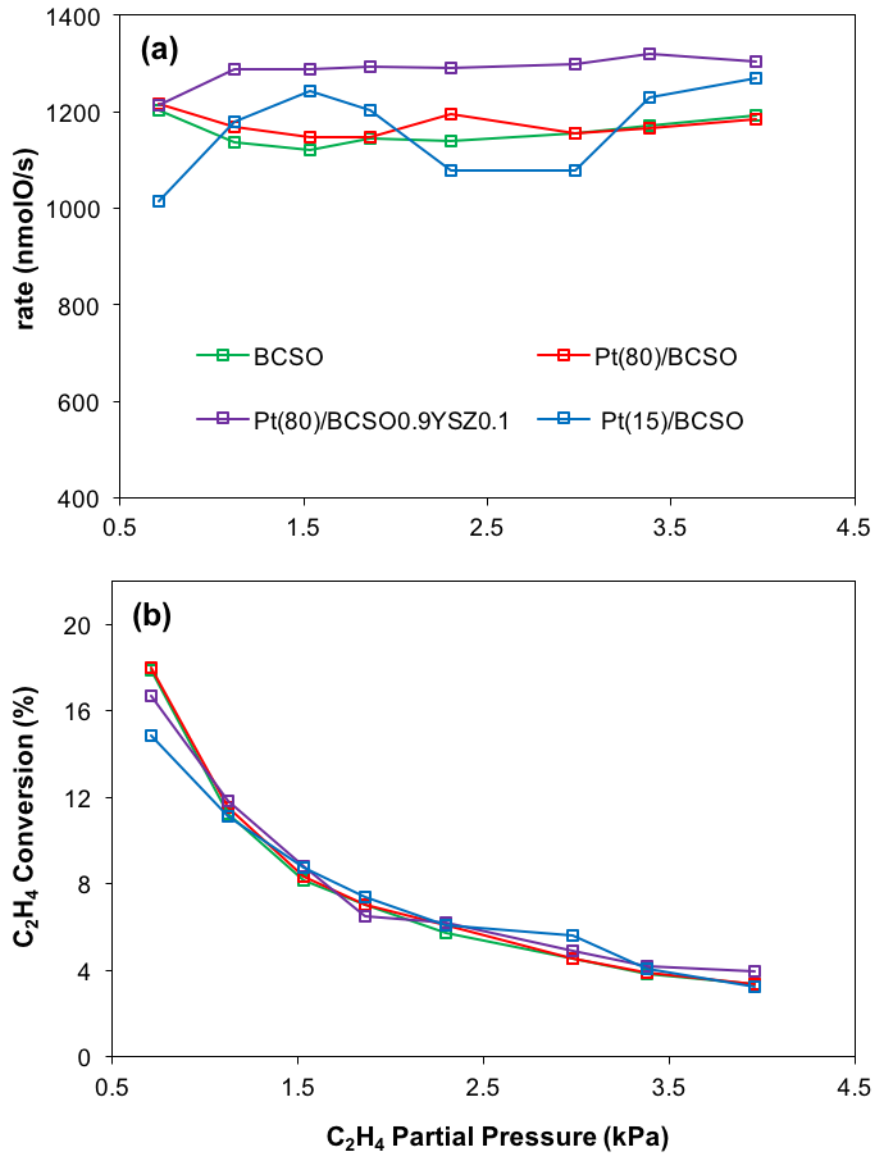


Figure 6-20. Ethylene oxidation reaction rate (a); conversion (b) as a function of ethylene partial pressure of Pt(15)BCSO, Pt(80)/BCSO, Pt(80)/ BiCuSeO_{0.9}YSZ_{0.1} and bare BCSO with thermoelectric promotion of catalysis.

Table 6-5. Summary of ethylene oxidation rate and conversion under different ethylene partial pressures for Pt(15)BCSO, Pt(80)/BCSO, Pt(80)/ BiCuSeO_{0.9}YSZ_{0.1} and bare BCSO with a specific Seebeck voltage and fixed temperature for each sample.

$T_c = 349$ K	BCSO	C ₂ H ₄ (kPa)	0.71	1.12	1.53	1.86	2.3	2.98	3.38	3.96
$T_h = 628$ K		C ₂ H ₄ Conv (%)	17.88	11.24	8.15	6.99	5.55	4.41	3.75	3.21
$V = -79.0$ mV		r (nmolO/s)	1203.15	1138.18	1121.72	1084.65	1071.21	1065.26	1058.69	1072.35
$T_c = 349$ K	Pt(80)/BCSO	C ₂ H ₄ (kPa)	0.71	1.12	1.53	1.86	2.3	2.98	3.38	3.96
$T_h = 593$ K		C ₂ H ₄ Conv (%)	18.01	11.53	8.35	7.01	6.08	4.54	3.87	3.35
$V = -79.5$ mV		r (nmolO/s)	1215.57	1168.30	1146.41	1148.32	1194.93	1155.90	1166.80	1185.37
$T_c = 342$ K	Pt(80)/BCSO_{0.9}YSZ_{0.1}	C ₂ H ₄ (kPa)	0.71	1.12	1.53	1.86	2.3	2.98	3.38	3.96
$T_h = 508$ K		C ₂ H ₄ Conv (%)	16.72	11.81	8.81	6.49	6.21	4.90	4.19	3.95
$V = -62$ mV		r (nmolO/s)	1213.30	1287.73	1287.48	1293.20	1291.75	1298.10	1319.67	1304.73
$T_c = 349$ K	Pt(15)/BCSO	C ₂ H ₄ (kPa)	0.71	1.12	1.53	1.86	2.3	2.98	3.38	3.96
$T_h = 633$ K		C ₂ H ₄ Conv (%)	14.85	11.14	8.77	7.38	6.07	5.59	4.08	3.25
$V = -62.7$ mV		r (nmolO/s)	1014.57	1180.29	1242.80	1202.11	1079.40	1079.01	1230.98	1268.50

Under fuel-lean conditions, no much difference between the Pt surface and BCSO surface existed across a range of Seebeck voltage in terms of the ethylene oxidation reaction rate. However, under fuel C₂H₄-rich conditions, a large difference existed between the reaction rate on the Pt surface and the BCSO surface. The rate on Pt surface is large, but on BCSO surface, the rate is almost non-existent until Seebeck voltage reached a certain value. And after this, the adsorption of C₂H₄ on BCSO increased very rapidly with even a small increase of the Seebeck voltage. However, further increase of the Seebeck voltage lead to the blocking of the catalysis sites, and this blocking is proportional to the Seebeck voltage, hence a reduction of the reaction rate, and an apparent linear relationship between the rate and the Seebeck voltage. Under fuel-rich conditions, the blocking of catalysis sites by adsorbed C₂H₄ plays an important role to the overall reaction rate, hence the linear relationship $\ln(r/r_0) \sim -eV/k_bT_h$ can no longer be strictly observed.

6.3 Conclusions

An innovative use of thermoelectric materials as catalyst supports has been investigated, through ethylene C₂H₄ oxidation to produce CO₂ and H₂O. It was found that the catalytic activity of Pt nanoparticles supported on thermoelectric materials can be promoted significantly by a Seebeck voltage generated through a temperature differential across the thickness of the thermoelectric support.

Moreover, the thermoelectric material itself can also be promoted significantly by a Seebeck voltage. It was further observed that there exist a linear relationship between the logarithm of the catalytic activity, and $-eV/k_bT$, which can be regarded as the ratio of extra electrochemical energy ($-eV$) induced by the thermoelectric effect and thermal energy (k_bT) of an electron. This linear relationship is explained as due to the change of work function of the metallic particles at the surface, through the change of its Fermi level induced by a thermoelectric effect.

The thermoelectric promotion of catalysis is accompanied by a charge transfer from the thermoelectric material to the metal catalyst on the surface or from the bulk to the surface thermoelectric materials, and this charge transfer lead to the formation of an energy barrier at the metal-thermoelectric interface. At higher temperature gradient or larger Seebeck voltage, the promoted catalytic reaction rate was found to linearly

increase with the Seebeck voltage, similar to the I-V curve of a p-n diode under a forward bias.

The generic nature of this mechanism suggests the possibility that many catalytic chemical reactions can be tuned in-situ to achieve much higher reaction rates, or at lower temperature, or have better desired selectivity through changing the backside temperature of the thermoelectric catalyst support. The high catalytic activity of the TE oxides point to the possibility of replacing or using a much reduced loading of the expensive noble metals in catalytic chemical processes.

7 *In-situ* Tuning of Catalytic Activity by the Thermoelectric Effect for Carbon Dioxide Hydrogenation

7.1 Introduction

The concentration of carbon dioxide in the atmosphere has risen from ≈ 280 ppm before the industrial revolution to ~ 400 ppm in 2013, and is projected to be ≈ 500 ppm by 2050 (Bishop *et al.*, 2015). This contributes to the increase in global temperature and climate changes due to the “greenhouse effect”. Hence there are extensive efforts to reduce CO₂ emissions around the world. There are three strategies to achieve this: (i) reduce CO₂ production; (ii) storage; and (iii) usage. The first two options, which involve improving energy efficiency, switching to renewable energy, and CO₂ capture and sequestration (Olah, Prakash and Goeppert, 2011), have been the major focus in the past. The third strategy, i.e. using CO₂ as a feedstock for making useful organic chemicals, is regarded as the most feasible and effective solution to our carbon conundrum (Olah, Goeppert and Prakash, 2009; Wang *et al.*, 2011; Hu, Guild and Suib, 2013; Jhong, Ma and Kenis, 2013; Hollingsworth *et al.*, 2015). For this reason, CO₂ hydrogenation has been chosen as the reaction to be investigated.

The CO₂ hydrogenation is the first step in a range of different processes for the formation of many commercially important chemicals (Xiaoding and Moulijn, 1996). The formation of syngas from CO₂ via RWGS reaction has developed a whole range of hydrocarbons with many syngas fed processes already well known and industrially used. The RWGS reaction is thermodynamically preferred at higher temperatures. Therefore, higher CO₂ concentration yields to a complete consumption of H₂, while higher concentration of H₂ will increase the consumption of CO₂. The later will be most useful for CO₂ utilisation as it encourages CO₂ consumption while ensuring that H₂ is still present to give a syngas (CO/H₂) product stream ready for use in the consecutive process (Kaiser *et al.*, 2013; Sousa-Aguiar *et al.*, 2014). Additionally, the formation of CO via RWGS reaction may be the best alternative way to traditional coal gasification technology, which will become a basis for the future green coal chemistry industry (Schlögl, 2013).

In this chapter, the realization of in situ, reversible, and significant modification of catalytic activity for both continuous thin film and highly dispersed (nanoscale particles) metal catalysts, by using TE materials as a catalyst support for CO₂

hydrogenation will be presented. Furthermore, we show that this profound promotional effect on catalytic activity by the TE effect also enables the oxide TE material itself to possess high catalytic activity for CO₂ hydrogenation. This reaction was also studied to clarify and confirm the conclusions that have been shown for the ethylene oxidation (Chapter 6).

7.2 Results and Discussion

7.2.1 Brief Experimental Introduction

The schematic diagram of the single-chamber reactor which can combine TE effect with catalytic chemical reaction is shown in Figure 3-2a. The reaction chamber was placed on top of a hot-plate to create a large temperature difference ($\approx 200\text{-}300\text{ K}$ when $T_h > 500\text{ K}$) between the bottom floor of the chamber and the hot surface T_h of the sample (Figure 3-3a). As discussed in the previous studies, the large temperature gradient in the chamber can induce strong convection along the vertical direction, which can bring in the reactants and remove the products quickly from the reaction surface T_h . Figure 6-2 shows that the samples were not porous; hence, there is no pore-diffusion limitation. For these reasons, it is assumed that there was no mass transportation limitation, and the intrinsic chemical reaction is the rate limiting step for all the reactions investigated.

Disc samples with a diameter of 20 mm and thickness of 2 mm were tested for catalytic activity as represented by CO₂ hydrogenation conversion X (%) at different temperatures (CO₂ conversion X is proportional to the CO₂ reaction rate r if the backward reaction of Equation 3-12 is ignored, this will be discussed later). Catalytic activities are then compared between the TE and RTE conditions, at the same front (hot) surface temperature. Under normal TE conditions, the back side of the disc was in contact with the water cooled stainless steel cap (with a thin mica sheet in between for electrical insulation). So, its temperature was never higher than 373 K, and a large temperature gradient across the disc thickness was created when the front surface reached a high temperature. Under the reduced TE (RTE) conditions, the backside of the disc was not in contact with the cooled cap, so the temperature gradient across the disc thickness was much smaller. At a particular hot-plate temperature, after reaching thermal equilibrium, the bottom surface of the disc sample was stabilised at a temperature T_h , while the top surface was at a temperature T_c . The Seebeck voltage

V between the surfaces T_c and T_h was monitored continuously during the whole period of the experiment (Figure 3-3a). Figure 7-1 displays the time profile of the measured voltage for Pt(80)/BCSO during a run of CO_2 hydrogenation reaction.

Table 7-1 summarise the measured gas partial pressures at different T_h , and the corresponding T_c , measured Seebeck voltage V, the CO_2 conversion, and CO and CH_4 selectivities, the calculated $-eV/K_bT_h$, and logarithm of CO_2 conversion X. From Table 7-1 and the predicted eq. (6-3) in Chapter 6, it is assumed that for all samples, the measured CO_2 conversion rate was contributed from the hot surface T_h only, the contributions from the cold surface T_c and the side wall of the disc sample are negligible.

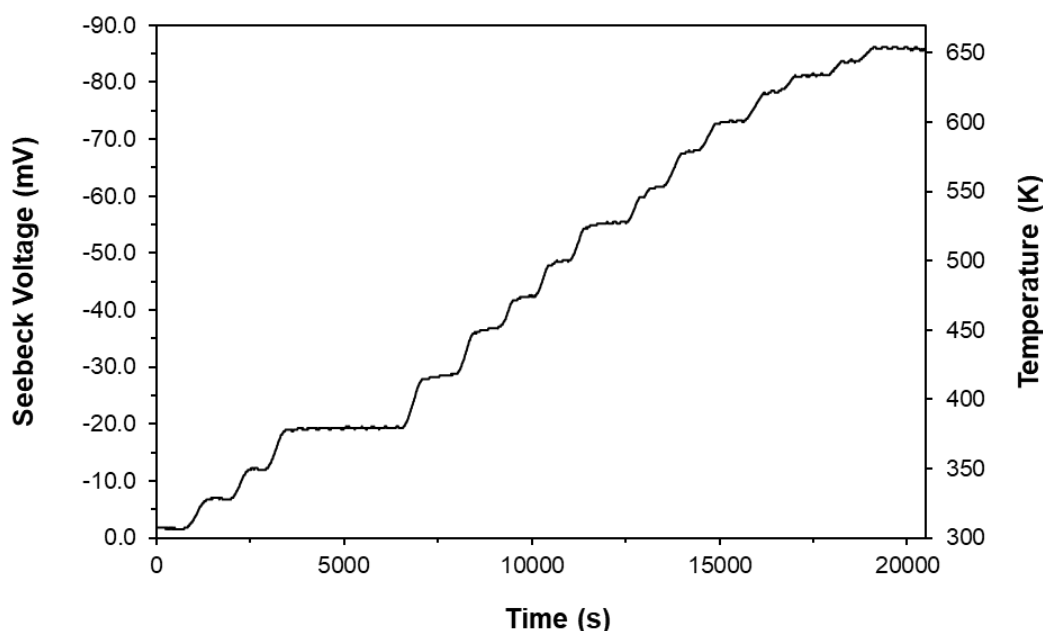


Figure 7-1. Measured Seebeck voltage as a function of elapsed time during the catalytic reaction characterisation experiment of Pt(80)/BCSO at $\text{CO}_2/\text{H}_2=1: 4$.

Table 7-1. Summary of experimental conditions and CO₂ hydrogenation reaction measurement results of Pt(80)/BCSO. T_c, T_h were the temperatures at the top cold surface and bottom hot surface respectively, V the Seebeck voltage. Gas amounts were obtained from their measured respective peak areas in GC.

T_c (K)	290.7	293.7	296.4	300	303	307	309	312	315	317	322	324	327	328	329	331
T_h (K)	301	323	343	369	403	430	448	468	493	523	553	583	613	628	638	656
V (-mV)	1.84	7.05	12.27	19.67	28.83	37	43	48.9	55.5	62	68	74	78.5	82	84	86
ΔT (T_h-T_c)	10.3	29.3	46.6	69	100	123	139	156	178	206	232	259	286	300	309	325
CO₂ (kPa)	1.05	1.05	1.05	1.06	1.06	1.05	1.04	1.02	0.97	0.92	0.85	0.77	0.70	0.64	0.61	0.57
H₂ (kPa)	4.18	4.20	4.41	4.21	4.24	4.11	3.89	3.88	3.88	3.77	3.76	3.64	3.63	3.64	3.56	3.60
CO (kPa)	0.00	0.00	0.00	0.00	0.00	0.00	0.03	0.04	0.10	0.15	0.23	0.31	0.39	0.46	0.50	0.54
CH₄ (Pa)	0.00	0.00	0.00	0.00	0.00	0.38	0.85	2.29	4.32	3.98	3.75	2.31	1.73	1.15	0.58	0.29
Selectivity CO (%)						91.31	97.03	94.99	95.68	97.37	98.36	99.26	99.56	99.75	99.89	99.95
Selectivity CH₄ (%)						8.69	2.97	5.01	4.32	2.63	1.64	0.74	0.44	0.25	0.11	0.05
CO₂ Conv X (%)	0.00	0.00	0.00	0.00	0.00	0.42	2.67	4.30	9.37	14.16	21.31	28.87	36.09	41.80	45.19	48.41
ln (X)							0.98	1.46	2.24	2.65	3.06	3.36	3.59	3.73	3.81	3.88
eV/K_bT_h (-)	0.07	0.25	0.41	0.62	0.83	1.00	1.11	1.21	1.31	1.37	1.43	1.47	1.48	1.51	1.53	1.52

7.2.2 Substantial Higher Catalytic Activity under Large TE Effect

Figure 7-2 shows the CO₂ conversion as a function of temperature T_h. The catalytic activity of Pt(80)/BCSO and BCSO was measured under TE and RTE condition with an inlet gas composition CO₂/H₂ = 1. As can be observed, the CO₂ conversions under TE conditions were much higher than under reduced temperature gradient RTE conditions. This was similar to that observed for ethylene oxidation reaction (Figure 6-3). For example, Pt(80)/BCSO at 573 K, the CO₂ conversion under TE condition was 12.4%, 42 times higher than 0.3% under RTE conditions. At 673 K, the CO₂ conversion under TE conditions was 10 times higher than under RTE conditions.

Another observation was that the BCSO TE sample, without any Pt catalyst, was catalytically active for CO₂ hydrogenation (Figure 7-2). This should not be a total surprise, as BCSO is electrically conductive, and other conductive oxides (e.g., IrO₂ and RuO₂) have been found to be good catalysts (Nicole *et al.*, 1997). The first measured CO₂ conversion (0.8%) was at 483 K under TE conditions, and 633 K under RTE conditions (0.8%). As for Pt(80)/BCSO, the CO₂ conversion under TE conditions was much higher than under RTE conditions for BCSO. At the same temperature 698 K, the CO₂ conversion was 20.8% under TE conditions, compared to 3.4% under RTE conditions.

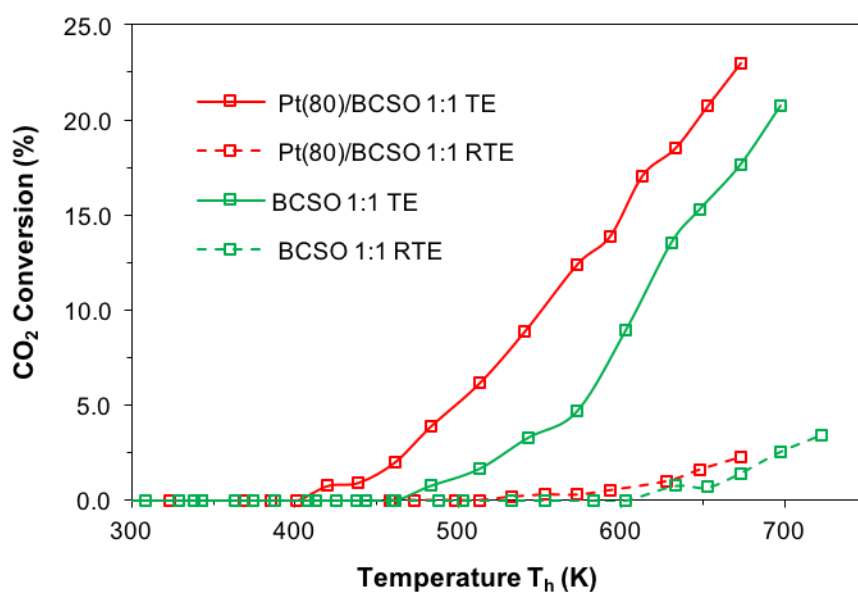


Figure 7-2. CO₂ conversion rate as a function of temperature of Pt(80)/BCSO and BCSO under TE and RTE effect conditions at CO₂/H₂=1.

The catalytic results shown in Figure 7-2 also indicate that the first measurable CO₂ conversion (0.8%) happened at 420 K under TE conditions, much lower than 533 K when it was first measured under the RTE conditions (0.2%). Similarly to C₂H₄ oxidation, the influence of TE effect was observed on CO₂ reduction. It is plausible to assume that relative to conditions without any TE effect the promotional effect should be even higher.

Figure 7-3 plots Ln(X) against $-eV/k_bT_h$ for the BCSO and Pt(80)/BCSO. It is observed that a very good linear relationship existed between Ln(X) and $-eV/k_bT_h$ for each sample. Under RTE conditions, the conversion rate was very low, so it was safe to assume that the backward water-gas reaction can be ignored and the CO₂ conversion X was linearly proportional to the reaction rate r. So at least under RTE conditions, the results confirmed the prediction of eq. 6-2. For the results under TE conditions to be explained by eq. 6-2 as well the assumption that the backward water-gas reaction under TE conditions can be ignored need also be true. This will be discussed later.

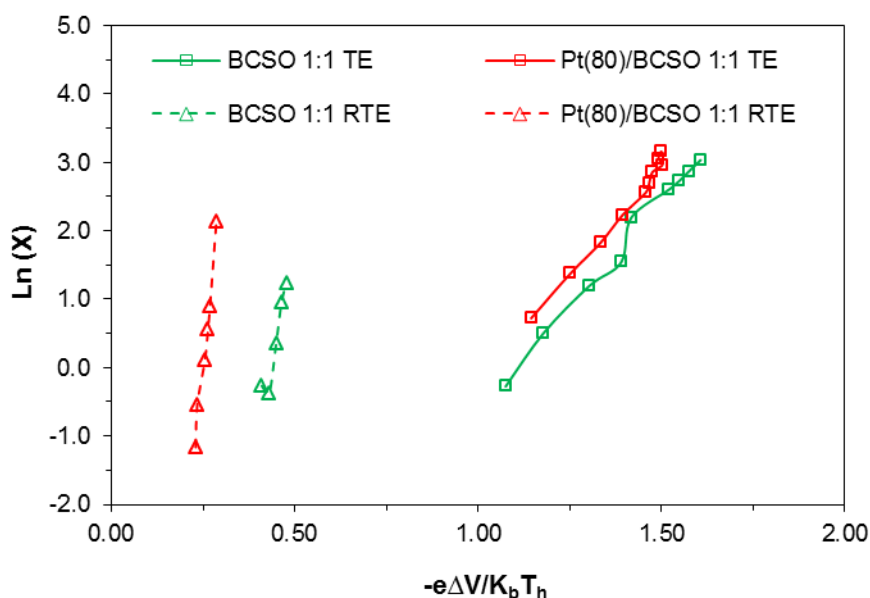


Figure 7-3. A linear relationship between Ln(X) and $-eV/k_bT_h$ of Pt(80)/BCSO and BCSO under TE and RTE effect conditions at CO₂/H₂=1.

7.2.3 Selectivity of CO₂ Hydrogenation into CO under Thermoelectric

Figure 7-4 displays the CO selectivity as a function of reaction temperature for the four catalysts, namely Pt(80)/BCSO, Pt(15)/BCSO, Pt(NP)/BCSO and bare BCSO only. It was found that all four catalysts were very selective to CO formation over the entire

tested temperature range, above 97% and 87% for 1:1 and 1:4 (CO_2/H_2) gas compositions, respectively. The CO formation is always significantly higher than CH_4 formation, suggesting that hydrogenation of CO_2 into CH_4 is less favourable to occur under the TE effect. Moreover, all four catalysts were more active for the RWGS in the presence of high Seebeck voltages at the hot-surface temperature T_h . This finding clearly confirms the results of C_2H_4 oxidation (Figure 6-5), which demonstrated the increase of TE voltage alone can enhance the reaction rate substantially.

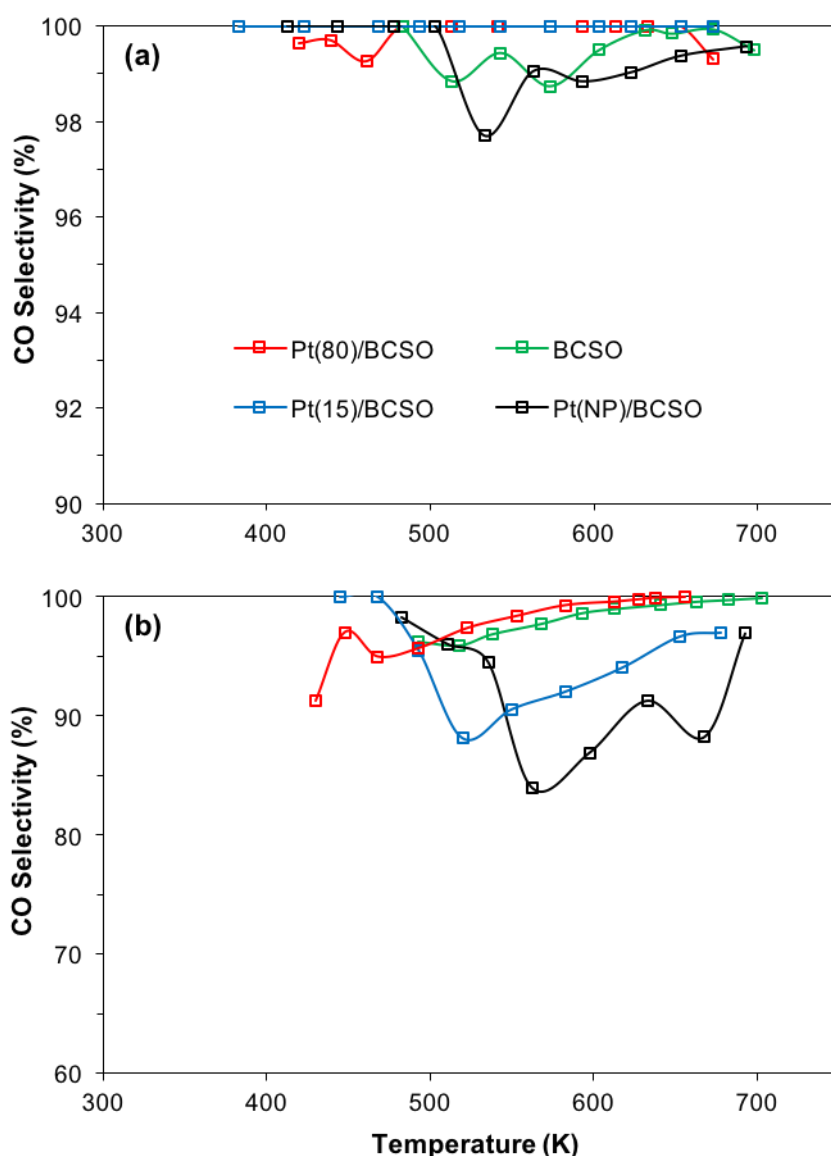


Figure 7-4. CO selectivity as a temperature function of BCSO, Pt(15)BCSO, Pt(80)/BCSO and Pt(NP)/BiCuSeO: (a) $\text{CO}_2/\text{H}_2 = 1$; (b) $\text{CO}_2/\text{H}_2 = 1/4$.

7.2.4 Relationships between Thermoelectric Effect and Catalytic Activity

To further investigate relationships among the temperature, Seebeck voltage, and catalytic activity, the CO₂ reduction reactions were studied for different samples under different gas compositions. Figure 7-5 displays the measured thermoelectric voltages as a function of the temperature gradient ΔT across the sample thickness for four previous samples at the inlet gas ratios of CO₂:H₂ = 1:1 and 1:4. All of the samples had zero voltages when their bottom and top surfaces were at the same (room temperature).

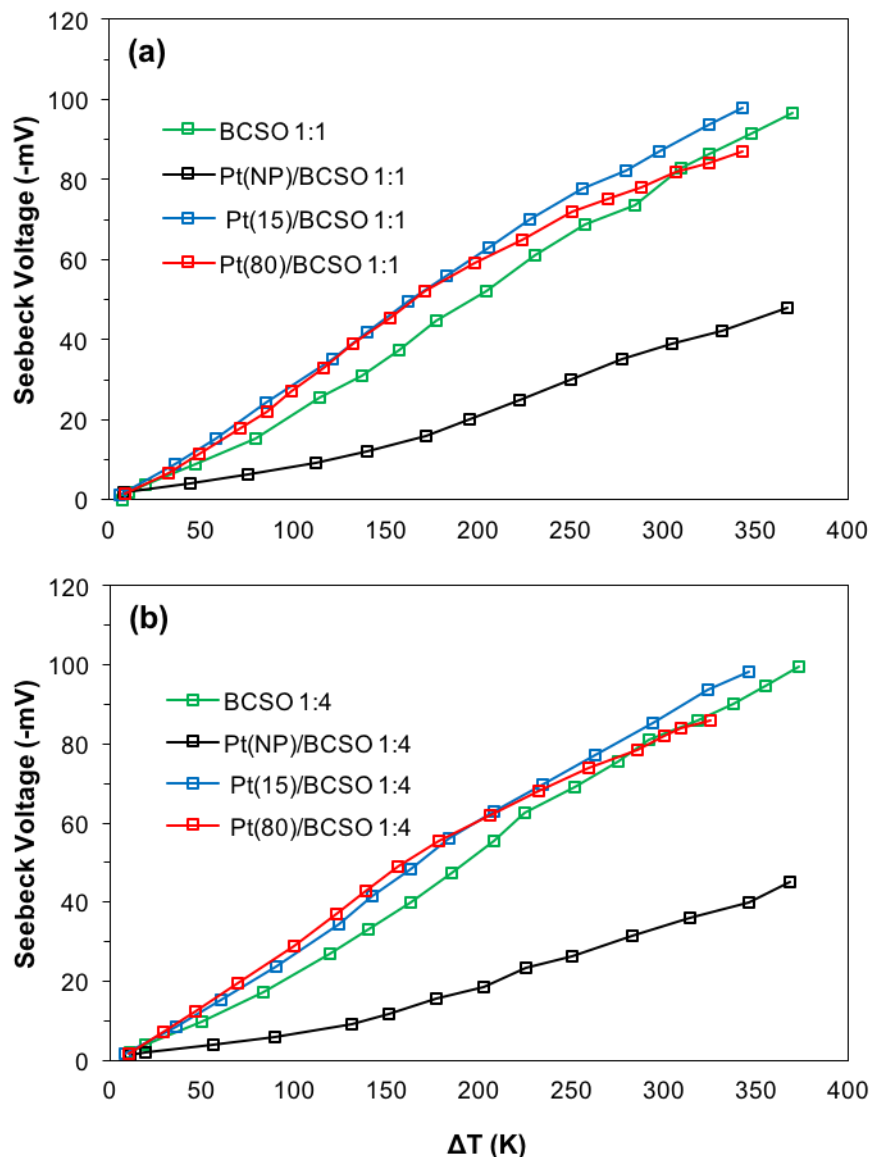


Figure 7-5. Measured thermoelectric voltage as a function of temperature difference across the sample thickness under TE effect of different samples BCSO at gas feed (a) CO₂:H₂ = 1; (b) CO₂:H₂ = 1/4.

The measured voltage for each sample increased linearly with the temperature difference. The linear gradient for Pt(80)/BCSO was 319 $\mu\text{V}/\text{K}$ for $\Delta T < 200\text{K}$, and then decreased with increasing ΔT . The gradients for BCSO and Pt(15)/BCSO were similar, and did not change with the change of the inlet gas compositions. These are typical values for Seebeck coefficient of BCSO (Barreteau *et al.*, 2014; F. Li *et al.*, 2014; Zhao *et al.*, 2014; C. Barreteau, Berardan and Dragoë, 2015).

Note that the Seebeck coefficient of 319 $\mu\text{V}/\text{K}$ here was lower than the values reported in Chapter 4 (Figure 4-9b) for SPS processed material. The main reason was that the BCSO used for catalysis experiments were not densified by SPS, so an inferior Seebeck coefficient was expected. Another reason was that the Seebeck coefficient obtained through the linear gradient here was the average value over a large temperature range, whilst those in Figure 4-9b (Chapter 4) were obtained by changing the temperature over a small range ($\sim 50\text{ K}$ over a 13mm long sample), and the Seebeck coefficient is temperature dependent.

The gradient for the Pt(NP)/BCSO was much lower, at about 136 $\mu\text{V}/\text{K}$, again, it also kept the same value when the inlet gases ratio was changed from 1:1 to 1:4. This much lower Seebeck coefficient was due to the fact that this sample was sintered at a lower temperature (823 K as compared for other BCSO), and there were still some second phase such as Bi_2O_3 and more voids existed in the samples (Figures 6-2f and 6-4). These results demonstrate that the measured voltage was determined by the temperature difference only, was not affected by the gas compositions.

Figure 7-6 shows the CO_2 conversion as a function of the hot-surface temperature T_h for different samples at gas compositions $\text{CO}_2/\text{H}_2 = 1$ and $1/4$. All the samples exhibited a similar trend i.e. the conversion increased with temperature. It can be observed that for the same sample, higher H_2 concentration lead to higher CO_2 conversion. Pt(80)/BCSO catalyst reached 48.4% conversion at 656 K, the highest for all the samples, indicating that the Pt surface had the highest catalytic activity among all these samples. Remarkable, even without any Pt catalyst, the TE material BCSO itself reached a conversion of 41.2% at 703 K.

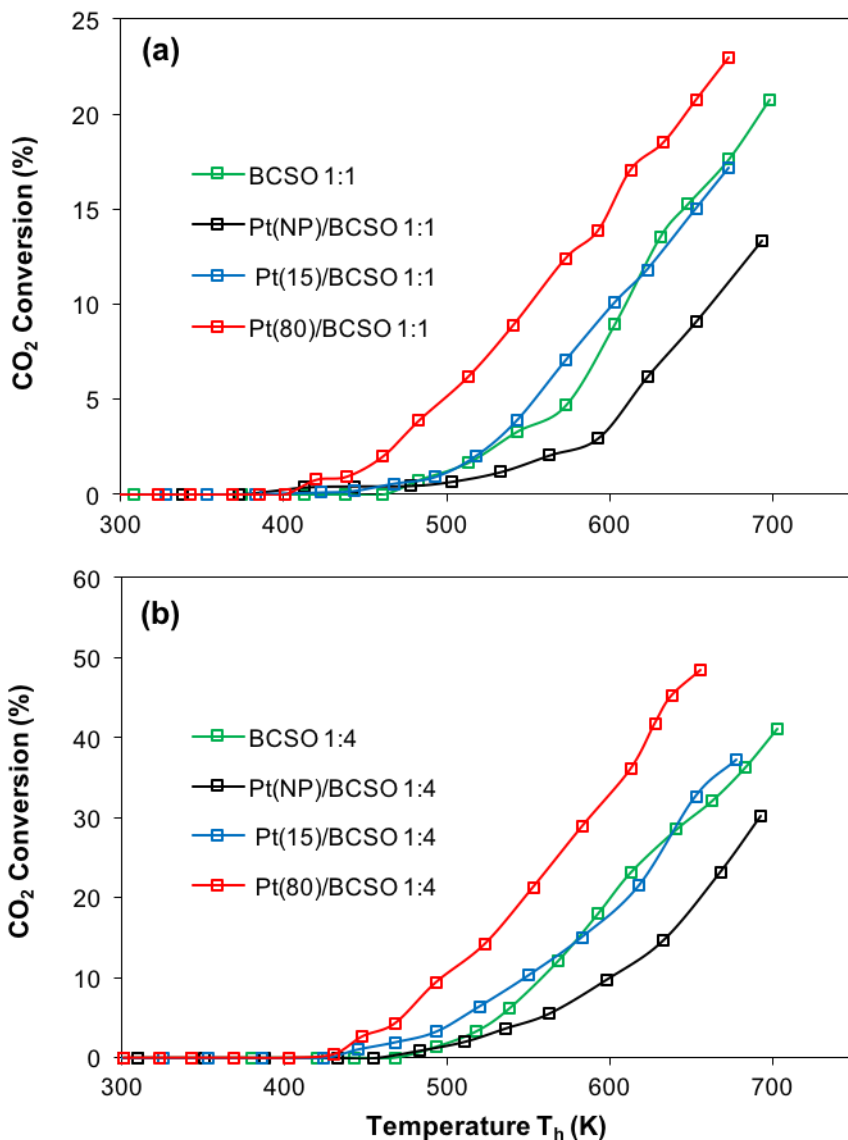


Figure 7-6. Effect of temperature on CO₂ conversion of the four samples under TE effect at gas feed (a) CO₂/H₂ = 1; (b) CO₂/H₂ = 1/4.

Figure 7-7 shows the CO₂ conversion as a function of Seebeck voltage under 1:1 and 1:4 (CO₂:H₂) gas ratios. At 673K, it was found that higher dispersed Pt(NP)/BCSO catalyst had lower CO₂ conversion with lower voltage (– 40 mV), yield to 21.82% CO and 2.74% CH₄. At similar conditions, a higher CO₂ conversion was achieved at higher Seebeck voltages. Take an example of Pt(80)/BCSO, the conversion of CO₂ was 48.41% at the Seebeck voltage of – 86mV, which correspond to 51.15% CO and 0.03% CH₄. Again, the reaction products were found to be CO and CH₄, with the majority (>85%) being CO and higher H₂ concentration in the inlet gases led to lower CO selectivity (see Figure 7-4).

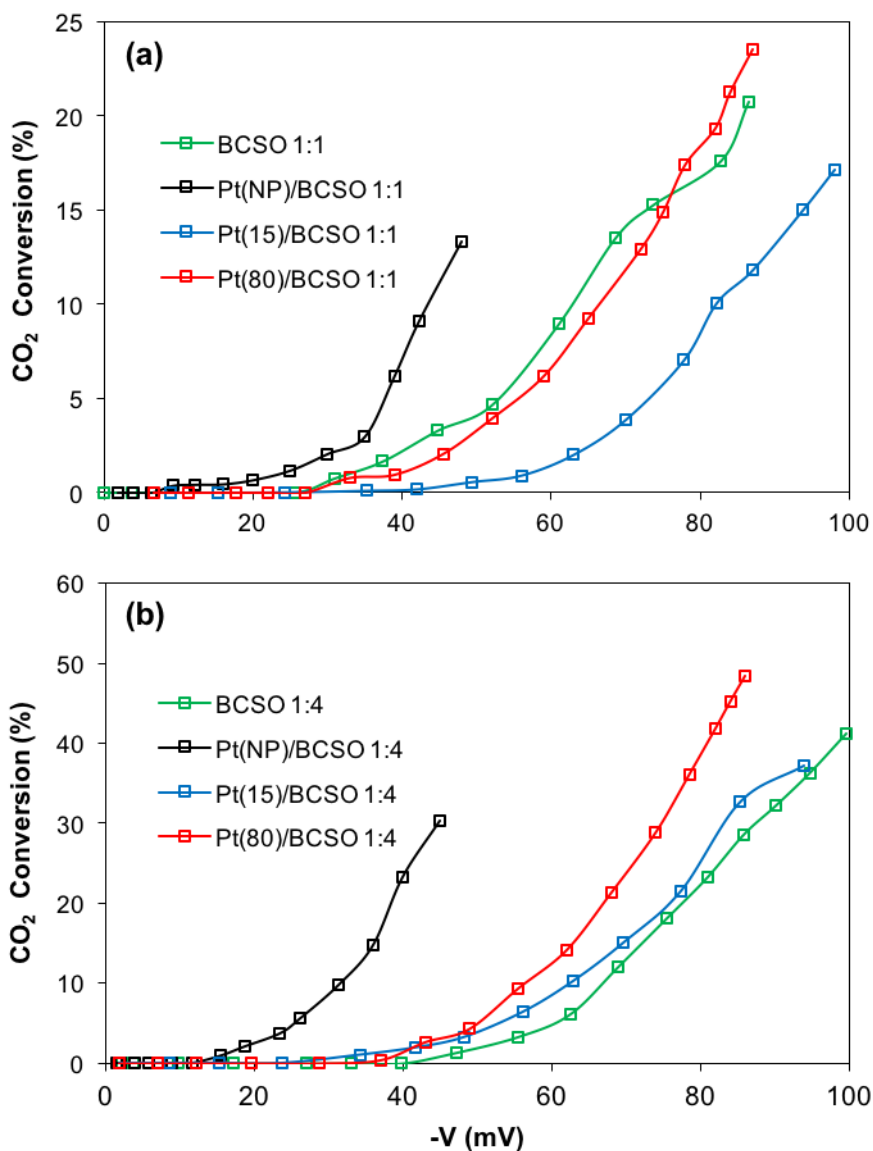


Figure 7-7. The CO₂ conversion proportional to the Seebeck voltage V of the four samples at gas feed (a) CO₂:H₂ = 1; (b) CO₂:H₂ = 4.

Combing these results with the products yield in Figure 7-8, it can be assumed that the CH₄ formation over Pt(NP)/BCSO was enhanced at lower Seebeck voltages as shown in Figure 7-8b. This is clear evidence that the presence of a high Seebeck voltage has a positive effect on catalytic enhancement of RWGS reaction under 1:1 and 1:4 conditions. Literature also demonstrated (NEMCA mechanism) that the CH₄ formation was promoted by applying positive potentials. While on the contrary CO formation was enhanced by applying negative potentials, which reduces the working electrode (due to an excess of electrons) (Gutierrez-Guerra *et al.*, 2015; Kalaitzidou *et al.*, 2015; Makri, Katsaounis and Vayenas, 2015).

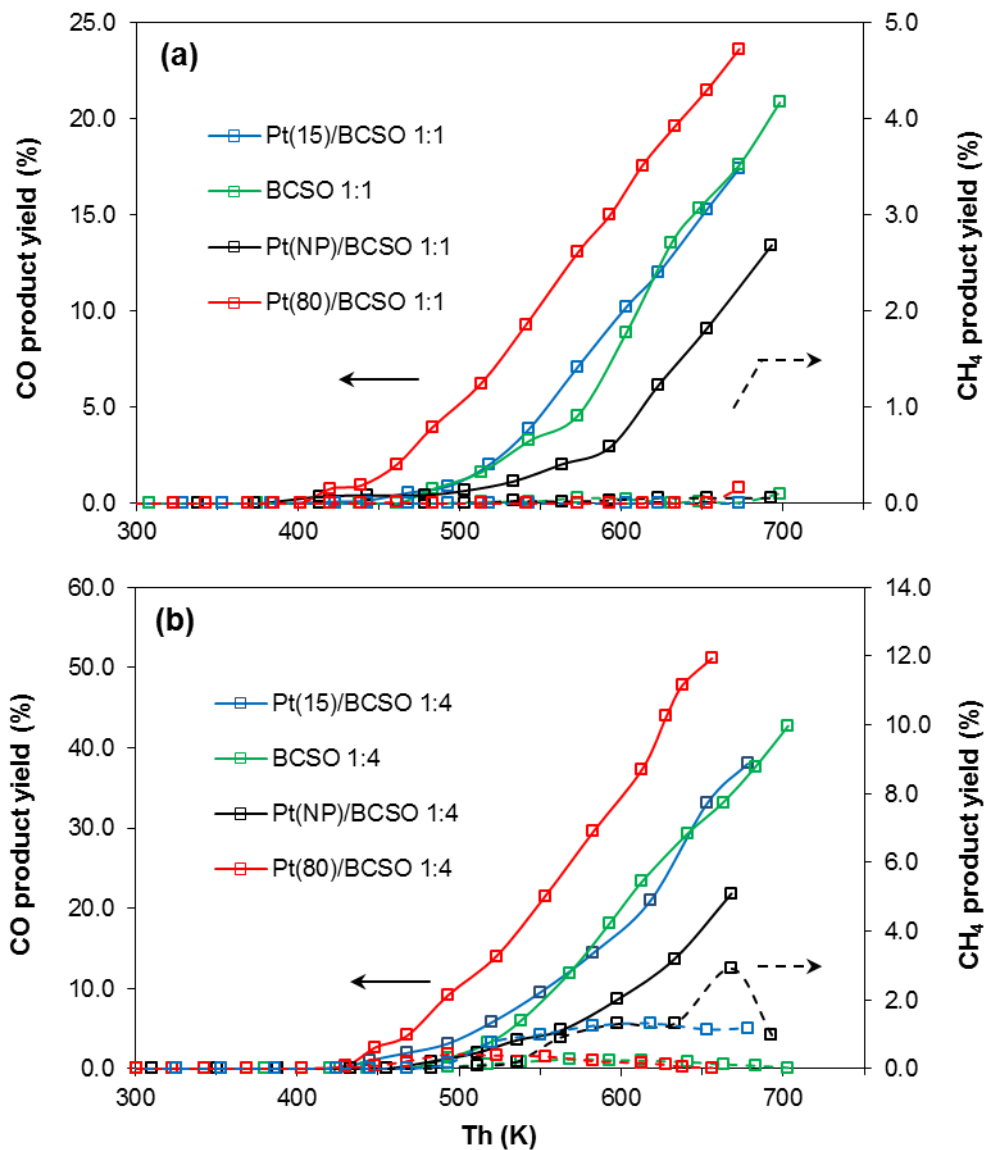


Figure 7-8. CO and CH₄ yields as a function of temperature for BCSO, Pt(15)BCSO, Pt(80)/BCSO and Pt(NP)/BCSO: (a) CO₂:H₂ = 1 and (b) CO₂:H₂ = 1/4.

Excellent linear relationships were observed between $\ln(X)$ and $-eV/k_bT_h$ for all these samples, as shown in Figures 7-3 and 7-9. The best-fit trend line gradients γ were obtained as: 6.6 for BCSO 1:4 and 6.22 for BCSO 1:1 TE, 6.06 for Pt(15)/BCSO 1:4 and 7.46 for Pt(15)/BCSO 1:1, 7.2 for Pt(80)/BCSO 1:1 and 7.15 for Pt(80)/BCSO 1:4, 9.09 for Pt(NP)/BCSO 1:4 and 9.73 for Pt(NP)/BCSO 1:1, 46 for Pt(80)/BCSO 1:1 RTE and 25.4 for BCSO 1:1 RTE. Generally speaking, as can be seen from Figures 7-3

and 7-9, line gradients (γ) had similar values for all the TE conditions and much higher values for the RTE conditions.

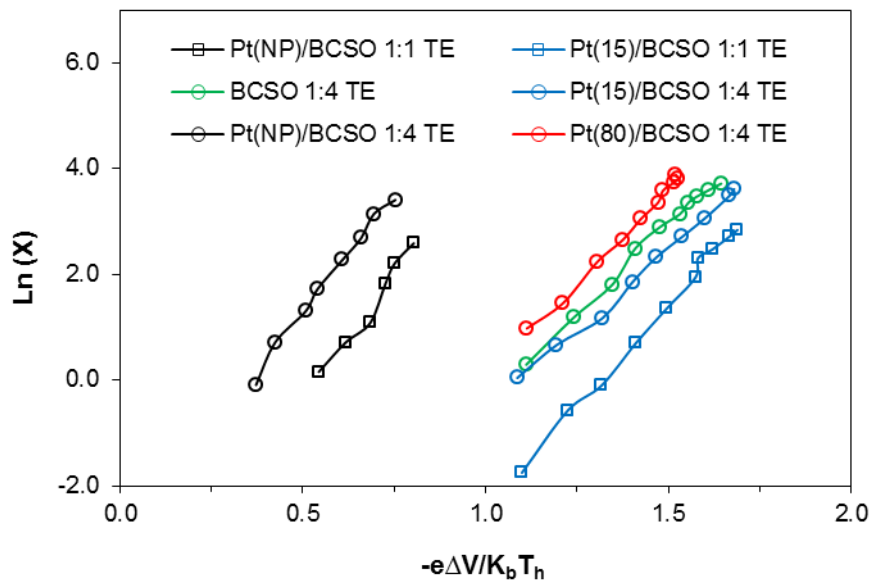


Figure 7-9. A linear relationship between $\ln(r)$ and $-eV/k_bT_h$ under TE condition for BCSO, Pt(15)BCSO, Pt(80)/BCSO and Pt(80)/BCSO with $\text{CO}_2:\text{H}_2 = 1$ and $\text{CO}_2:\text{H}_2 = 1/4$.

Combining the results as shown in Figures 7-3 and 7-9, the relationship can be summarised in eq. 7-1:

$$\ln(X/X_0) = -\gamma eV/K_bT_h \quad \text{Equation 7-1}$$

Here X_0 is the conversion rate when V equals zero, i.e. when $T_c=T_h$. For the p-type TE material BCSO, V at T_h surface is negative, so $-\gamma eV$ is positive and the conversion rate at the hot side T_h could be much higher with a TE voltage than without. Take a data point for Pt(80)/BCSO 1:4, $\gamma = 7.15$, $V = -86$ mV, and $T_h = 656$ K, so $\ln(X/X_0) = -\gamma eV/k_bT_h = 10.88$, and $X/X_0 = 53103$. This means that at 656 K, the conversion rate with a Seebeck voltage of -86 mV was more 53000 times higher than without a Seebeck voltage.

Equation (6-2) can lead to equation (7-1), and vice-verse, if the conversion rate X was proportional to the reaction rate r . This requires that the conversion rate X is much lower than the thermal equilibrium conversion (TEC) of the reactions in equation (3-12) and equation (3-13), so that the backward reactions were negligible. The TECs at

673 K for CO₂ conversion in RWGS reaction without methanation (to CO only) are about 22% and 42% for an inlet gas ratio CO₂/H₂ =1:1 and 1:4 respectively; with methanation, the corresponding values are about 23% and 80% respectively (Unde, 2012; Kharaji, Shariati and Ostadi, 2014; Oshima *et al.*, 2014). Under RTE conditions, the conversion rate was very low; hence, the CO₂ conversion on both Pt(80)/BCSO and BCSO were far away from the TEC, so it was safe to assume that the backward water-gas shift reaction can be ignored and the CO₂ conversion rate X was linearly proportional to the reaction rate r. So for the two cases under RTE conditions, the experimental results confirmed the prediction of equation (6.2).

Figures 7-2 and 7-6 show that at high temperatures around 673K, when there is a high Seebeck voltage, the CO₂ conversion rate reached TEC (22.9% for Pt(80)/BCSO 1:1 TE at 673 K), or just slightly below TEC (17.6% for BCSO 1:1 TE at 673 K, 37.2% for Pt(15)/BCSO 1:4 at 678 K, and 36.3% for BCSO 1:4 at 683 K), even above the TEC (48.4% for Pt(80)/BCSO 1:4 at 656 K) without methanation. For the purpose of comparison, the TEC values for CO₂ conversion in RWGS reactions with and without methanation at CO₂/H₂ ratios 1/1 and 1/4 at 673 K are also presented in Figure 7-7. To the best of our knowledge, 48.4% is the highest reported CO₂ conversion to CO (with 100% CO selectivity) at atmospheric pressure below 673 K with the inlet gas ratio H₂/CO₂ no larger than 4 (Papaioannou *et al.*, 2009; Jiménez *et al.*, 2011; Oshima *et al.*, 2014; Daza and Kuhn, 2016; Gonçalves *et al.*, 2017).

How can the CO₂ conversion to CO exceed the TEC at 673 K? It can be seen from Figure 7-4 that at temperatures T_h > 678 K, the CO selectivity was > 95% for all the samples. Particularly for Pt(80)/BCSO 1:4, the CO selectivity was 100% at 656 K. The CO selectivities observed at these temperatures were also much higher than the predicted under the consideration of thermal equilibrium (Papaioannou *et al.*, 2009; Jiménez *et al.*, 2011; Oshima *et al.*, 2014; Daza and Kuhn, 2016; Gonçalves *et al.*, 2017). These results indicated that the Seebeck voltage promoted the conversion to CO and forward reaction in equation (3-12), hence changed the TEC. This agrees with the observation that an electric field (via the NEMCA mechanism) shifted the chemical equilibrium, increased the RWGS reaction and decreased the water-gas shift reaction (Oshima *et al.*, 2014). With the assist of an electric voltage of 1.6 kV, CO₂ conversion to CO on a Pt/La-ZrO₂ catalyst reached 40.6% with the inlet gas ratio CO₂/H₂ =1:1 at

648K, much higher than the TEC of about 20% without electric field at the temperature (Oshima *et al.*, 2014).

This shifted chemical equilibrium and TEC by the electrochemical energy $-eV$ may also be the reason why the linear relationship was observed in Figures 7-3 and 7-9. Strictly speaking, if the conversion rate is close to the TEC and the backward water-gas-shift reaction cannot be ignored, the conversion rate X is not determined by the reaction rate, eq. 6-2 cannot lead to eq. 7-1, nor can eq. 7-1 lead to eq. 6-2. Nevertheless, a very good linear relationship between $\ln(X)$ and $-\gamma eV/k_bT_h$ is observed for all the samples investigated. The most plausible explanation is that the Seebeck voltage V (or electrochemical energy $-eV$) shifted the reactions in equation (3-12) towards the forward reaction, i.e. the RWGS against the backward water-gas shift reaction. Hence the achieved conversion rate is still far away from the new chemical equilibrium, and equation (7-1) can still be explained by equation (6-2).

Referring to Figures 7-3 and 7-9, all the samples, either bare BSCO, or BCSO with a continuous Pt thin film Pt(80)/BCSO, or BCSO with discontinuous Pt nanoparticles Pt(NP)/BCSO and Pt(15)/BCSO, shows similar CO₂ conversion dependence with the temperature T_h (Figure 7-6) and the Seebeck voltage V (Figure 7-7). The samples with similar high Seebeck voltages at a particular temperature, i.e. BCSO at 1:4, Pt(15) BCSO at 1:1, Pt(15)/BCSO at 1:4, and Pt(80)/BCSO at 1:4, also had similar $\ln(X)$ and $-eV/k_bT_h$ relationships. The sample Pt(NP)/BCSO at 1:1 and 1:4 had the lowest Seebeck voltage and also had a similar $\ln(x)$ and $-eV/k_bT_h$ relationship. This suggests that the Seebeck voltage, not specific surface property, is the most important factor in determining the catalytic activity. This also agrees with the observation that the CO₂ conversion depends on the effect of the electric field stronger than the nature of the catalyst (Oshima *et al.*, 2014). These results also agree with the observations in NEMCA of CO₂ hydrogenation in that a negative (reduced) potential increased the selectivity and reaction rate to CO, and a positive (increased) potential increased the selectivity and reaction rate to CH₄ (Gutierrez-Guerra *et al.*, 2015; Kalaitzidou *et al.*, 2015; Makri, Katsaounis and Vayenas, 2015).

7.2.5 *In-situ* Modification of Catalytic Activity via Seebeck Effect

Combining the above experimental with the data presented in Chapter 6 on the oxidation of ethylene, it can be assumed that the thermoelectric promotion of catalysis

can be understood from the change of Fermi level for TE materials when there is a temperature change, as shown in Chapter 6 (Figure 6-15). At equilibrium, a change of the surface work function lead to an exponential change of chemical reaction (J. Li *et al.*, 2014), so this explains the rate eq. (6-1) in general and eq. (6-2) and eq. (6-3) for the TE materials BCSO, and Pt particles supported on BCSO.

Considering the eq. (6-2) is similar to the rate equation for NEMCA (Vayenas, Bebelis and Ladas, 1990; Vayenas *et al.*, 2001; Vayenas, Brosda and Pliangos, 2003), which is

$$\ln (r/r_o) = \alpha (\Delta\phi - \Delta\phi^* / K_b T) \quad \text{Equation 7-2}$$

where r_o is the open-circuit reaction rate, α and $\Delta\phi^*$ are empirically determined constants, $\Delta\phi$ is the change of work function due to the applied external voltage.

From the theoretical consideration and the experimental results presented, it can be said that both TEPOC and NEMCA are electrochemical promoters of catalysis, through the change of the catalyst work function. However, they differ on the mechanisms used to achieve it. TEPOC achieves the changing of the work function electronically, by the Seebeck effect. On the contrary, NEMCA achieves the changing of work function indirectly, through an induced back spillover of ionic species onto the catalyst surfaces, which form a double layer to affect the energy of electrons in the catalyst particles. In practice, there are several important differences between NEMCA and TEPOC as summarised below:

- (i) No electrolyte nor external voltage are needed in the TEPOC system, whilst for NEMCA, an electrical insulating electrolyte layer is crucial otherwise the back spillover of ionic species cannot happen. In fact, the unusually low thermal conductivity of BCSO has been attributed to its negligible ionic conductivity, so back spillover of ionic species in BCSO is negligible (Vaquero *et al.*, 2015; Zhao and Li, 2016).
- (ii) In TEPOC the catalyst (e.g. Pt) needs not to be continuous, as TE materials are electrically conductive, real catalysts such as nanoparticle catalysts can also be promoted.
- (iii) The constant $|\alpha|$ in NEMCA is smaller than unity, but the constant γ in TEPOC were larger than 1. The fact that $\gamma > 1$ in the rate Eqs. 6-2 to 6-4 for TEPOC

indicates that there is an amplification effect when the extra electrochemical energy eV is used for catalytic chemical reaction, the mechanism for this is not clear yet, but it was speculated that this is related to the increase of the number of electrons available for catalytic reaction with the increasing temperature, as no change of electron density with temperature should mean $\gamma = 1$.

The significant promotional effect of the TE effect when there is a large Seebeck voltage can also be understood from the energy point of view. $-eV/k_bT_h$ can be regarded as the ratio between the extra electrochemical energy induced by thermoelectric effect and the thermal energy of an electron at the reaction surface. At 300K the thermal energy k_bT is 25.9 meV. So, 104 mV of Seebeck voltage gives 104 meV extra electrochemical energy to an electron at the Fermi level, which is equivalent to the thermal energy of an electron at 1200 K, but the 104 mV Seebeck voltage can be generated by a temperature difference of 347 K by a TE material (such as BCSO) with an average Seebeck coefficient of 300 $\mu\text{V}/\text{K}$. So, thermoelectric effect is a very efficient way to enhance the electrochemical energy of an electron at the reaction surface.

7.3 Conclusions

The novel phenomenon of thermoelectric promotion has been investigated and confirmed through the CO_2 hydrogenation to produce CO and CH_4 . These results add evidence to the ethylene oxidation investigation. A very high CO_2 conversion of 48.4% to CO with 100% CO selectivity under atmosphere at temperatures below 673 K with the inlet gas ratio $\text{CO}_2/\text{H}_2 = 1:4$ has been obtained. It was observed in experiments that the catalytic activity of metallic particles supported on the thermoelectric materials, as represented by the CO_2 conversion, can be promoted significantly by a Seebeck voltage generated through a temperature difference across the thickness of a thermoelectric material. Furthermore, the extra electrochemical energy $-eV$, can also change the chemical equilibrium and selectivity of the reaction. Overall, these studies demonstrated the feasibility of using the thermoelectric material to promote non-continuous and highly-dispersed heterogeneous catalysts and enabled the BCSO itself to possess high catalytic activity.

8 Conclusions and Recommendations for Future Work

8.1 Conclusions

In summary, the following objectives have been fulfilled:

- A single-chamber reactor, which is heated by a hot-plate at its bottom and cooled by running water at its cover plate, has been designed, manufactured, and validated to investigate the feasibility of combining thermoelectric energy harvesting and electrochemical promotion of catalysis for a typical heterogeneous catalytic reaction.
- A newly developed experimental system has been assembled, and validated for the investigation of oxidation and reduction reactions. The blank (empty reactor or blank supports) measurements confirmed that the reaction chamber and the blank supports YSZ and γ -Al₂O₃ showed no or negligible catalytic activity for ethylene oxidation. Moreover, the catalytic activity of supported Pt nanoparticles on supports (Pt/YSZ and Pt/ γ -Al₂O₃) showed significant catalytic activity. Thus, total conversion of ethylene has been achieved for both catalysts. Furthermore, the promoting effect of O²⁻ for ethylene oxidation over Pt/YSZ film catalyst was demonstrated in the classical NEMCA system under applied polarisation.
- The development of a high-quality, cost effective, and scalable production of BCSO thermoelectric materials have been achieved using an eco-friendly B₂O₃ flux method. It was found that the flux process can be re-produced with short processing times and performed in air at 923 K with little risk of oxidation. Additionally, the BCSO powder prepared by the flux method further improved the thermoelectric properties as compared to the traditional solid state reaction method. The ZT at 680 K was increased from 0.37 for pristine BiCuSeO to 0.66 for Bi_{0.995}Cs_{0.005}CuSeO, which is about 78 % higher than that of the pristine BCSO.
- Several different catalyst systems, including Pt(80)/BCSO, Pt(15)/BCSO, Pt(NP)/BCSO, Pt(80)/BCSO_{0.9}YSZ_{0.1}, have been prepared using sputtering, impregnation and polyol modified methods. Their phases, microstructures, and chemical compositions have been characterised.

- An innovative use of the thermoelectric materials as a catalyst support and promoter has been investigated through the ethylene C_2H_4 oxidation to produce CO_2 and H_2O . The catalytic activity of Pt nanoparticles supported on the thermoelectric material BCSO can be promoted significantly by a Seebeck voltage generated through a temperature difference across the thickness of the thermoelectric support. It was found that the BCSO itself is catalytically active for ethylene oxidation with a high Seebeck voltage. These are the main findings of this research. It established an innovative approach to enhancing the catalytic activity and open-up a new class of promoters previously unknown in heterogeneous catalysis. This was named thermoelectric promotion of catalysis (TEPOC).
- To further investigate the effect of thermoelectric promotion, the catalytic activity dependence on oxygen and ethylene partial pressure, under fuel-lean and fuel-rich conditions, has also been studied. It has been seen that the rate increased linearly with the O_2 pressure when $O_2/C_2H_4 > 1$, relied on oxygen partial pressure strongly but ethylene pressure weakly. However, under fuel-rich conditions with $C_2H_4/O_2 > 1.4$, at a high Seebeck voltage, C_2H_4 became strongly adsorbed (probably chemisorbed) to the BCSO surface, this blocked the catalyst surface, reducing the catalytic active area, hence the conversion rate became smaller.
- A similar thermoelectric promotional phenomenon has been confirmed for the carbon dioxide hydrogenation reaction. It was found that the catalytic activity of metallic particles supported on thermoelectric materials can be promoted significantly. A very high CO_2 conversion of 48.4% to CO with 100% CO selectivity under atmosphere at temperatures below 673 K with the inlet gas ratio $CO_2/H_2 = 1:4$ has been obtained. This result was above the thermodynamic equilibrium conversion without methanation. It has been suggested that the thermoelectric Seebeck voltage shifted the chemical equilibrium towards the RWGS reaction and CO selectivity.
- In order to support and further confirm the experimental observations, the work function, Fermi level of BCSO and their temperature dependence have been calculated using the first principle method. The work function of the intrinsic BCSO (3.94 eV) was found to be lower than that of the Pt (5.67 eV), which lead to the charge transfer from BCSO to Pt. Moreover, the thermoelectric promotion was

accompanied by a charge transfer from the thermoelectric materials to the metal catalyst on the surface or from the bulk to the surface thermoelectric materials. Therefore, the mechanism based on metal-semiconductor contact theory, or the change of the Fermi level or work function of the surface, has been proposed to interpret this phenomenon of thermoelectric promotion of catalysis (TEPOC).

- It was further observed that there exists a linear relationship between the logarithm of the catalytic activity, and $-eV/k_bT$, which can be regarded as the ratio of extra electrochemical energy ($-eV$) induced by the thermoelectric effect and thermal energy (k_bT) of an electron. This linear relationship is explained as due to the change of work function of the metallic particles at the surface, through the change of its Fermi level induced by the thermoelectric effect.
- At higher temperature gradients or larger Seebeck voltages, the promoted catalytic reaction rate was found to linearly increase with the Seebeck voltage. This has been attributed to the change of rate limiting steps of the relevant chemical reactions, from the intrinsic activation energy limited, to mass transfer limited.
- Comparing the TEPOC and NEMCA, there are several important differences between these two phenomena. (i) no electrolyte nor external voltage are needed in the TEPOC system, whilst for NEMCA, an electrical insulating electrolyte layer is crucial otherwise the back spillover of ionic species cannot happen. (ii) in TEPOC the catalyst (e.g. Pt) need not be continuous, as TE materials are electrically conductive, nanoparticle catalysts can also be promoted. (iii) the constant α in NEMCA is always smaller than unity, but γ values in TEPOC were found to be larger than 1. (iv) TE material itself can be used as a catalyst when there is a large Seebeck voltage. (v) Furthermore, the mechanism for the change of work function at the catalyst surface in TEPOC is different from that in NEMCA. In NEMCA, the external voltage induces the diffusion of ionic species, which forms a double layer on the catalyst surface, and causes the change of the work function. Hence the change of work function $\Delta\phi$ is an indirect consequence of the external voltage V , the linear relationships between $\Delta\phi$ and V is true only under certain conditions and may be sample dependent. In TEPOC, relationship between $\Delta\phi$ and the Seebeck voltage V is directly, linked by the change of Fermi level, not through the formation of a double layer.

In summary, all the objectives of the project have been fulfilled and the aim of the project, i.e., to achieve the self-sustainable, electrochemical promotion of non-continuous nanoparticles catalyst, has been achieved.

8.2 Recommendations for Future Work

- In this study, water cooling was used to set the backside temperature below 373 K. It would be beneficial to decrease further the cooling temperature by introducing liquid nitrogen cooling. In this way, the TEPOC effect can be studied at a temperature as low as 400 K on the hot side of the BCSO.
- Further investigation on different TE materials, which possess a higher Seebeck coefficient, could be performed. Recently, a TE material $\text{NaTaO}_3\text{-Fe}_2\text{O}_3$ with a Seebeck coefficient between 500 and 600 $\mu\text{V/K}$ has been found to be stable up to 1623 K (Wunderlich, Mori and Sologub, 2013), suggesting a temperature difference of less than 200 K across this TE material can enhance the catalytic activity of an electron the same as increasing the temperature to 1200 K.
- Recently, experimental data and kinetic modelling of the catalytic and electrochemical promoted CH_4 oxidation over Pd catalyst-electrodes in the temperature range 573 – 673 K is investigated (Jiménez-Borja *et al.*, 2013). It was reported that the NEMCA has no influence on the kinetic order but on the adsorption of the reactants. Similarly, a fundamental connection between MSI and TEPOC could be investigated through this type of modelling, which could be beneficial in understanding the mechanism in a more efficient way.
- It would be of great interest to investigate the novel application of TEPOC on some complex or realistic industrial reactions, i.e., the reduction of NO_x being one of the main challenges in diesel automotive exhaust emission control. Also, thermal water splitting, water gas shift (WGS), NH_3 decomposition and more catalytic chemical processes should be investigated in the future to demonstrate the wide range of applications for TEPOC.
- Finally, ex-situ and in-situ techniques such as Temperature-Programmed Techniques (TPD), X-ray Photoelectron Spectroscopy (XPS) could provide more useful information about the nature of TEPOC. Furthermore, not only the performance of the catalyst should be improved but it is recommended that the

newly designed reactor to a simpler and compacted system can be improved to obtain the maximum potential.

REFERENCES

- Alam, H. and Ramakrishna, S. (2013) 'A review on the enhancement of figure of merit from bulk to nano-thermoelectric materials', *Nano Energy*, 2(2), pp. 190–212.
- Alcalá, M. D. and Real, C. (2006) 'Synthesis based on the wet impregnation method and characterization of iron and iron oxide-silica nanocomposites', *Solid State Ionics*, 177(9–10), pp. 955–960.
- Altin, E. *et al.* (2015) 'Magnetic and thermoelectric properties of B-substituted NaCoO_2 ', *Applied Physics A: Materials Science and Processing*, 119(3), pp. 1187–1196.
- Amani, M., Tougas, I. and Gregory, O. J. (2012) 'Thermoelectric materials discovery using combinatorial chemistry', *Materials Research Society Symposium Proceedings*, 1315, pp. 1–6.
- Baba, J. *et al.* (1982) 'The Conversion of methanol into hydrocarbons over Dedecatungstophosphoric Acid', *The Chemical Society of Japan*, 55, p. 2555.
- Baba, T. and Ono, Y. (1986) 'Heteropolyacids and their salts supported on acidic ion-exchange resin as highly active solid-acid catalysts', *Applied Catalysis*, 22(2), pp. 321–324.
- Balomenou, S. P. *et al.* (2006) 'Monolithic electrochemically promoted reactors: A step for the practical utilization of electrochemical promotion', *Solid State Ionics*, 177, pp. 2201–2204.
- Baran, J. D. *et al.* (2015) 'Tuning Thermoelectric Properties of Misfit Layered Cobaltites by Chemically Induced Strain', *The Journal of Physical Chemistry C*, 119(38), pp. 21818–21827.
- Baranova, E. *et al.* (2010) 'Formic acid electro-oxidation on carbon supported $\text{Pd}_x\text{Pt}_{1-x}$ ($0 \leq x \leq 1$) nanoparticles synthesized via modified polyol method', *Electrochimica Acta*, 55(27), pp. 8182–8188.
- Baranova, E. A. *et al.* (2010) 'Single-step polyol synthesis of alloy Pt_7Sn_3 versus bi-phase Pt/SnO_x nano-catalysts of controlled size for ethanol electro-oxidation', *Journal of Applied Electrochemistry*, 40(10), pp. 1767–1777.

Barreteau, C. *et al.* (2012) 'Structural and Electronic Transport Properties in Sr-Doped BiCuSeO', *Chemistry of Materials*, 24, pp. 3168–3178.

Barreteau, C. *et al.* (2014) 'Layered oxychalcogenide in the Bi–Cu–O–Se system as good thermoelectric materials', *Semiconductor Science and Technology*, 29(6), p. 64001.

Barreteau, C., Berardan, D. and Dragoe, N. (2015) 'Studies on the thermal stability of BiCuSeO', *Journal of Solid State Chemistry*, 222, pp. 53–59.

Barreteau, Berardan, D. and Dragoe, N. (2015) 'Studies on the thermal stability of BiCuSeO', *Journal of Solid State Chemistry*, 222, pp. 53–59.

Bebelis, S. and Vayenas, C. G. (1989) 'Non-faradaic electrochemical modification of catalytic activity: 1. The case of ethylene oxidation on Pt', *Journal of Catalysis*, 118(1), pp. 125–146.

Bebelis, S. and Vayenas, C. G. (1989) 'Non-faradaic electrochemical modification of catalytic activity. 1. The case of ethylene oxidation on Pt', *Journal of Catalysis*, 118(1), pp. 125–146.

Bécue, T., Davis, R. J. and Garces, J. M. (1998) 'Effect of Cationic Promoters on the Kinetics of Ammonia Synthesis Catalyzed by Ruthenium Supported on Zeolite X', *Journal of Catalysis*, 179(1), pp. 129–137.

Birkholz, U., Fettig, R. and Rosenzweig, J. (1987) 'Fast semiconductor thermoelectric devices', *Sensors and Actuators*, 12(2), pp. 179–184.

Bishop, K. A. *et al.* (2015) 'Is there potential to adapt soybean (*Glycine max* Merr.) to future [CO₂]? An analysis of the yield response of 18 genotypes in free-air CO₂ enrichment', *Plant, Cell and Environment*, 38(9), pp. 1765–1774.

Blatt, F. J. *et al.* (1976) *POWER OF METALS POWER OF METALS*.

Bobev, S. and Sevov, S. C. (2002) 'Naked Clusters of 56 Tin Atoms in the Solid State', *Journal of the American Chemical Society*. American Chemical Society, 124(13), pp. 3359–3365.

Bock, C. *et al.* (2004) 'Size-selected synthesis of PtRu nano-catalysts: Reaction and size control mechanism', *Journal of the American Chemical Society*, 126(25), pp.

8028–8037.

Bockris, J. O. and Minevski, Z. S. (1994) 'Electrocatalysis: past, present and future', *Electrochimica Acta*, 39(11–12), pp. 1471–1479.

Boudart, M. (1969) 'Catalysis by Supported Metals', *Advances in Catalysis*, 20, pp. 153–166.

Brophy, J. J. (1990) *Basic Electronics for Scientists and Engineers*. New York: McGraw-Hill.

Bruix, A. *et al.* (2012) 'A new type of strong metal-support interaction and the production of H₂ through the transformation of water on Pt/CeO₂(111) and Pt/CeO_x/TiO₂(110) catalysts', *Journal of the American Chemical Society*. Elsevier B.V., 134, pp. 8968–8974.

Bulusu, A. and Walker, D. G. (2008) 'Review of electronic transport models for thermoelectric materials', *Superlattices and Microstructures*, 44(1), pp. 1–36.

Caballero-Calero, O. and Martín-González, M. (2016) 'Thermoelectric nanowires: A brief prospective', *Scripta Materialia*, pp. 54–57.

Cai, W. *et al.* (2012) 'Oxidative steam reforming of ethanol over Ir/CeO₂ catalysts: A structure sensitivity analysis', *Journal of Catalysis*. Elsevier Inc., 286, pp. 137–152.

Callaway, J. (1961) 'Low-temperature lattice thermal conductivity', *Physical Review*, 122(3).

Callaway, J. and Von Baeyer, H. C. (1960) 'Effect of point imperfections on lattice thermal conductivity', *Physical Review*, 120(4).

Campbell, C. T. (2012) 'Catalyst–support interactions: Electronic perturbations', *Nature Chemistry*. Nature Publishing Group, 4(8), pp. 597–598.

Carlsson, M. (2015) 'Carbon Formation in Steam Reforming and Effect of Potassium Promotion', (4), pp. 313–318.

Chasmar, R. P. and Stratton, R. (1959) 'The Thermoelectric Figure of Merit and its Relation to Thermoelectric Generators†', *Journal of Electronics and Control*, 7(1), pp. 52–72.

Chinta, S. Thorman, J. (2013) 'Reactors and processes for the oxidative coupling of hydrocarbons'. US Patent 0142707 A1.

Das, D. *et al.* (2016) 'Tuning of thermoelectric properties with changing Se content in Sb_2Te_3 ', *European Physical Letters*, 13, p. 4.

Das, S. *et al.* (2016) 'Thermoelectric properties of Sn doped BiCuSeO ', *Applied Surface Science*.

Daza, Y. and Kuhn, J. N. (2016) 'CO₂ conversion by reverse water gas shift catalysis: Comparison of catalysts and mechanisms and their consequences for CO₂ conversion to liquid fuels', *RSC Adv. Royal Society of Chemistry*, 6, pp. 49675–49691.

Delmon, B. and Froment, G. F. (1996) 'Remote control of catalytic sites by spillover species: A chemical reaction engineering approach', *Catalysis Reviews - Science and Engineering*, 38(1), pp. 69–100.

Derouane, E. G. (1990) 'Principles of catalyst development', *Journal of Molecular Catalysis*, 60(1), p. 138.

Desborough, G. A. *et al.* (2000) *Low temperature volatilization of selenium from rock samples of the phosphoria formation on southeastern Idaho*. U.S. Dept. of the Interior, U.S. Geological Survey,.

Dole, H. A. E. *et al.* (2014) 'Electrochemically enhanced metal-support interaction of highly dispersed Ru nanoparticles with a CeO_2 support', *Journal of Catalysis*, 318, pp. 85–94.

Dorado, F. *et al.* (2007) 'Electrochemical promotion of platinum impregnated catalyst for the selective catalytic reduction of NO by propene in presence of oxygen', *Applied Catalysis B: Environmental*, 73(1–2), pp. 42–50.

Dughaish, Z. H. (2002) 'Lead telluride as a thermoelectric material for thermoelectric power generation', *Physica B: Condensed Matter*, 322(1–2), pp. 205–223.

Eley, D. D. and Rideal, E. K. (1941) 'The catalysis of the parahydrogen conversion by tungsten', *The Royal Society Publishing*, 178(975).

Enescu, D. and Virjoghe, E. O. (2014) 'A review on thermoelectric cooling parameters and performance', *Renewable and Sustainable Energy Reviews*, pp. 903–916.

Ertl, G., Knözinger, H. and Weitkamp, J. (1997) *Handbook of Heterogeneous Catalysis*. Wiley-VCH.

Ertl, G., Lee, S. B. and Weiss, M. (1982) 'Adsorption of nitrogen on potassium promoted Fe(111) and (100) surfaces', *Surface Science*, 114(2), pp. 527–545.

Fagherazzi, G. *et al.* (1972) 'Structural study of the Al₂O₃-promoted ammonia synthesis catalyst: II. Reduced state', *Journal of Catalysis*, 26(3), pp. 344–347.

Foo, M. L. *et al.* (2004) 'Charge Ordering, Commensurability, and Metallicity in the Phase Diagram of the Layered Na_xCoO₂', *Physical Review Letters*, 92(24), p. 247001.

Fortunato, M. A. *et al.* (2011) 'Dispersion measurement of platinum supported on Ytria-Stabilised Zirconia by pulse H₂ chemisorption', *Applied Catalysis A: General*, 403(1–2), pp. 18–24.

Fujishiro, Y. *et al.* (2005) 'Characterization of Thermoelectric Metal Oxide Elements Prepared by the Pulse Electric-Current Sintering Method', *Journal of the American Ceramic Society*, 87(10), pp. 1890–1894.

Goddard, J. D. (2011) 'On the thermoelectricity of W. Thomson: Towards a theory of thermoelastic conductors', *Journal of Elasticity*, 104(1–2), pp. 267–280.

Gonçalves, R. V. *et al.* (2017) 'Selective hydrogenation of CO₂ into CO on a highly dispersed nickel catalyst obtained by magnetron sputtering deposition: A step towards liquid fuels', *Applied Catalysis B: Environmental*, 209, pp. 240–246.

Goodman, D. W. (1995) 'Model Studies in Catalysis Using Surface Science Probes', *Chemical Reviews*, 95(3), pp. 523–536.

Gutierrez-Guerra, N. *et al.* (2015) 'Electrochemical activation of Ni catalysts with potassium ionic conductors for CO₂ hydrogenation', *Topics in Catalysis*, 58(18), pp. 1256–1269.

Hagen, J. (2006) *Industrial Catalysis*. Wiley-VCH.

Haller, G. L. and Resasco, D. E. (1989) 'Metal–Support Interaction: Group VIII Metals and Reducible Oxides', in, pp. 173–235.

Hamid Elsheikh, M. *et al.* (2014) 'A review on thermoelectric renewable energy:

Principle parameters that affect their performance', *Renewable and Sustainable Energy Reviews*, pp. 337–355.

Hammad, A. *et al.* (2011) 'Electrochemical promotion of the SO₂ oxidation over thin Pt films interfaced with YSZ in a monolithic electropromoted reactor', *Applied Catalysis B: Environmental*, 103(3–4), pp. 336–342.

Han, C. *et al.* (2016) 'Thermoelectric Enhancement of Different Kinds of Metal Chalcogenides', *Advanced Energy Materials*, 6(15).

Harkness, I. . R. *et al.* (1996) 'Ethylene oxidation over platinum: In situ electrochemically controlled promotion using Na-beta" alumina and studies with a Pt(111)/Na model catalyst', *Journal of Catalysis*, 160(1), pp. 19–26.

Harman, T. C. *et al.* (2002) 'Quantum dot superlattice thermoelectric materials and devices.', *Science (New York, N.Y.)*, 297(5590), pp. 2229–32.

Haruta, M. (2002) 'Catalysis of Gold Nanoparticles Deposited on Metal Oxides', *CATTECH*, 6(3), pp. 102–115.

He, C., Yu, Y., Shen, Q., *et al.* (2014) 'Catalytic behavior and synergistic effect of nanostructured mesoporous CuO-MnO_x-CeO₂ catalysts for chlorobenzene destruction', *Applied Surface Science*. Elsevier B.V., 297, pp. 59–69.

He, C., Yu, Y., Yue, L., *et al.* (2014) 'Low-temperature removal of toluene and propanal over highly active mesoporous CuCeO_x catalysts synthesized via a simple self-precipitation protocol', *Applied Catalysis B: Environmental*, 147, pp. 156–166.

Hereijgers, B. P. C. and Weckhuysen, B. M. (2009) 'Selective Oxidation of Methanol to Hydrogen over Gold Catalysts Promoted by Alkaline-Earth-Metal and Lanthanum Oxides', *ChemSusChem*, 2(8), pp. 743–748.

Hinshelwood, C. N. (1926) 'The Kinetics of Chemical Change in Gaseous Systems.', *Oxford Press*, p. 390.

Hollingsworth, N. *et al.* (2015) 'CO₂ capture and electrochemical conversion using superbasic [P 66614][124Triz]', *Faraday Discuss.*, 183, pp. 389–400.

Hölzl, J. and Schulte, F. K. (1979) 'Work function of metals', in *Solid Surface Physics*. Berlin, Heidelberg, pp. 1–150.

Hsu, K. F. *et al.* (2004) 'Cubic AgPbmSbTe_{2+m}: Bulk Thermoelectric Materials with High Figure of Merit', *Science mag*, pp. 818–821.

Hu, B., Guild, C. and Suib, S. L. (2013) 'Thermal, electrochemical, and photochemical conversion of CO₂ to fuels and value-added products', *Journal of CO₂ Utilization*, 1, pp. 18–27.

Huang, H. *et al.* (2012) 'A kinetic model for analyzing partial oxidation reforming of heavy hydrocarbon over a novel self-sustained electrochemical promotion catalyst', *The 2011 Asian Bio-Hydrogen and Biorefinery Symposium (2011ABBS)*, 37(20), pp. 15125–15134.

Huang, T.-J., Hsu, S.-H. and Wu, C.-Y. (2012) 'Simultaneous NO_x and Hydrocarbon Emissions Control for Lean-Burn Engines Using Low-Temperature Solid Oxide Fuel Cell at Open Circuit', *Environmental science & technology*, 46(4), pp. 2324–2329.

Huazhang, L. and Xiaonian, L. (2000) 'Precursor of iron catalyst for ammonia synthesis: Fe₃O₄, Fe_{1-x}O, Fe₂O₃ or their mixture?', in *12th International Congress on Catalysis*, pp. 2207–2212.

Ibrahim, N., Poulidi, D. and Metcalfe, I. S. (2013) 'The role of sodium surface species on electrochemical promotion of catalysis in a Pt/YSZ system: The case of ethylene oxidation', *Journal of Catalysis*, 303, pp. 100–109.

Ioannides, T. and Verykios, X. E. (1996) 'Charge transfer in metal catalysts supported on doped TiO₂: A theoretical approach based on metal-semiconductor contact theory', *Journal of Catalysis*, 161(2), pp. 560–569.

Isaifan, R. J. (2014) *Self-induced Electrochemical Promotion of Noble Metal Nanoparticles for Environmentally Important Reaction Systems*. PhD Thesis. University of Ottawa.

Jhong, H. R. M., Ma, S. and Kenis, P. J. (2013) 'Electrochemical conversion of CO₂ to useful chemicals: Current status, remaining challenges, and future opportunities', *Current Opinion in Chemical Engineering*, 2(2), pp. 191–199.

Jiménez-Borja, C. *et al.* (2013) 'Experimental data and kinetic modeling of the catalytic and electrochemically promoted CH₄ oxidation over Pd catalyst-electrodes', *Chemical Engineering Journal*, 225, pp. 315–322.

Jiménez, V. *et al.* (2011) 'Electrochemical promotion of the CO₂ hydrogenation reaction on composite ni or ru impregnated carbon nanofiber catalyst-electrodes deposited on YSZ', *Applied Catalysis B: Environmental*, 107(1–2), pp. 210–220.

Jood, P. *et al.* (2011) 'Al-doped zinc oxide nanocomposites with enhanced thermoelectric properties', *Nano Lett*, 11(10), pp. 4337–4342.

Joshi, G. *et al.* (2008) 'Enhanced Thermoelectric Figure-of-Merit in Nanostructured p-type Silicon Germanium Bulk Alloys', *Nano Letters*. American Chemical Society, 8(12), pp. 4670–4674.

Jothimurugesan, K. *et al.* (1985) 'Role of rhenium in Pt-Re-Al₂O₃ reforming catalysis—An integrated study', *AIChE Journal*, 31(12), pp. 1997–2007.

Kaiser, P. *et al.* (2013) 'Production of liquid hydrocarbons with CO₂ as carbon source based on reverse water-gas shift and fischer-tropsch synthesis', *Chemie-Ingenieur-Technik*, 85(4), pp. 489–499.

Kalaitzidou, I. *et al.* (2015) 'Electrochemical promotion of the hydrogenation of CO₂ on Ru deposited on a BZY proton conductor', *Journal of Catalysis*, 331, pp. 98–109.

Kambolis, A. *et al.* (2012) 'Electrochemical promotion of catalysis with highly dispersed Pt nanoparticles', *Electrochemistry Communications*, 19(1), pp. 5–8.

Kasap, S. (2001) *Thermoelectric Effects in Metals: Thermocouples*.

Katsaounis, A. (2008) 'Electrochemical promotion of catalysis (EPOC) perspectives for application to gas emissions treatment', *Global Nest Journal*, 10(2), pp. 226–236.

Katsaounis, A. (2010) 'Recent developments and trends in the electrochemical promotion of catalysis (EPOC)', *Journal of Applied Electrochemistry*, 40(5), pp. 885–902.

Kharaji, A. G., Shariati, A. and Ostadi, M. (2014) 'Development of Ni-Mo/Al₂O₃ catalyst for reverse water gas shift (RWGS) reaction.', *Journal of nanoscience and nanotechnology*. United States, 14(9), pp. 6841–6847.

Konsolakis, M. *et al.* (2000) 'Strong Promotion by Na of Pt/ β -Al₂O₃ Catalysts Operated under Simulated Exhaust Conditions', *Journal of Catalysis*, 193(2), pp. 330–337.

- Konsolakis, M. and Yentekakis, I. V (2001) 'The Reduction of NO by Propene over Ba-Promoted Pt/ γ -Al₂O₃ Catalysts', *Journal of Catalysis*, 198(1), pp. 142–150.
- Kotarba, A. *et al.* (2004) 'Modification of Electronic Properties of Mo₂C Catalyst by Potassium Doping: Impact on the Reactivity in Hydrodenitrogenation Reaction of Indole', *The Journal of Physical Chemistry B*, 108(9), pp. 2885–2892.
- Koumoto, K. *et al.* (2013) 'Thermoelectric ceramics for energy harvesting', *Journal of the American Ceramic Society*, 96(1), pp. 1–23.
- Kresse, G. and Furthmüller, J. (1996) 'Efficient iterative schemes for ab initio total-energy calculations using a plane-wave basis set', *Phys. Rev. B. American Physical Society*, 54(16), pp. 11169–11186.
- Lan, J.-L. *et al.* (2013) 'Enhanced thermoelectric properties of Pb-doped BiCuSeO ceramics', *Advanced Materials*, 25(36), pp. 5086–5090.
- Langmuir, I. (1918) 'The Adsorption of Gases on Plane Surfaces of Glass, Mica and Platinum', *Journal of the American Chemical Society*, 40(9), pp. 1361–1403.
- Langmuir, I. (1922) 'The mechanism of the catalytic action of platinum in the reactions 2CO+O₂=2CO₂ and 2H₂+O₂=2H₂O.', *Transactions of the Faraday Society*, 17, pp. 621–654.
- LeBlanc, S. *et al.* (2014) 'Material and manufacturing cost considerations for thermoelectrics', *Renewable and Sustainable Energy Reviews*, 32, pp. 313–327.
- Li, F. *et al.* (2012) 'Polycrystalline BiCuSeO oxide as a potential thermoelectric material', *Energy and Environmental Science*, 5(5), pp. 7188–7195.
- Li, F. *et al.* (2013) 'Enhanced thermoelectric performance of Ca-doped BiCuSeO in a wide temperature range', *Journal of Materials Chemistry A*, 1(38), pp. 11942–11949.
- Li, F. *et al.* (2014) 'Thermal stability and oxidation resistance of BiCuSeO based thermoelectric ceramics', *Journal of Alloys and Compounds*, 614, pp. 394–400.
- Li, J., Sui, J., Pei, Y., *et al.* (2012) 'A high thermoelectric figure of merit ZT > 1 in Ba heavily doped BiCuSeO oxyselenides', *Energy & Environmental Science*, 5(9), p. 8543.

- Li, J., Sui, J., Barreteau, C., *et al.* (2012) 'Thermoelectric properties of Mg doped p - type BiCuSeO oxyselenides', *Journal of Alloys and Compounds*.
- Li, J. *et al.* (2014) 'The roles of Na doping in BiCuSeO oxyselenides as a thermoelectric material', *Journal of Materials Chemistry A*, 2(14), p. 4903.
- Li, W. C., Comotti, M. and Schüth, F. (2006) 'Highly reproducible syntheses of active Au/TiO₂ catalysts for CO oxidation by deposition-precipitation or impregnation', *Journal of Catalysis*, 237(1), pp. 190–196.
- Lin, S. *et al.* (2014) 'Redox behavior of active PdO_x species on (Ce,Zr)_xO₂-Al₂O₃ mixed oxides and its influence on the three-way catalytic performance', *Chemical Engineering Journal*, 247, pp. 42–49.
- Liu, H. *et al.* (2013) 'Mechanical relaxation in thermoelectric oxide Ca_{3-x}Sr_xCo₄O₉₊ (x=0, 0.25, 0.5, 1.0) associated with oxygen vacancies', *Journal of Solid State Chemistry*, 200, pp. 305–309.
- Liu, W. *et al.* (2012) 'Recent advances in thermoelectric nanocomposites', *Nano Energy*, 1(1), pp. 42–56.
- Liu, Y. *et al.* (2014) 'Thermoelectric properties of Ni doped p-type BiCuSeO oxyselenides', *Key Engineering Materials*, 602–603, pp. 906–909.
- Liu, Y. *et al.* (2016) 'Synergistically Optimizing Electrical and Thermal Transport Properties of BiCuSeO via a Dual-Doping Approach', *Advanced Energy Materials*, 6(9).
- De Lucas-Consuegra, A., González-Cobos, J., Gacia-Rodriguez, Y., *et al.* (2012) 'Electrochemical activation of the catalytic methanol reforming reaction for H₂ production', *Electrochemistry Communications*, 19(1), pp. 55–58.
- De Lucas-Consuegra, A., González-Cobos, J., García-Rodríguez, Y., *et al.* (2012) 'Enhancing the catalytic activity and selectivity of the partial oxidation of methanol by electrochemical promotion', *Journal of Catalysis*, 293, pp. 149–157.
- M. N. Tsampas, F. M. S. and P. V. (2015) 'Applications of yttria stabilized zirconia (YSZ) in catalysis', *Catalysis Science & Technology*. Royal Society of Chemistry, 5, pp. 4884–4900.

- Madre, M. A. *et al.* (2013) 'Preparation of high-performance $\text{Ca}_3\text{Co}_4\text{O}_9$ thermoelectric ceramics produced by a new two-step method', *Journal of the European Ceramic Society*, 33(10), pp. 1747–1754.
- Makri, M., Katsaounis, A. and Vayenas, C. G. (2015) 'Electrochemical promotion of CO_2 hydrogenation on Ru catalyst-electrodes supported on a $\text{K-}\beta\text{-Al}_2\text{O}_3$ solid electrolyte', *Electrochimica Acta*, 179, pp. 556–564.
- Martin, J., Tritt, T. and Uher, C. (2010) 'High temperature Seebeck coefficient metrology', *Journal of Applied Physics*, 108(12).
- Marwood, M. and Vayenas, C. G. (1998) 'Electrochemical Promotion of a Dispersed Platinum Catalyst', *Journal of Catalysis*, 178(2), pp. 429–440.
- Matsubu, J. C. *et al.* (2016) 'Interactions in oxide-supported Rh catalysts', *Nature Chemistry*, 9, pp. 120–127.
- McClure, S. M., Lundwall, M. J. and Goodman, D. W. (2011) 'Planar oxide supported rhodium nanoparticles as model catalysts.', *Proceedings of the National Academy of Sciences of the United States of America*, 108(3), pp. 931–6.
- Mériaudeau, P. *et al.* (1982) 'Metal-support interaction. Catalytic properties of TiO_2 -supported platinum, iridium, and rhodium', *Journal of Catalysis*, 75(2), pp. 243–250.
- Metcalfe, I. S. (2001) 'Electrochemical Promotion of Catalysis: II: The Role of a Stable Spillover Species and Prediction of Reaction Rate Modification', *Journal of Catalysis*, 199(2), pp. 259–272.
- Mihaiu, S. *et al.* (2015) 'Advanced ceramics in the $\text{SnO}_2\text{-ZnO}$ binary system', *Ceramics International*, 41, pp. 4936–4945.
- Minami, T. *et al.* (1998) 'New transparent conducting $\text{ZnO-In}_2\text{O}_3\text{-SnO}_2$ thin films prepared by magnetron sputtering', *Thin Solid Films*, 317(1–2), pp. 318–321.
- Mitsui, T. *et al.* (2008a) 'Support effect on complete oxidation of volatile organic compounds over Ru catalysts', *Applied Catalysis B: Environmental*, 81(1), pp. 56–63.
- Mitsui, T. *et al.* (2008b) 'Support effect on complete oxidation of volatile organic compounds over Ru catalysts', *Applied Catalysis B: Environmental*, 81(1–2), pp. 56–63.

- Morales, A. and de Agudelo, M. M. R. (1986) 'Promoter role of octahedral Co (and Ni) in modified Co(Ni)Mo-Al₂O₃ catalysts for hydrodesulfurization reactions', *Applied Catalysis*, 23(1), pp. 23–34.
- Muta, H. *et al.* (2006) 'Substitution Effect on Thermoelectric Properties of ZrNiSn Based Half-Heusler Compounds', 47(6), pp. 1453–1457.
- Nag, A. and Shubha, V. (2014) 'Oxide thermoelectric materials: A structure-property relationship', *Journal of Electronic Materials*, 43(4), pp. 962–977.
- Nagaraju, P. *et al.* (2008) 'Preparation, characterization and catalytic properties of promoted vanadium phosphate catalysts', *Catalysis Communications*, 9(14), pp. 2449–2454.
- Nicole, J. *et al.* (1997) 'Activation of Catalyst for Gas-Phase Combustion by Electrochemical Pretreatment', *Journal of The Electrochemical Society*, 144(12), pp. L312–L314.
- Nicole, J. *et al.* (2001) 'Electrochemical Promotion and Metal–Support Interactions', *Journal of Catalysis*, 204(1), pp. 23–34.
- Nicole, J. and Comninellis, C. H. (1998) 'Electrochemical promotion of IrO₂ catalyst activity for the gas phase combustion of ethylene', *Journal of Applied Electrochemistry*, 28, pp. 223–226.
- Niemantsverdriet, J. W. (2007) *Spectroscopy in Catalysis: An Introduction*. Wiley-VCH.
- Nolas, G. S. *et al.* (1998) 'Semiconducting Ge clathrates: Promising candidates for thermoelectric applications', *Applied Physics Letters*. American Institute of Physics, 73(2), pp. 178–180.
- Nordström, L. and Singh, D. J. (1996) 'Electronic structure of Ce-filled skutterudites', *Physical Review B*, 53(3), pp. 1103–1108.
- Olah, G. A., Goeppert, A. and Prakash, G. K. S. (2009) 'Beyond Oil and Gas: The Methanol Economy: Second Edition', *Beyond Oil and Gas: The Methanol Economy: Second Edition*, pp. 1–334.
- Olah, G. A., Prakash, G. K. S. and Goeppert, A. (2011) 'Anthropogenic chemical

carbon cycle for a sustainable future', *Journal of the American Chemical Society*, 133(33), pp. 12881–12898.

Onsager, L. (1931) 'Reciprocal Relations in Irreversible Processes. II.', *Phys. Rev. American Physical Society*, 38(12), pp. 2265–2279.

Orr, B. *et al.* (2016) 'A review of car waste heat recovery systems utilising thermoelectric generators and heat pipes', *Applied Thermal Engineering*, 101, pp. 490–495.

Oshima, K. *et al.* (2014) 'Low temperature catalytic reverse water gas shift reaction assisted by an electric field', *Catalysis Today*, 232, pp. 27–32.

Özbek, M. O. and van Santen, R. A. (2013) 'The Mechanism of Ethylene Epoxidation Catalysis', *Catalysis Letters*, 143(2), pp. 131–141.

Pacchioni, G., Lomas, J. R. and Illas, F. (1997) 'Electric field effects in heterogeneous catalysis', *Journal of Molecular Catalysis A: Chemical*, 119(1–3), pp. 263–273.

Pakulska, M. M., Grgicak, C. M. and Giorgi, J. B. (2007) 'The effect of metal and support particle size on NiO/CeO₂ and NiO/ZrO₂ catalyst activity in complete methane oxidation', *Applied Catalysis A: General*, 332(1), pp. 124–129.

Papaioannou, E. I. *et al.* (2009) 'Electrochemical promotion of the CO₂ hydrogenation reaction using thin Rh, Pt and Cu films in a monolithic reactor at atmospheric pressure', *Catalysis Today*, 146(3–4), pp. 336–344.

Pei, Y.-L. *et al.* (2013) 'High thermoelectric performance of oxyselenides: Intrinsically low thermal conductivity of Ca-doped BiCuSeO', *NPG Asia Materials*, 5.

Pei, Y.-L. *et al.* (2014) 'High thermoelectric performance realized in a bicusseo system by improving carrier mobility through 3D modulation doping', *Journal of the American Chemical Society*, 136(39), pp. 13902–13908.

Pei, Y., Wang, H. and Snyder, G. J. (2012) 'Band engineering of thermoelectric materials', *Advanced Materials*, 24(46), pp. 6125–6135.

Peng-Ont, S. *et al.* (2013) 'Reaction kinetic-induced changes in the electrochemically promoted C₂H₄ oxidation on Pt/YSZ', *Catalysis Letters*, 143(5), pp. 445–453.

- Perdew, J. P., Burke, K. and Ernzerhof, M. (1996) 'Generalized Gradient Approximation Made Simple', *Phys. Rev. Lett.* American Physical Society, 77(18), pp. 3865–3868.
- Pliangos, C. *et al.* (1996) 'Non-faradaic electrochemical modification of catalytic activity: 9. Ethylene oxidation on Pt deposited on TiO₂', *Journal of Catalysis*, 159(1), pp. 189–203.
- Pliangos, C. *et al.* (1996) 'Non-Faradaic Electrochemical Modification of Catalytic Activity 9. Ethylene Oxidation on Pt Deposited on TiO₂', *Journal of Catalysis*, 159, pp. 189–203.
- Poulidi, D., Anderson, C. and Metcalfe, I. S. (2008) 'Remote control of the activity of a Pt catalyst supported on a mixed ionic electronic conducting membrane', *Solid State Ionics*, 179(27–32), pp. 1347–1350.
- Qiu, P. *et al.* (2010) 'Effect of antisite defects on band structure and thermoelectric performance of ZrNiSn half-Heusler alloys', *Applied Physics Letters*. American Institute of Physics, 96(15), p. 152105.
- Regalbuto, J. (2006) *Catalyst Preparation: Science and Engineering* By John R. Regalbuto, *AIChE Journal*.
- Ren, G. *et al.* (2014) 'Electrical and Thermal Transport Behavior in Zn-Doped BiCuSeO Oxyselenides', *Journal of Electronic Materials*.
- Ren, G.-K. *et al.* (2015) 'Enhanced thermoelectric properties in Pb-doped BiCuSeO oxyselenides prepared by ultrafast synthesis', *RSC Advances*, 5, pp. 69878–69885.
- Rideal, E. K. (2008) 'A note on a simple molecular mechanism for heterogeneous catalytic reactions', *Mathematical Proceedings of the Cambridge Philosophical Society*, 35(1), p. 130.
- Rodriguez, J. A. *et al.* (2007) 'Water gas shift reaction on Cu and Au nanoparticles supported on CeO₂(111) and ZnO(0001): Intrinsic activity and importance of support interactions', *Angewandte Chemie - International Edition*, 46(8), pp. 1329–1332.
- Rogl, G. and Rogl, P. (2017) 'Skutterudites, a most promising group of thermoelectric materials', *Current Opinion in Green and Sustainable Chemistry*, 4, pp. 50–57.

- Ruleova, P. *et al.* (2010) 'Thermoelectric properties of Bi₂O₂Se', *Materials Chemistry and Physics*, 119(1–2), pp. 299–302.
- Rull, M. and Fernández, J. F. (2015) 'Skutterudites as Thermoelectric Materials: Revisited', *RSC Advances*. Royal Society of Chemistry, 5, pp. 41653–41667.
- Saadatjou, N., Jafari, A. and Sahebdehfar, S. (2015) 'Ruthenium Nanocatalysts for Ammonia Synthesis: A Review', *Chemical Engineering Communications*. Taylor & Francis, 202(4), pp. 420–448.
- Sameera Devi, C., Kumar, G. S. and Prasad, G. (2015) 'Spectroscopic and electrical studies on Nd³⁺, Zr⁴⁺ ions doped nano-sized BaTiO₃ ferroelectrics prepared by sol-gel method', *Spectrochimica Acta - Part A: Molecular and Biomolecular Spectroscopy*, 136(PB), pp. 366–372.
- Sasajima, K. and Uchida, H. (2011) 'Conductive perovskite-type metal oxide thin films prepared by chemical solution deposition technique', *Materials Science and Engineering*, 18(6).
- Schlögl, R. (2008) 'Ammonia Synthesis', in *Handbook of Heterogeneous Catalysis*. Wiley-VCH Verlag GmbH & Co. KGaA.
- Schlögl, R. (2013) *Chemistry Energy Storage*.
- Schwab, G.-M. (1969) 'Catalytic effects on the surface of semiconductors supports by metals', *Surface Science*, 13, pp. 198–200.
- Schwab, G.-M. (1970) 'Chemical Effects at the Solid / Solid Phase Boundary', *Journal of Colloid and Interface Science*, 34(3), pp. 337–342.
- Schwab, G. M. (1983) 'On the apparent compensation effect', *Journal of Catalysis*, 84(1), pp. 1–7.
- Shakouri, A. (2011) 'Recent developments in semiconductor thermoelectric physics and materials', *Annual Review of Materials Research*, 41, pp. 399–431.
- Shao, H. *et al.* (2016) 'A first-principles study on the phonon transport in layered BiCuOSe', *Scientific Reports*, 6, p. 21035.
- Sharma, B. L. (1984) *Metal-Semiconductor Schottky Barrier Junctions and Their*

Applications. New York and London: Plenum Press.

Shekhah, O., Ranke, W. and Schlögl, R. (2004) 'Styrene synthesis: in situ characterization and reactivity studies of unpromoted and potassium-promoted iron oxide model catalysts', *Journal of Catalysis*, 225(1), pp. 56–68.

Shen, Q. *et al.* (2001) 'Effects of partial substitution of Ni by Pd on the thermoelectric properties of ZrNiSn-based half-Heusler compounds', *Applied Physics Letters*, 79(25), pp. 4165–4167.

Shi, X. *et al.* (2005) 'Filling Fraction Limit for Intrinsic Voids in Crystals: Doping in Skutterudites', *Physical Review Letters*, 95(18), p. 185503.

Sikora, E. and Sikora, J. (1998) 'Work Function and Catalytic Activity Measurements of an IrO₂ Film Deposited on YSZ Subjected to In Situ Electrochemical Promotion', 145(3), pp. 905–908.

Slack, G. A. and Tsoukala, V. G. (1994) 'Some properties of semiconducting IrSb₃', *Journal of Applied Physics*, 76(3), pp. 1665–1671.

Snyder, G. J. *et al.* (2002) 'Supercooling of Peltier cooler using a current pulse', *Journal of Applied Physics*, 92(3), pp. 1564–1569.

Solymosi, F., Tombácz, I. and Kocsis, M. (1982) 'Hydrogenation of CO on supported Rh catalysts', *Journal of Catalysis*, 75(1), pp. 78–93.

Souentie, S., Hammad, A. and Vayenas, C. G. (2009) 'Steady-state multiplicity phenomena during the electrochemical promotion of NO reduction by C₂H₄ in presence of O₂ on thin Rh and Pt catalyst-electrodes in a monolithic electropromoted reactor', *Catalysis Today*, 146, pp. 285–292.

Sousa-Aguiar, E. F. *et al.* (2014) 'Some important catalytic challenges in the bioethanol integrated biorefinery', *Catalysis Today*, 234, pp. 13–23.

Stoukides, M. and Vayenas, C. G. (1981) 'The effect of electrochemical oxygen pumping on the rate and selectivity of ethylene oxidation on polycrystalline silver', *Journal of Catalysis*, 70(1), pp. 137–146.

Sui, J. *et al.* (2013) 'Texturation boosts the thermoelectric performance of BiCuSeO oxyselenides', *Energy & Environmental Science*, 6(10), p. 2916.

- Sun Lee, D. *et al.* (2013) 'Density of state effective mass and related charge transport properties in K-doped BiCuOSe', *Applied Physics Letters*, 103(23), pp. 2011–2015.
- Sze, S. M. and Ng, K. K. (2006) *Physics of Semiconductor Devices: Third Edition*, *Physics of Semiconductor Devices: Third Edition*.
- Tauster, S. J., Fung, S. C. and Garten, R. L. (1978) 'Strong Metal-Support Interactions. Group 8 Noble Metals Supported on TiO₂', *Journal of American Chemical Society*, 100(1), pp. 170–175.
- Terasaki, I., Sasago, Y. and Uchinokura, K. (1997) 'Large thermoelectric power in NaCo₂O₄ single crystals', *Phys. Rev. B*, 56(20), pp. R12685--R12687.
- Thomas, J. M. and Thomas, W. J. (1996) *Principles and Practise of Heterogenous Catalysis*. VCH.
- Tritt, T. M. and Subramanian, M. a (2006) 'Thermoelectric Materials, Phenomena, and Applications : A Bird's Eye View', *MRS Bulletin*, 31, pp. 188–198.
- Tsiplakides, D. *et al.* (1998) 'Work function and catalytic activity measurements of an IrO₂ film deposited on YSZ subjected to in situ electrochemical promotion', *Journal of the Electrochemical Society*, 145(3), pp. 905–908.
- Tsiplakides, D. and Balomenou, S. (2008) 'Electrochemical promoted catalysis: Towards practical utilization', *Chemical Industry and Chemical Engineering Quarterly*, 14(2), pp. 97–105.
- Unde, R. B. (2012) *Kinetics and Reaction Engineering Aspects of Syngas Production by the Heterogeneously Catalysed Reverse Water Gas Shift Reaction*, PhD. Universität Bayreuth.
- Valden, M. (1998) 'Onset of Catalytic Activity of Gold Clusters on Titania with the Appearance of Nonmetallic Properties', *Science*, 281, pp. 1647–1650.
- Vaqueiro, P. *et al.* (2015) 'The role of copper in the thermal conductivity of thermoelectric oxychalcogenides: do lone pairs matter?', *Phys. Chem. Chem. Phys.*, 17, pp. 31735–31740.
- Varkaraki, E. *et al.* (1995) 'Electrochemical promotion of IrO₂ catalyst for the gas phase combustion of ethylene', *Journal of Applied Electrochemistry*, 25(10), pp. 978–981.

Vayenas, C. G. *et al.* (2001) *Electrochemical Activation of Catalysis: Promotion, Electrochemical Promotion, and Metal-Support Interactions*. New York: KLUWER ACADEMIC PUBLISHERS.

Vayenas, C. G., Bebelis, S. and Ladas, S. (1990) 'Dependence of catalytic rates on catalyst work function', *Nature*, 343, pp. 625–627.

Vayenas, C. G. and Brosda, S. Pliangos, C. (2002) 'Rules and Mathematical Modeling of Electrochemical and Classical Promotion 2. Modeling', *Journal of Catalysis*, 208(1), pp. 38–53.

Vayenas, C. G., Brosda, S. and Pliangos, C. (2003) 'The double-layer approach to promotion, electrocatalysis, electrochemical promotion, and metal–support interactions', *40th Anniversary Commemorative Issue*, 216(1–2), pp. 487–504.

Vernoux, P. *et al.* (2013) 'Ionically conducting ceramics as active catalyst supports', *Chemical Reviews*, 113(10), pp. 8192–8260.

Vernoux, P., Guth, M. and Li, X. (2009) 'Ionically Conducting Ceramics as Alternative Catalyst Supports', *Electrochemical and Solid-State Letters*, 12(7), pp. E9–E11.

Vikram *et al.* (2017) 'Bismuth based half-Heusler alloys with giant thermoelectric figures of merit', *Journal of Materials Chemistry A*, 5(13), pp. 6131–6139.

Wan, C. L. *et al.* (2006) 'Effect of point defects on the thermal transport properties of $(\text{La}_x \text{Gd}_{1-x})_2\text{Zr}_2\text{O}_7$: Experiment and theoretical model', *Physical Review B - Condensed Matter and Materials Physics*, 74(14).

Wang, J. *et al.* (2017) 'High-efficiency thermoelectric $\text{Ba}_8\text{Cu}_{14}\text{Ge}_6\text{P}_{26}$: bridging the gap between tetrel-based and tetrel-free clathrates', *Chemical Science*, 0, pp. 1–9.

Wang, W. *et al.* (2011) 'Recent advances in catalytic hydrogenation of carbon dioxide', *Chem. Soc. Rev.*, 40(7), p. 3703.

Wang, Z. *et al.* (2012) 'Self-sustained electrochemical promotion catalysts for partial oxidation reforming of heavy hydrocarbons', *International Journal of Hydrogen Energy*, 37(23), pp. 17928–17935.

Wieckowski, A., Savinova, E. R. and Vayenas, C. G. (2003) *Catalysis and Electrocatalysis At Nanoparticle Surfaces, Chemistry*. New York: Marcel Dekker Inc.

Wood, C. (1988) 'Materials for thermoelectric energy conversion', *Reports on Progress in Physics*, 51(4), p. 459.

Wu, N. *et al.* (2014) 'High temperature thermoelectric properties of $\text{Ca}_3\text{Co}_4\text{O}_9^{+\delta}$ by auto-combustion synthesis and spark plasma sintering', *Journal of the European Ceramic Society*, 34(4), pp. 925–931.

Wunderlich, W., Mori, T. and Sologub, O. (2013) 'Large Seebeck Coefficient and Electric Current', *Condensed Matter*, pp. 2–6.

Xia, C. *et al.* (2010) 'Quantifying electrochemical promotion of induced bipolar Pt particles supported on YSZ', *Electrochemistry Communications*, 12(11), pp. 1551–1554.

Xia, C. *et al.* (2011) 'Electrochemical promotion of CO combustion over non-percolated Pt particles supported on YSZ using a novel bipolar configuration', *Electrochemistry Communications*, 13(1), pp. 99–101.

Xiaoding, X. and Moulijn, J. (1996) 'Mitigation of CO_2 by Chemical Conversion: Plausible Chemical Reactions and Promising Products', *Energy & Fuels*, 10(2), pp. 305–325.

Yan, X. *et al.* (2017) 'Dependences of phase stability and thermoelectric properties of type-I clathrate $\text{Ba}_8\text{Cu}_4.5\text{Si}_6\text{Ge}_{35.5}$ on synthesis process parameters', *Journal of Alloys and Compounds*, 725, pp. 783–791.

Yang, J. *et al.* (2014) 'Low effective mass leading to an improved ZT value by 32% for n-type BiCuSeO : A first-principles study', *Journal of Materials Chemistry A*, 2(34), pp. 13923–13931.

Yentekakis, I. V *et al.* (1994) 'In Situ controlled promotion of catalyst surfaces via NEMCA: The effect of Na on the Pt-catalyzed CO oxidation', *Journal of Catalysis*, 146(1), pp. 292–305.

Yentekakis, I. V *et al.* (1998) 'Promotion by Sodium in Emission Control Catalysis: A Kinetic and Spectroscopic Study of the Pd-Catalyzed Reduction of NO by Propene', *Journal of Catalysis*, 176(1), pp. 82–92.

Yentekakis, I. V *et al.* (1999) 'Extraordinarily effective promotion by sodium in emission

control catalysis: NO reduction by propene over Na-promoted Pt/ γ -Al₂O₃', *Applied Catalysis B: Environmental*, 22(2), pp. 123–133.

Yu, C. *et al.* (2008) 'Thermal conductivity reduction in oxygen-deficient strontium titanates', *Applied Physics Letters*, 92(19), pp. 1–4.

Zhang, Q. *et al.* (2012) 'Suppression of grain growth by additive in nanostructured p-type bismuth antimony tellurides', *Nano Energy*, 1(1), pp. 183–189.

Zhang, X. *et al.* (2017) 'BiCuSeO Thermoelectrics: An Update on Recent Progress and Perspective', *Materials*, 10(2), p. 198.

Zhang, X. and Zhao, L. (2015) 'Thermoelectric materials : Energy conversion between heat and electricity', *Journal of Materiomics*. Elsevier Ltd, 1(2), pp. 92–105.

Zhang, Z. and Yates, J. T. (2012) 'Band bending in semiconductors: Chemical and physical consequences at surfaces and interfaces', *Chemical Reviews*, 112(10), pp. 5520–5551.

Zhao, L.-D. *et al.* (2014a) 'BiCuSeO oxyselenides: new promising thermoelectric materials', *Energy & Environmental Science*, 7, pp. 2900–2924.

Zhao, L.-D. and Li, J.-F. (2016) 'Chapter 9 BiCuSeO', in *Materials Aspect of Thermoelectricity*. CRC Press, pp. 317–350.

Zhao, L. D. *et al.* (2010) 'Bi_{1-x}Sr_xCuSeO oxyselenides as promising thermoelectric materials', *Applied Physics Letters*, 97(9).

Zhao, X. B. *et al.* (2005) 'Bismuth telluride nanotubes and the effects on the thermoelectric properties of nanotube-containing nanocomposites', *Applied Physics Letters*. American Institute of Physics, 86(6), p. 62111.

Zheng, J.-C. (2008) 'Recent advances on thermoelectric materials', *Frontiers of Physics in China*, 3, p. 10.

Zheng, X. F. *et al.* (2014) 'A review of thermoelectrics research - Recent developments and potentials for sustainable and renewable energy applications', *Renewable and Sustainable Energy Reviews*, 32, pp. 486–503.

Zhou, X. (2012) 'Self sustained electrochemical promotion catalysts'. US Patent

8697597 B2.

Zhou, X., Huang, H. and Liu, H. (2013) 'Study of partial oxidation reforming of methane to syngas over self-sustained electrochemical promotion catalyst', *International Journal of Hydrogen Energy*, 38(15), pp. 6391–6396.

APPENDICES

Appendix A – Analytical Method Development and Validation

A.1 GC/TCD Method and Apparatus

The GC instrumentation used was HRGC 8340 series (Fisons Instruments, Italy) equipped with a single stage dual-packed column for separating the target gas component from their mixture. The detection was performed by using a thermal conductivity detector (TCD) and the output signal was monitored using TotalChrom Workstation (Version 6.2.1 for Windows) data system. For introducing the gas sample into the GC system, all of the necessary parameters for the analysis have been pre-programmed into the G.C. controller (MFC800). The parameters for the GC/TCD method of analysis (Table A-1) were based on the method developed.

Table A-1. GC/TCD experimental parameters for the gas analysis.

Apparatus	GC-8340
Carrier gas	Helium
Carrier flow rate (mL/min)	50
Injection Time (min)	1.50
Oven Temperature (°C)	50
Injector Temperature (°C)	50
Detector Temperature (°C)	210
Injection Volume(mL)	5
Detector	TCD

A.2 GC Instrument Calibration

External calibration standards were used to carry out the gases analysis via GC/TCD. In order to validate this analytical method, BOC gases certified standards of O₂, CO₂ and C₂H₄ mixture in He were balanced using a pure helium gas (BOC, 99.996%) to obtain desired concentrations. The calibration curve was made by plotting the peak area of gas components versus their concentration. In addition, the concentrations of all components in the gas sample were determined by inserting the peak area of corresponding gas component into their calibration curve.

A.3 Method Validation

The GC/TCD method was validated following the International Conference on Harmonisation (ICH) and Food and Drug Administration (FDA) guidelines. All analyses were carried out under the same condition except for the carrier gas flow rate for repeatability. Specifically, the GC/TCD method was evaluated for linearity, accuracy, repeatability / precision, reproducibility, and robustness and specificity to demonstrate that the technique meets the guidelines standards. The accuracy of the technique was determined by direct comparison against an IR analyser (G150 O₂ and CO₂, Gem Scientific), which is known to be highly accurate. The precision of the GC/TCD method was ascertained by 10 successive analysis for each of 3 gases. Reproducibility is the closeness of the agreement between the repeated measurements results that carried out with the same test method at different flow rates. The robustness of the GC/TCD technique of three gases were evaluated by the repeated analysis of 10 of the standard samples by repeating analysis after a period of over 10 and 100 days. The specificity is demonstrated from the analysis of the chromatogram presented in Chapter 3.

A.4 Results

A.4.1 Linearity

Linearity verifies that the standards in a concentration range where the analyte response is proportional to concentration. Linearity is expressed by the correlation coefficient (r^2). The mixed standard (Table A-2) was diluted to five different lower-concentration levels for calibration. The five calibration standards were analysed by GC/TCD. The resultant calibration curve exhibited excellent linearity results with $R^2 = 0.9999$ over 5 levels spanning of all the gas components of 100 – 1000 ppm (Table A-3).

Table A-2. Concentration of BOC certified standard gases.

Components	O ₂	CO ₂	C ₂ H ₄
Conc. (ppm)	1055	1027	1091

Table A-3. Linearity results of TCD channel.

Conc. (ppm)	O ₂	CO ₂	C ₂ H ₄
Level 1	95	104	103
Level 2	255	253	252
Level 3	508	504	505
Level 4	760	755	754
Level 5	1055	1027	1091
R ²	1.0000	0.9999	0.9998

A.4.2 Accuracy

The accuracy of the GC-TCD method was validated against an IR analyser (G150 O₂ and CO₂, Gem Scientific), which was considered to give the true gas concentration. The analyses of the 10 samples of O₂ (1055 ppm) and CO₂ (1027 ppm) presented in Table A-4. An excellent agreement was found between the two techniques, with average relative errors of 3.79 % and 1.70% for O₂ and CO₂ respectively.

Table A-4. Accuracy results of O₂ and CO₂ from TCD channel and IR analyser.

Conc. ppm	GC/TCD	IR analyser	GC/TCD	IR analyser
	CO ₂	O ₂	CO ₂	CO ₂
Average	1038.8	1000.9	1020.8	1003.7
Std. Dev	7.97	4.25	8.56	2.41
RSD %	0.77	0.43	0.84	0.24
Error %		3.79		1.70

A.4.3 Repeatability / Precision

The repeatability of a measurement method is the agreement between the results of successive measurements of the same measured carried out under the same conditions of measurement. The precision of an analytical method is degree of repeatability of the results in a series of experiments run during a single session by single operator with identical reagents and equipment. To examine the repeatability of the method, the average and standard deviation of a set of ten measurements made on the same day and under the same conditions, was determined. The relative standard deviations (RSD) for O₂, CO₂ and C₂H₄ components were lower than 1.2%,

0.7% and 0.9% by using TCD channel respectively. The results in terms of peak area repeatability based on 10 consecutive runs of all compounds were show in Table A-5. Results also exhibit excellent repeatability.

Table A-5. TCD Channel Repeatability.

Peak area	O ₂	CO ₂	C ₂ H ₄
Average	28945.12	34603.25	35992
Std. Dev	341.03	243.32	315.22
RSD%	1.18	0.70	0.88

A.4.4 Reproducibility

Reproducibility is the closeness of the agreement between the repeated measurements results that carried out with the same test method at different flow rates at 50 and 55 mL/min. In this reproducibility precision estimation, the value in term of RSD of repeated measurements was compared and the results were listed in Table A-6 for flow rate change. It can be seen that the lowest % RSD values at 50 ml/min showed an exceptional repeatability precision, which suggested that the flow rate of 50 ml/min was the most reproducible measurement.

Table A-6. TCD Channel Reproducibility.

Flow rate (ml/min)		50	55
O₂	Area Avg.	29252.36	26052.36
	Std. Dev	123.2	123.20
	RDS %	0.42	0.47
CO₂	Area Avg.	33768.93	30161.01
	Std. Dev	257.28	235.45
	RDS %	0.76	0.78
C₂H₄	Area Avg.	35408.33	29990
	Std. Dev	77.51	101.12
	RDS %	0.22	0.34

A.4.5 Robustness

The robustness of the GC/TCD method of gas analysis was demonstrated by the repeated analysis of 10 samples after a period of over 10 and 100 days. The results in Table A-7 show very good agreement for the all measurements. Therefore, it can be concluded that a delay time prior to analysis, even on the order of days, will not significantly affect the results.

Table A-7. TCD Channel Repeatability.

Time Periods (Days)		1	10	100
O ₂	Avg.	30904.2	29494.8	29158.1
	Std. Dev	951.39	446.15	88.3
	RDS %	3.08	1.51	0.3
CO ₂	Avg.	34870	34702.5	34362.5
	Std. Dev	203.65	247.57	159.82
	RDS %	0.58	0.71	0.47
C ₂ H ₄	Avg.	36340	36145	35688.3
	Std. Dev	212.9	480.03	223.07
	RDS %	0.59	1.33	0.63

A.5 Summary Report

A GC/TCD method for the determination of O₂, CO₂ and C₂H₄ concentrations was developed and validated. Results of the analytical method validation are presented in Table A-7. It can be summarised:

- The method did not show peaks' interference.
- The method was precise and accurate.
- The validation parameters were within specified limits.

Table A-8. Summary validation results parameters.

Parameters	Acceptance criteria	Results
Linearity	The lowest Correlation coefficient was 0.9998.	Graph linearity $r^2 \geq 0.995$
Accuracy	Meets the acceptance criteria.	RSD ≤ 2.0
Robustness	Meets the acceptance criteria.	RSD ≤ 2.0
Precision	The RSD of 10 replicates was within the limit; Area: 1.18 for O ₂ , 0.7 for CO ₂ and 0.88 for C ₂ H ₄ .	% RSD : NMT 2.0

Appendix B – Supplementary Information for Chapter 6

The below experiments have been repeated once and the results were reproducible. Figure B-1. shows the ethylene oxidation reaction rates at different front surface temperature T_h for a sample of Pt thin films of 80 nm supported on BCSO with a large TE effect (solid red line, Pt(80)/BCSO TE), and under a reduced TE effect (dashed red line, Pt(80)/BCSO RTE) conditions respectively.

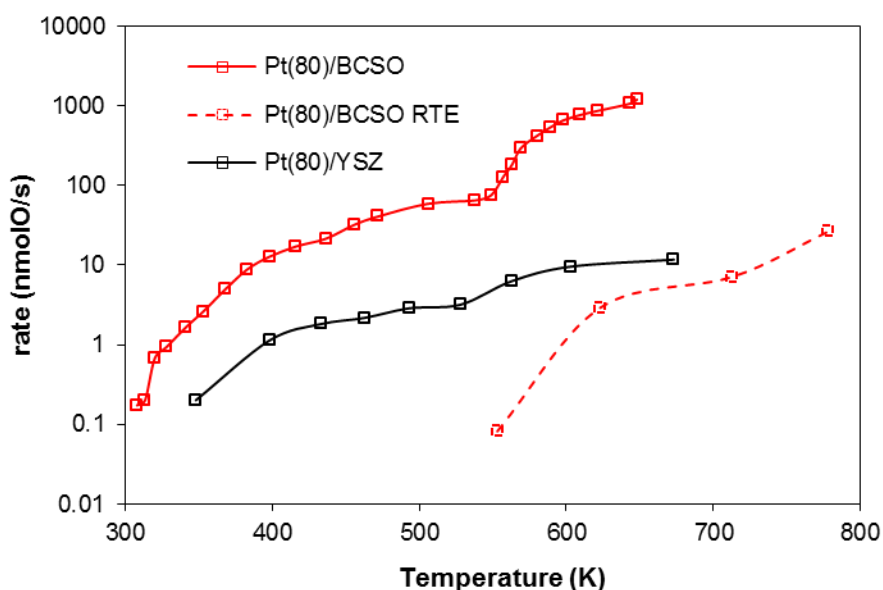


Figure B-1. Ethylene oxidation rates as a function of temperature at the catalyst surfaces, for Pt(80)/YSZ which has no thermoelectric effect, and for Pt(80)/BCSO under large TE effect (Pt(80)/BCSO TE) and reduced TE effect (RTE) conditions. Much higher Seebeck voltages were generated across the thickness of the catalyst support BCSO under TE than under RTE conditions. Notice the logarithm scale for rate.

Figure B-2 shows their temperature dependences of the reaction rates. All four samples, including the BCSO without any Pt, showed a similar behaviour as Pt(80)/BCSO TE (Figure B-1).

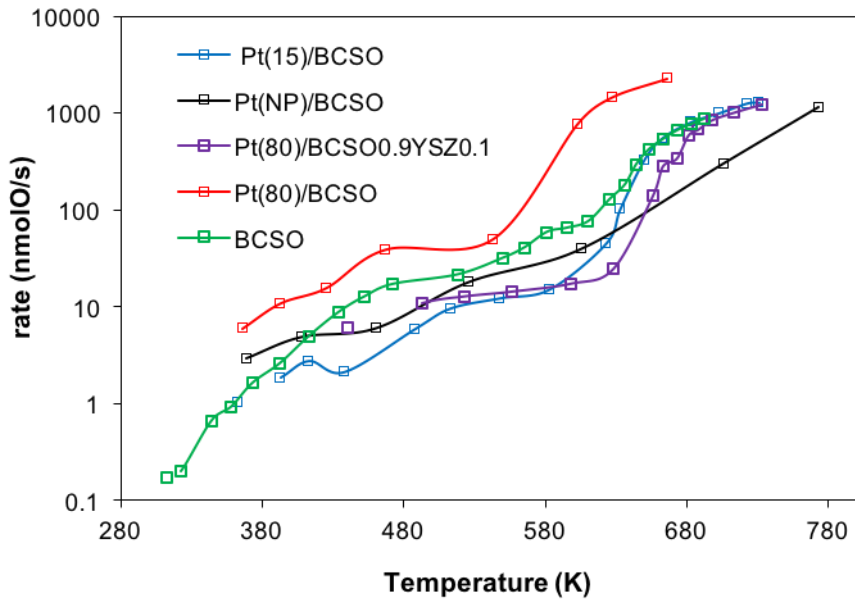


Figure B-2. Reaction rate r as a temperature function of the five samples: BCSO, Pt(NP)/BCSO, Pt(15)BCSO, Pt(80)/BCSO and Pt(80)/BiCuSeO_{0.9}YSZ_{0.1}. The rate (r) increased by more than 3 orders with T_h temperature increase.

The Seebeck voltages at different temperature differences for all the five samples are shown in Figure B-3.

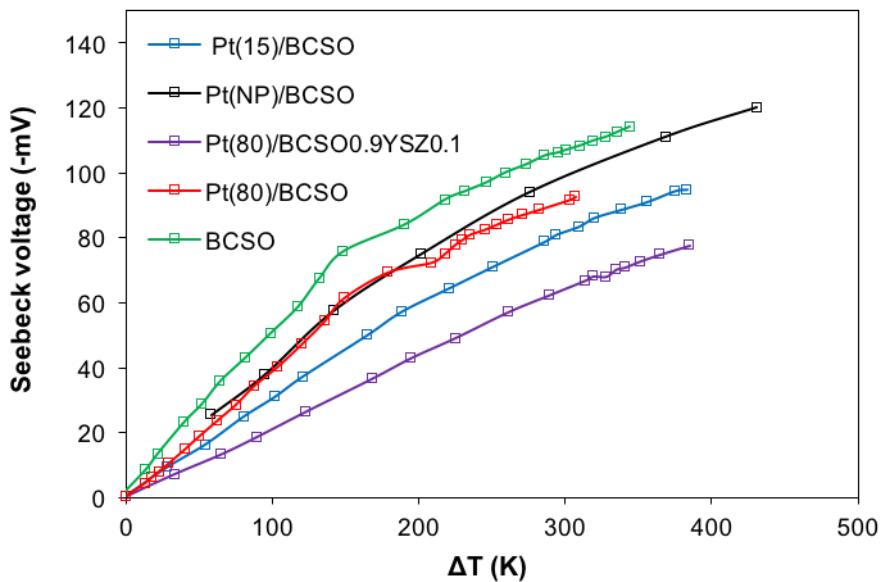


Figure B-3. Measured Seebeck voltage as functions of temperature difference across the sample thickness of the five samples: BCSO, Pt(NP)/BCSO, Pt(15)BCSO, Pt(80)/BCSO and Pt(80)/BiCuSeO_{0.9}YSZ_{0.1}.

Ln(r) vs 1/T for Pt(80)/YSZ was depicted in Figure B-4, indeed demonstrating a linear relationship.

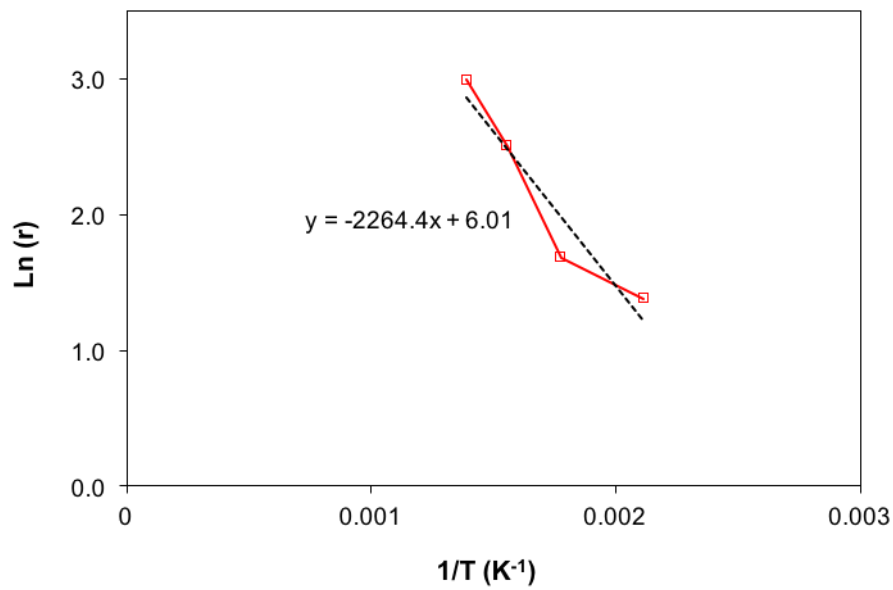


Figure B-4. Arrhenius law for ethylene oxidation on Pt. Ln(r) as a function of 1/T for ethylene oxidation rate on Pt(80)/YSZ. YSZ is not a thermoelectric material.

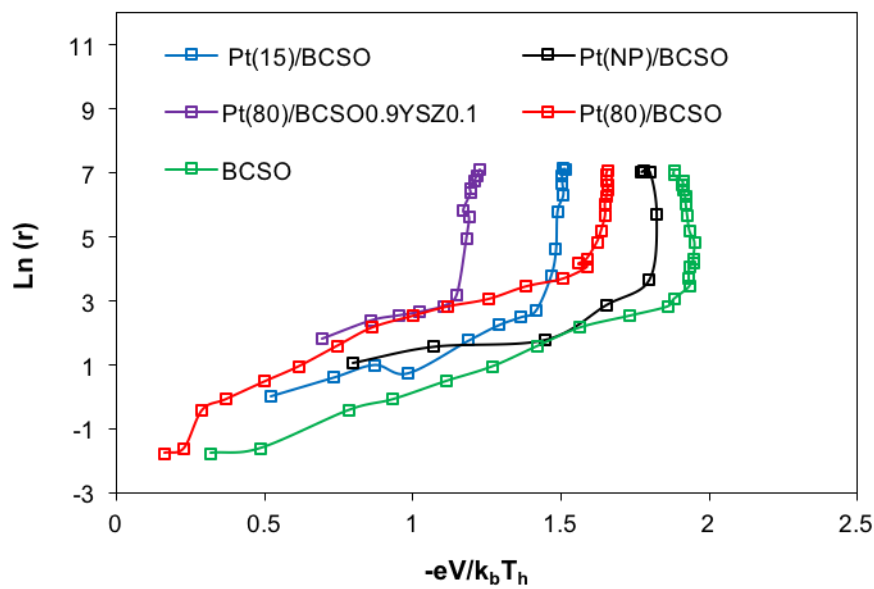


Figure B-5. A linear relationship between Ln(r) and $-eV/k_bT_h$ of the five samples: BCSO, Pt(NP)/BCSO, Pt(15)BCSO, Pt(80)/BCSO and Pt(80)/BiCuSeO_{0.9}YSZ_{0.1}.

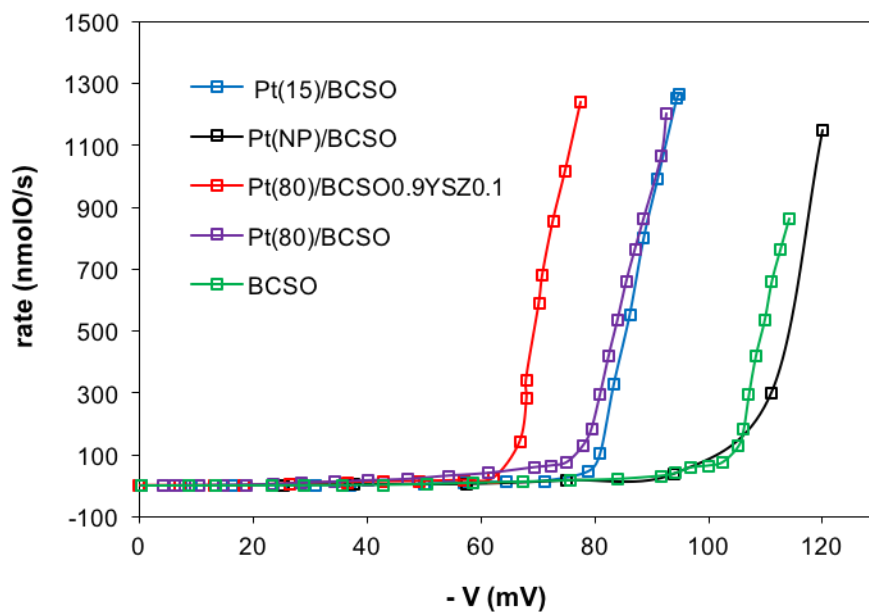


Figure B-6. The rate r as a function of Seebeck voltage V of the five samples: BCSO, Pt(NP)/BCSO, Pt(15)BCSO, Pt(80)/BCSO and Pt(80)/BiCuSeO_{0.9}YSZ_{0.1}.

Appendix C – Scholarly Contributions

C.1 Refereed journal articles (Published, accepted or submitted)

- Achour A, Chen K, Reece M, and Huang Z (2017) “*Tuning of catalytic activity by thermoelectric materials for carbon dioxide hydrogenation*”, *Advanced Energy Materials*, In Press.
- Achour A, Chen K, Reece M, and Huang Z “*Enhanced thermoelectric performance of Cs doped BiCuSeO prepared by flux synthesis*”, *Journal of Alloys and Compounds*, In Press.
- Achour A, Liu J, Peng P, and Huang Z “*In-situ tuning of metal-support interaction and catalytic activity by thermoelectric effect*”, *Advanced Energy Materials*, Submitted.
- Achour A, and Huang Z, “*In-situ tuning of catalytic activity by thermoelectric effect under rich O₂ conditions on ethylene oxidation*”, Article manuscript in progress.

C.2 Patent

- Achour A, and Huang Z “*Thermoelectrical promotion of catalysis*”, the UK Intellectual Property Office, Patent Pending.

C.3 Conference Oral and Poster Presentations

- Achour A*, Chen K, Reece M, and Huang Z “*Enhanced thermoelectric performance of Cs doped BiCuSeO prepared by flux synthesis.*” Oral presentation - 19th Conference on Energy, Materials Science and Engineering, Feb 16-17, 2017 Venice, Italy.
- Achour A*, Chen K, Reece M, and Huang Z “*Thermoelectrical properties of Cs doped BiCuSeO as promising oxide materials for thermoelectric energy converter.*” Poster session - 5th Conference on Multifunctional, Hybrid and Nanomaterials, Mar 06-10, 2017 Lisbon, Portugal.

* Presenting author

Paper 1: Tuning of Catalytic Activity by Thermoelectric Materials for Carbon Dioxide Hydrogenation

FULL PAPER

Thermoelectric Materials

ADVANCED
ENERGY
MATERIALS

www.advenenergy.com

Tuning of Catalytic Activity by Thermoelectric Materials for Carbon Dioxide Hydrogenation

Abdenour Achour, Kan Chen, Michael J. Reece, and Zhaorong Huang*

An innovative use of a thermoelectric material (BiCuSeO) as a support and promoter of catalysis for CO₂ hydrogenation is reported here. It is proposed that the capability of thermoelectric materials to shift the Fermi level and work function of a catalyst lead to an exponential increase of catalytic activity for catalyst particles deposited on its surface. Experimental results show that the CO₂ conversion and CO selectivity are increased significantly by a thermoelectric Seebeck voltage. This suggests that the thermoelectric effect can not only increase the reaction rate but also change chemical equilibrium, which leads to the change of thermodynamic equilibrium for the conversion of CO₂ in its hydrogenation reactions. It is also shown that this thermoelectric promotion of catalysis enables BiCuSeO oxide itself to have a high catalytic activity for CO₂ hydrogenation. The generic nature of the mechanism suggests the possibility that many catalytic chemical reactions can be tuned in situ to achieve much higher reaction rates, or at lower temperatures, or have better desired selectivity through changing the backside temperature of the thermoelectric support.

T absolute temperature.^[1] Most currently used TE materials are heavy-metal-based, such as Bi₂Te₃ and PbTe, due to their high ZT. However, these materials are not best suited for medium to high temperature, large scale applications, because of problems such as their low melting, or decomposition, or oxidation temperatures. They are also harmful to environment and contain scarce constituent elements. On the other hand, oxide TE materials, such as p-type layered BiCuSeO, cobalt oxide A_xCoO₂ (A = Na, Ca, Sr), and n-type NaTaO₃-Fe₂O₃, CaMnO₃ and SrTiO₃ based perovskites, can overcome these disadvantages.^[2] TE devices are usually configured in modules by connecting the p-type and n-type TE legs electrically in series and thermally in parallel. We report here an innovative use of TE materials as a catalyst support and show its substantial promotional effect on catalytic activity.

BiCuSeO (BCSO) was selected as the thermoelectric materials for this investigation because it possesses good TE properties to over 900 K, an extraordinary low intrinsic thermal conductivity of less than 0.5 W m⁻¹ K⁻¹; therefore, a high temperature difference can easily built up across this material; high Seebeck coefficient up to 500 μV K⁻¹ at room temperature and greater than 300 μV K⁻¹ at high temperatures, and no decomposition below 773 K.^[2]

Catalyst promoters improve the activity, selectivity, or lifetime of a catalyst and can generally be divided into structural and electronic promoters. Structural promoters enhance and stabilize the dispersion of the catalyst on the support. Electronic promoters induce changes of electronic state of the catalyst near the Fermi level.^[3] These promoters are added and fixed during the catalyst preparation and therefore can be subject to degradation during the catalytic process. On the other hand, electrochemical promotion, also called non-Faradaic electrochemical modification of catalytic activity (NEMCA), which allows for controlled in situ introduction of promoters on catalyst surfaces under operating conditions.^[3,4] NEMCA has proved to be an excellent research technique but its large scale industrial use has been limited due to its shortcomings: (i) low efficiency of catalyst materials (which are often expensive noble metals) because it requires a continuous electrode to maintain conductivity, (ii) need to maintain electrical connection under often harsh conditions, and (iii) the incompatibility of its reactor configuration (often a fuel cell configuration) with typical chemical reactors (fixed bed, monolithic, and fluidized bed).^[5]


We report here the realization of in situ, reversible, and significant modification of catalytic activity for both continuous

1. Introduction

Thermoelectric (TE) materials have recently attracted widespread interest in research because they can convert a temperature difference directly into an electrical voltage via the Seebeck effect, $S = -V/\Delta T$, where V is the voltage between the two ends of the TE material and ΔT the temperature difference, S is the Seebeck coefficient. The performance of a TE material is ranked by its figure of merit $ZT = S^2\sigma T/\kappa$, where σ is the electrical conductivity, κ the thermal conductivity, and

A. Achour, Dr. Z. Huang
Surface Engineering and Nanotechnology Institute
Cranfield University
Bedfordshire MK43 0AL, UK
E-mail: z.huang@cranfield.ac.uk

Dr. K. Chen, Prof. M. J. Reece
School of Engineering and Materials Science
Queen Mary
University of London
Mile End Rd, London E1 4NS, UK

 The ORCID identification number(s) for the author(s) of this article can be found under <https://doi.org/10.1002/aenm.201701430>.

© 2017 The Authors. Published by WILEY-VCH Verlag GmbH & Co. KGaA, Weinheim. This is an open access article under the terms of the Creative Commons Attribution License, which permits use, distribution and reproduction in any medium, provided the original work is properly cited.

The copyright line for this article was changed on 15 Nov 2017 after original online publication.

DOI: 10.1002/aenm.201701430

Paper 2: Enhanced thermoelectric performance of Cs doped BiCuSeO prepared by flux synthesis

Journal of Alloys and Compounds 735 (2018) 861–869



Contents lists available at ScienceDirect

Journal of Alloys and Compounds

journal homepage: <http://www.elsevier.com/locate/jalcom>



Enhanced thermoelectric performance of Cs doped BiCuSeO prepared through eco-friendly flux synthesis



Abdenour Achour^{a,*}, Kan Chen^b, Michael J. Reece^b, Zhaorong Huang^a

^a Surface Engineering and Nanotechnology Institute, Cranfield University, Bedfordshire, MK43 0AL, UK

^b Department of Materials, Queen Mary University of London, Mile End Road, London, E1 4NS, UK

ARTICLE INFO

Article history:

Received 12 June 2017

Received in revised form

6 October 2017

Accepted 7 November 2017

Available online 10 November 2017

Keywords:

BiCuSeO

Thermoelectric materials

Cs doping

Flux synthesis

Thermal conductivity

ABSTRACT

The synthesis of BiCuSeO oxyselenides by a flux method in air has been investigated. A maximum power factor of $230 \mu\text{Wm}^{-1}\text{K}^{-2}$ and a very low thermal conductivity of $0.42 \text{ Wm}^{-1}\text{K}^{-1}$ were obtained, leading to a high ZT value of 0.37 at 680 K for pristine BiCuSeO. With Cs doping, a large enhancement in electrical conductivity coupled with a moderate decrease in Seebeck coefficient lead to a power factor of $340 \mu\text{Wm}^{-1}\text{K}^{-2}$ at 680 K. In addition, Cs doping reduced the thermal conductivity further to $0.35 \text{ Wm}^{-1}\text{K}^{-1}$ at 680 K. The combination of higher power factor and reduced thermal conductivity results in a high ZT value of 0.66 at 680 K for $\text{Bi}_{0.995}\text{Cs}_{0.005}\text{CuSeO}$.

© 2017 Elsevier B.V. All rights reserved.

1. Introduction

Nearly 70% of the world's useful energy is lost as waste heat. Among the viable technologies for energy recovery, thermoelectrics (TE) can capture and transform waste heat directly into electric power [1–3]. This is based on the Seebeck effect, where an electromotive force develops when a material is exposed to a temperature gradient. Moreover, these TE devices do not have moving parts, such as in a compressor, which make them free of noise and vibration. The existing TE technologies can convert less than 10% of heat energy into electricity [3,4]. This conversion efficiency depends on a dimensionless figure of merit ZT, which only depends on the intrinsic properties of the materials, defined as [5]:

$$ZT = \frac{S^2 \sigma T}{\kappa} \quad (1)$$

where σ is the electrical conductivity, S is the Seebeck coefficient, κ is the thermal conductivity and T is the absolute temperature. Despite the high ZT values of some metallic alloys, their thermal instability, high-cost and toxic constituent elements, make these materials difficult to use for large scale application and

commercialisation [6]. To overcome these disadvantages, several families of oxide-based materials have been investigated as promising TE materials, these include: perovskite-like compounds such as SrTiO_3 [7,8], CaMnO_3 [9]; layered compounds such as $\text{Ca}_3\text{Co}_4\text{O}_9$ [10] and NaCoO_2 [11], and simple oxides like ZnO [12] and In_2O_3 [13].

Recently, a promising middle temperature range TE system based on the oxyselenides BiCuSeO (BCSO) has been reported. BCSO materials have high ZT values due to its intrinsically low thermal conductivity and relatively large Seebeck coefficient. As a p-type TE, the Seebeck coefficient for BCSO was found to be over $300 \mu\text{V/K}$ at about 600 K [14–19], as compared to less than $200 \mu\text{V/K}$ for other p-type TE materials such as $\text{Na}_{0.85}\text{CoO}_2$ and $\text{Ca}_3\text{Co}_4\text{O}_9$ at 673 K [10,11]. Moreover, its ZT value has been improved by optimizing electrical conductivity through the partial substitution of Bi^{3+} with bivalent elements (ZT value for Mg, Sr, Ca and Ba were 0.67, 0.76, 0.9 and 1.1 respectively at 923 K) and a monovalent element (ZT values for Na was 0.97 at 873 K) [14–19]. More recently, a high ZT value of 1.4 for Ba-doped BCSO via grain-texturing and modulating doping has been obtained [20,21]. Furthermore, the ZT has been boosted to the maximum value of 1.5 at 873 K via a dual doping approach [22]. However, little attention has been paid to new methods of synthesis.

In this paper, a B_2O_3 flux method to synthesise BCSO thermoelectric compounds in air is reported. Boron oxide serves as a

* Corresponding author.

E-mail address: a.achour@cranfield.ac.uk (A. Achour).

<https://doi.org/10.1016/j.jalcom.2017.11.104>

0925-8388/© 2017 Elsevier B.V. All rights reserved.